Local Helioseismology with Solar Optical Telescope onboard Hinode

by

Kaori Nagashima

A dissertation submitted to the Department of Astronomical Science,
the Graduate University for Advanced Studies,
in partial fulfillment of the requirement for the degree of Doctor of Philosophy

Mitaka, Tokyo

January, 2010

Abstract

Helioseismology is the unique way to probe the solar interior by measuring the surface oscillation signals. We have carried out local helioseismology analyses, exploiting the recent *Hinode*/SOT data, ultimately motivated by a desire to understand the activity phenomena on the Sun. Part of our endeavour has been in theoretical regime as well.

Mechanism of solar activity is one of the biggest remaining mysteries of the Sun. Sometimes sunspots appear on the Sun and explosions in the solar atmosphere are observed around them. Sunspots are manifestation of the solar magnetic fields which have floated from the deep interior of the Sun. Interaction between magnetic field and flows is considered to play a key role in the mechanism driving the solar activity and its cycle, although we cannot see through the subsurface layers of the Sun where the magnetic field is generated and interacts with flows, unless we use the helioseismological techniques.

The Solar Optical Telescope (SOT) onboard the *Hinode* satellite is capable of observing the Sun with the highest-resolution from a space-bourne instrument. The dataset obtained by SOT is not designed for, but potentially very useful for helioseismology observation, although the field of view is not so large. Therefore, we have set out to carry out local helioseismology analyses by SOT data.

First, we have examined the solar oscillation itself in SOT signal, focusing on the oscillations in sunspots. In the umbrae of sunspots, we have detected 3-minute oscillation in the chromospheric lines, the so-called 'umbral flash'. All the sunspots investigated have shown the umbral flash, although the strength of the signal varies. One of the sunspots we have examined, a nearly circular one, showed the oscillation

power deficit around the center of the umbra. Such a feature has never been reported and is not readily explained by existent models of the umbral flash. We have also examined the oscillation signals using other instruments, namely, *SOHO*/MDI and Nobeyama Radio Heliograph, and have compared signals with those detected by *Hinode*/SOT. By these analyses, we have established that the peak frequency of the oscillation is higher in the inner part of the sunspot, as well as confirmed that the umbral flash propagates mainly outwards. These results give important constraints on the sunspot models, although Dopplergram datasets with higher cadence are required for further study.

Second, we have investigated an emerging active region on the Sun by measuring acoustic travel times. We have found a signature of chromospheric downflows by combining chromospheric and photospheric datasets; we have found a travel-time anomaly in the chromospheric measurement of the active region, but not in the photospheric measurement. We discuss the behaviour of the supposedly evanescent acoustic waves in the solar atmosphere, and how it impacts on interpretation of travel-time measurement. We then interpret this travel-time anomaly as evidence for chromospheric downflow. The downflow speed we have obtained is $5 - 8$ kms^{-1}, which is consistent with magnetohydrodynamic numerical simulations of emerging active regions and chromospheric observations in the past. This result demonstrates a new possibility of studying dynamics not only in the subsurface layers but also in the upper atmosphere by multiwavelength time–distance helioseismology. This kind of signature reminds us that chromospheric helioseismology data may include information of dynamics in the chromosphere as well as in the subsurface layers. This needs to be taken into account in time–distance analyses, but it has not been considered sufficiently in the past.

Third, we consider the statistical property of the cross-correlation function, which is used to measure the acoustic travel times in time–distance method. By modelling the stochastic excitation of the solar oscillation, we discuss that the distribution function of cross-correlation function is a normal distribution, and have acquired expressions for average and variance of the distribution. This would enable us to do forward *statistical* modelling of cross-correlation function, and provide us with means to estimate the error in the travel times as well as the inversion results.

Finally, we have studied the supergranulation in the polar region of the Sun. It is difficult to observe the polar regions of the Sun in details because of foreshortening. The high-resolution of SOT gives us an advantage in this regard. By time–distance helioseismology technique, we investigated the structure of supergranular cells, and have found the tendency that the east-west width is smaller and the depth is larger, in the higher-latitude regions, compared to the equatorial region. Moreover, we found some kind of cell alignment in higher-latitude regions. We need further data and work for confirmation, but it may be an indication of giant cells, the largest convection cell of the Sun. To understand polar region dynamics is of great importance in comprehending how the solar dynamo mechanism works.

Acknowledgements

I would like to express my largest gratitude to my supervisor, Takashi Sekii, for his guidance during my work. I owe it to him that I have made it this far; he not only led me in my study of helioseismology but also provided me with environment in which I was able to focus on my work. I cannot thank him enough.

I am grateful to my collaborators, Alexander Kosovichev and Junwei Zhao for their kind supports and useful discussions. Junwei was kind enough to provide me with his inversion codes.

I thank Takaaki Yokoyama, who introduced me into the solar physics and helped my master thesis work a lot. Yukio Katsukawa and Tetsuya Watanabe, my advisers in the Graduate University for Advanced Studies, and Kazunari Shibata, my adviser during master course in Kyoto University, are also thanked for their kind encouragement. I acknowledge Hiromoto Shibahashi and Masao Takata, who introduced me to helioseismology in my undergraduate days at University of Tokyo, and Kiyoto Shibasaki, who offered me the very first chance to look at the Sun using scientific instruments.

I am grateful to my friends whom I met through studying astrophysics; their high motivation always was source of encouragement to me.

The members in Hinode Science Center in National Astronomical Observatory of Japan supported me in many ways. I thank Hinode team members in helping us to carry out observation plans for helioseismology.

I thank Marie Fujiyoshi in Hinode Science Center and the members of Kenkyu-Shien-Gakari in NAOJ who have taken care of my paperworks, and more.

I have been supported by the Research Fellowship from the Japan Society for the

Promotion of Science for Young Scientists.

Hinode is a Japanese mission developed and launched by ISAS/JAXA, with NAOJ as domestic partner and NASA and STFC (UK) as international partners. It is operated by these agencies in co-operation with ESA and NSC (Norway). This work was carried out at the NAOJ Hinode Science Center, which is supported by the Grant-in-Aid for Creative Scientific Research "The Basic Study of Space Weather Prediction" from MEXT, Japan (Head Investigator: K. Shibata), generous donations from Sun Microsystems, and NAOJ internal funding.

SOHO is a project of international cooperation between ESA and NASA.

Finally, I thank my family for their patient and continuous support without which I could not finish my study.

Contents

List of Figures

List of Tables

Chapter 1

Introduction

We have been watching activity of the Sun in detail for a long time; the Sun is the only star that we can observe with high spatial resolution. The mechanism of the solar activity phenomena, however, is still a great mystery. Our work is intended to be part of the first step in our attempt to solve this mystery of the Sun, solar activity phenomena and solar cycle, via helioseismology.

1.1 Solar Activity and Solar Cycle

1.1.1 Activity phenomena on the Sun

Sunspots, which are dark and cooler areas with stronger magnetic field, sometimes appear on the solar surface. Magnetic fluxes are generated in the solar convection zone, and then they float to the solar surface. Such emerging magnetic fluxes may form sunspots or active regions, and may cause magnetic reconstructuring in the upper atmosphere to induce violent explosions known as flares. A flare is observed as a transient brightening in a wide range of wavelength, and its energy source is considered to be magnetic energy. Owing to recent space-bourne observations, particularly *Yohkoh* (Ogawara et al. 1991) observations in the 1990s (e.g., Tsuneta et al. 1992; Masuda et al. 1995), it is widely accepted that magnetic reconnection (Sweet 1958; Parker 1957; Petschek 1964) plays a key role in energy release processes in solar flares. The physics of the magnetic reconnection is not fully understood, however. For instance, what determines the high efficiency of conversion from magnetic energy into thermal and kinetic ones, are still unknown (e.g., Nagashima & Yokoyama 2006). According to observations, the amount of energy released in a flare is $10^{29} - 10^{31}$erg

and the temporal scale of flares is a few minutes to a few hours. The triggering mechanism is another puzzle in study of flares (e.g., Nagashima et al. 2007a).

Flares sometimes accompany large-scale plasma ejections, such as filament eruptions and/or coronal mass ejections. These events will affect the earth; they will disturb the earth's magnetic fields, and the ejected plasma will cause geomagnetic storms. In this way, studying the Sun could be important not only from the astrophysical point of view but also from the practical point of view.

To reveal mechanisms of the activity phenomena, examining what happens above the surface is not always enough; we need to understand the subsurface structure and dynamics, since they affect the processes in the solar atmosphere. However, we cannot see through the solar interior where the magnetic flux is generated, and we cannot see the emerging process of the flux directly, as far as we rely on electromagnetic waves.

1.1.2 Solar cycle and dynamo

Not only the mechanism of each activity phenomenon, but the mechanism of long-term temporal variation of the solar activity also remains an unsolved mystery. Solar activity changes with the period of 11 years and we still do not know exactly why. The topic has recently become more challenging, because around the year of 2009, the Sun stayed unexpectedly quiet and nearly spotless, although it is supposed to be in the rising phase towards the next maximum anticipated around 2011. We do not know why this is happening.

The solar magnetic activity and its cycle is thought to be driven by a dynamo mechanism, i.e., a process involving interaction between the magnetic field and the plasma flow in the Sun. The theory of dynamo mechanism has not yet been established, however. It has not been confirmed from an observational point of view, either. Naturally, the future solar activity forecasted by various groups are still in disagreement (e.g., Dikpati & Gilman 2006; de Jager & Duhau 2009).

We believe that understanding the interior dynamics of the Sun is the key to study the dynamo mechanism from observational points of view. It is known that there are various flows in the Sun: convection, differential rotation, and meridional flows, for example. However, how much each type of flow contributes to the dynamo mechanism and in what ways is not yet clear. Therefore, at this stage, we may well need to investigate every type of flow in the Sun.

1.2 Solar Oscillations and Helioseismology

We can investigate the subsurface structure and dynamics of the Sun by observing the waves on the solar surface and examining their spectrum, or the way they propagate. This is the technique of helioseismology, the only way to probe the subsurface layers of the Sun.

Helioseismology started from examining the eigenfrequency spectrum of the Sun and has been successful in revealing the global structure and dynamics of the Sun. Since 1990s, a method more suitable for examining local structures and dynamics, local helioseismology, has been developing. In this thesis we focus on local helioseismological techniques, but here we briefly review the basics of helioseismology in general.

1.2.1 Solar oscillations

On the solar surface, we observe oscillations with the period of about 5 minutes. Now we consider that the '5-min oscillations' are excited by turbulent convection in the convection zone and that they are manifestation of the solar eigenmodes.

The 5-minute oscillations were first discovered by Leighton et al. (1962). By subtracting two images in red and blue wings of a spectral line, they obtained surface Doppler velocity fields. When they examined temporal variation, they noticed that there were periodic oscillations with a main period of about 5 minutes in the velocity fields as well as in the brightness fluctuation. Evans & Michard's (1962) independent observation confirmed the existence of the oscillations.

Later, the 5-minute oscillations were theoretically interpreted as standing acoustic waves trapped in the Sun (e.g., Ulrich 1970; Leibacher & Stein 1971; Wolff 1972; Ando & Osaki 1975). Observation by Deubner (1975) and Rhodes et al. (1977) yielded clear power spectra of the solar oscillation with a ridge structure (see Figure 1.2), which is basically consistent with the theoretical expectation, thus providing the observational supports.

1.2.1.1 Spectrum of the solar oscillations

We can observe the oscillation of the solar surface as a fluctuation in intensity, or in Doppler velocity measured by spectral lines. The solar oscillation signal, $u(x, y, t)$, is decomposed into components with the wavenumbers k_x, k_y and the frequency ω by Fourier

transform;

$$a(k_x, k_y, \omega) \equiv \int\int\int dxdydt\ u(x, y, t) \exp\{i(k_x x + k_y y + \omega t)\}. \tag{1.1}$$

The power of each components, $P(k_x, k_y, \omega)$, is defined as $P(k_x, k_y, \omega) = |a(k_x, k_y, \omega)|^2$. For the solar oscillation signal, this oscillation power in three-dimensional (k_x, k_y, ω) space shows high power at a series of trumpet-shaped surfaces. Figure 1.1 shows cross sections of $P(k_x, k_y, \omega)$ computed from 758-min of Ca II H line data by *Hinode* Solar Optical Telescope (SOT). In each cross section, concentric rings with high powers are seen. Taking the azimuthal average, $P(k_h, \omega)$, where $k_h = \sqrt{{k_x}^2 + {k_y}^2}$, we obtain a diagnostic diagram, or a '$k - \omega$' diagram (Figure 1.2).

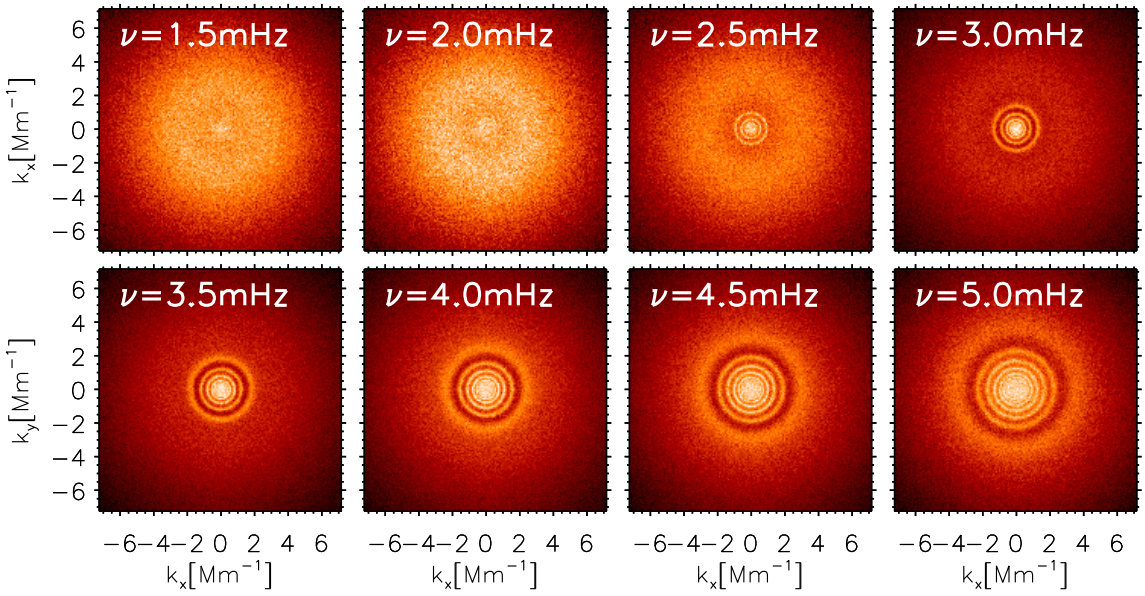

Figure 1.1 An example of the three-dimensional oscillation power spectrum of the Sun. Each panel shows a cross section of $P(k_x, k_y, \omega)$ at a certain frequency $\nu = \omega/(2\pi)$. This power is computed from a 758-min observation by *Hinode*/SOT on November 23, 2007 in the Ca II H line. Power is displayed in logarithmic colour scaling, with bright parts indicating high powers.

To be more precise, we need to take into account the fact that shape of the Sun is a sphere. Using the spherical polar coordinate systems (θ, ϕ, t), where θ is colatitude and ϕ is azimuthal angle, instead of Cartesian coordinate (x, y, t), the oscillation signal $u(\theta, \phi, t)$ is decomposed into spherical harmonics Y_l^m in the spatial domain. The spherical harmonics

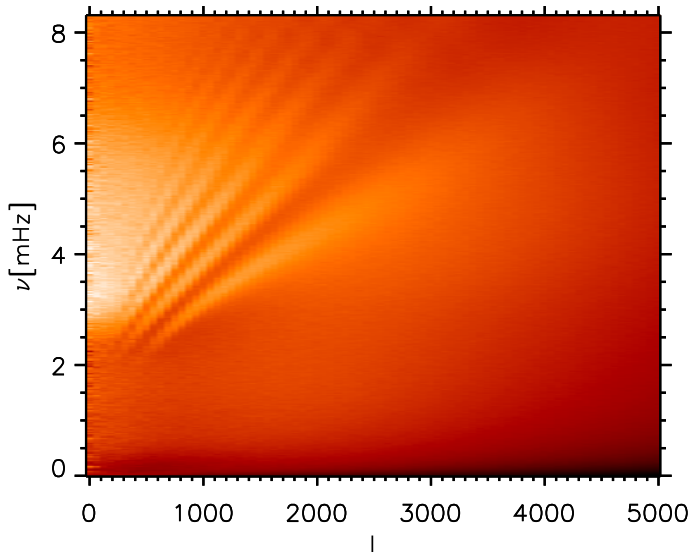

Figure 1.2 An example of diagnostic diagram of the Sun. The data used to compute the diagram is the same as that for Figure 1.1. Power is displayed in logarithmic colour scaling and bright part indicates high power. The diagnostic diagram is shown in (l, ν) plane, where $l = k_h R_\odot$.

are eigenfunctions of the angular part of Laplacian in three dimension, and are of the form

$$Y_l^m(\theta, \phi) = A_{lm} P_l^m(\cos\theta) e^{im\phi}, \tag{1.2}$$

where P_l^m is the associated Legendre polynomial of degree l and azimuthal order m, and A_{lm} is a normalization factor. In the temporal domain, it is decomposed by Fourier transform. Thus, the decomposition is

$$a_{lm}(\omega) = \int dt \int d\Omega \; v(\theta, \phi, t) Y_l^{m*}(\theta, \phi) e^{i\omega t}, \tag{1.3}$$

where $d\Omega \equiv \sin\theta d\theta d\phi$.

The relationship between l and k_h is determined by the property of the spherical harmonics to be

$$k_h = \sqrt{l(l+1)}/R_\odot \quad (\text{or} \quad k_h = l/R_\odot \text{ in the limit of large } l), \tag{1.4}$$

where $R_\odot$ is the solar radius. The power spectrum is usually shown in l–ν plane (see Figure 1.2). We discuss how the shapes of these ridges in power spectrum are determined, by internal thermal structure of the Sun, in Appendix D.

1.2.1.2 Oscillation modes of the Sun

The ridges in the power spectrum (Figure 1.2) are signatures of acoustic global oscillations, except the lowest ridge, which is manifestation of surface gravity waves that are called fundamental mode, or f mode. For waves in the Sun, if we neglect rotation and magnetic field, only possible restoring forces are pressure and gravity. In the limit of high frequency, pressure is the main restoring force and the waves are acoustic waves. The acoustic modes are called p modes, where 'p' is for pressure, after Cowling (1941). In the limit of low frequency range, gravity is the main restoring force, and the modes are called g modes, where 'g' is for gravity. In theory, the Sun should also be oscillating in g modes. Since g-mode waves are damped in the convection zone, however, it is hard to detect from the surface oscillation signal. There has not been unanimously approved confirmation of g modes from observations yet.

1.2.2 Global helioseismology

The ridges in the k–ω power map of the solar oscillations are where eigenmodes of the Sun are. Since the eigenmode frequencies are determined by the internal structure and dynamics of the Sun, we can inversely investigate the subsurface structure and dynamics by examining the eigenmode frequencies. The way oscillations take place is determined by restoring forces, which are gravity and pressure for the case of the Sun. Therefore, the eigenmode frequencies contain information on density and sound speed distribution in the Sun.

To calculate the solar eigenoscillation, we linearize hydrodynamic equations, such as continuity equation, equation of motion, energy equation, and Poisson's equation for gravity. Considering perturbations of the internal structure, we obtain the differential equation for displacement $\boldsymbol{\xi}$ as

$$\begin{aligned} \omega^2\rho\boldsymbol{\xi} &= -\nabla[\rho c^2\nabla\cdot\boldsymbol{\xi}] - \nabla(\nabla p\cdot\boldsymbol{\xi}) + \frac{\nabla p}{\rho}\nabla\cdot(\rho\boldsymbol{\xi}) + \rho\nabla\left[G\int\frac{\nabla'\cdot(\rho\boldsymbol{\xi})}{|\boldsymbol{r}-\boldsymbol{r'}|}dV'\right] \\ &\equiv \mathcal{L}(\xi) \end{aligned} \tag{1.5}$$

(see Lynden-Bell & Ostriker 1967). The operator, $\mathcal{L}$, is indeed determined by the internal structure, such as sound speed and density distribution. By setting appropriate boundary conditions, we can calculate the eigenvalue ω^2, and eigenfunction $\boldsymbol{\xi}$, for the operator $\mathcal{L}$.

This process of determining the eigenoscillation for a given solar internal structure

model is normally considered to be a forward problem. In this case, $\mathcal{L}$ is already known and eigenfrequencies are at first unknown. In our case, eigenfrequencies are observationally known and $\mathcal{L}$ is unknown; we would like to constrain the internal structure using these eigenfrequencies. This is a so-called inverse problem, and in this process, we compute properties of $\mathcal{L}$ using observationally obtained sets of ω^2.

By denoting perturbation of squared sound speed c^2 and density ρ by δc^2 and $\delta\rho$, respectively, in the linear perturbation regime, the shift of the eigenfrequency for the perturbed Sun, $\delta\omega$, can be written for each mode (n, l) in the form

$$\frac{\delta\omega_{n,l}}{\omega_{n,l}} = \int_0^{R_\odot} dr \left[K_{nl,c^2}(r) \frac{\delta c^2(r)}{c^2(r)} + K_{nl,\rho}(r) \frac{\delta\rho(r)}{\rho(r)} \right], \tag{1.6}$$

where $K_{nl,c^2}(r)$ and $K_{nl,\rho}(r)$ are the kernels (for the lack of m-dependence, see below). This set of integral equations is then 'inverted' to estimate δc^2 and $\delta\rho$ in the Sun, by requiring that each $\delta\omega$ matches as closely as possible the difference in the observed frequency and the frequency calculated from a model.

The solar internal model has been refined using these methods. For example, Kosovichev et al. (1997) showed that the difference between the sound speed distribution in the Sun, inferred by inversions, and the one in the current standard model (Christensen-Dalsgaard et al. 1996), is less than 1%.

Using the eigenfrequencies, we can infer the rotation rate in the solar interior as well. If the Sun does not rotate and is spherically symmetric, the eigenfrequencies with the same l and different m are identical (the modes are degenerated). However, since the Sun rotates, with a period of about one month, it affects the eigenfrequencies, and the degeneracy is lifted. The "splitting" of the frequency is derived once again using the linear perturbation theory and can be written in the form

$$\delta\omega_{nlm} = \omega_{nlm} - \omega_{nl} = \int\int K_{nlm}(r,\theta)\Omega(r,\theta) r dr d\theta, \tag{1.7}$$

where Ω is the angular velocity in the Sun and K_{nlm} is the rotational splitting kernel. By measuring the shifts of eigenfrequencies $\delta\omega_{nlm}$ of many modes, we obtain a set of integral equations. As is the case with the inversion for the sound speed and the density, the set of integral equations are solved for $\Omega(r,\theta)$. Thus, we obtain the distribution of the rotational angular velocity of the Sun from splitting data. The solar differential rotation throughout most of the convection zone has been revealed by this technique (e.g., Schou et al. 1998).

1.2.3 Local helioseismology

Global helioseismology has revealed global properties of the Sun: the spherically symmetric structure and the axial symmetric dynamics (rotation). In addition to such techniques, the way to probe local structures and flows has also been developed. This is the so-called local helioseismology. Instead of using eigenmode frequencies, we examine how waves propagate in the Sun to investigate the structures in the invisible regions of the Sun, such as subsurface layers or even the far-side of the Sun. The development of space-borne satellites enabled us to obtain stable high-resolution datasets with long periods, and this allowed us to exploit local helioseismological techniques.

Local helioseismology includes various different approaches, such as ring-diagram analysis, acoustic holography, and acoustic imaging. In this thesis, however, we focus on the time–distance method.

1.2.3.1 Time-distance method

Time-distance method is one of the main methods in local helioseismology. By measuring travel times of the waves between pairs of points on the Sun, we can detect local sound speed anomaly or flows along the paths of the waves. This method has been traditionally used in geo-seismology, and was first demonstrated in the solar case to be feasible by Duvall et al. (1993). Kosovichev & Duvall (1997) showed the first inversion results.

In the case of the earth, since each earthquake has a single seismic center, the travel time of the seismic wave from the seismic center can be measured by seismometers distributed around the earth. Using the travel times, they have studied underground structures of the earth. On the other hand, oscillations of the Sun have stochastic sources of excitation distributed widely in the (upper) convection zone. Therefore, we require a sophisticated way to measure wave travel times on the Sun. Duvall et al. (1993) succeeded in measuring travel times directly by cross-correlating wave signals on the solar surface.

There are two principal methods to measure acoustic travel times proposed so far (Kosovichev & Duvall 1997; Gizon & Birch 2004). Inversion results of several sunspots have been reported (Kosovichev et al. 2000; Zhao & Kosovichev 2003). For example, Kosovichev et al. (2000) showed dynamics of an emerging active region, and Zhao et al. (2001) detected flows around and below a sunspot. In Zhao & Kosovichev (2003), they showed the dynamics of a rotating sunspot. Although the rotation of the sunspot at the surface was counter-

clockwise, they found clockwise flow field at the depth of 0-3 Mm.

This is the method we mainly use in this thesis. We will discuss this analysis method as well as what the outstanding issues are in more details later (see Chapter 3).

1.2.3.2 Other branches of local helioseismology

Ring-diagram analysis Ring-diagram analysis was introduced by Hill (1988). The basic idea which was proposed in Gough & Toomre (1983) is to infer the flow by measuring distortion of the ridges in k–ω diagram. A cross section of the three-dimensional k–ω diagram shows a series of concentric rings, as shown in Figure 1.1. These rings correspond to ridges in two-dimensional k–ω diagram, due to the eigenmodes of the Sun. If some horizontal flows exist in the wave propagation region, the waves are advected by the flows and the rings are shifted or distorted. Therefore, examination of the oscillation power spectrum of a particular region of the Sun in three-dimensional space helps us infer the horizontal flow in the region.

Although this technique was proposed before the local helioseismology 'officially' started, we usually include this as a branch of local helioseismology. This analysis have been used to investigate rotation speed and meridional flows (e.g., Schou & Bogart 1998; Haber et al. 2002).

Acoustic Holography The basic concept of visualization of the Sun by acoustic holography was first proposed by Roddier (1975). Using the wavefield observed on the Sun, one can estimate the wavefield at any location at any time; this is the basic idea of acoustic holography and analogy to optical holography.

Lindsey & Braun (1990) introduced acoustic holography for imaging surface feature on the far-side of the Sun. Later, Lindsey & Braun (1997) discussed it as a tomographic method to infer the subsurface structure. Using this technique, Lindsey & Braun (2000) succeeded in imaging sunspots on the far-side of the Sun using *SOHO*/MDI datasets.

This method, described in Lindsey & Braun (1997), is a kind of downward migration which is used in geoseismology or underwater acoustics. By considering propagation of the acoustic signal at the solar surface reversely in time according to a wave equation, we can reconstruct the wavefield at a target point inside the Sun or on the far-side of the Sun, if the scattering of the wave along the path is not strong.

Note that Chang et al. (1997) introduced the concept of acoustic imaging, which is the technique quite similar to the acoustic holography; see Chou et al. (2003) for a recent review on acoustic imaging.

1.3 The Solar Optical Telescope onboard the *Hinode* Satellite

The *Hinode* satellite (Solar-B; Kosugi et al. 2007) was launched in September 2006 and has been obtaining datasets of unprecedented quality at high spatial resolution. Since the orbit is sun-synchronous polar orbit of about 680-km attitude, which is above the day-night boundary on the earth, *Hinode* can observe the Sun continuously without 'night' nine months a year. The orbital period is 98 minutes.

Hinode has three solar telescopes: the Solar Optical Telescope (SOT; Tsuneta et al. 2008), the X-Ray Telescope (XRT; Golub et al. 2007), and the EUV Imaging Spectrometer (EIS; Culhane et al. 2007). In this work, we use the SOT datasets for helioseismology analyses.

SOT is a 50-cm Gregorian telescope equipped with three focal-plane instruments, the Narrowband Filter Imager (NFI), the Broadband Filter Imager (BFI), and the Spectro-Polarimeter (SP).

The BFI provides intensity images in six bands: CN band centred at 388.35 nm with a width of 0.7 nm, Ca II H line centred at 396.85nm with a width of 0.3 nm, G band (CH molecular band) centred at 430.50nm with a width of 0.8 nm, blue continuum centred at 450.45 nm with a width of 0.4 nm, green continuum centred at 555.05 nm with a width of 0.4 nm, and red continuum centred at 668.40 nm with a width of 0.4 nm. The CN band and the G band are of photospheric origin, while the Ca II H line is from the lower chromosphere. The maximum field of view is 218×109 arcsec, and the CCD has 4096×2048 pixels. Minimum spatial sampling is 0.0541 arcsec pixel^{-1}.

The NFI uses a tunable birefringent filter (Lyot filter) and takes filtergrams, Dopplergrams, and magnetograms in several lines of Mg I and Fe I, as well as Hα and Na D lines, in the wavelength ranging from 571.0 to 657.0 nm. The maximum field of view is 328×164 arcsec, and the CCD is shared with BFI. Minimum spatial sampling is 0.081 arcsec pixel^{-1}. The NFI can take Dopplergrams in the magnetic-insensitive (with Lande g factor of zero)

Fe I 557.6nm line, which we consider useful for Helioseismological observation.

The SP is a spectrometer that takes Stokes polarimetric line profiles in Fe I 630.25nm and 630.15nm spectral lines. Stokes I, Q, U, and V are the primary products of the SP for deriving vector magnetogram maps.

Aside from these instruments, SOT has an image stabilization system (Shimizu et al. 2008), the Correlation Tracker (CT). The CT camera takes images of the solar granules around the center of the field of view, and the system calculates the displacements by tracking the granulation pattern. Thanks to the system, the remaining jitter on orbit is reported to be less than 0.03 arcsec on the Sun (Shimizu et al. 2008).

SOT team provides us calibration tools via Solar Software (SSW)[1], which is a library for solar observation data analyses in IDL (Interactive Data Language). For BFI and NFI datasets, they provide calibration program, "fg_prep.pro". It is for dark subtraction, flat fielding, and bad pixel corrections. For NFI datasets, however, it does not support flat fielding due to a problem in filter (Tsuneta et al. 2008) mentioned in §3.4.1.

1.4 Local Helioseismology by SOT

Ultimate goal we have in our mind is to understand mechanism of the solar activity phenomena including the activity cycle. To approach the goal as much as possible, we need to establish methods to probe the solar interior, local helioseismology, as well as to obtain high-quality observation datasets.

In this thesis, we focus on local helioseismology study exploiting *Hinode*/SOT datasets.

First, we examined oscillation signals acquired by SOT in the regions with strong magnetic field, sunspots. In Chapter 2, we report on this portion of the work.

Second, using the oscillation signals on the solar surface, we carried out time–distance analysis. We briefly summarize the time–distance analysis procedures as well as discuss the outstanding issues for the method in Chapter 3. An application to the *Hinode*/SOT datasets of time–distance technique is described in Chapter 4, where we report that we found travel-time anomaly in two active regions and discuss that this can be interpreted as evidence for chromospheric downflows by considering wave propagation of sub-critical frequencies into the chromosphere as a transient phenomenon.

[1] http://www.lmsal.com/solarsoft/

Third, we examined the statistical properties of the cross-correlation functions which is used in the time–distance analyses. As described in Chapter 5, the only almost purely theoretical chapter in this thesis, we determine the distribution function of the cross-correlation function and discuss possible applications.

Fourth, we investigate supergranulation in the polar region of the Sun using the time–distance analysis method on *Hinode*/SOT datasets. This is the topic presented in Chapter 6, before summary of the current work and discussions of future works are given in Chapter 7.

Chapter 2

Sunspot Oscillations [1]

As the first step in our attempt to use Solar Optical Telescope (SOT) onboard *Hinode* for helioseismology, we examine oscillation signals in datasets obtained by SOT, focusing on the region in and around active regions. First, we investigate the spatial distribution of power spectral density. In the umbra, so-called umbral flashes are clearly seen with the power peaking around 5.5 mHz in the chromospheric Ca II H line, but not in the photospheric G band. The oscillation power is enhanced in the most of the umbrae. In a fairly circular sunspot, NOAA 10935, however, there is a region with suppressed power at the center of the umbra. No other sunspots so far examined has shown this node-like feature. We have also examined the oscillation signals using other instruments, namely, *SOHO*/MDI and NoRH.

2.1 Introduction

Oscillations within sunspots have been studied since Beckers & Tallant (1969) discovered transient brightenings in the umbra in chromospheric lines, which are called 'umbral flashes'. In addition to oscillations in intensity in various spectral lines, fluctuations in velocity and magnetic field strength were also observed. Three types of oscillations are observed within sunspots: 3-mHz (five-minute) oscillations in the photospheric umbrae, 5-mHz (and hight-frequency) oscillations in the chromospheric umbrae, and running penumbral waves (see review articles by Thomas 1985; Lites 1992; Staude 1999; Bogdan 2000 and references therein). In spite of this classification, the difference may not be so meaningful, as some say that the chromospheric oscillations in umbrae (umbral flashes) and the running penumbral

[1] Part of this chapter was published in Publications of the Astronomical Society of Japan (Nagashima et al. 2007b).

waves might be different manifestations of the same phenomenon (Rouppe van der Voort et al. 2003; Tziotziou et al. 2007). Three-minute oscillations in the photosphere of umbrae have also been reported, firstly by Beckers & Schultz (1972), although for their detection a possibility of chromospheric contamination has been pointed out since then (see Lites 1992).

How these oscillations are driven remains unestablished, however. Lites (1992) summarized in his review that two theoretical pictures of the umbral oscillations in the chromosphere were drawn: one was that umbral oscillations are the resonant response of the atmosphere to forcing by a broad-band power sources below (Zhugzhda et al. 1983; Lites 1992), and the other was that the oscillations are driven by a trapped fast magnetosonic waves (Uchida & Sakurai 1975).

As for the transient brightening, Havnes (1970) suggested the flashes are produced by compressional waves in umbrae. Since in more recent observations the waves show non-linear property, the idea was later extended to upward-propagating shock waves (Lites 1992; López Ariste et al. 2001; Rouppe van der Voort et al. 2003; Centeno et al. 2006; Tziotziou et al. 2007). Rouppe van der Voort et al. (2003) concluded that the umbral flashes are near-acoustic field-guided upward-propagating shock waves (see Figure 2.1). Centeno et al. (2006) and Tziotziou et al. (2007) reported saw-tooth shaped temporal variation of Stokes V and light curves, respectively. Since they suggest steepening of waves, they are evidence for shock waves propagating upward in umbral regions.

Umbral oscillations were also observed in higher atmosphere; Shibasaki (2001) reported a radio brightness oscillation of 3-minute period above a sunspot umbra and interpreted it as an upward-traveling acoustic wave. In the transition region, 3-minute oscillations above umbrae are observed (e.g., Brynildsen et al. 1999; Maltby et al. 2001); they reported the oscillations are not non-linear and interpreted them as upward-propagating acoustic waves.

The issue of how the oscillations in sunspots are driven, and how the waves that are associated with these oscillations propagate in magnetized atmosphere is important in probing subsurface structure of sunspots using detailed observations of sunspot oscillations, which was first proposed by Thomas et al. (1982) and now is an actively pursued goal of local helioseismology (see e.g., Kosovichev et al. 2000). Using local helioseismological technique, by measuring travel times for given distances of (primarily) acoustic waves, one can extract information about subsurface local structures, that is crucial in our attempt to reveal how the active regions are generated, evolve, and dissipate.

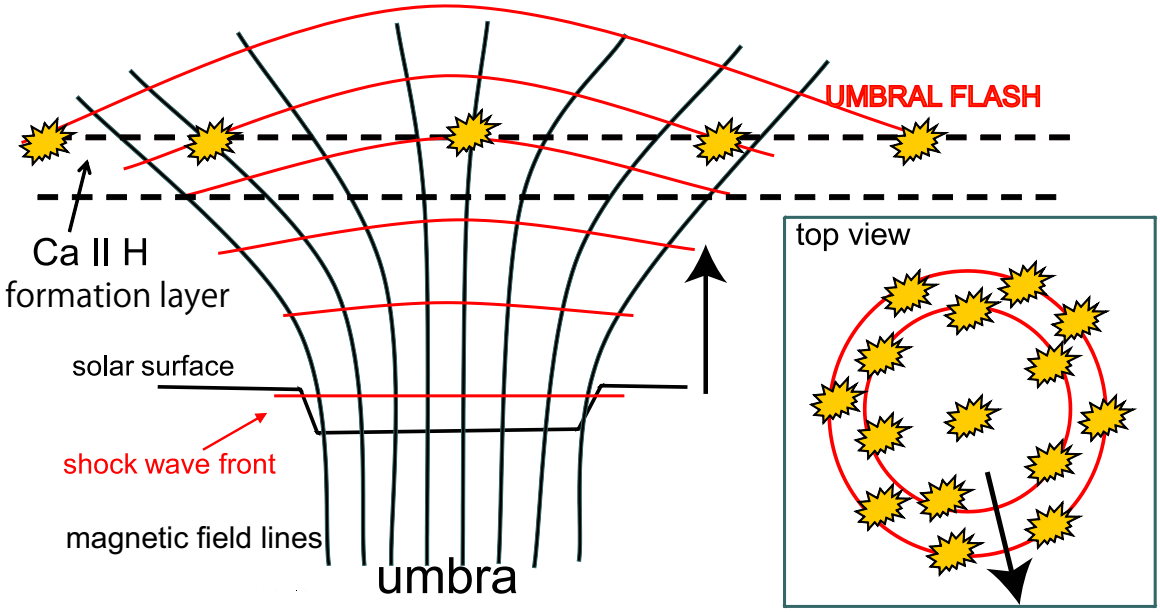

Figure 2.1 A cartoon of field-guided upward-propagating shock wave observed as umbral flash (Rouppe van der Voort et al. 2003). The solid lines indicate magnetic field lines in a sunspot umbra, and the red lines indicate the shock wave fronts. When the wave fronts hit the formation layer of Ca II H lines (the dotted line), the layer brightens up and the umbral flashes are seen. The right small panel shows the top view of this sunspot.

Solar Optical Telescope (SOT; Tsuneta et al. 2008) onboard *Hinode* (Kosugi et al. 2007) reveals many fine structures in sunspots, such as the penumbral flows and the light bridges. In this chapter, we report SOT observations of sunspot oscillations in chromospheric and photospheric lines with unprecedented high resolution. We observe the lower chromospheric oscillations using the Ca II H line data, while the photospheric oscillations are investigated mainly in the G band.

2.2 Oscillation 'Node' in a Circular Sunspot

First, we investigate oscillation signals in and around a circular sunspot, NOAA 10935 using SOT observation datasets.

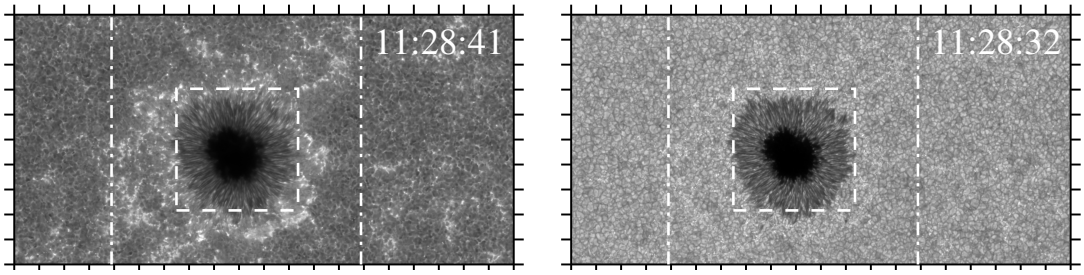

Figure 2.2 Sample intensity maps in the Ca II H line (left) and the G band (right). We examined the intensity oscillations in this field of view (201 arcsec × 101 arcsec). The ticks are spaced by 10 arcsec. The central boxes with dashed lines indicate the field of view in Figure 2.3, while the dot-dashed boxes indicate the field of view of the power maps in Figures 2.4 and 2.7.

2.2.1 Observations and data reduction

A fairly round sunspot close to the disc centre (NOAA 10935) was observed with the Solar Optical Telescope (SOT) onboard *Hinode* over a duration of 4 hr 42 minutes (11:18 - 16:00 UT) on January 8, 2007. Using Broadband Filter Imager (BFI; Tsuneta et al. 2008) of SOT, we obtained series of 218 arcsec × 109 arcsec filtergrams in Ca II H (3968.5 Å) and G band (4305 Å) with a cadence of $\sim$ 1 min. The cadence was slightly irregular, although it hardly affects the Fourier analyses we carry out (see Sekii et al. 2007). To reduce the data amount, 2 × 2 summing was carried out onboard; hence, the pixel size was $\sim$ 0.1 arcsec. About 10 seconds after taking each G-band image, a Ca II H image was taken. During the period, the correlation tracker (CT; Shimizu et al. 2008) was used to stabilize the images. Since CT only estimates and compensates for the movement in the granules, we need additional tracking to account for the proper motion of the sunspot. We used a two-dimensional cross-correlation technique to compute the displacement. The displacement was then smoothed by polynomial fitting before applied to the series of images. The difference between the original displacements and the smoothed ones were less than 0.7 arcsec, and we consider this value as an estimate of the tracking error. The field of view that we used for our analysis is slightly smaller (201 arcsec × 101 arcsec) than the original one owing to this sunspot tracking. Figure 2.2 shows intensity maps in the Ca II H line and in the G band. We studied the intensity oscillations in this field of view.

For dark subtraction, flat fielding, and correcting for bad pixels, we used a calibration

program provided by the SOT team. Running difference images were used to remove any possible remnant spatial trend. Then, in each pixel, the intensity difference was normalized by the mean intensity in the two running frames. This was mainly in attempt to detect oscillations even in the region with very low intensity, i.e., the umbra. It also permits us to observe a smooth transition between umbra and penumbra. We then used Fourier transform of the relative intensity difference time series at each pixel to produce power-spectral-density maps. The Nyquist frequency is 8.3 mHz in our analyses in accordance with the 1-min cadence. Since taking the running difference is equivalent to taking the time derivative on the discrete time grid, we divided the obtained power by squared angular frequency ω^2. Thus the main remaining effect of taking the running difference is the reduced spatial trend.

It should be noted that the power maps measure the intensity variation due to both (magneto)convection and oscillation. These two components cannot be distinguished by this kind of analysis, except for that the convection spectrum is expected to be continuous with a monotonic decrease with frequency.

Another technical point is that because the oscillation spectra are broad-band, normalization by temporally local mean does not affect them very much. We confirmed this by carrying out the analysis without the normalization, where we found no qualitative change, aside from much reduced power in the umbra, which was to be expected.

2.2.2 Results

2.2.2.1 Umbral Oscillations observed in Ca II H

Figure 2.3 shows one example of umbral oscillations in our data set. Running difference intensity maps in Ca II H are shown in this figure, except the upper-left panel of the intensity map for reference. Please note that, although here we present the running differences for visual enhancement, power spectra are always corrected for the ω^2 factor. Localized brightening randomly occurs in most of the umbra; in a snapshot of the filtergram, small bright patches are seen. These are "umbral flashes". In the running difference intensity maps, there are some elements with the size of 5 arcsec where a bright region is adjacent to a dark region. Since this means the region with enhanced intensity has just moved from the dark region to the adjacent bright region, we can roughly estimate the propagation speed of the flashes based on separation between these structures; the features moved $\sim$ 4 arcsec in a minute, so the propagation speed is up to 50 km s^{-1}. When we see the running difference

movie, these wave-like structures seem to move outward rather than inward. Unlike in the Ca II H data, we cannot find any umbral oscillations in the G-band intensity data.

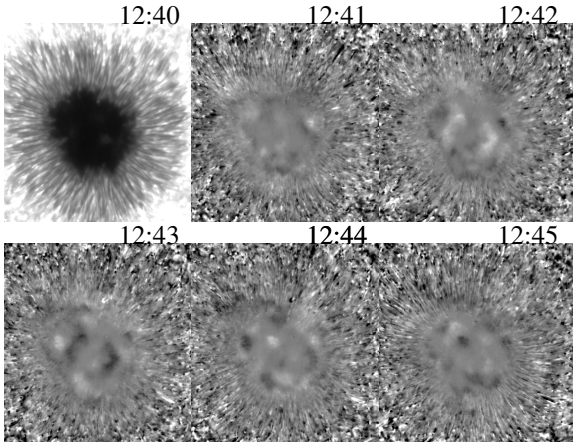

Figure 2.3 A Ca II H intensity map (upper-left) and running difference intensity maps (the others) showing umbral oscillations. White marks the region where the intensity increases compared with that in the previous frame. The field of view is a 49-arcsec square. The figure in the upper-right corner of each panel indicates time. An extended version of these figures are available as an mpeg animation in the PASJ electronic edition at http://pasj.asj.or.jp/v59/sp3/59s310/59s310_mov1.mpg .

2.2.2.2 Relative Intensity Power Maps

Since oscillations were seen in the Ca II H running difference intensity movie, we investigated these oscillations in detail by decomposing them into Fourier components. Figures 2.4 and 2.5 show the power maps derived from the Ca II H intensity data as well as a sample Ca II H intensity map. In Figure 2.4, we show the relative intensity power maps averaged over 1 mHz wide frequency ranges, from 1 mHz to 7 mHz with logarithmic greyscaling, while in the Figure 2.5 the power map averaged over the wider frequency range from 0.5 mHz to 7.5 mHz. Figure 2.6 shows the cross sections of the power maps: we consider circles around the center of the 'node' (the center of the dotted circle shown in Figure 2.5) and average the power on each circle to obtain the azimuthally averaged power distribution as a function of the distance from the center of the node. The solid curve indicates the cross section of the averaged power map (Figure 2.5), while the dotted, dashed, and dot-dashed curves show the cross section of the power maps averaged over 0.5–3.5 mHz, 3.5–4.5 mHz, 4.5–7.5 mHz

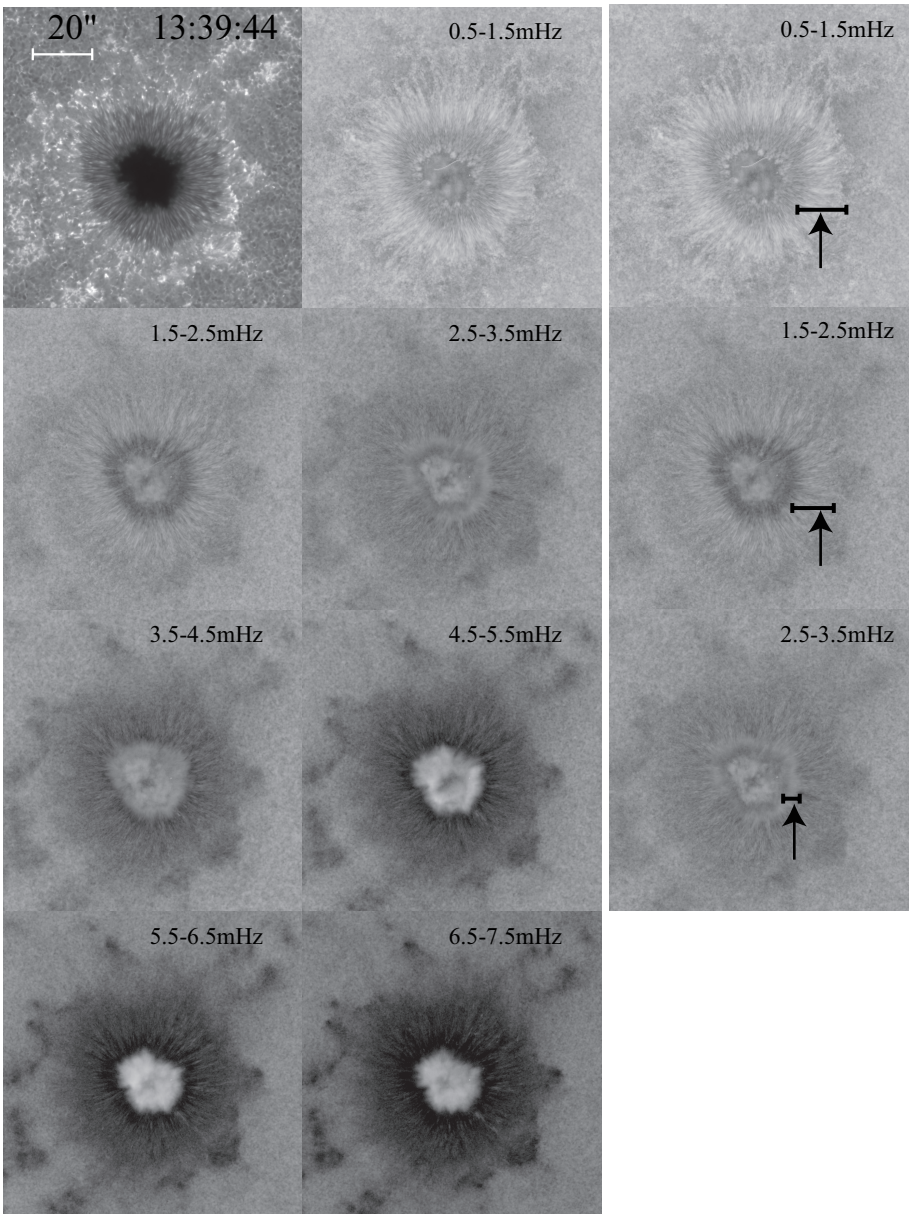

Figure 2.4 A Ca II H intensity image (top-left) and the power maps from Ca II H intensity data of active region NOAA 10935. The field of view is 100 arcsec square in all the panels. The power is displayed in logarithmic greyscaling and the same colour range is used in Figures 2.4, 2.5, 2.7, and 2.8. In the third column, the bright rings are indicated by arrows in the power maps in the 1, 2, and 3mHz ranges (see text).

ranges, respectively. Figures 2.7 and 2.8 are the G-band counterparts of Figures 2.4 and 2.5. In Figure 2.7, we omit the 6 mHz and 7 mHz power maps, because they are essentially identical to the 5 mHz power map, except throughout the maps the power was smaller than that in 5-mHz range. We find the following from inspecting these power maps:

1. In the Ca II H power maps, in all the frequency ranges, there is a small area ($\sim$ 6 arcsec in diameter) near the center of the umbra where the power was suppressed. This node-like structure is seen more clearly in the power maps averaged over a wider frequency range (Figure 2.5) and in its cross section (Figure 2.6). This type of 'node' has never been reported, except perhaps the 'calmest umbral position' found by Tziotziou et al. (2007) in Doppler power maps (however, for discussion of umbral oscillation patterns, see Uchida & Sakurai (1975) who compared their calculation with Giovanelli's (1972) observation). Possibly, stable high-resolution observation made by *Hinode*/SOT was required to find such a tiny node, although it is also possible that only a particular type of sunspots, e.g., round ones with axisymmetric geometry, exhibit such a node-like structure; we need to observe various types of sunspots to investigate the possible geometrical effects. We discuss this node in more detail later (§2.2.6.3).

2. Above 4 mHz in the Ca II H power maps, power in the umbra is remarkably large. In the power maps averaged over narrower frequency range (0.05 mHz wide, not shown), the region with high power in the umbra seems to be more patchy. This probably corresponds to the elements of umbral flashes mentioned in the previous subsection. We discuss relationships between this structure and the umbral flashes in §2.2.6.3.

3. In the lower-frequency range (1 mHz), the power is enhanced at the umbra/penumbra boundary in G-band power maps. A similar feature was also reported by Hill et al. (2001); a bright ring around a sunspot was seen in their *SOHO*/MDI intensity power map in the 0–1 mHz range. This bright ring is discussed in §2.2.6.1. In the higher-frequency ranges, this bright region encircling the umbra is also seen although less striking. The dark regions in the power maps are smaller than the umbra in the intensity map because of the bright ring.

4. In the Ca II H power maps, a bright ring (indicated by arrows in the panels in the third column of Figure 2.4) in the penumbra is found in lower frequencies, due to penumbral running waves. Lites (1992) reported that chromospheric oscillatory frequency in the

penumbra decreases from 4 mHz at the inner boundary to less than 1.5 mHz at the outer boundary. In the current data, this is seen as the bright ring decreasing in size as the frequency increases.

5. The region with enhanced power in high-frequency ranges around the active region, so-called "acoustic halo" (Braun et al. 1992; Brown et al. 1992), is not found in our power maps. However, this is not inconsistent with the previous works, because acoustic halos were reported to be in the velocity power maps obtained by Dopplergrams, but not in the intensity power maps (Hindman & Brown 1998).

6. In the regions that are outside the sunspot but are bright in the Ca II H intensity (such as moat region and plage-like features), not only Ca II H power map but also the G-band power map, exhibits remarkable suppression of signal in the higher frequency range, say above 5mHz. Since these regions are where the magnetic field strength is relatively strong, these features suggest that, outside the sunspot, the power is suppressed as the magnetic field strength increases; this confirms the previous view (e.g., Hindman & Brown 1998; Jain & Haber 2002).

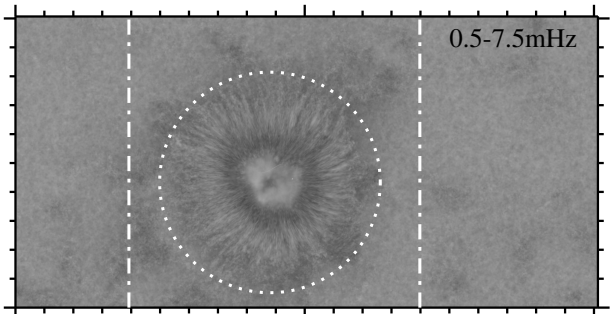

Figure 2.5 Ca II H line relative intensity power maps averaged over the frequency range from 0.5 mHz to 7.5 mHz in the full field of view. The dot-dashed lines indicate the field of view in Figure 2.4. The center of the dotted circle is located at the center of gravity of the node-like dark region. The radius of the circle is 38 arcsec, and the cross sections in the circle is shown in Figure 2.6.

2.2.2.3 Power Spectra

To see how the power distributions in the umbra, penumbra, and the quiet region differ from each other, we examined the power spectrum in each region. Figure 2.9 shows the

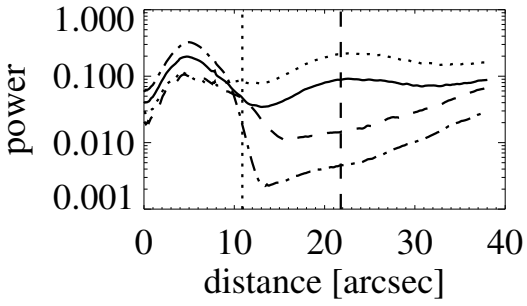

Figure 2.6 Cross sections of the Ca II H power map in the sunspot shown in Figures 2.4 and 2.5. Distance is measured from the center of the node. The solid line indicate the cross section of the power map averaged over the frequency range from 0.5 mHz to 7.5 mHz. The dotted, dashed, and dot-dashed lines indicate the cross section of the power maps averaged over the 0.5–3.5 mHz, 3.5–4.5 mHz, and 4.5–7.5 mHz ranges, respectively. The umbra/penumbra boundary is marked by the dotted vertical line, and the dashed vertical line indicates the penumbra/moat boundary.

power spectra of the G-band and the Ca II H intensity oscillations. Each power spectrum is averaged over 39303 pixels (in the umbra), 44000 pixels (in the quiet region), 62000 pixels (in the penumbra), or 21500 pixels (around the boundary between the umbra and penumbra). Here, the umbra and penumbra were defined according to the average Ca II H intensity over the observing period. We defined the quiet region as the region that is outside the sunspot and is not bright in Ca II H, and selected a part of this region so that the area is comparable to those of the umbra and penumbra. The boundary between the umbra and penumbra was defined as the annulus with the inner radius of 11 arcsec and the outer radius of 14 arcsec. The center of the annulus is placed at the center of the node (the center of the circle shown in Figure 2.5).

In all the regions considered, the G-band intensity power decreases monotonically with the frequency. Addition to that, the power spectrum in the quiet region shows a broad peak around 4 mHz which corresponds to the global five-minute oscillation. The reason for the lack of power excess in the umbral G-band intensity is not understood. The Ca II H intensity power in the quiet region shows the similar trend, while the power spectrum in the penumbra exhibits almost monotonic decrease, as is expected from the power maps in

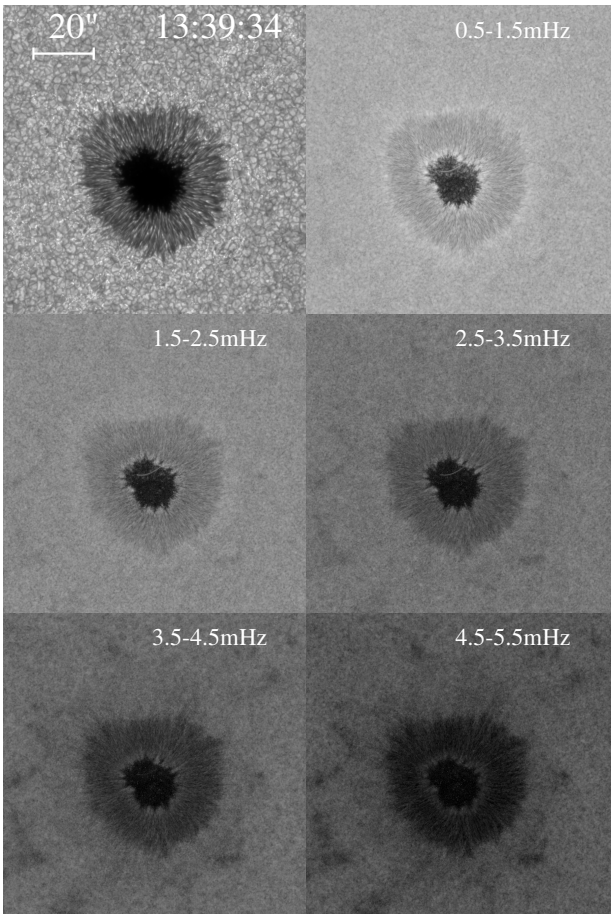

Figure 2.7 A G-band intensity image (top-left) and the power maps from G-band intensity data of active region NOAA 10935. The field of view is the same as that in Figure 2.4.

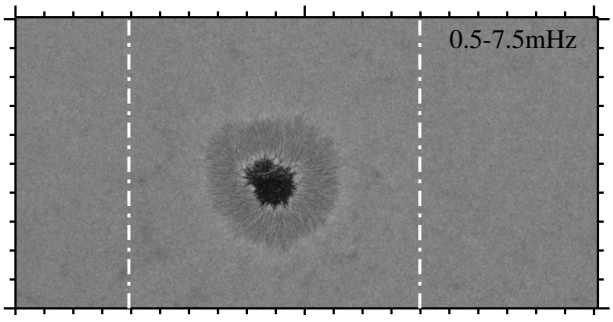

Figure 2.8 G-band relative intensity power maps averaged over the frequency range from 0.5 mHz to 7.5 mHz in the full field of view. The dot-dashed lines indicate the field of view in Figure 2.7.

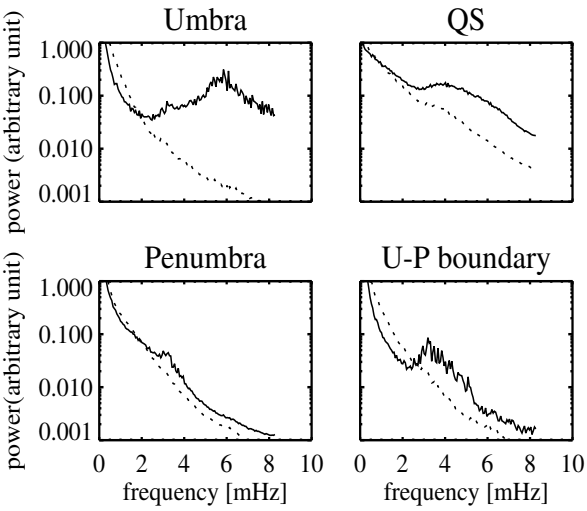

Figure 2.9 Power spectra averaged in the umbra (upper left), in the quiet region (upper right), in the penumbra (lower left), and around the boundary between the umbra and the penumbra (lower right). The Ca II H (solid) and the G-band (dotted) intensity power spectra are shown. The ordinate is in an arbitrary unit in logarithmic scale.

Figure 2.4, except for the narrow peak at 3 mHz. The Ca II H intensity power spectrum in the umbra has two peaks: one around 3 mHz and the other around 5.5 mHz. In the previous works (e.g., a review by Lites 1992), the dominant period of oscillation in the chromosphere was above 5.5 mHz, and, in contrast to our results, no significant power peaks were found in the 3 mHz range. The power spectrum around the boundary between the umbra and penumbra in Figure 2.9 indicates that the 3 mHz peaks in the umbral and penumbral spectra originate in the boundary region. The broad peak in the boundary region, between 2 mHz and 5 mHz, is brought about by running penumbral waves.

2.2.3 Spectra in various positions in the sunspot

We examined the difference of power spectra between different positions in the sunspot. First, we changed the Cartesian coordinate into the cylindrical one with the origin set at the center of the umbra. The radial grid width is 5 pixels and the azimuthal grid size is $\pi/16$, and we chose the region within 200 pixels from the center. And then we took the Fourier transform of the time-series intensity with cylindrical coordinate. After averaging over the azimuthal wavenumber, we calculated the power as a function of the frequency and radius.

In Figure 2.10, spectra of these powers are shown. The left-upper panel is the power spectrum in the most inner umbra, and the left-lower panel shows the power spectrum around the umbra/penumbra boundary. The spectra in the right column correspond to those in the penumbra. As is also shown in the next subsection, dominant components of oscillation vary with locations.

2.2.4 Peak frequency distribution

Lites (1992) mentioned that the oscillatory frequency in the penumbra increases from $\leq$ 1.5mHz at the outer penumbral boundary to 4mHz near the umbra/penumbra boundary in the chromospheric lines. This relationship may be extrapolated to the umbra. Tziotziou et al. (2007) showed distribution of the period of oscillation in a sunspot observed in Ca II H and Hα. In one of their figures, from the center of the umbra to the outer boundary of the penumbra the oscillation period increases.

Figure 2.11 shows various distributions of quantities related to the umbral oscillation. The first panel shows the 5-mHz power map, and the third panel shows the average intensity map over the observation period. The second panel presents the distribution of the mean frequency weighted by the power. We calculate the weighted mean only above 2 mHz. The fourth panel shows the distribution of the peak frequency. This figure tells that in the central part of the umbra where the 'node' exists the peak frequency is the greatest. This frequency distribution in the sunspot is discussed in §2.2.6.2.

2.2.5 Examining the propagation direction of the umbral flash

Umbral flash pattern seems to propagate outwards, and the field-guided-propagating-shock-wave model is consistent with this property. To confirm that the umbral flash propagates outward, we analyzed the dataset of the circular sunspot in the following way.

First, we found the center of the 'node' in the umbra. Second, we changed the Cartesian coordinate into the cylindrical coordinate with the origin set at the center of the node. The original intensity map, $I(x, y, t)$, was changed into $I(r, \theta, t)$. Using this, we computed Fourier transform of the intensity map, $\tilde{I}(k_r, m, \omega)$, i.e.,

$$\tilde{I}(k_r, m, \omega) \propto \int I(r, \theta, t) e^{-i(k_r r + m\theta + \omega t)} dr d\theta dt. \tag{2.1}$$

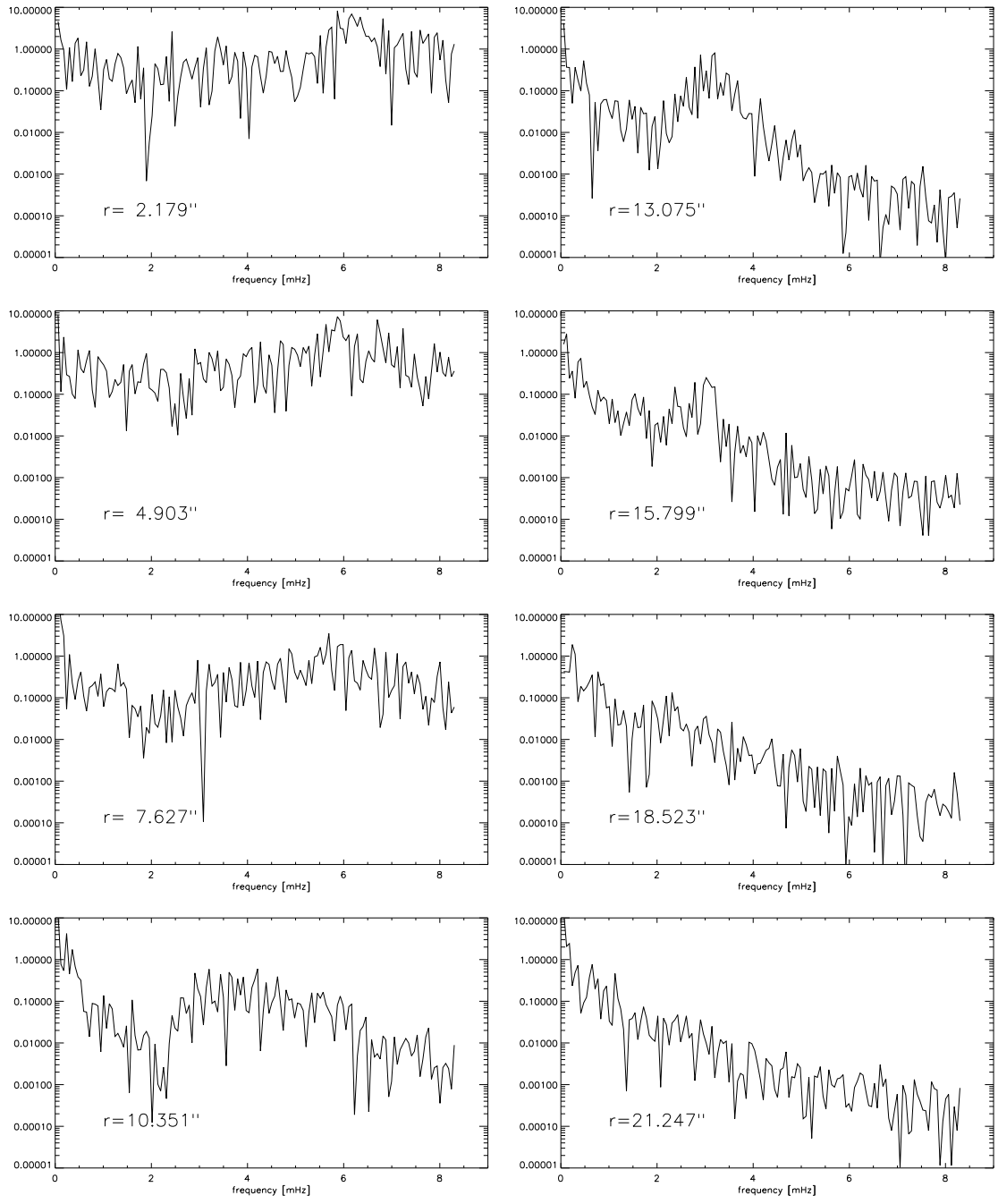

Figure 2.10 Ca II H intensity power spectra in umbra and penumbra at several distances from the center of the umbra.

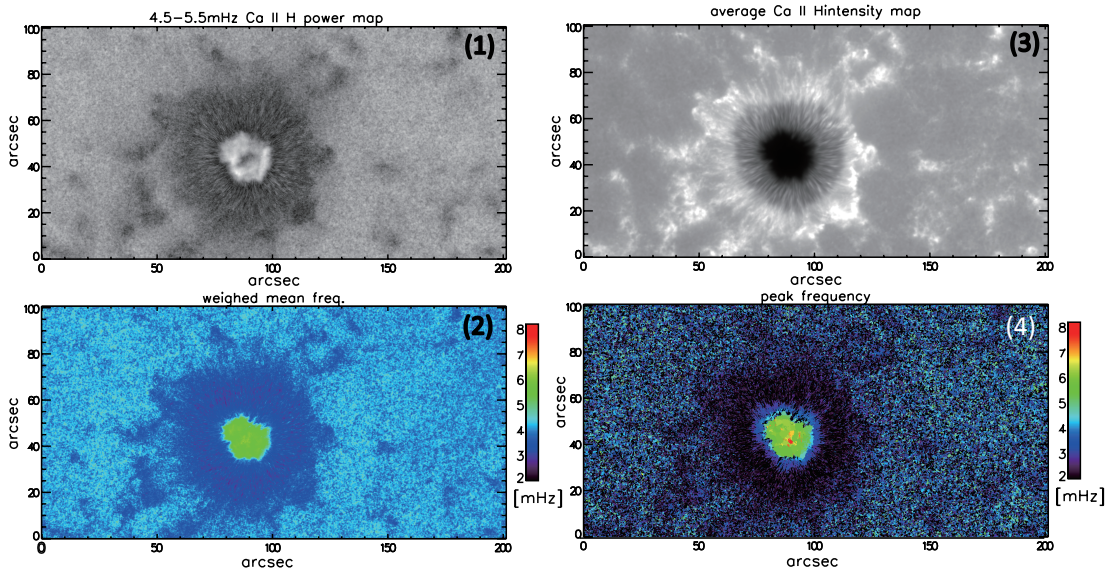

Figure 2.11 (1)Ca II H intensity power map of 5-mHz range. (2)Mean frequency distribution weighted by power. (3)Average Ca II H intensity over the observation period. (4)Peak frequency distribution.

We use the relative intensity difference time series, i.e.,

$$2\frac{I(x,y,t_{j+1}) - I(x,y,t_j)}{I(x,y,t_{j+1}) + I(x,y,t_j)},$$

instead of the raw intensity data, to compute the Fourier transform to remove any possible spatial trend.

After changing the coordinate, we made 32 equally-spaced cuts in the azimuthal direction (θ) and 70 equally-spaced cuts in the radial direction (r). The azimuthal and radial grid sizes are $\Delta\theta = \pi/16$ and $\Delta r = 5$ pixels, respectively. Figure 2.12 shows the averaged Ca II intensity map over the whole observation period. Three circles centered on the center of the umbra are overlaid: 100-, 200-, and 350-pixel radii, respectively. The region inside the largest circle corresponds to the region we examined in this section.

First, after the 3-dimensional Fourier transform, we took the average of the power $P \equiv |\tilde{I}|^2$ over m. Figure 2.13 shows the maps of $P_{\rm av}(k_r, \omega)$ in Ca II H and G band. In the Ca II H map, the power distribution is not symmetric with respect to the Nyquist frequency and the regions where power is enhanced are located in the upper-left and lower-right parts of the map. This implies that the outward components of wave are stronger. (See Figure 2.14 for reference.) In the G-band map, some ridges were clearly seen. They are probably

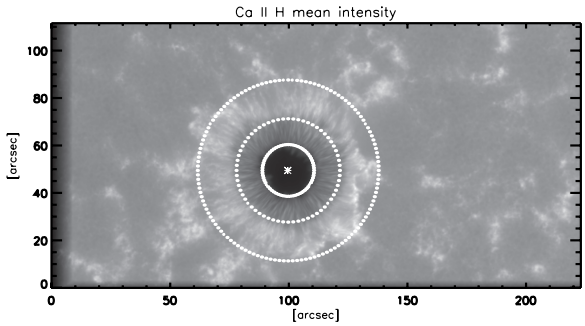

Figure 2.12 Average Ca II H intensity map over the whole observation period with circles of 10-, 20-, and 35-arcsec radii. The center of the circle is put on the center of the umbra.

due to 5-min oscillations in the quiet region outside the sunspot.

Next, we checked not only the power averaged over m but also the powers averaged over $k_{\rm r}$ and ν. In Figure 2.15 is shown a sample image in cylindrical coordinate (*upper-left*) and power maps averaged over m (*upper-right*, essentially the same as Figure 2.13), ν (*lower-left*), and $k_{\rm r}$ (*lower-right*). In the lower-left panel, the mode $m = 0$ seems to be dominant. It means that the wave power does not depend on azimuthal angle of propagation.

In the lower-right panel, the mode $m = 1$ is dominant especially in low-frequency range. This feature is an artifact, however. This mode corresponds to time-dependent distortion of the umbra, and incomplete tracking may have caused it. Actually, we confirmed that this mode can be removed with more careful tracking of the sunspot, though with an increased level of noise overall.

We should note that in this analysis we did not exclude the region outside the umbra. Therefore, waves in the penumbra, such as propagating penumbral waves, may be included in the power maps. We also checked the results if we use only the umbra. The power maps are essentially the same, but the umbral region is so small that the power maps are too noisy.

In summary, we examined the propagation direction of the umbral flash pattern by decomposing the waves in cylindrical coordinates, and confirmed that the outward components are stronger.

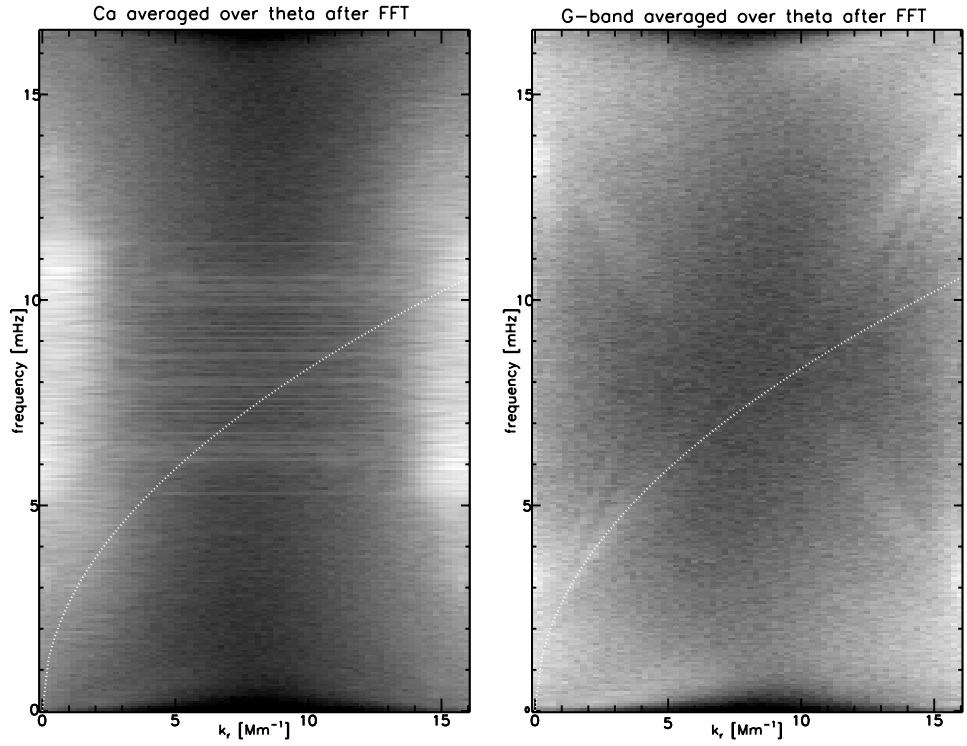

Figure 2.13 k_r - ν diagrams. *Left*: Ca II H intensity power. *Right*: G-band intensity power. The dotted line indicates the f-mode ridge.

2.2.6 Discussions

2.2.6.1 Bright Ring in the Power Maps

As was shown in the G-band power maps in Figure 2.7, there was a bright ring-shaped structure around the penumbra, which appeared in all the frequency ranges, and was most visible in the 1 mHz frequency range. A similar bright ring was reported by Hill et al. (2001). Their power maps derived from *SOHO*/MDI intensity data showed a bright ring around the sunspot in the 0–1 mHz range. In their case, a strong enhancement of power within a sunspot was also observed in Ca II K intensity in all frequency ranges obtained by TON data only to be identified as artifacts due to terrestrial seeing. In the case of space-borne observation, seeing never comes into play. There is some possibility that artificial oscillation signals are produced by a poor tracking of the sunspot, since at the sunspot boundary the intensity has a large contrast. However, at 0.7 arcsec, the tracking error is smaller than the width of the bright ring around the penumbra ($\sim$ 3 arcsec). We therefore conclude the structures are not due to the tracking error. The true nature of this ring is not

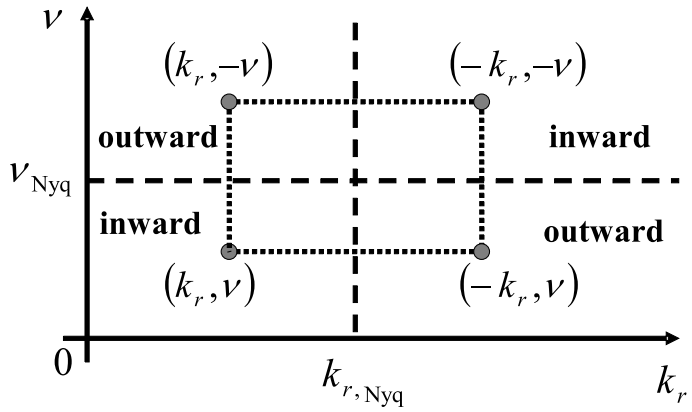

Figure 2.14 Figure showing how to read a k_r-ν diagram that includes the range above the Nyquist frequency and wave number.

known, though it seems to be associated with various motions around the umbra/penumbra boundary including penumbral bright filaments breaking into the umbra (e.g., Katsukawa et al. 2007b; Ichimoto et al. 2007), and boundary itself moving around by up to $\sim$ 2 arcsec, which is similar to the thickness of the ring, during the observation. These motions themselves may be manifestations of MHD oscillatory phenomena.

2.2.6.2 Peak frequency distribution

In this sunspot, higher-frequency components are dominant in its inner part, as was shown in Figure 2.11. This can be explained by considering the funnel-shape structure of the magnetic field in the sunspot (See Figure 2.16). This idea was first proposed by Beckers & Schultz (1972). In the outer part of a sunspot, magnetic field lines incline greatly, and due to the strong magnetic flux density in the sunspots the waves propagate along the inclined field lines. Since for the waves propagating along field lines, effective scale height H in the outer part is larger than that in the central part, the acoustic cutoff frequency $\omega_{\rm ac} \sim C_{\rm s}/(2H)$ decreases outward and lower-frequency component can propagate upward in the outer part. Vecchio et al. (2007) reported that magnetic network elements can also channel low-frequency photospheric oscillations into chromosphere even in the quiet region (see also Jefferies et al. 2006).

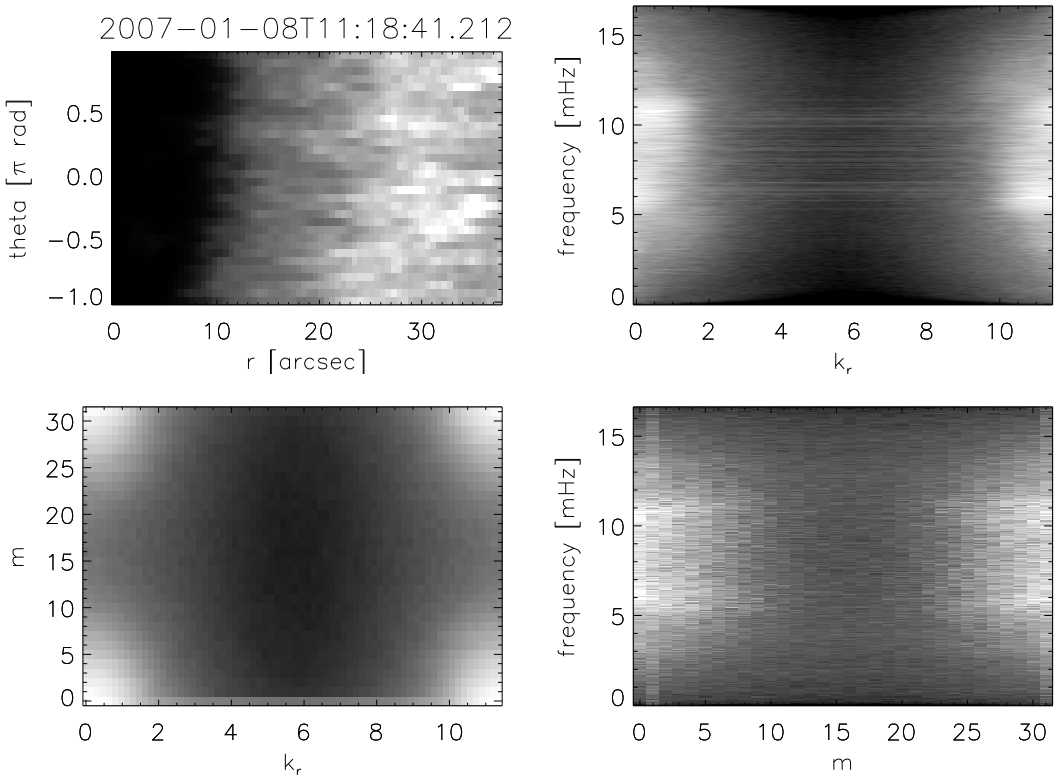

Figure 2.15 Upper-left panel shows Ca II H intensity map in cylindrical coordinate. The other panels show the Ca II H intensity power distribution in k_r–ν, k_r–m, m–ν domains.

2.2.6.3 Umbral Flashes

Umbral flashes are localized transient brightenings in chromospheric umbrae. Since Beckers & Tallant (1969) discovered them in Ca II H and K lines, many observations and theoretical works have been carried out on the subject (Recent examples are Rouppe van der Voort et al. 2003; Tziotziou et al. 2007). According to them, the period of the umbral flashes is around 3 minutes, and each brightening element is 3–5 arcsec wide. In our *Hinode*/SOT Ca II H data, we confirmed these properties, or at least found the correspondent features: the strong peak around 5.5 mHz in the umbral power spectrum, and the patchy structure of the transient brightenings of about 5 arcsec in the running difference intensity movie. It was also reported that they expand outward in the shape of arcs at the speed of 5–20 km s^{-1} and run into the penumbra. As was mentioned in §2.2.2.1, we find as a very rough estimate that they seem to move outward at a speed of up to 50 km s^{-1}. For a better estimate, a higher cadence is required.

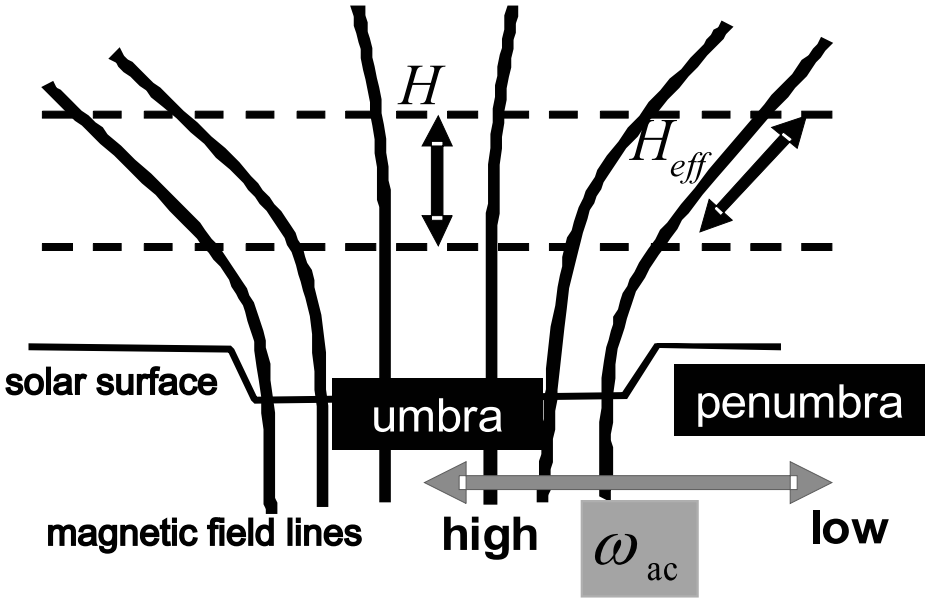

Figure 2.16 A schematic image of magnetic structure of a sunspot.

So far the umbral flashes are interpreted as upward-propagating shocks (Lites 1992; López Ariste et al. 2001; Rouppe van der Voort et al. 2003; Centeno et al. 2006; Tziotziou et al. 2007) . Since umbral flashes are known to occur only when the velocity amplitudes exceed a certain threshold, say, $\sim$ 5 km s^{-1}, as Rouppe van der Voort et al. (2003) and Tziotziou et al. (2007) mentioned, Rouppe van der Voort et al. (2003) suggested that a large Dopplershift due to upward propagating shocks along the line-of-sight results in a drop of opacity at the line center and causes the brightness enhancements, i.e., the umbral flashes. On the basis of their speculation, we check whether the intensity variation (brightening) during the umbral flash can be explained by a large Doppler shift or not. In an umbral-flash event, the maximum absolute value of the intensity difference between two successive frames normalized by the mean intensity of the two successive epochs at the position was around 0.75. The Ca II H filter on-board *Hinode*/SOT is one of broad-band filters. The bandwidth is about 0.3 nm and the center wavelength is 396.85 nm (Tsuneta et al. 2008). Taking Ca II H line profile and the filter profile into account, we can calculate the intensity difference due to the Doppler shift of the Ca II H line profile. In our calculation, if the line-of-sight velocity is 20 km s^{-1}, the same order of the sound speed, the normalized intensity difference is only 0.017. To attain the observational normalized intensity difference (0.75), we need the LOS velocity up to 200 km s^{-1}; in this case, the normalized intensity difference can be

0.88. Such a high velocity is unlikely in the umbral atmosphere, however. Therefore, we conclude that the umbral flash cannot be explained by Doppler shift only.

Moreover, the proposed models, such as some kinds of MHD waves (Havnes 1970) and upward-propagating shocks (Rouppe van der Voort et al. 2003; Centeno et al. 2006), do not readily explain the node-like structure we find around the center of the umbra as one then expects the umbral flashes are the most visible in the umbral center. There is NO apparent reason for power suppression around the center according to the models. Of course, there may be no wave. But there is a possibility, for example, that the brightening period is TOO SHORT to observe. This can be explained by considering the funnel-shape structure of the magnetic field in the sunspot. If the wave front is inclined to the horizontal plane (the formation layer of Ca II H line), its horizontal propagation phase speed $v_{\rm h} = v/\sin\theta$, where v is the propagation speed of the wave and θ is the angle of incidence of the wave. If the magnetic field line is nearly vertical, the angle of incidence of the wave along the field line (θ) is close to 0. Hence, around the center of the umbra, the horizontal propagation phase speed $v_{\rm h}$ diverges, so the bright region moves out rapidly and the brightening period can be too short to observe. This can be an explanation of 'node'.

Feature somewhat similar to our 'node' was reported by Tziotziou et al. (2007). In their Doppler velocity maps in Ca II 8542 Å there was a small area around the center of the umbra where the velocity amplitude was lowest. They suggested at the 'calmest umbral position' there is no umbral flash.

It has to be mentioned that the running umbral waves in the chromosphere reported by Kobanov & Makarchik (2004) may be the same oscillational phenomenon as the umbral flashes. In their study, using Hα data instead of Ca II data, they found line-of-sight velocity oscillations in the sunspot umbra, but they did not find the brightenings in Hα. Therefore, they concluded that the running umbral waves they found was different from the umbral flashes. However, as they mentioned, brightening in Hα does not always accompany the umbral flashes; since the other properties of the running umbral waves are similar to those of the umbral flashes, we cannot exclude the possibility that they are the same phenomenon.

Compared with oscillation signals detected in Dopplergrams, oscillation signals detected in intensity maps are not easily interpretable, because the intensity oscillations are affected not only by the motion of the plasma, but also by how the fluctuation of density, temperature, degree of ionization, and other thermodynamic quantities affect the line formation. Detailed radiative transfer calculation needs to be undertaken. For further

study, we need to compare the oscillations in intensity maps with those in Dopplergrams to understand the relationships between the oscillation parameters.

2.3 Other Sunspots

We checked *Hinode*/SOT datasets of several other sunspots. All the sunspots we observed in chromospheric lines showed umbral flash, although the strength varied.

We compared the SOT data of a well-developed Japan-shaped sunspot (NOAA 19353) with *SOHO*/MDI intensity and Dopplergram datasets. As for a sunspot which appeared very close to the circular sunspot (NOAA 10935) on the solar disc (NOAA 10933), we compared the SOT data with the radio data obtained by Nobeyama Radioheliograph.

2.3.1 Japan Sunspot (NOAA 10953)

The Sun shows a well-developed sunspot in the beginning of May, 2007. *Hinode*/SOT observed the Japan-shaped sunspot with several observation programs. Thanks to a joint observation of *SOHO*/MDI, we could compare the sunspot datasets obtained by MDI and SOT. Before the joint observation, SOT took some Hα datasets with relatively high cadence. Exploiting these datasets, we investigate the sunspot oscillations in this non-circular sunspot.

2.3.1.1 Comparison with MDI data on May 2, 2007

Michelson Doppler Imager (MDI; Scherrer et al. 1995) on board *Solar and Heliospheric Observatory (SOHO)* observed NOAA Active Region 10953 on May 2, 2007, with 1-minute cadence with high-resolution mode. It was a joint observation with *Hinode*/SOT, and was carried out from 17:02 to 22:50, while SOT observation was carried out over 12-hour period from 17:00.

In this section, we report on the comparison between these two data. We used the data obtained during the period where the two observations overlapped: from 17:02 to 22:50. During this period, SOT observed in Ca II H and blue continuum with 56-sec cadence. The pixel size of the MDI data and SOT data were 0.6 arcsec and 0.1 arcsec, respectively.

Calibration For dark subtraction, flat fielding, and correcting for bad pixels of SOT data, we used a calibration program provided by the SOT team. For MDI data, we used

interpolation to fill the data gaps.

We coaligned SOT data and MDI data using the SOT blue continuum data and the MDI intensity data as references. Although the field of view was much larger, we focus on the field of 80 arcsec × 80 arcsec around the sunspot.

Power maps We used running difference intensity normalized by the mean intensity of two running frames to obtain intensity power map in order to remove any possible remnant spatial trend.

Figure 2.17 shows power maps in the Ca II H and blue continuum intensity obtained by *Hinode*/SOT. Figure 2.18 shows Doppler signal power maps obtained by *SOHO*/MDI. The power maps in the right panel of Figure 2.18 were calculated by taking the running difference of the Doppler signals, while the power maps in the left panel were obtained by the raw Doppler signals. Since we do not find any significant difference between these two, the power distribution is not affected by artifacts such as spatial trends. Figure 2.19 shows MDI intensity power maps together with an intensity image.

From these datasets, we found the followings:

1. Blue continuum intensity power maps obtained by SOT data are essentially the same as intensity power maps obtained by MDI data. Both of them are photospheric lines.

2. We have found 5-mHz signal in the umbra in MDI (photospheric) Doppler power maps, although in the photospheric intensity maps, i.e., SOT blue continuum and MDI intensity maps, the power is suppressed in the umbra in all frequency ranges. The 5-mHz signal in Doppler power maps may be the photospheric counterpart of umbral flashes.

3. MDI Doppler power maps show a region of suppressed power on the lower-right corner of the umbra (around Kanto district in Japan), especially in 2 – 4 mHz ranges, while the power around this region is enhanced in the Ca II H intensity power maps.

Conclusions We have compared the SOT chromospheric and photospheric intensity power maps with the *SOHO*/MDI photospheric intensity and Doppler signal power maps. In the photospheric intensity power maps, power is suppressed in the umbra, which is similar to the result by SOT photospheric-line intensity power maps. On the other hand, enhanced

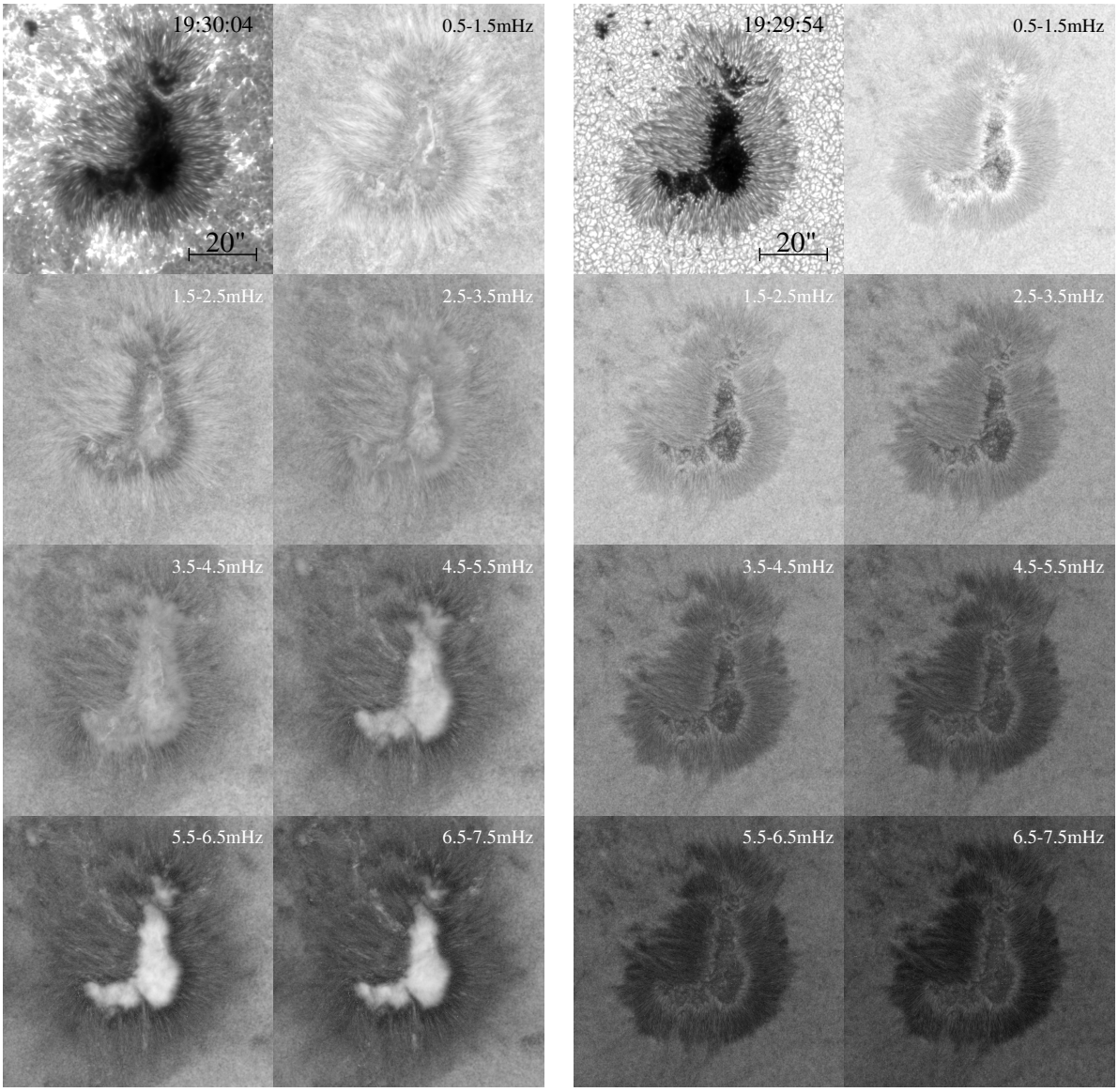

Figure 2.17 *Left*: Ca II H intensity power maps (*Hinode*/SOT) of NOAA 10953. The upper-left panel shows a sample intensity map in Ca II H. The figure in the upper-right corner in the upper-left panel indicates time. The power is displayed in logarithmic greyscaling (4 order of magnitude). *Right*: Blue continuum intensity power maps (*Hinode*/SOT) and a sample intensity map.

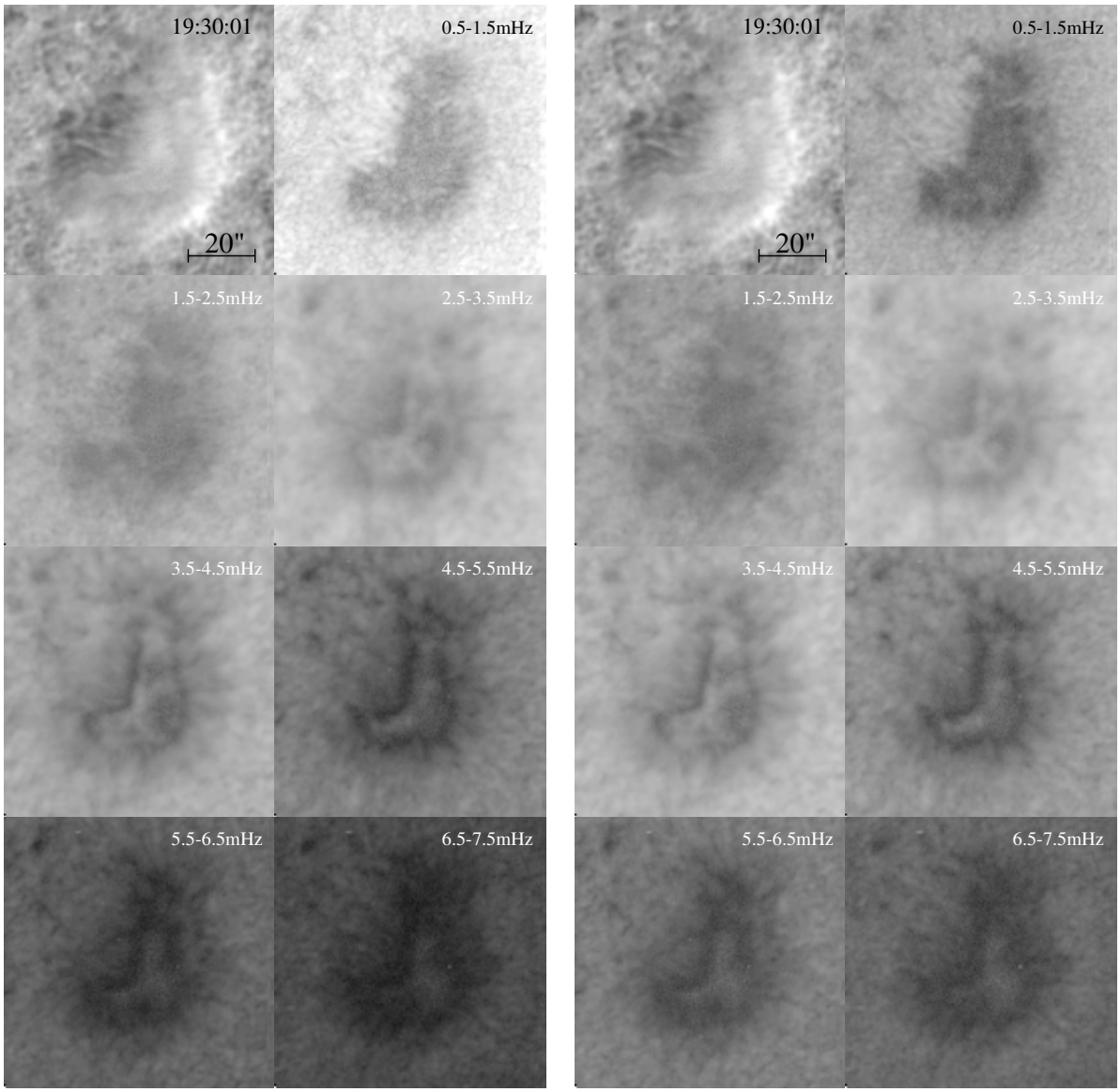

Figure 2.18 MDI Doppler power maps of NOAA 10953. For the power maps in the right columns, we used running difference. A sample Doppler signal map is shown in the upper-left panel.

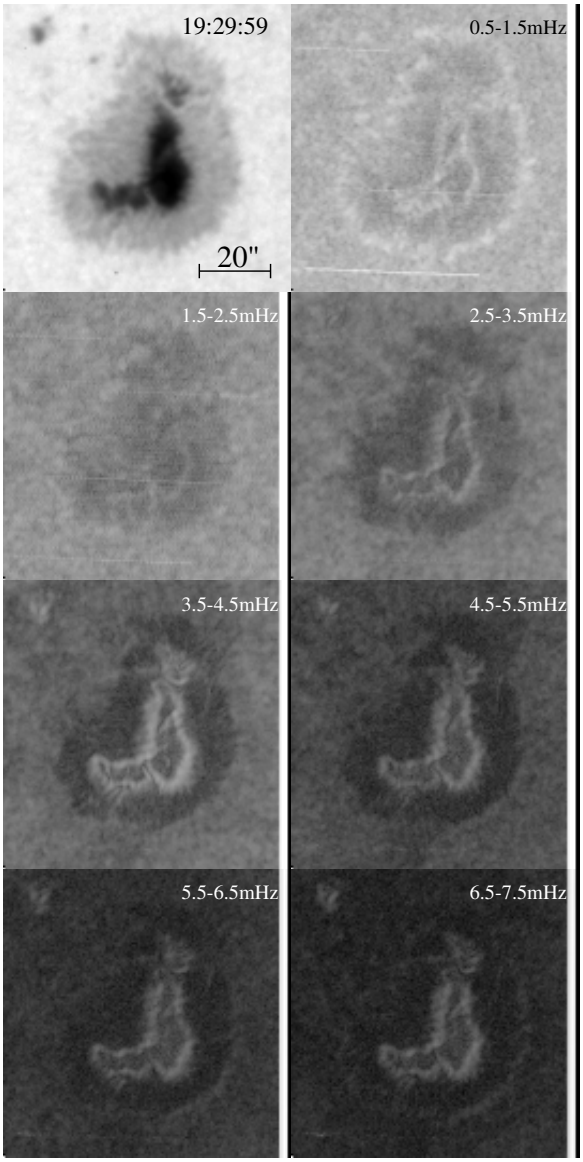

Figure 2.19 MDI intensity power maps and a sample intensity map of NOAA 10953.

power in 5-mHz frequency range is found in the photospheric Doppler signal power maps. This may be a photospheric counterpart of the umbral flash, which is prominent in the chromospheric intensity power maps.

2.3.1.2 High-cadence Hα data on April 30, 2007

SOT on *Hinode* observed NOAA 10953, the Japan sunspot, with a high cadence not only in Ca II H but also in Hα. On April 30, 2007, SOT observed the active region with 9.6-second cadence for 40 minutes (13:00 - 13:40 UT). It took Ca II H line images using BFI and also took Hα line-centre images using NFI. The pixel size is $\sim$ 0.1 arcsec in Ca II H line images and $\sim$ 0.08 arcsec in Hα images. Sample images are shown in Figure 2.20. One cannot tell from these sample images only, but if one check the movie from these datasets, umbral flash patterns are seen; umbral flashes are observed not only in Ca II H line but also in Hα line.

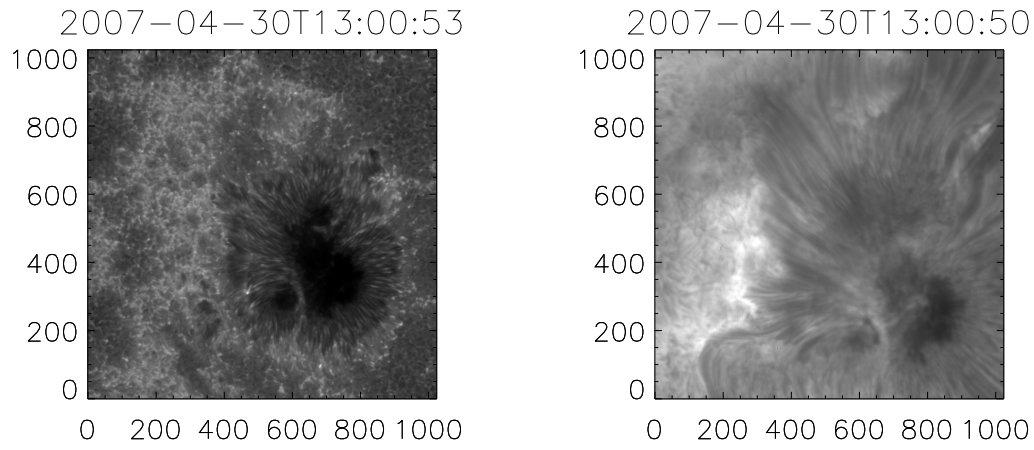

Figure 2.20 Image samples. *Left*: Ca II H intensity map. *Right*: Hα intensity map. The unit of both axes are pixel. The field of view is 60 Mm (82 arcsec) square.

The calibration procedure is same as that in previous section. However, the calibration method for NFI datasets is not established yet and the Hα dataset is still contaminated due to the bubble (see §3.4.1). The outcome of this Hα dataset is an admittedly crude but initial test for detecting umbral flash in another chromospheric line, Hα.

Power spectra Figure 2.21 shows the power spectra of Ca II H line and Hα intensity data. Since the observation was carried out with 9.6-sec cadence, the Nyquist frequency is 52 mHz. The resolution of frequency is 0.42 mHz.

For the Ca II H intensity power spectrum, umbra, penumbra, and moat region are defined according to Ca II H intensity averaged over the observing period. The moat region is defined as a bright region to the left of the umbra. The quiet sun is defined as the region that is outside the sunspot and that is not bright in Ca II H, so we consider the upper-right corner of the FOV as the quiet sun.

For the Hα intensity power spectrum, the umbra is defined according to the average Hα intensity over the observing period. The quiet sun is defined the same region in terms of pixel as that in the Ca II H intensity power spectrum, although the pixel size is different.

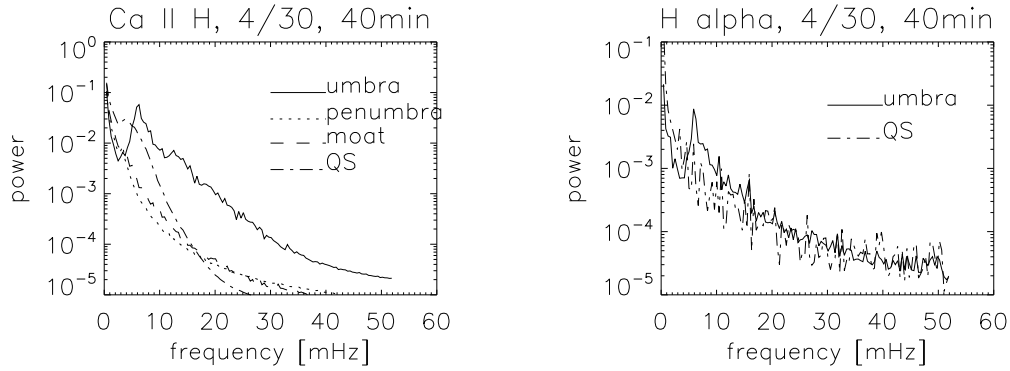

Figure 2.21 Ca II H (*left*) and Hα (*right*) intensity power spectra.

The Ca II H intensity power in the quiet sun has a broad peak at 3.8 mHz, while that in the umbra has a sharp peak at 6.3 mHz. A 4-mHz peak are barely identifiable in the penumbra. The power spectrum in the moat region seems to decrease almost monotonically. On the other hand, the Hα intensity power spectrum in the umbra has a significant peak at 5.9 mHz. This component corresponds to the umbral flash. The spectrum is too noisy to discuss other possible features, however; more elaborate calibration for Hα dataset is required.

Peak frequency distribution In each pixel, we searched the peak frequency in Ca II H intensity power density spectrum, and spatial variation of the peak is shown in Figure 2.22. We did not make a corresponding map of Hα data, because the data were too noisy (c.f.,

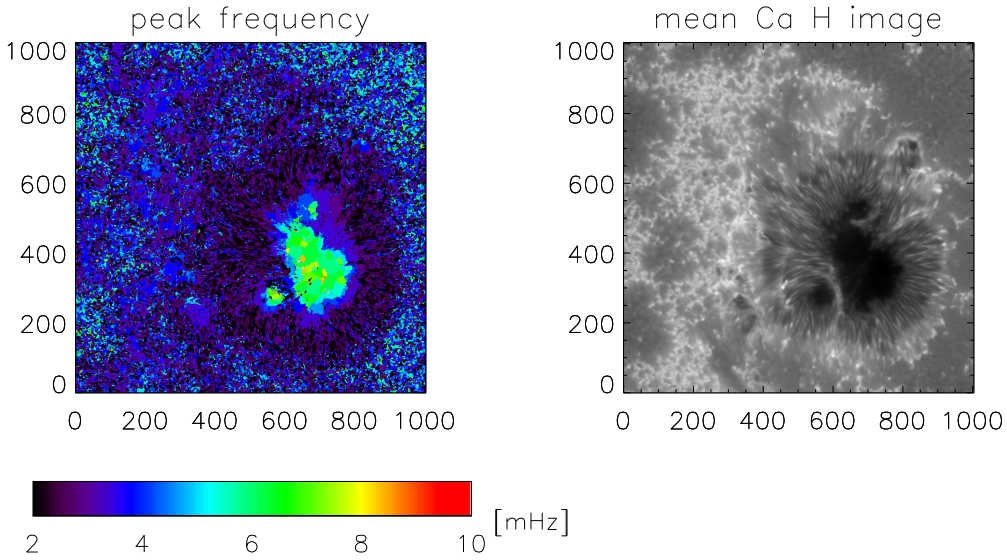

Figure 2.22 *Left*: Peak frequency distribution of Ca II H intensity power spectra. *Right*: Average Ca II H intensity. The unit in both axes are pixel.

Figure 2.21). Like in the case of the circular sunspot (see Figure 2.11), the peak frequency in this sunspot is also higher in the inner part.

Hα observations of umbral flash We confirmed that the umbral flash is seen in two chromospheric lines: Ca II H line and Hα line.

In the past, Giovanelli (1972) reviewed that the umbral flashes were visible in the H and K lines above sunspot umbrae but hardly visible, or even invisible, in Hα filtergrams, citing Beckers & Tallant (1969). But they found in Hα analogous phenomena which may be related to the umbral flashes detected in Ca lines. More recently, Tziotziou et al. (2007) reported that Hα intensity power spectra in umbra has a 3-min peak. But their observation with 8-second cadence was only 17 minutes long. For the short dataset, they used a cross-wavelet transform for spectral analysis. They also reported that there is no clear Hα Doppler velocity-intensity relation "due to the nature of the Hα wing formation which has intensity contributions from several atmospheric layers".

Though noisy, our results are not inconsistent with the previous ones.

2.3.2 NOAA active region 10933: Comparison with radio observations

NOAA active region 10933 appeared on the Sun in the same period as NOAA active region 10935 mentioned in §2.2. We chose this active region to analyze because (1) it was observed by SOT with 30-second cadence for about 4 hours on January 9, 2007 , (2) we have Nobeyama Radioheliograph data of the sunspot since the observation period was during the daytime in Japan, and (3) the active region was relatively bright in radio.

We examined this active region by comparing the umbral oscillation seen in the 17-GHz data with that in Ca II H line data in order to find a clue to the generation and propagation mechanism of the umbral flash.

Figure 2.23 shows the full-disc MDI intensity map and magnetogram on January 9, 2007. The sunspot group closer to the west limb is the active region NOAA 10933; the other one is NOAA 10935 mentioned in §2.2.

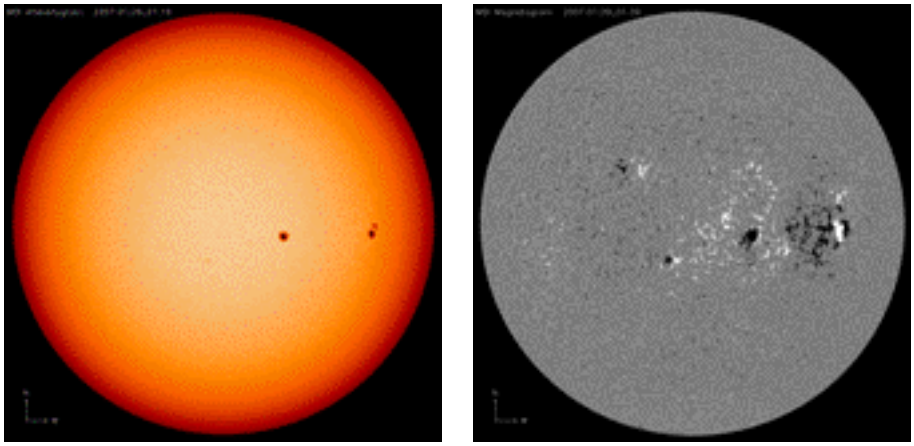

Figure 2.23 MDI intensity map (left panel) and magnetogram (right panel) on January 9, 2007. Courtesy of *SOHO*/MDI consortium.

2.3.2.1 *Hinode*/SOT data

SOT onboard *Hinode* observed the sunspot over a duration of 249 minutes on January 9, 2007. We obtained series of filtergrams in Ca II H, blue continuum, and G band with 30-second cadence. The Nyquist frequency is 16.7 mHz.

Power maps Figure 2.24 shows a Ca II H intensity map and the intensity power maps averaged over 1-mHz-wide frequency ranges, from 1 mHz to 15 mHz with logarithmic greyscal-

ing. Above 4 mHz the oscillation power is enhanced in the umbra. No clear node-like structure was present in this sunspot.

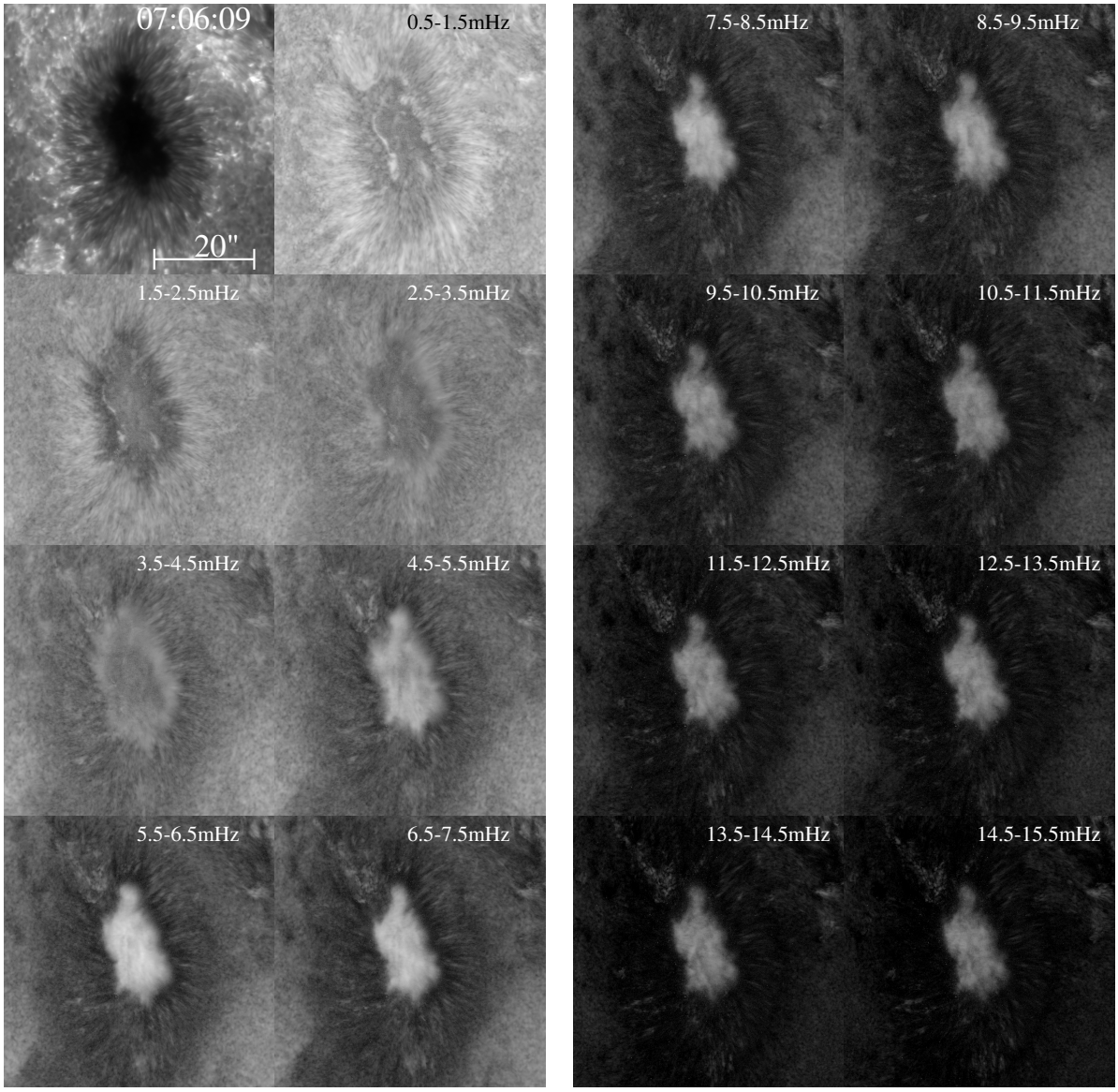

Figure 2.24 Ca II H power maps of NOAA active region 10933.

Power spectra Figure 2.25 shows the power spectrum in the umbra. This spectrum is averaged over 73224 pixels. It shows a clear peak around 6 mHz, and a rather broad peak around 12 mHz, i.e., the overtone of the 6 mHz oscillation. As we will discuss later, this overtone peak is not found in the radio power spectrum in the umbra.

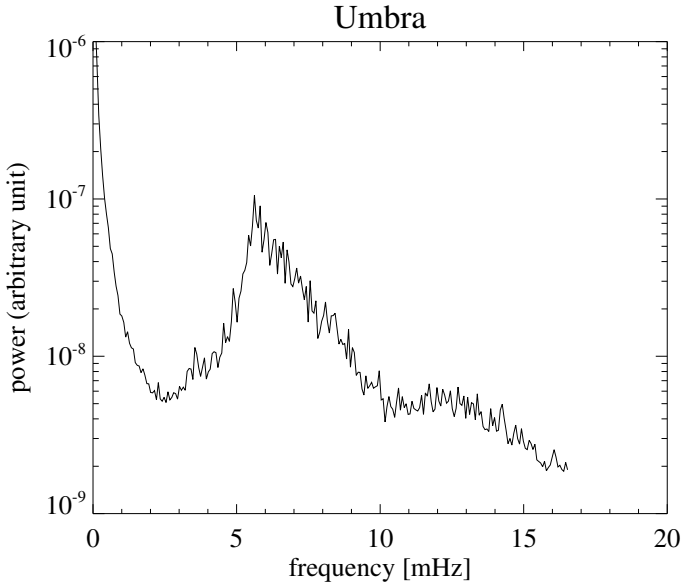

Figure 2.25 Ca II H intensity power spectrum in the umbra.

Figure 2.26 shows 5-mHz power maps and the Ca II H intensity map averaged over the entire observation period as well as a sample intensity image. In the umbra we chose one area (B) with slightly suppressed power and four areas (C, H, T, and S) with relatively large power to compare the power spectra in these areas. The positions of the five areas are indicated in the upper-right panel in Figure 2.26. Figure 2.27 shows their power spectra, the three panels in the right column being for the outer part of the umbra. We do not note any significant difference between the power spectrum in the hump (area B) and the rest. We do observe, however, once again the peak frequencies in the outer areas tend to be lower than in the inner areas.

2.3.2.2 NoRH radio data

The umbral oscillations have been observed in radio data (e.g., Shibasaki 2001).

The radio observation was carried out by Nobeyama Radioheliograph (NoRH; Nakajima et al. 1994), a radio interferometer. The full-disc observation is routinely carried out with 1-second cadence in 17 and 34 GHz. We used 17-GHz data taken during the period when the SOT also observed the active region, i.e., during the period from 5:00 to 6:30 UT on January 9, 2007. A sample radio image is shown in Figure 2.28. The bright region on

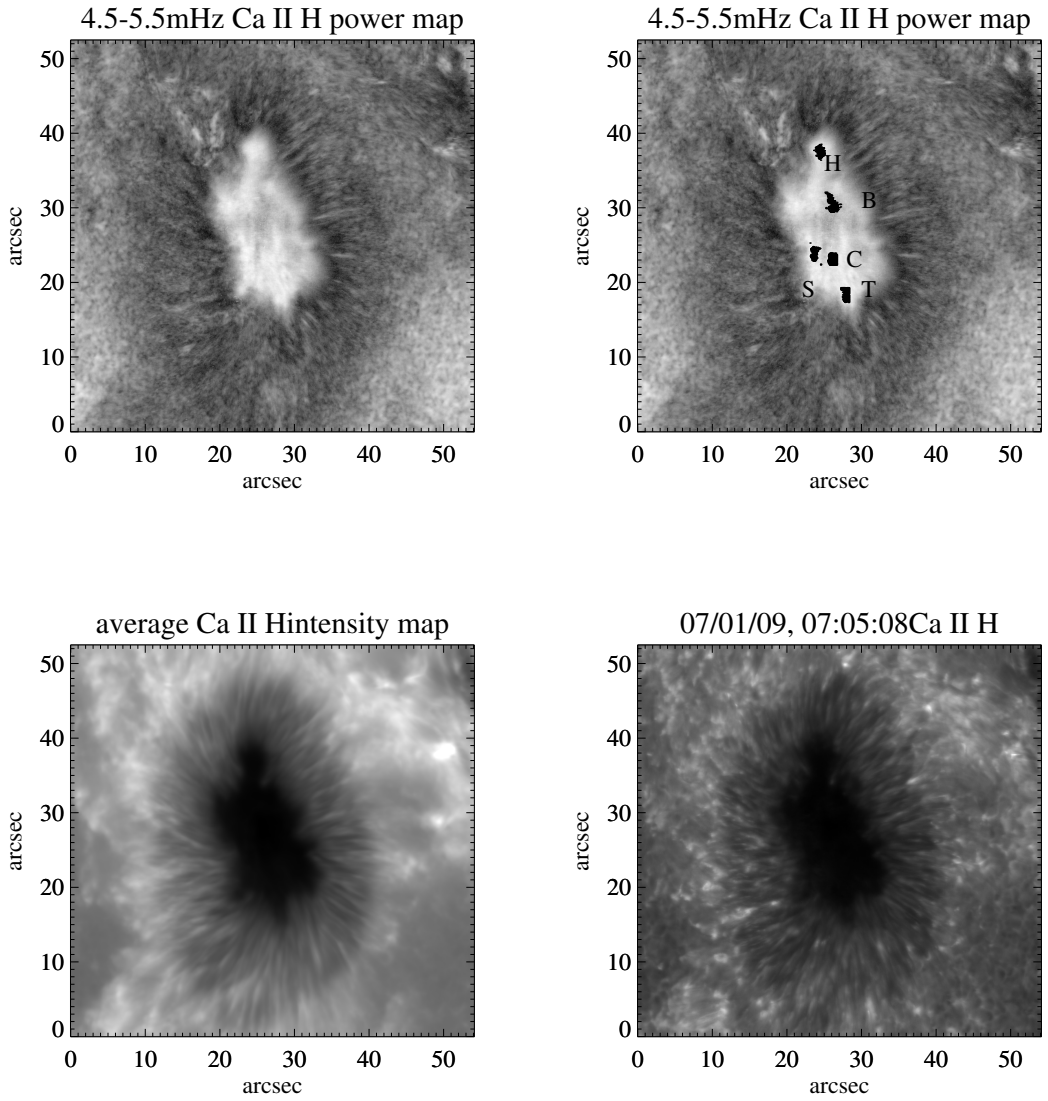

Figure 2.26 *Upper-left*: Ca II H intensity power map averaged over the frequency range of 4.5-5.5mHz. *Upper-right*: the same Ca II H intensity power map in 5-mHz range with marks. Marked areas (B, C, H, T, and S) are the areas where the spectra shown in Figure 2.27 are calculated. *Lower-left*: Ca II H intensity map averaged over the whole observation period. *Lower-right*: A snapshot of the sunspot in Ca II H line.

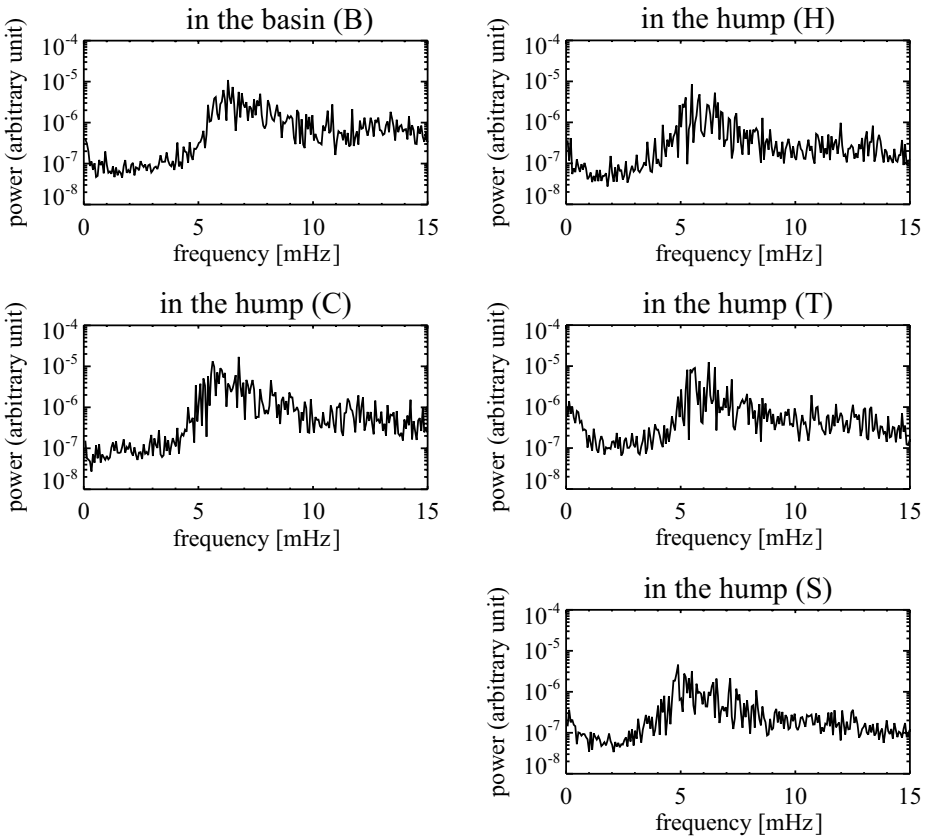

Figure 2.27 Ca II H intensity power spectrum at the five areas (B, C, H, T, and S) in the umbra shown in Figure 2.26. The panels in the right column are for the outer part of the umbra and show the peak at lower frequency.

the west hemisphere is the active region. The emission mechanism of this compact radio source, a sunspot, is considered to be gyroresonance emission. At 17 GHz, the emission region corresponds to a 2000-G iso-magnetic-field-strength layer (Shibasaki et al. 1994; Shibasaki 2001).

The so-called "correlation coefficient" and its Fourier power spectrum are shown in Figure 2.29. This "correlation coefficient plot" is not a real light curve in radio, but mean value of signal correlations between each pair of antennas in the interferometer, and the value is known to be associated with the strength of radio signal, except for the case of strong radio emission, such as flares. Therefore, we used it as an alternative for a light curve. This power spectrum has a broad peak at 6 mHz, but unlike the Ca II H power spectrum (Figure 2.25), it has no peak corresponding to its overtone. If the oscillation is a

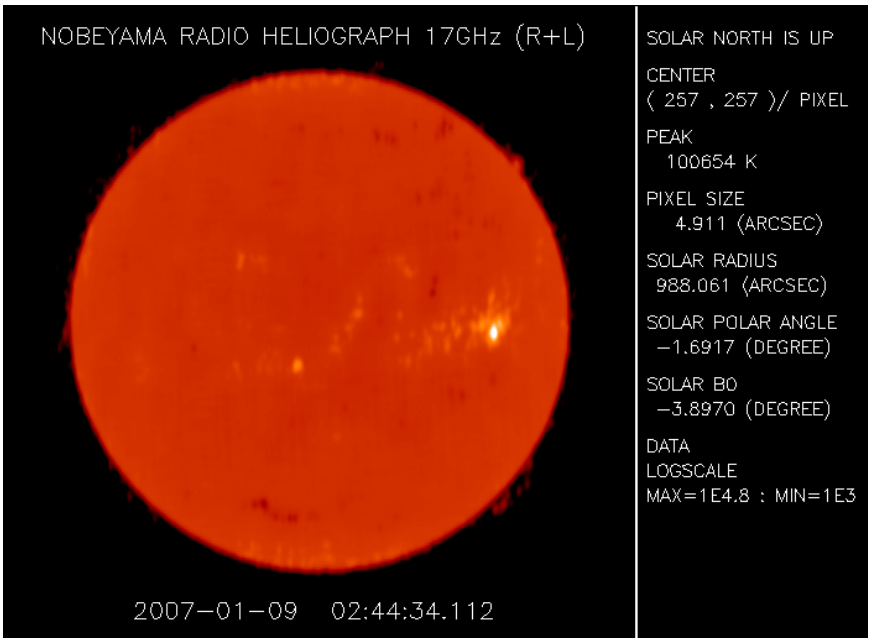

Figure 2.28 NoRH full disc image (17GHz) on January 9, 2007. The bright region on the right is the NOAA active region 10933. Note that the NOAA active region 10935, which was located on the left of 10933, was not bright in 17GHz at that time. Courtesy of Nobeyama Solar Radio Observatory (http://solar.nro.nao.ac.jp/norh/html/daily/).

non-linear wave, such as shock waves, we expect overtones in the power spectrum. How we reconcile the signature of non-linear waves in the chromosphere observed in Ca II H lines and the lack of such signatures in radio is of a great interest.

The correlation coefficient plot decomposed into two polarization components, right and left circular polarization components (RCP and LCP), is shown in Figure 2.30. We find 3-minute oscillation only in RCP curve. The polarization of the emission from sunspots depends on the magnetic polarity of the sunspot (Shibasaki 2001).

We compare light curves of Ca II H and 17-GHz radio in Figure 2.31. The SOT light curve seems to be somewhat ahead of the radio one, although we cannot say that with confidence. The cross-correlation function between these light curves (shown in the right panel in Figure 2.31) is also ambiguous.

The formation layer of Ca II H line, although it is broad, is about 250km above the photosphere (in the lower chromosphere; Carlsson et al. 2007). On the other hand, the radio emission is said to be formed in the 2000-G iso-gauss layer (Shibasaki et al. 1994;

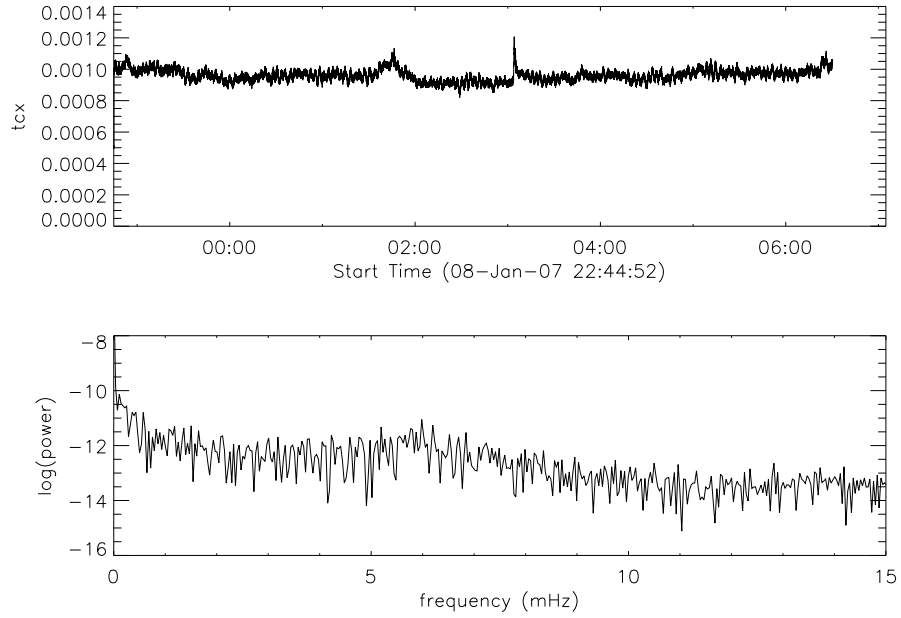

Figure 2.29 *Top*: NoRH correlation plot (tcx) on January 9, 2007. *Bottom*: Fourier transform of the correlation plot.

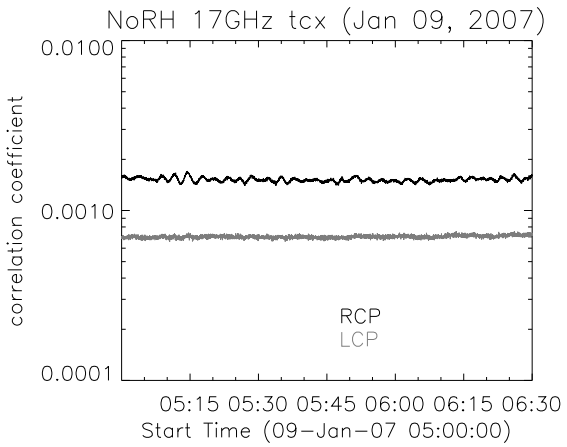

Figure 2.30 NoRH correlation plot (tsx) on January 9, 2007.

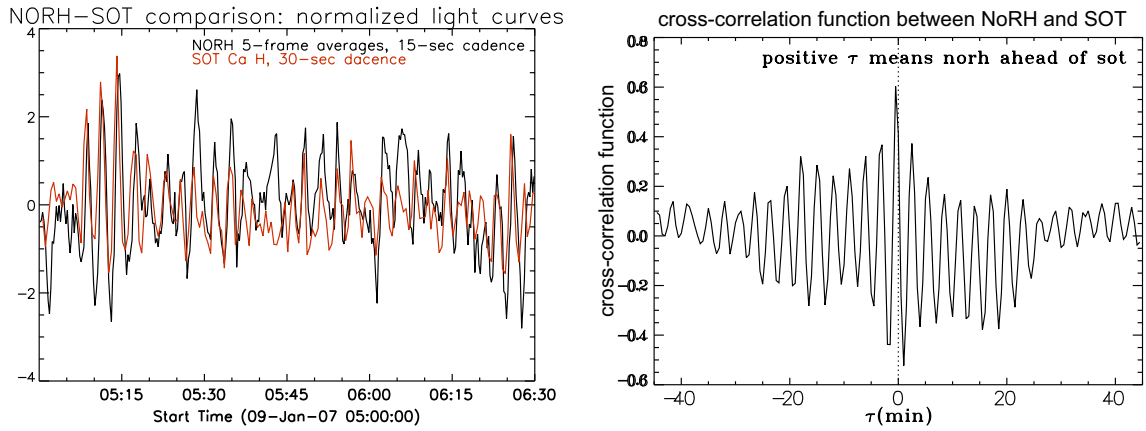

Figure 2.31 NoRH-SOT comparison: normalized light curves (*left*) and cross correlation function between NoRH and SOT(*right*). In the left panel, the black line indicates the NoRH (17GHz) 5-frame average brightness with 15-sec cadence. The red line indicates the SOT Ca II H light curve with 30-sec cadence.

Shibasaki 2001). If we assume the radio formation height is below that of Ca II line, it is consistent with the fact that the overtone is found only in the spectrum in Ca II line, and the assumption that the wave steepens as it travels upward. It is not consistent, however, with the finding in the cross correlation between two light curves, however ambiguous it might be.

For more detailed analyses, we need higher-cadence SOT data.

2.3.3 NOAA 10926 on December 5, 2006

NOAA Active Region 10926 appeared in December, 2006. It was observed by SOT from 19:30 to 20:59 UT on December 5. The Ca II H observation was carried out with about 8-second cadence. This means that the Nyquist frequency is 62.5 mHz and the resolution of frequency is 0.2 mHz. At that time, the active region was located 810" west and 170" south from the disc centre, i.e., at a heliocentric distance of 56°.

Figure 2.32 shows a Ca II H intensity sample image and power maps of the active region. We use normalized running difference intensity to compute the power. This sunspot had two umbrae. Umbral flash was also found in this active region. But for the upper-right umbra, the umbral flash was rather faint. It may be due to its location (closer to the limb). On the other hand, the left umbra seemed to have two 'epicentres' of umbral flash. But we

cannot find any node-like structure in this sunspot.

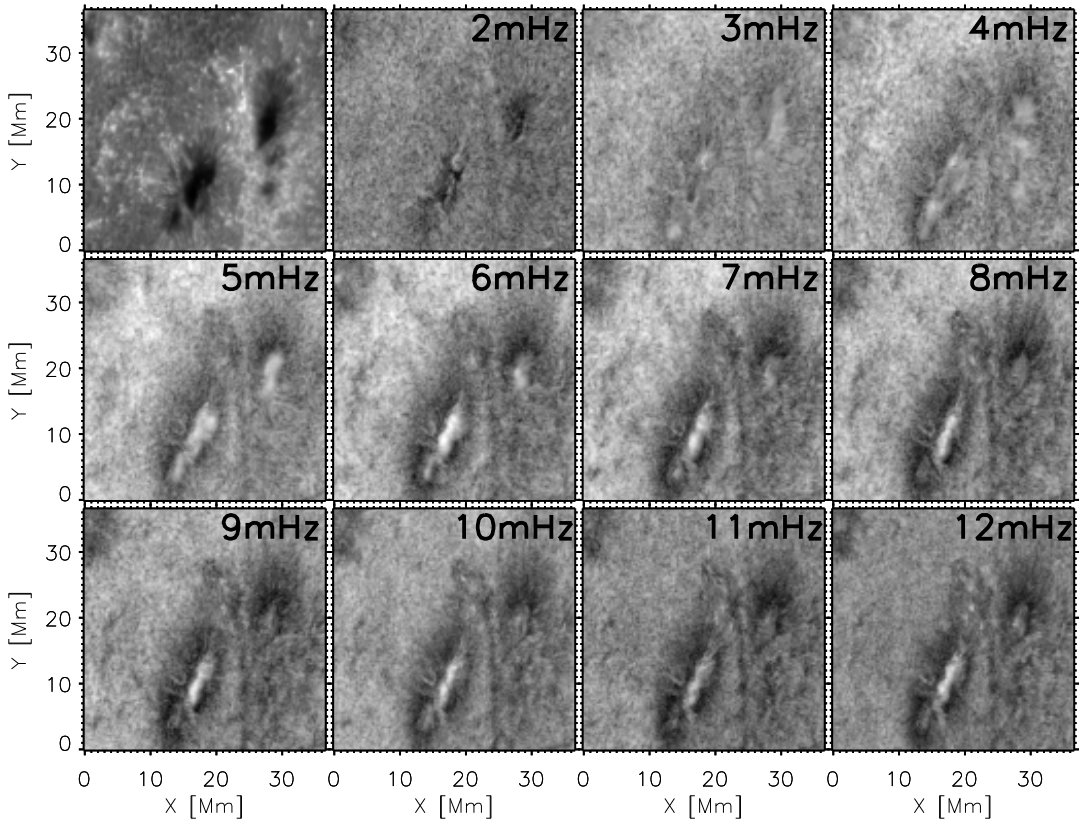

Figure 2.32 Ca II H intensity map (*upper-left*) and power maps of NOAA Active Region 10926. In the power maps, the power in each frequency range is displayed in logarithmic greyscaling (3 order of magnitude). In higher frequency ranges than shown in this figure the power is much weaker and the power distribution is similar to that in 11-12 mHz power maps.

2.3.4 NOAA 10956 on May 20, 2007

NOAA Active Region 10956 appeared in May, 2007. On May 20, SOT observed the active region from 6:41 to 7:52 in Ca II H, blue continuum, and red continuum. The cadence was about 24 second, but not quite regular. The Nyquist frequency is ∼19 mHz and the resolution of frequency is ∼0.23 mHz.

This active region has three major umbrae and a few pores. Sample images are shown in Figure 2.33. In Ca II H data, not only in the major umbrae but also in small pores,

umbral flash was found in this sunspot. It was located rather close to the disc centre during the observation period. The strength of the umbral flash may depend on the location on the Sun. In this sunspot, the umbral flash seems to propagate outward concentrically.

In blue and red continua data, we cannot find umbral flash. We must admit that the red continuum data was not in a clear focus.

In the blue continuum intensity map, we find many umbral dots, especially in the eastern major umbra. The southern part of the western major umbra was very narrow and had a larger number of umbral dots than the northern part of the umbra. In this umbra, umbral flash was seen more clearly in the northern part of the umbra than in the southern part. However, we cannot find any clear relationships between umbral flash and umbral dots. The relationships are discussed in Rouppe van der Voort et al. (2003), for example, but they did not find obvious relation between them, either.

2.3.5 NOAA 10999 on June 19, 2008

NOAA Active Region 10999 appeared in June, 2008. SOT observed the active region with a relatively high cadence. Here we used the Ca II H dataset taken on 19 June from 3:05UT to 4:10UT with 16-second cadence. Figure 2.34 shows a sample image in Ca and the oscillation power maps. In the spectrum in the umbra shown in Figure 2.35, peaks corresponding to overtones appear in 10-15 mHz range. This is another example showing nonlinear nature of the umbral oscillation.

2.4 Summary of Study on Sunspot Oscillations

We investigated oscillations in several sunspots using the high-resolution datasets taken by *Hinode*/SOT. We succeeded in detecting oscillation signals both in umbrae and penumbrae. The umbral flash was detected in all the sunspots we observed in chromospheric lines by SOT.

In this series of studies, we confirmed the properties which were reported in previous works, for example:

- Umbral flash is seen in the chromospheric lines, such as Ca II H and Hα lines, and the dominant components of the flash are above 4 mHz.
- Umbral flash is not seen in photospheric intensity datasets.

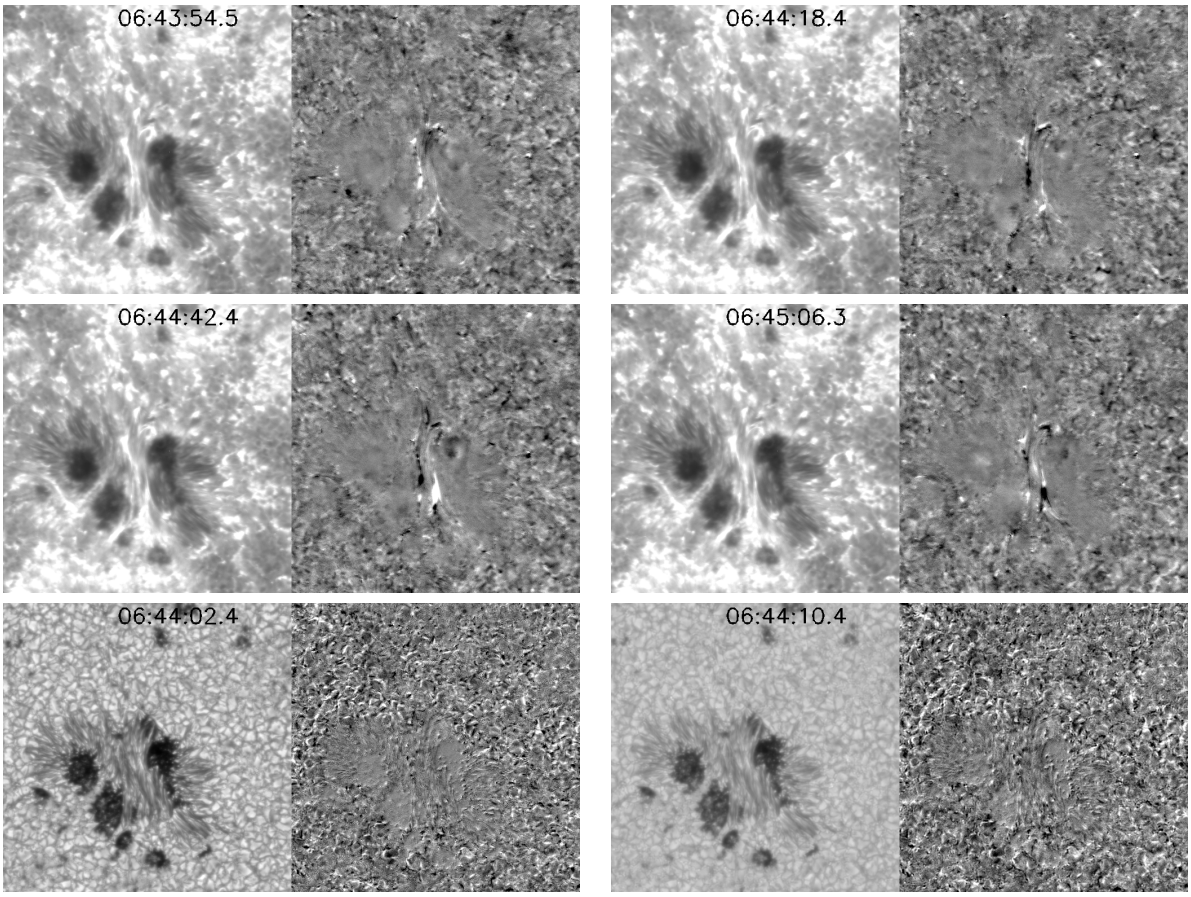

Figure 2.33 *Top and middle rows*: Ca II H intensity (*left*) and running difference intensity (*right*) maps of NOAA Active Region 10956. Four successive frames are shown. *Lower-left*: Blue continuum intensity and running difference intensity maps of the active region. *Lower-right*: Red continuum intensity and running difference intensity maps of the active region. All figures on the left panels indicate times. The field of view is 39.8 Mm (54.3 arcsec) square in all the panels.

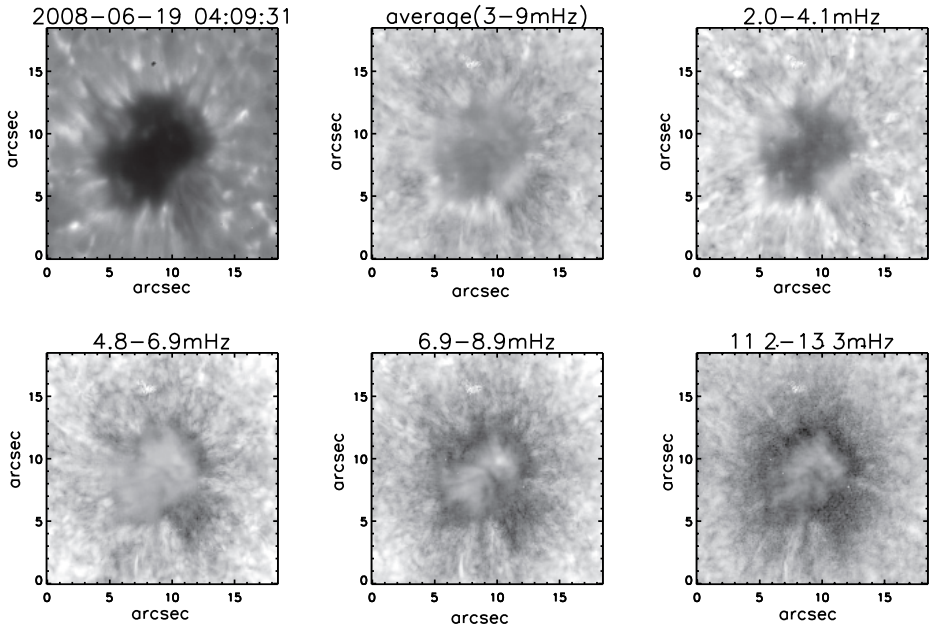

Figure 2.34 Power maps and a sample image of NOAA 10999. The upper-left panel shows an intensity map in Ca II H line. Other panels show power maps for the frequency ranges indicated in the panels. The field of view is 13.7 Mm (18.5 arcsec) square in all the panels.

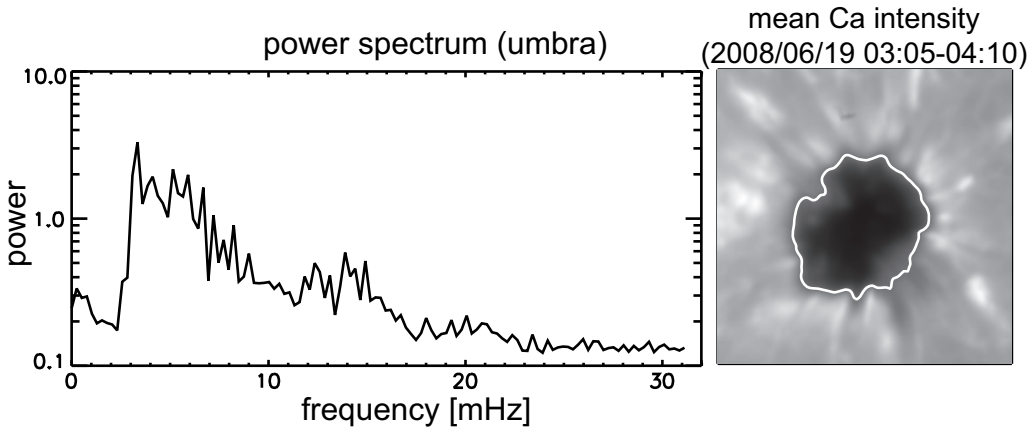

Figure 2.35 Power spectrum of an umbra in NOAA 10999. The umbra is defined by the intensity; the umbra area is within the white lines in the right panel, which shows the intensity map averaged over the whole observing period. The field of view of the right panel is the same as that in Figure 2.34.

- Umbral oscillation is also observed in 17-GHz radio.

- The dominant frequency component in sunspots is the highest in the central part of umbrae and decreases towards penumbrae and beyond, to outside of the sunspots. Although the frequency distribution in penumbrae has been reported before, as far as we know, it has never been so clearly demonstrated throughout a sunspot.

- The umbral oscillation observed with chromospheric lines show a non-linear nature.

So far, we obtained only intensity signals of oscillation which are more difficult to interpret than Doppler signals. Doppler shift signals simply indicate velocity fields in sunspots, while intensity signals are affected by not only the motion but also some thermodynamic quantities. As we mentioned in §2.3.1.1, in the power maps computed from MDI photospheric Dopplergrams possible counterparts of umbral flash are found, while they are not found in photospheric intensity power maps. For further study, we need to take Dopplergrams and intensity images in chromospheric lines as well as photospheric lines. In addition to that, Spectropolarimetory (SP) datasets of SOT will provide us Doppler shift distribution in the sunspots besides vector magnetogram of the sunspots. Due to the large amount of data SP produces and the telemetry limit of the satellite, cadence and/or field of view and/or observation period has to be compromised, but it may still be useful.

The 'node'-like structure mentioned in §2.2 was not found in any other sunspots. One possible reason for that is the sunspot mentioned in §2.2 was the only sunspot that is circular. To solve the riddle of the 'node', we need to observe well-developed circular sunspots, with high cadence (less than 30 seconds at least).

To understand the mechanism of the umbral flash, we need dynamical simulation of a sunspot including radiative magnetohydrodynamics based on a sunspot model. Conversely, a successful dynamical sunspot model, which has not been completed yet, should explain the properties of umbral flash, such as frequency distribution in sunspots or 'node'-like structure we have found.

After the observations we have mentioned in this chapter, the solar activity reached the very minimum. It was expected that the activity level would come up by mid 2008, but this did not happen; the activity is still very low as of the time of writing. Hence, we did not have a chance to acquire further sunspot data including Doppler signals and/or Spectropolarimetory datasets. The fact that instrumental issue of SOT/NFI which is used

for taking Dopplergrams has not been solved before the sunspots ceased to appear is another reason for the lack of sunspot data. We cannot carry out further analyses in this thesis. In the near future the Sun will be active, and it may be a good time to resume the observational study of sunspots oscillations.

Chapter 3

Time–Distance Method

In this chapter, we summarize the time–distance analysis procedure and also discuss a few outstanding issues in local helioseismology. Behaviour of acoustic waves around and above the photosphere, issues of strong perturbation in strong magnetic field region, and issues of definition of travel times are discussed.

After the analysis method is reviewed in this chapter, an application to the *Hinode*/SOT datasets is described in Chapter 4. We investigate statistical property of the cross-correlation function used in the time–distance analysis (Chapter 5). Another application to the *Hinode*/SOT datasets in the quiet region of the Sun is shown in Chapter 6.

3.1 An Outline of Time–Distance Method

Time–distance helioseismology is a branch of local helioseismology. By measuring travel times of waves between pairs of points on the solar surface, we investigate the subsurface structures and/or dynamics, such as sound speed anomaly, flows, and magnetic fields.

An acoustic wave propagating into the Sun is refracted because the deeper it goes the larger the sound speed becomes. At some depth, it reflects and propagates back to the surface. Around the surface, it is reflected again, because of the steep decline in density and in sound speed around the photosphere.

If there is a local sound speed perturbation below the surface in the region of propagation, the travel time between two surface points is modified. Hence, we find the subsurface sound speed anomaly by the travel time anomaly on the surface. Moreover, if there is a

flow along the path, travel time against the flow is longer than that on the flow. The travel time difference between one direction and the opposite tells us the existence of a subsurface flow.

Under the ray theory, the region of propagation is along the ray path. Since the ray for the larger distance, Δ_1, reaches deeper than the ray for the smaller distance, Δ_2, the ray for Δ_1 is sensitive to anomalies in deeper layers, and, hence, the travel times for Δ_1 and Δ_2 reflect structures of different depths. Thus, by 'differentiate' the travel time we would be able to isolate anomalies in the layers between. In this way, we obtain properties of wave medium at various depths using travel times with various distances.

3.2 Time-Distance Diagram of the Sun

Since solar oscillations do not consist of a series of pulses, we cannot measure the travel time by recording the arrival times of the pulses. Instead, we measure travel times of acoustic waves between two given points on the solar surface by cross-correlating the oscillation signals on the two points. This was first introduced by Duvall et al. (1993), and after D'Silva (1996) further formulated the method under the ray approximation, Kosovichev & Duvall (1997) showed first inversion results of near-surface convective flows.

The cross correlation of wave field can be calculated as a Fourier transform of oscillation power. Here we show the derivation based on Sekii & Shibahashi (2003).

By using observed wavefield $u(\boldsymbol{x}, t)$, where $\boldsymbol{x} = (x, y)$ is position on the solar surface, and time t, we define the cross-correlation function for displacement vector $\boldsymbol{\Delta}$ and time lag τ as

$$C(\boldsymbol{x}, \boldsymbol{\Delta}, \tau) = \int_{-\infty}^{\infty} u^*(\boldsymbol{x}, t) u(\boldsymbol{x} + \boldsymbol{\Delta}, t + \tau) dt. \tag{3.1}$$

With $a(\boldsymbol{k}, \omega)$, Fourier transform of $u(\boldsymbol{x}, t)$, defined as

$$a(\boldsymbol{k}, \omega) = \int d\boldsymbol{k} \int d\omega u(\boldsymbol{x}, t) e^{i(\boldsymbol{k}\cdot\boldsymbol{x} - \omega t)}, \tag{3.2}$$

the correlation between the two points on $\boldsymbol{x}$ and $\boldsymbol{x} + \boldsymbol{\Delta}$ is written as

$$C(\boldsymbol{x}, \boldsymbol{\Delta}, \tau) = \int dt d\omega d\omega' a^*(\boldsymbol{k}, \omega) a(\boldsymbol{k'}, \omega') e^{i[(\boldsymbol{k'} - \boldsymbol{k})\cdot\boldsymbol{x} - (\omega - \omega')t + \boldsymbol{k'}\cdot\boldsymbol{\Delta} - \omega'\tau]}, \tag{3.3}$$

and since

$$\int_{-\infty}^{\infty} dt e^{-(\omega - \omega')t} = 2\pi\delta(\omega - \omega'), \tag{3.4}$$

where $\delta(\omega)$ is the delta function, the cross-correlation function is now

$$C(\boldsymbol{x}, \boldsymbol{\Delta}, \tau) = \int d\omega \int d\boldsymbol{k} \int d\boldsymbol{k'} a^*(\boldsymbol{k}, \omega) a(\boldsymbol{k'}, \omega) e^{i[(\boldsymbol{k'}-\boldsymbol{k})\cdot\boldsymbol{x}+\boldsymbol{k'}\cdot\boldsymbol{\Delta}-\omega'\tau]}. \tag{3.5}$$

Taking the spatial average, we obtain

$$\begin{aligned} C(\boldsymbol{\Delta}, \tau) &\equiv \int d\boldsymbol{x} C(\boldsymbol{x}, \boldsymbol{\Delta}, \tau) \\ &= (2\pi)^3 \int d\omega d\boldsymbol{k} |a(\boldsymbol{k}, \omega)|^2 e^{i(\boldsymbol{k}\cdot\boldsymbol{\Delta}-\omega\tau)}, \end{aligned} \tag{3.6}$$

where we used

$$\int_{-\infty}^{\infty} d\boldsymbol{x} e^{[-(\boldsymbol{k}-\boldsymbol{k'})\cdot\boldsymbol{x}]} = (2\pi)^2 \delta(\boldsymbol{k} - \boldsymbol{k'}). \tag{3.7}$$

Since $|a(k, \omega)|^2$ is the oscillation power distribution, the spatially-averaged cross-correlation function, $C(\boldsymbol{\Delta}, \tau)$, is described as the Fourier transform of oscillation power. One example of cross-correlation function is shown in Figure 3.1. The relationship between the travel time and travel distance of acoustic wave is indicated by the ridge along which the absolute value of correlation is large in the cross-correlation function. Because of this property, such figures are called time–distance diagrams.

3.3 Ray Theory

In the ray theory, or geometrical optics, we assume that a wave is locally approximated by a plane wave. This is a good approximation in the limit of short wavelength. In this approximation, we consider ray perpendicular to the wave front as a path characterizing propagation of the wave. Note that although in some studies using time–distance technique they apply Born approximation (e.g., Birch et al. 2004), we only consider the ray approximation in this thesis work.

Calculation of the ray path in this approximation is shown in Appendix A in details. Figure 3.2 shows some examples of the acoustic ray path in the Sun. The ray path, or the depth of the propagation region, depends on the ratio l/ν, where l is horizontal wavenumber (or spherical harmonic degree) and ν is frequency (see Equation (A.25)). This one can see in Figure 3.2, where the ray path for $(l, \nu) = (100, 5\text{mHz})$ is similar to that for $(l, \nu) = (80, 4\text{mHz})$. A wave which is in phase when it superposes to itself corresponds to an eigenmode of the Sun.

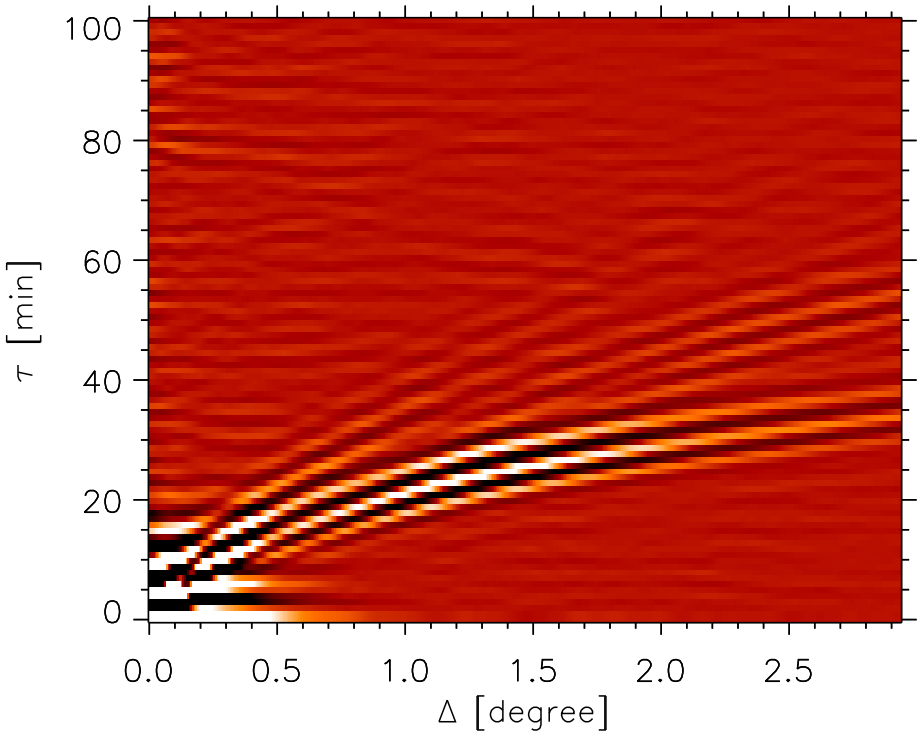

Figure 3.1 A spatially averaged Time-distance diagram computed from a 758-min observation by *Hinode*/SOT on November 23, 2007 in Ca II line. The dataset used is same as that in Figures 1.1 and 1.2. The lowest ridge indicates the time–distance curve for the ray without bounce at the surface, while the upper ridge indicates that for the waves which reflected once at the surface on the way.

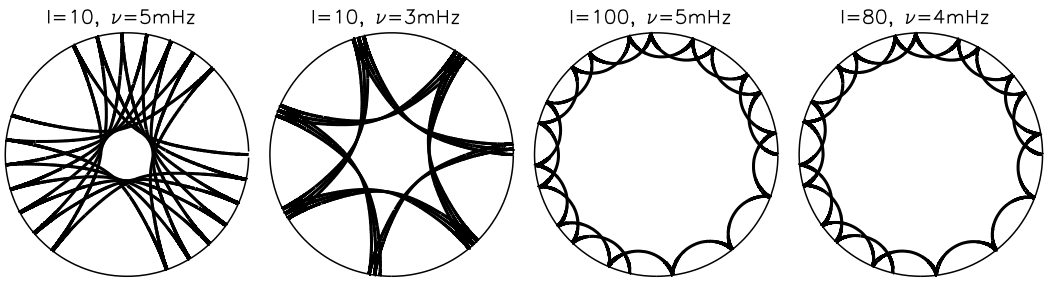

Figure 3.2 Examples of acoustic ray path in the Sun.

Under the ray approximation, the travel times are affected only by the perturbations along the ray path. The followings are based on the descriptions in Kosovichev & Duvall (1997). The ray path is given by

$$\frac{d\boldsymbol{r}}{dt} = \frac{\partial\omega}{\partial\boldsymbol{k}}, \tag{3.8}$$

where $\boldsymbol{r}$ is a position vector and $\boldsymbol{k}$ is a wavenumber vector. The travel time, τ, for the acoustic wave packet with the central frequency of ω along the ray path Γ is described as

$$\tau = \frac{1}{\omega}\int_{\Gamma} \boldsymbol{k}\cdot d\boldsymbol{r}. \tag{3.9}$$

The perturbation of the travel time, therefore, is

$$\delta\tau = \frac{1}{\omega}\int_{\Gamma} \delta\boldsymbol{k}\cdot d\boldsymbol{r}, \tag{3.10}$$

where Γ is the unperturbed ray path, and $\delta\boldsymbol{k}$ is the perturbation of the wave vector. The wave vector is perturbed by the structure anomaly and/or flows along the ray path. Since the unperturbed ray path is determined so as to make the travel time its extremum (Fermat's principle), we can neglect the perturbation of the path, when we consider only the first-order terms of perturbation.

The dispersion relation for acoustic waves in the stratified media is given by

$$(\omega - \boldsymbol{k}\cdot\boldsymbol{v})^2 = {\omega_{\rm ac}}^2 + \boldsymbol{k}^2 {c_f}^2, \tag{3.11}$$

where $\omega_{\rm ac}$ is the acoustic cutoff frequency (see §3.5.1), and c_f is the (fast) magneto-acoustic speed:

$$c_f = \frac{1}{2}\left(c^2 + {c_A}^2 + \sqrt{(c^2 + {c_A}^2 - 4c^2\frac{(\boldsymbol{k}\cdot\boldsymbol{c_A})^2}{k^2}}\right) \tag{3.12}$$

($\boldsymbol{c_A} = \boldsymbol{B}/\sqrt{4\pi\rho}$ is Alfvén velocity, $\boldsymbol{B}$ is magnetic field strength, and c is sound speed). Let us consider the flow, $\boldsymbol{v}$, and the magnetic field strength, $\boldsymbol{B}$, as the first-order perturbation (i.e., $\boldsymbol{v} = 0$ and $\boldsymbol{B} = 0$ in the unperturbed state). Then, the first-order travel-time perturbation is written as

$$\delta\tau = -\int_{\Gamma}\left\{\frac{\boldsymbol{n}\cdot\boldsymbol{v}}{c^2} + \frac{\delta c}{c}\frac{k}{\omega} + (\frac{\delta\omega_{\rm ac}}{\omega_{\rm ac}})\frac{{\omega_{\rm ac}}^2}{\omega c^2 k} + \frac{1}{2}\frac{k}{\omega}\left(\frac{{c_A}^2}{c^2} - \frac{(\boldsymbol{k}\cdot\boldsymbol{c_A})^2}{k^2c^2}\right)\right\} ds, \tag{3.13}$$

where $\boldsymbol{n}$ is a unit tangent vector to the ray and ds is the small element of Γ.

Taking the difference and the mean of the reciprocal travel times, we disentangle the effects of flow perturbations and structural perturbations:

$$\delta\tau_{\rm diff} = -2\int_\Gamma \frac{\boldsymbol{n}\cdot\boldsymbol{v}}{c^2}ds \tag{3.14}$$

$$\delta\tau_{\rm mean} = -\int_\Gamma \left\{ \frac{\delta c}{c}\frac{k}{\omega} + (\frac{\delta\omega_{\rm ac}}{\omega_{\rm ac}})\frac{{\omega_{\rm ac}}^2}{\omega c^2 k} + \frac{1}{2}\frac{k}{\omega}\left(\frac{{c_A}^2}{c^2} - \frac{(\boldsymbol{k}\cdot\boldsymbol{c_A})^2}{k^2c^2}\right)\right\} ds. \tag{3.15}$$

In addition, in the expression for $\delta\tau$, the magnetic field strength $\boldsymbol{B}$ is included in the term

$$\frac{{c_A}^2}{c^2} - \frac{(\boldsymbol{k}\cdot\boldsymbol{c_A})^2}{k^2c^2}.$$

Hence, the travel time depends on the propagation direction $\boldsymbol{k}$. The anisotropy of travel time perturbation would indicate the magnetic field direction.

3.4 Time–Distance Analysis Procedure

3.4.1 Filtering

In practice, we often filter out certain components in the wavefields, as is explained in the below.

Surface oscillation signal includes not only acoustic modes (p-mode) but also surface gravity modes (f-mode). Since they have different origins, and therefore different time–distance characteristics, we need to choose one of them in our time–distance helioseismological analysis. In this thesis, we use the p-modes, so we remove the f-modes in $k-\omega$ space, i.e., filter out the f-mode ridge in the $l-\nu$ diagram.

We need phase-speed filters to enhance signal-to-noise ratio of cross-correlation function as well (see also §5.4.1). If an incident angle and a frequency of a p-mode wave are given, horizontal phase speed is determined uniquely, and the travel time and the skip angle of the wave are also determined, as long as the solar structural model is known (see Appendix A). Therefore, we first determine the skip angle, or the distance between the two points where we cross-correlate the oscillation signals, and choose the appropriate phase-speed filter for the skip angle. The appropriate phase speed for the ray of each skip angle is presented in Figure A.3 in Appendix A.2; for example, for the skip distance 14.86 Mm which corresponds to the skip angle 1.22 degree, we chose the filter centred at 22 km $\rm s^{-1}$. Since the phase speed is calculated as ω/k_h, in the $l-\nu$ diagram, a straight line with a slope of ω/k_h indicates the constant phase-speed. An implicit assumption is that the subsurface anomalies we are

looking for is not large enough to shift the main components of waves beyond the region in $k - \omega$ space that is selected by the filter.

To select main p-mode components, we also use a Gaussian frequency filter centred around 3.3mHz.

Additional filtering for NFI datasets When we use SOT NFI datasets, such as Dopplergrams in Fe I 557.6 nm line, we apply low-wavenumber filter to remove known artifact (Tsuneta et al. 2008); since main components of the artifact lie in the low-wavenumber domain in the $l - \nu$ plane, we use cosine-bell shaped filter in wavenumber to drop them. This artifact is caused by air bubbles inside the tunable filter of NFI. Thanks to the effort of the SOT team, the bubble is kept under control to some extent. However, the images obtained by NFI are somewhat distorted by the bubbles, and as the satellite moves around on the orbit, the pattern due to bubble undergoes a periodic variations. Therefore, the period of the main component is the orbital period, but the variation is not limited to this component. We do not have complete calibration tool for the NFI datasets, but as was mentioned above, we attempt to improve the data quality by trial and error.

3.4.2 Calculation of cross-correlation function

Due to the stochastic nature of the solar oscillation, cross-correlation function is generally too noisy when we cross-correlate oscillation signal at a single pixel with signal at another pixel (See Chapter 5). Therefore, we usually take some spatial average.

Annular geometry is frequently used. First, a target point is chosen. Second, around that point, an annulus with a central radius of Δ is drawn. Third, we average the signal over the annulus. Finally, we cross-correlate the signal at the target point with the signal average over the annulus. Travel times calculated from the cross-correlation function indicates the outward travel time from the target point to points on the annulus and the inward travel time from the points on the annulus to the target point. The difference between the outward and inward travel times represents the divergence or convergence of the flow around the target point. Sometimes, we divide the annulus into 4 segments, i.e., north, west, south, and east parts, and use these segments instead of the whole annulus. In this case, we obtain travel times for each direction of propagation.

3.4.3 Travel-time measurements by fitting Gabor wavelet

Kosovichev & Duvall (1997) fitted the cross-correlation function by a Gabor-type wavelet, $G(\Delta, \tau)$. The fitting function for spatial displacement Δ and time lag τ has the form

$$G(\Delta, \tau) = A \cos(\omega_0(\tau - \tau_{\rm p})) \exp\left[- \left(\frac{\delta\omega}{2}(\tau - \tau_{\rm g}) \right)^2 \right], \tag{3.16}$$

where A is the amplitude, ω_0 is the central frequency, $\delta\omega$ is the frequency bandwidth, and $\tau_{\rm g}$ and $\tau_{\rm p}$ are the group and phase travel times. This is a general form of a wavepacket with the phase speed $v_{\rm p}$ and the group velocity $v_{\rm g}$, where $\tau_{\rm g} = \Delta/v_{\rm g}$ and $\tau_{\rm p} = \Delta/v_{\rm p}$.

The five parameters are determined by applying a nonlinear least-squares fitting method. Since the phase travel times are determined with higher precision than the group travel times, usually phase travel times are used. Kosovichev & Duvall (1997) formulated that the difference and mean of reciprocal travel times is affected by flows and sound speed structure, respectively (see §3.3).

3.4.4 Travel-time definition by Gizon & Birch (2004)

Gizon & Birch (2004) introduced a new definition of the travel time. Instead of fitting the Gabor-type wavelet, they use a linearized relationship between the travel times and the cross-correlation functions. They set a reference cross-correlation function $C^{\rm ref}$ and the corresponding travel time $\tau^{\rm ref}$. The travel time which corresponds to cross-correlation function, C, which is different from the reference, $C^{\rm ref}$, will shift from $\tau^{\rm ref}$, and if the difference between two cross-correlation functions is small enough, the travel time shift is proportional to the difference. In the case of finite difference case, they still use the same relationship. Therefore, their definition of the travel time is of the form

$$\tau - \tau^{\rm ref} = \sum_t W(t)[C(t) - C^{\rm ref}(t)], \tag{3.17}$$

where $W(t)$ is a weight function (symbolically $\Delta\tau/\Delta C$, a kind of Fréchet derivative). As a result, they obtained the travel time as a linear combination of cross-correlation functions. This linearity has several advantages compared to the wavelet fitting. However, in the active region, for example, the amplitude of cross-correlation functions differs depending on the propagation directions. This affects calculation of the travel time. For example, in deriving the expression for $W(t)$, it is assumed that $C(t)$ and $C^{\rm ref}(t)$ differ only in travel time τ.

But currently in such a case, they use only *ad hoc* phenomenological adjustment, i.e., they just normalized the amplitude by making the maximum unity. How one should treat an amplitude change has not been fully considered yet.

3.4.5 Inversion

Using the ray approximation, we obtain the subsurface flow field $\boldsymbol{v}$ and the subsurface sound speed perturbation δc by inversion of travel times. First, we measure the travel times for several distances and for north-south, east-west, and inward-outward directions (see §3.4.2). Next, we calculate the inversion kernels for each component of flow (v_x, v_y, v_z) and sound speed δc using Standard solar model (model S; Christensen-Dalsgaard et al. 1996).

$$\frac{\delta\tau_{\mathrm{mean},i}}{\tau_{\mathrm{mean},i}} = \int_\Gamma ds K^{c^2,i} \frac{\delta c^2}{c^2} \tag{3.18}$$

$$\frac{\delta\tau_{\mathrm{diff},\alpha,i}}{\tau_{\mathrm{diff},\alpha,i}} = \int_\Gamma ds K^{v_\alpha,i} \frac{v_\alpha}{c} \tag{3.19}$$

where K^{c^2} is the inversion kernel for the sound speed, K^{v_α} is the inversion kernel for the flow, i indicates the position where the travel time is measured and the distance between the two points, and α means the direction (x, y, z). We write a series of integral equations with different i.

In practice, we rewrite the integral equations in the discretized form. For the structural inversion equations, for example,

$$\frac{\delta\tau_{\mathrm{mean},i}}{\tau_{\mathrm{mean},i}} = \sum_{jkl} K^{c^2,i}_{jkl} \frac{\delta c^2_{jkl}}{c^2_{jkl}}, \tag{3.20}$$

where (j, k, l) indicates the locations in three-dimensional space. In matrix form, this is

$$\begin{pmatrix} \delta\tau_{\mathrm{mean},i_1}/\tau_{\mathrm{mean},i_1} \\ \delta\tau_{\mathrm{mean},i_2}/\tau_{\mathrm{mean},i_2} \\ \vdots \end{pmatrix} = \begin{pmatrix} K^{c^2,i_1}_{j_1k_1l_1} & K^{c^2,i_1}_{j_2k_2l_2} & \cdots \\ K^{c^2,i_2}_{j_1k_1l_1} & K^{c^2,i_2}_{j_2k_2l_2} & \cdots \\ \vdots & \vdots & \ddots \end{pmatrix} \begin{pmatrix} \delta c^2_{j_1k_1l_1}/c^2_{j_1k_1l_1} \\ \delta c^2_{j_2k_2l_2}/c^2_{j_2k_2l_2} \\ \vdots \end{pmatrix}. \tag{3.21}$$

What we would like to do is to solve the equations for $\delta c^2/c^2$ using the observed travel times $\delta\tau/\tau$ and the kernels K^{c^2} calculated from the solar model. A simple matrix inversion would not work because often the kernel matrix is highly ill-conditioned. The details will be discussed in Chapter 6.

3.5 Acoustic Wave Behaviour above the Photosphere

In time–distance analysis, we use the acoustic travel times between pairs of points on the solar surface. However, the waves with a period of 5 minutes normally are not considered to propagate as a wave above the photosphere. In this section, motivated by observation discussed in Chapter 4 we consider the real picture of the behaviour of acoustic waves in evanescent regions and discuss how we should treat them in the time–distance analyses.

3.5.1 Acoustic Cutoff Frequency

Let us consider acoustic wave propagation in isothermal stratified medium under constant gravity with constant sound speed, c. In this medium, basic equations in hydrodynamics are given as

$$\frac{\partial \rho}{\partial t} + \nabla \cdot (\rho \boldsymbol{v}) = 0 \tag{3.22}$$

$$\text{and} \qquad \rho \frac{\partial \boldsymbol{v}}{\partial t} = -\nabla p - \rho g \boldsymbol{e_z}, \tag{3.23}$$

where ρ is density, p is pressure, g is gravity acceleration, and $\boldsymbol{v}$ is oscillation velocity. Here we assume that all the variables depend only on the height, z. Let us consider in terms of the equilibrium quantities ρ_0 and p_0, and the perturbed quantities ρ_1 and p_1. Displacement caused by oscillation is denoted by $\boldsymbol{\xi}$, where $\boldsymbol{v} = \partial \boldsymbol{\xi}/\partial t$. The zeroth order equations are

$$\frac{\partial \rho_0}{\partial t} = 0 \quad \text{and} \quad \frac{\partial p_0}{\partial t} + \rho_0 g = 0, \tag{3.24}$$

and the first order equations are

$$\rho_1 + \frac{\partial}{\partial z}(\rho_0 \xi) = 0 \quad \text{and} \quad \rho_0 \frac{\partial^2 \xi}{\partial t^2} = -\frac{\partial p_1}{\partial z} - \rho_1 g. \tag{3.25}$$

Sound speed, c, is defined as

$$c^2 = \left(\frac{\partial p}{\partial \rho} \right)_{\text{ad}}, \tag{3.26}$$

where the differentiation is taken under adiabatic process (normally under constant entropy). The perturbations p_1 and ρ_1 are Eulerian perturbations. Lagrangian perturbations, δp and $\delta \rho$, defined as

$$\delta p = p_1 + \boldsymbol{\xi} \cdot \nabla p_0 \quad \text{and} \quad \delta \rho = \rho_1 + \boldsymbol{\xi} \cdot \nabla \rho_0, \tag{3.27}$$

are related to the sound speed by $c^2 = \delta p/\delta\rho$, assuming that the oscillation is adiabatic. Eliminating ρ_1 and p_1 from the equations above, we obtain a wave equation for acoustic wave as

$$\frac{\partial^2\xi(z,t)}{\partial t^2} - \frac{1}{\rho_0(z)}\frac{\partial}{\partial z}\left(\rho(z)c^2(z)\frac{\partial\xi(z,t)}{\partial z}\right) = 0. \tag{3.28}$$

Assuming $\xi \propto \exp(z/2H)\exp i(kz - \omega t)$, we obtain a dispersion relation of acoustic wave in the stratified media as

$$k = \frac{\sqrt{\omega^2 - {\omega_{\rm ac}}^2}}{c}\ , \tag{3.29}$$

where H is density scale height, $H = -dz/d\log\rho$, and $\omega_{\rm ac}$ is acoustic cutoff frequency, $\omega_{\rm ac} = c/(2H)$. Since here we consider the upward propagation, we have taken the positive sign before the square root in Equation (3.29).

If $\omega > \omega_{\rm ac}$, the perturbation propagates upward as a wave. Since around the solar photosphere the cutoff frequency $\omega_{\rm ac}/(2\pi)$ is about 5.4mHz, the five-minute oscillation on the Sun, or 3-mHz oscillation, is evanescent around the photosphere and does not propagate as a wave. Indeed, in the ray approximation, we normally consider that the waves reflect at the boundary between propagation and evanescent regions.

In fact, the formation heights of spectral lines used in helioseismology observations by *SOHO*/MDI or GONG are located in the evanescent regions of the 5-minute oscillation. Therefore, we have to take it into consideration not only when we use chromospheric lines but also when we use photospheric lines.

3.5.2 Travel-time Measurements in the Evanescent Region of the Waves

In the propagation region, displacement due to oscillations, $\xi(z,t)$, is written in the form

$$\xi(z,t) \propto \exp i(kz - \omega t), \tag{3.30}$$

whereas the displacement in the evanescent region is

$$\xi(z,t) \propto \exp(\kappa z - i\omega t), \tag{3.31}$$

where k and κ are real numbers. Hence, in the evanescent region, fluid oscillates with an angular frequency, ω, all in phase irrespective of height.

In global helioseismological techniques, we measure the eigenfrequencies using the oscillation signals in evanescent regions. Measuring eigenfrequencies is not affected whether the oscillation is in evanescent regions or not because of the behaviour mentioned above. In time-distance helioseismology analysis, however, we measure travel times. If the waves are in the evanescent region, we cannot measure the travel times between the two points on the layer we observe along the ray path shown in the right panel of Figure 3.3.

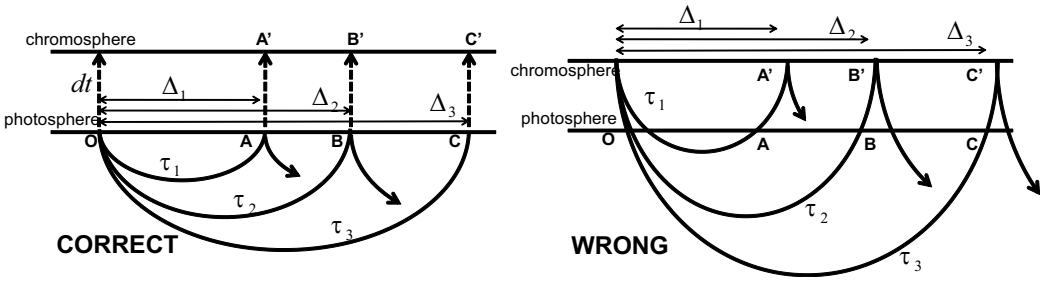

Figure 3.3 Ray path around and above the photosphere. The left panel shows the correct picture, while the right panel shows the wrong picture.

In the treatment shown in §3.5.1 we assume the displacement as the form of $\xi = \exp i(kz - \omega t)$, i.e., we assume stationary waves. However, it is not always appropriate in local helioseismology, because oscillations are excited randomly in space and time and we need to consider transient oscillation source instead, particularly when the time series and/or the mode life time is short.

In this case, we add a source term $f(z,t)$ in the wave equation

$$\frac{\partial^2 \xi(z,t)}{\partial t^2} - \frac{1}{\rho_0(z)} \frac{\partial}{\partial z} \left(\rho(z) c^2(z) \frac{\partial \xi(z,t)}{\partial z} \right) = f(z,t) \ . \tag{3.32}$$

We solve this wave equation under the conditions:

1. in the isothermal atmosphere (constant sound speed, $c(z) = c$)
2. assuming stratification of the density is in the form of $\rho(z) = \rho_0 \exp(-z/H)$, where H is a constant scale height.
3. assuming the source of the oscillations is in the form of $f(z,t) = f(t)\delta(z)$, where $\delta(z)$ is the delta function.

With some algebra (see Appendix C for details), we obtain the solution as

$$\xi(z,t) = e^{z/(2H)} \int_{-\infty}^{+\infty} G(z, t-t') f(t') dt' \tag{3.33}$$

where $G(z, t-t')$ is a Green's function:

$$\begin{aligned} G(z,t-t') &= \frac{1}{4c}J_0(\frac{\omega_{\rm ac}}{c}\sqrt{c^2(t-t')^2-z^2})H(\frac{\omega_{\rm ac}}{c}(c(t-t')-z)) \\ &= \frac{1}{4c}J_0(\sqrt{(\tau-\tau')^2-\zeta^2})H((\tau-\tau')-\zeta)\ , \end{aligned} \tag{3.34}$$

$\tau = t\omega_{\rm ac}$ and $\zeta = z/(2H)$.

Since the argument of the zeroth Bessel function, J_0, should be larger than zero, $c^2(t-t')^2 - z^2 \geq 0$. This means the wavefront, where $c(t-t') = z$, propagates with the speed of c. In the limit of $t >> t'$, the argument of the zeroth Bessel function J_0 is sufficiently large, and by the asymptotic formula

$$J_0(x) \sim \sqrt{\frac{2}{\pi x}}\cos(x-\frac{\pi}{4}) \quad (x \to \infty)\ , \tag{3.35}$$

the Green's function is approximated by

$$G(z,t-t') \propto \frac{1}{\sqrt{(c(t-t'))^2-z^2}}\cos(\omega_{\rm ac}\sqrt{(t-t')^2-(z/c)^2}-\frac{\pi}{4})\ . \tag{3.36}$$

Therefore, for large t, the oscillation with a frequency of $\omega_{\rm ac}$ is dominant.

Figure 3.4 shows the Green's function for the case of $t' = 0$; this infers the oscillation which is caused by a pulse source located at $z = 0$ at the moment of $t = 0$. In the figure 1) the wavefront propagates upward with the sound speed, and 2) after a sufficiently long time, the atmosphere oscillates with the acoustic cutoff frequency.

Using the Green's function, we calculate the oscillation behavior with several sources. We assume the source function as

$$f(z,t) = \begin{cases} 0 & (t<0) \\ e^{i\alpha t}\delta(z) & (t>0) \end{cases}, \tag{3.37}$$

i.e., the oscillation at $z = 0$ starts at $t = 0$ with a frequency of α. In this case, the displacement, ξ, is

$$\begin{aligned} \xi(z,t) &\propto e^{z/2H}\int_{-\infty}^{+\infty}dz'\int_0^{+\infty}dt'e^{i\alpha t'}\delta(z')G(z-z',t-t') \\ &= e^{z/2H}\int_0^{t-z/c}e^{i\alpha t'}J_0\left(\frac{\sqrt{c^2(t-t')^2-z^2}}{2H}\right). \end{aligned} \tag{3.38}$$

Figure 3.5 shows the results. Note that in this figure we omit the factor $e^{z/2H}$ because it grows too rapidly. We consider the cases that the frequency, α, is 0.1, 0.5, 1 and 2 times

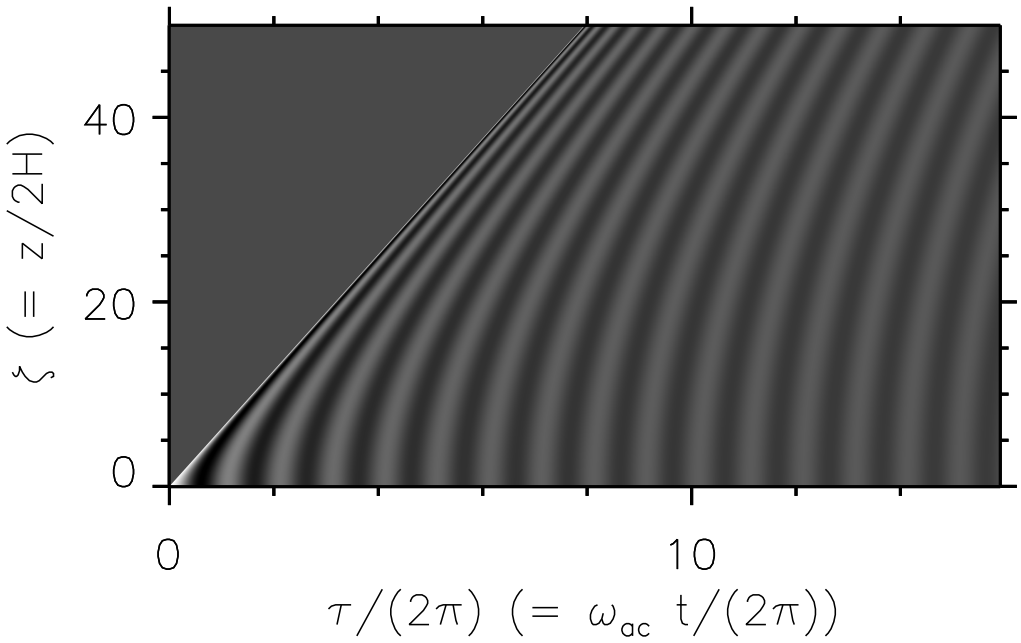

Figure 3.4 Green's function (Equation 3.34) in the case of $t' = 0$. The oscillation with a period of $\tau/(2\pi) = 1$ corresponds to the oscillation with $\omega_{\rm ac}$.

acoustic-cutoff frequency, $\omega_{\rm ac}$. In all panels the wave front propagates with the sound speed after the oscillation starts at $t = 0$. If $\alpha \geq \omega_{\rm ac}$, the oscillation propagates with the same speed. In the case of $\alpha < \omega_{\rm ac}$, however, only the region very close to the source at $z = 0$ shows the oscillation with the frequency of the source, α. In the upper layer, the oscillation frequency is equal to $\omega_{\rm ac}$ and a long time after the oscillation starts the coherent oscillation occurs throughout the upper layers. This implies oscillation is evanescent.

In reality, oscillation is excited stochastically all the time. The frequency of the component is also randomly distributed. Moreover, there is damping which we have ignored in the modelling above. If the lifetime of the oscillation is sufficiently long, the whole picture is not significantly different from the oscillation in a steady state, even if the oscillation is excited stochastically. The lifetime of the oscillation is indicated by reciprocal of the width of the peaks in power spectrum.

In the following, we report the normal discussion for this; a model equation for a one-dimensional damped oscillator with an external force would be

$$\ddot{x} - 2\gamma\dot{x} + \alpha^2 x = f(t), \tag{3.39}$$

where x is a displacement of the oscillator and a function of t, and the dots over x indicate

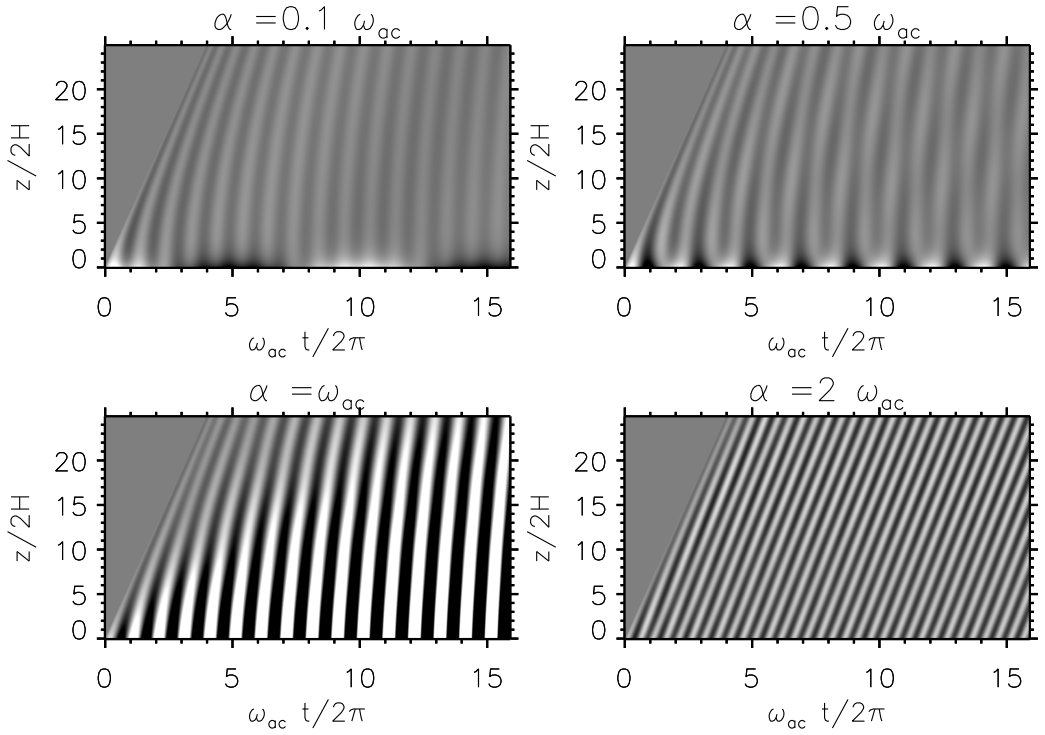

Figure 3.5 Examples of oscillation field made by several sources.

taking time derivative of x. γ is a damping factor. The power of the oscillation for a certain ω is described with Fourier transform of x, $\tilde{x}$:

$$P(\omega) = |\tilde{x}|^2 = \frac{|\tilde{f}|^2}{(\omega^2 - \alpha^2)^2 + (2\gamma\omega)^2}. \tag{3.40}$$

Since the contribution is significantly large for the ω close to α only, this is approximated by

$$P(\omega) \sim \frac{1}{4\omega^2} \frac{|\tilde{f}|^2}{(\omega - \alpha)^2 + \gamma^2}, \tag{3.41}$$

and this indicates that the full width at the half maximum is 2γ, and the lifetime is the reciprocal of this one.

In our analysis, we have applied several filters, such as phase-speed filters and f-mode removal filters, to the power spectrum. Since the width of the main components in the filtered power spectrum is about 1 mHz (see Figure 5.13, for example), the lifetime is about 20 minutes, which is only a few times of the main period of the oscillation. In the non-filtered wavefield, the lifetime is shorter owing to the broader distribution. Therefore, the transient stochastic excitation picture holds.

In summary, in the case of an isothermal atmosphere with a constant sound speed, if a layer begins to oscillate at an epoch, then the wave front travels upwards (and, in fact, downwards) at the sound speed. If the frequency of the oscillation is above the acoustic cut-off frequency, this propagation takes place smoothly, as a wave propagation. If, on the other hand, the frequency is below (but somewhat comparable to) the cut-off frequency, as the perturbation travels upwards the component that oscillates in the acoustic cut-off frequency begins to dominate the wavefield. However, it is not until after travelling for a few wavelengths (i.e. a few scale heights, for these two length scales are comparable) that this component dominates the wavefield; closer to the original layer oscillations around the sub-critical frequency are still strong.

The wavelength of 3-mHz waves at the photosphere is around 2000 km. Therefore, we expect that an incident wavepacket of the central frequency of 3 mHz will send up perturbation towards the formation layers of photospheric spectral lines, such as those used in *SOHO*/MDI and GONG observations, or even lower-chromospheric lines, such as Ca II H lines, still retaining the wave-like feature around the original frequency.

Therefore, even in the evanescent region, if the height from the evanescent/propagation boundary is small enough compared to the wavelength, we may consider that the perturbation does propagate upward with sound speed above the boundary. It does not point to the picture shown in the right panel of Figure 3.3, but to that shown in the left panel of Figure 3.3. The wave reflects at the boundary, not at the layer observed. The oscillation signal propagates only upward from the boundary, and the fluid in the upper layer oscillates with some delay time after the fluid oscillates at the photosphere. The observational confirmation is discussed in §4.4.

3.6 Perturbation in Strong Magnetic Field Regions

In time–distance analysis, we assume that the difference of sound speed from the model, or the absolute value of the flows or magnetic field strength can be treated as perturbation. However, in the regions with strong magnetic flux density, such as active regions or sunspots, it is doubtful that the magnetic strength is within the perturbation regime.

For example, using the typical magnetic field strength in sunspots, $B = 1$ kG, and the density around the photosphere, $\rho = 10^{-4}$ kg m^{-3}, the Alfvén velocity, $c_A = B/\sqrt{(4\pi\rho)}$, is estimated at 10^2 km s^{-1}, while the typical sound speed, c, around the photosphere is

10 km s^{-1}. Therefore, $c \ll c_A$, that is to say, the magnetic field strength is not appropriate to be treated as a small perturbation.

In fact, as Gizon et al. (2009) reported that inversion results of a sunspot obtained by various local helioseismological techniques are not consistent with each other and did not produce a unified picture of the subsurface structure of a sunspot. Since they depict much more consistent picture in the quiet sun using various methods of local helioseismological techniques, the discrepancy may be, at least partly, due to the inapplicable perturbation theory. In a different method, they used a different approximation, but all of them applied the perturbation theory. Currently, it is not clear which method is better, or if any of them can produce satisfactory results.

Suppression of oscillation power in sunspots, such as the one we showed in photospheric intensity power maps in Chapter 2, has known for a long time (e.g., Braun et al. 1987; Hindman & Brown 1998). One suggestion is that the suppression is due to wave absorption by sunspot magnetic fields. Another possibility is that it is due to strong magnetic fields inhibiting convection and hence the acoustic emission. The numerical simulation of this kind of power suppression has also been attempted (e.g., Parchevsky & Kosovichev 2007). Either way, how these power modification in and around the sunspot affects the travel-time analysis is not clear, and is still being debated (Rajaguru et al. 2006; Nigam & Kosovichev 2010). Actually, this was one of reasons for us to promote the study of the sunspot oscillations reported in the previous chapter.

In future we need to consider the behaviour of acoustic waves in magnetized regions in more details, if only to refine the way we practice local helioseismology in active regions.

Chapter 4

Helioseismic Signature of Chromospheric Downflows in Acoustic Travel-Time Measurements from *Hinode* [1]

In this chapter, we report on a signature of chromospheric downflows in two emerging-flux regions detected by time–distance helioseismology analysis. We use both chromospheric intensity oscillation data in the Ca II H line and photospheric Dopplergrams in the Fe I 557.6nm line obtained by *Hinode*/SOT for our analyses. By cross-correlating the Ca II oscillation signals, we have detected a travel-time anomaly in the plage regions; outward travel times are shorter than inward travel times by $0.5 - 1$ minute. However, such an anomaly is absent in the Fe I data. These results can be interpreted as evidence of downflows in the lower chromosphere. The downflow speed is estimated to be below 10 km s^{-1}. This result demonstrates a new possibility of studying chromospheric flows by time–distance analysis.

4.1 Introduction

As an application of travel-time measurement, we examine whether we can detect flows in emerging magnetic flux regions.

Magnetic flux tubes are generated in the convection zone. They emerge into the photosphere due to magnetic buoyancy, forming sunspots and/or restructuring the coronal

[1] Most part of this chapter was published in the Astrophysical Journal Letters (Nagashima et al. 2009).

magnetic configuration, eventually leading to activity phenomena, such as flares. Emerging flux regions are the place where such flux tubes are first observed directly; their configurations and dynamics are manifestations of interaction between plasma and magnetic flux in the subphotosphere. Thus, studying various aspects of flux emergence is vitally important in understanding solar and stellar dynamo mechanisms.

Numerous studies about emerging flux regions have been done both observationally and theoretically, and revealed complicated structures and flow patterns (e.g., Strous et al. 1996; Kosovichev et al. 2000; Kozu et al. 2006; Pevtsov & Lamb 2006; Magara 2008; Cheung et al. 2008). It is generally thought that along the flux tube are plasma downflows. The evacuated plasma decelerates as it descends due to the increasing density; in fact, the observed speed is $30 - 50$ km s^{-1} in the chromosphere and $1 - 2$ km s^{-1} in the photosphere (e.g., Tajima & Shibata 2002 and references therein). To understand how emerging flux regions evolve and how they affect activity phenomena, it is essential to study them in a range of layers from the subphotosphere to the upper atmosphere.

In this chapter, we report on a signature of chromospheric flows detected by a time–distance helioseismology analysis. Examining two emerging flux regions observed by *Hinode*, we detect a signal in the travel-time differences, which may be caused by plasma downflows in the chromosphere. Another implication of the present work is that chromospheric dynamics must be taken into account when chromospheric lines are used in helioseismology analysis. We briefly introduce *Hinode* observations in §4.2, and describe the analysis methods and results in §4.3. Discussion of our interpretation and conclusion are given in §4.4.

4.2 Observations

The Solar Optical Telescope (SOT; Tsuneta et al. 2008) onboard the *Hinode* satellite (Kosugi et al. 2007) made two observing runs for helioseismology around the solar disc centre: on 2007 November 23 (11:17–23:55 UT) and on 2007 December 04 (0:14–23:58 UT). Hereafter, we refer to the first (12-hour) run as dataset 1, and the second (24-hour) run as dataset 2. In the field of view of dataset 1, an emerging flux region appeared before the observation started, showing a plage and small sunspots. This region was registered as NOAA Active Region 10975. It disappeared within two days after the *Hinode* observations. In the field of view of dataset 2, a decaying active region (NOAA Active Region 10976) was observed. Sample images of these regions are shown in Figure 4.1.

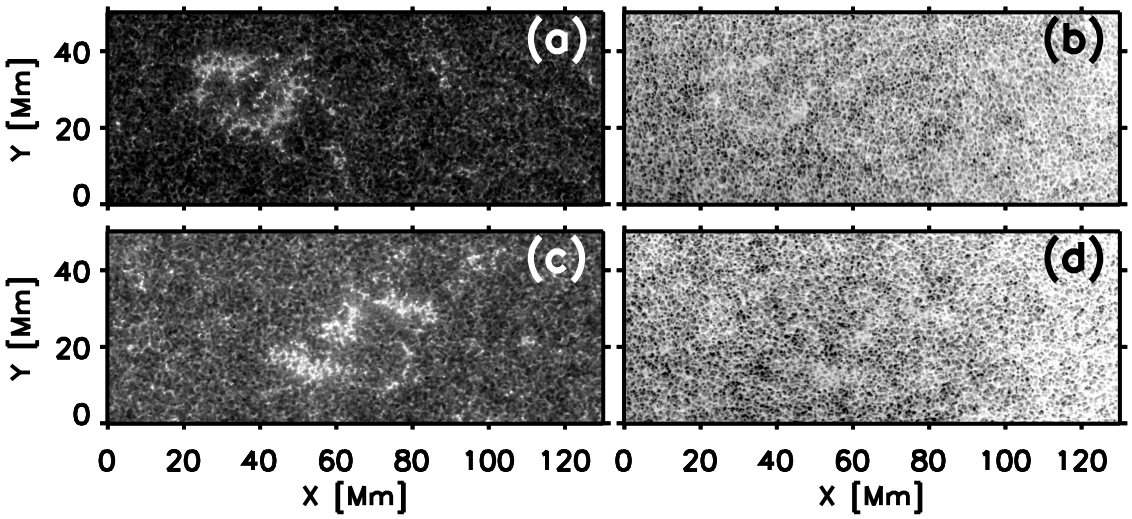

Figure 4.1 Sample images from two datasets. *Top row:* plage region observed on 2007 November 23 (dataset 1), Ca II H line intensity image (a) and Fe I 557.6 nm Dopplergram (b). *Bottom row:* decaying region observed on 2007 December 04 (dataset 2), Ca II H intensity image (c) and Fe I Dopplergram (d). In the Dopplergrams, white indicates a redshifted signal, while black indicates a blueshifted signal.

During these observations, both SOT instruments, the Narrowband Filter Imager (NFI) and the Broadband Filter Imager (BFI), were used: the BFI took Ca II H images, while the NFI took non-magnetic Fe I 557.6 nm filtergrams. The time cadence was 60 seconds. The Fe I Dopplergrams are calculated from the blue-wing and the red-wing intensities of the Fe I 557.6 nm line; that is, the (blue – red) signal is divided by the (blue + red) signal. During the each observing period *Hinode* tracked the regions using the correlation tracker (CT; Shimizu et al. 2008) to stabilize the images. The field of view is 218 × 109 arcsec for the Ca II H data and 328 × 164 arcsec for the Fe I data, while the pixel sizes are 0.108 arcsec (for Ca II H) and 0.16 arcsec (for Fe I). In this analysis, we use only the field of view of the Ca II H data. The Fe I data are interpolated to the Ca II H data grid. We also apply 2 × 2 pixel summing, increasing the pixel scale to about 0.2 arcsec. For the intensity datasets, we use running difference of images to remove possible spatial trends.

4.3 Time–Distance Analysis and Its Results

We analyze the 12-hour and 24-hour datasets (datasets 1 and 2) by a time–distance helioseismology technique (Duvall et al. 1993). First, we apply three filters in the frequency–wavenumber space: (1) an f-mode filter to remove the f-mode signal, since we use p-mode waves only, (2) low-wavenumber filters and a Gaussian frequency filter with a 1-mHz width peaking at 3.3 mHz to remove the known artifacts (see §3.4.1) and select the main p-mode signal, (3) a phase-speed filter with a width of 4.4 km s^{-1} centred at a speed of 22 km s^{-1} to select waves travelling to a distance of 14.86 Mm, which is chosen for this study.

Second, by cross-correlating the filtered signals, we measure the travel-time difference between the outward and inward wave components following the standard time–distance helioseismology procedure (Kosovichev & Duvall 1997). For this, we average the signals over an annulus of the radius of 14.86 Mm around a target point, and cross-correlate the signals at the target point and that of the annulus. We measure outward (from the target to annulus) and inward (from annulus to the target) travel times at each point in the field of view by fitting a Gabor-wavelet function to the cross-correlation function. The fitting function, $G(\Delta, \tau)$, for spatial displacement Δ, and time lag τ has the form

$$G(\Delta, \tau) = A \cos(\omega_0(\tau - \tau_{\rm p})) \exp\left[- \left(\frac{\delta\omega}{2}(\tau - \tau_{\rm g}) \right)^2 \right], \tag{4.1}$$

where A is the amplitude, ω_0 is the central frequency, $\delta\omega$ is the frequency bandwidth, and $\tau_{\rm g}$ and $\tau_{\rm p}$ are the group and the phase travel times. These five parameters are determined by applying a nonlinear least-squares fitting method (Levenberg–Marquardt method; see, e.g., Press et al. 1992). It should be mentioned that we used the phase travel time in the following discussions, because the phase travel time is determined with higher precision than the group travel time.

Errors of the fitted parameters are derived as follows: in the nonlinear least-squares fitting method, we determine the five fitting parameters, $\boldsymbol{a}$, by minimizing the merit function,

$$\chi^2 = \sum_i \left(\frac{C(\tau_i) - G(\tau_i; \boldsymbol{a})}{\sigma_i} \right)^2, \tag{4.2}$$

where C is the cross-correlation function to fit. Since we do not know the uncertainty of $C(\tau_i)$ at each data point, σ_i, we assume $\sigma_i = \sigma$ is a constant and after calculating

$\sum_i (C(\tau_i) - G(\tau_i; \boldsymbol{a}))^2$, we rescale σ in such a way that χ^2 is equal to the number of the data point. The covariance matrix,

$$\mathrm{Cov}[a_i, a_j] \equiv < a_i a_j > - < a_i >< a_j >, \tag{4.3}$$

where brackets indicate the expectation value, is then estimated and used to compute the error of the fitted parameters, $\sqrt{< a_i^2 > - < a_i >^2}$.

Figure 4.2 shows outward–inward travel-time difference maps. In these maps, misfitted points are assigned null travel-time differences; the number of misfittings is insignificant. In the quiet regions, both the Ca II H intensity data and Fe I Doppler data show the same pattern of flow divergence due to supergranulation. This is similar to the results from a previous *Hinode* observation reported by Sekii et al. (2007). In the plage region, we find a strong travel-time anomaly in the Ca II H data: the outward travel time is shorter than the inward travel time by about 0.5 – 1 minute on average. This anomaly, however, is not present in the Fe I 557.6 nm Doppler data. We also analyze the Fe I 557.6 nm intensity data from the same observing runs. These data are noisier, but they show the travel-time difference maps consistent with these obtained from the Fe I 557.6 nm Dopplergrams. Particularly, they do not show the travel-time anomaly, either.

The anomaly in the outward–inward travel-time difference in the chromospheric data is seen also in the averaged cross-correlation function. We average the cross-correlation functions in the quiet Sun (QS) region and in the plage for both datasets 1 and 2. We define the plage as a region where the Ca II H intensity is 25% larger than the average intensity of QS. By fitting the Gabor wavelet to the averaged cross-correlation functions, we obtain the travel times listed in Table 4.1. We find that in the plage the outward travel time is about 0.67 min (for dataset 1) or 0.42 min (for dataset 2) shorter than the inward travel time only in the chromospheric Ca II H data, while in the QS the difference between the outward and inward travel times is insignificant in both the chromospheric and the photospheric data.

We also have checked temporal variation of the travel-time anomaly for dataset 2. The 24-hr run is divided into three 8-hr runs, and the travel times are measured for each 8-hr run. As a result, we obtain the following sequences of the outward–inward travel-time difference in the chromospheric Ca II H data: $(-5.35 \pm 0.04) \times 10^{-1}$ min, $(-4.16 \pm 0.04) \times 10^{-1}$ min, and $(-4.21 \pm 0.06) \times 10^{-1}$ min in the plage region, and $(-1.11 \pm 0.03) \times 10^{-1}$ min, $(-0.14 \pm 0.07) \times 10^{-1}$ min, and $(+1.37 \pm 0.03) \times 10^{-1}$ min in the QS. In the plage, for all the

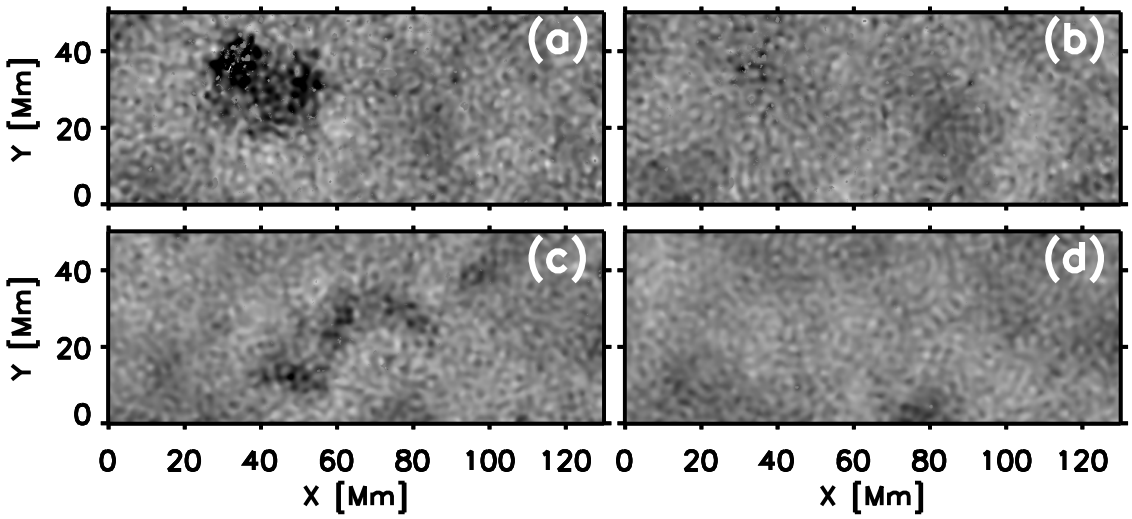

Figure 4.2 Outward–inward travel-time difference maps. *Top row:* dataset 1, (a) Ca II H line intensity and (b) Fe I 557.6 nm (Dopplergram). *Bottom row:* dataset 2, (c) Ca II H line intensity and (d) Fe I 557.6 nm (Dopplergram). The gray scale corresponds to the range from −1 minute to +1 minute. The field of view is the same as in Figure 4.1.

8-hr runs the anomaly similar to the one detected in the entire run is detected again, and particularly it is rather stronger in the first 8-hr run. This variation is consistent with a decaying behaviour of the plage region if we interpret that the travel-time anomaly results from a chromospheric downflow (see §4.4 for details), and that the downflow weakened during the observation. We also find, in the developing plage in dataset 1, the anomaly being stronger in the latter half of the observation. In the QS, the weak travel-time anomaly simply corresponds to the supergranular pattern. The observed variation with time implies that the lifetime of supergranules is slightly less than 1 day. This is consistent with previous studies (e.g., Stix 2002).

4.4 Discussions

In our analysis, we have used only acoustic (p-mode) waves with the central frequency of 3.3 mHz. Although stationary harmonic p-mode waves at this frequency are evanescent in the chromosphere, in reality such perturbations excited by impulsive subphotosphere sources do propagate upward (e.g., Lamb 1975; Goode et al. 1992). This certainly requires further

careful modelling, but here for the initial interpretation we assume that the waves travel roughly with the chromospheric sound speed, as discussed in §3.5. Thus, a chromospheric signal is observed after the corresponding photospheric signal is observed and the time delay is the acoustic travel time between the two layers, which is estimated by $L/c \sim 25$ second, where $L \sim 250\,\mathrm{km}$ is the Ca II H line formation height from the photosphere (Carlsson et al. 2007) and $c \sim 10\,\mathrm{km\,s^{-1}}$ is the sound speed in the chromosphere. Indeed, the phase shift between the photospheric G-band intensity signal and chromospheric Ca II intensity signal around 4 mHz on the p-mode ridge, reported by Mitra-Kraev et al. (2008), implies a $\sim$ 30-second propagation time between the photosphere and the chromosphere. Such a direct measurement in our case is not straightforward because our photospheric signal is Doppler velocity; understanding phase shifts between Doppler signal and intensity signal would be part of a future work. Please note, however, the travel-time analysis we use is not affected by such a difficulty as we cross-correlate the same observables.

Figure 4.3 shows how the disturbance caused by a source at point C propagates. If the wave arrival times at points A and C in the photosphere are t_A and t_C, the travel time from C to A is simply $t_{\mathrm{C\,to\,A}} = t_\mathrm{A} - t_\mathrm{C}$. The 'travel time' from C′ to A′, defined through the cross-covariance fitting procedure, $t_{\mathrm{C'\,to\,A'}}$, is identical to $t_{\mathrm{C\,to\,A}}$ if the time delays at A, dt_A, and at C, dt_C, are the same. Our travel-time measurements in the QS are consistent with this picture; the photospheric and the chromospheric travel times are essentially the same (see Table 4.1).

If there is a downflow above C, however, and there is no downflow above A, then the time delays at two points are different: $dt_\mathrm{C} > dt_\mathrm{A}$. By setting point C as the centre of an annulus, or as the target point, and point A as a point on the annulus around the target point, we can describe the outward travel time at the photospheric level, $t_\mathrm{out,ph}$, and the travel time at the chromospheric level, $t_\mathrm{out,ch}$, as

$$t_\mathrm{out,ph} = t_{\mathrm{C\,to\,A}} = t_\mathrm{A} - t_\mathrm{C} \tag{4.4}$$

$$t_\mathrm{out,ch} = t_{\mathrm{C'\,to\,A'}} = t_{\mathrm{C\,to\,A}} + (dt_\mathrm{A} - dt_\mathrm{C}) < t_{\mathrm{C\,to\,A}}\ , \tag{4.5}$$

and also the corresponding inward travel times $t_\mathrm{in,ph}$ and $t_\mathrm{in,ch}$ as

$$t_\mathrm{in,ph} = t_{\mathrm{A\,to\,C}} = t_{\mathrm{C\,to\,A}} \tag{4.6}$$

$$t_\mathrm{in,ch} = t_{\mathrm{A'\,to\,C'}} = t_{\mathrm{A\,to\,C}} - (dt_\mathrm{A} - dt_\mathrm{C}) > t_{\mathrm{A\,to\,C}}\ , \tag{4.7}$$

where we assume for simplicity that there is no perturbation in the subphotospheric layer,

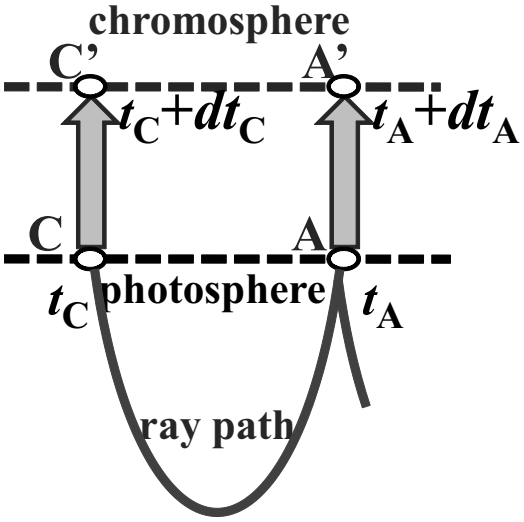

Figure 4.3 Schematic illustration showing wave propagation (ray path) from the subphotosphere to the chromosphere. If the wave arrival times at A and C in the photosphere are $t_{\rm A}$ and $t_{\rm C}$, the disturbance reaches at A$'$ and C$'$ in the chromosphere after some time delay, i.e., at $t_{\rm A} + dt_{\rm A}$ and $t_{\rm C} + dt_{\rm C}$ (see the text in §4.4).

or, equivalently, removed the subphotospheric components from the discussion. Then, the outward–inward travel-time difference in the chromosphere, $\Delta t_{\rm ch}$, is

$$\Delta t_{\rm ch} = t_{\rm out,ch} - t_{\rm in,ch} = 2(dt_{\rm A} - dt_{\rm C}) < 0. \tag{4.8}$$

The time delay difference between the two points $dt_{\rm A} - dt_{\rm C}$ can be estimated by

$$dt_{\rm A} - dt_{\rm C} = -\frac{L}{c}\frac{V}{c}, \tag{4.9}$$

where V is the downflow speed. Using Equations (4.8) and (4.9), we can roughly estimate the downflow speed: at $V \sim 8$ km s^{-1} for the plage in dataset 1 ($\Delta t_{\rm ch} \sim -0.67$ minute) and at $V \sim 5$ km s^{-1} for the plage in dataset 2 ($\Delta t_{\rm ch} \sim -0.42$ minute).

Note that Equations (4.5) and (4.7) imply that the chromospheric mean travel time $(t_{\rm out,ch} + t_{\rm in,ch})/2$ should essentially be identical to the photospheric mean travel time $(t_{\rm out,ph} + t_{\rm in,ph})/2$. Table 4.1 shows that this is indeed the case.

Actually, we do detect the photospheric downflows in the plage region in the photospheric Fe I Dopplergram[2]. Although we still need a more fine-tuned calibration of the

[2]It has been pointed out by K. Ichimoto that the signal may be largely due to the lack of convective blueshift in the region. This issue is been investigated.

NFI data to derive the better estimates of the speed, a redshift signal is clearly seen in the Dopplergram (see Figure 4.1). Since the signal is somewhat comparable though weaker than the Doppler shift due to the solar rotation, the downflow speed is roughly estimated at a few hundred m s^{-1}, compared to the chromospheric value of a few km s^{-1}. This is consistent with the deceleration picture in emerging flux regions.

In our analysis, we use 14.86-Mm annulus to measure the inward and outward travel times. We chose this size because we know that this size of annulus is suitable for detecting spatial patterns of the size of the supergranular flow, as is mentioned in the previous works by Sekii et al. (2007). We also check the cases for different sizes of annulus for dataset 1: from 4 Mm to around 20 Mm. Phase-speed filters are changed depending on the annulus size. For these calculations, so that we can measure travel times for smaller annuli, we use a Gaussian frequency filter 2.4-times broader than that mentioned in §4.3, although it renders wavepackets narrower, and makes the phase travel-time measurement less precise. For the case of annuli larger than the original one, the low-wavenumber filter, required for removing the artifacts in Fe I data, cannot be used. Thus, for these annuli the travel-time can be measured only for the Ca II data. Results are shown in Figure 4.4. In the QS, the travel-time difference remains small regardless of the size, while the difference in plage increases as the annulus size increases. This can be explained by increasingly large part of an annulus located outside plage where there is no downflow, which contributes to the travel-time anomaly. In fact, when the size attains the spatial extent of the plage ($\sim 15 - 20$ Mm), the anomaly seems to reach a plateau.

We note that a sound speed anomaly in the chromosphere can also lead to an outward–inward travel-time difference through affecting the chromospheric time delay. Such an anomaly may arise from magnetic field. However, generally in plage regions magnetic field is not strong enough to explain the travel-time difference we have found. Indeed, in MDI (Scherrer et al. 1995) magnetogram the plage magnetic field in dataset 1 is a few hundred Gauss, which translates to only a few hundred m s^{-1} (magneto-)sound-speed anomaly, and in dataset 2 it is even weaker. A temperature increase in the plage does not explain the travel-time difference either, since it will *decrease* the time delay rather than increase it.

Let us also consider the effect of horizontal motions in the plage. The plage regions changed their shape and the bright patches and/or the small sunspots in the field of view were moving during the observation periods. The speed of these motions was ~ 1 km s^{-1} at most, and this is slower than the sound speed by an order of magnitude. Our estimates

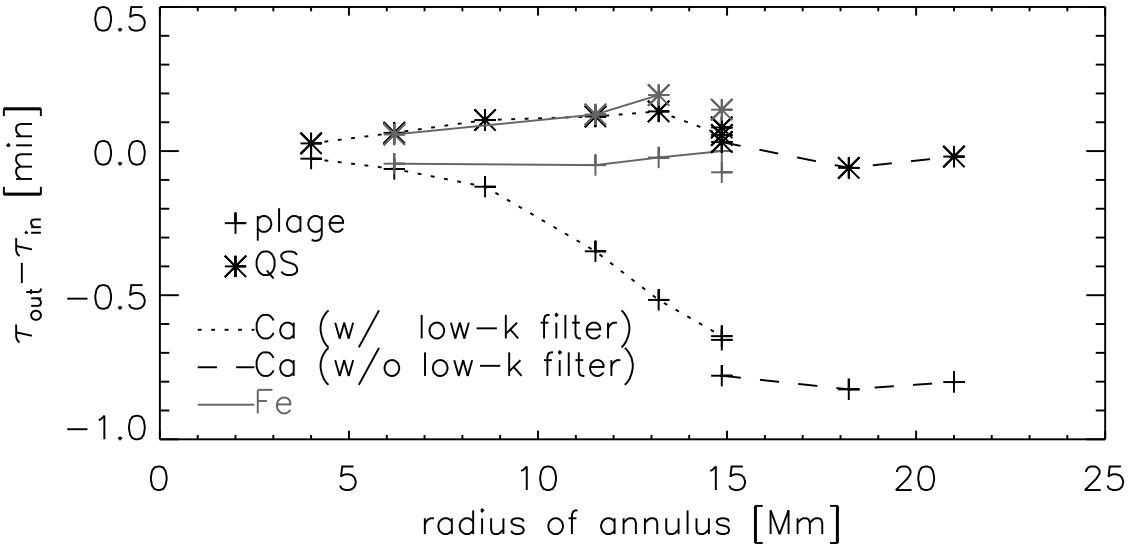

Figure 4.4 Outward–inward travel-time difference for dataset 1 plotted against annulus size. The crosses and asterisks indicate the difference measured in plage and QS, respectively. The gray solid lines indicate the differences for Fe I Dopplergram. The dotted and dashed lines are for the Ca II intensity data; the former and the latter are the differences measured with and without low-wavenumber filters (see the text for the details). Original values are also shown at 14.86 Mm, which are measured using a frequency filter different from others, although the values with different filters are essentially the same. Error bars are smaller than the symbol size.

show that these motions are too slow to affect the estimates of the chromospheric downflows in any way.

4.5 Conclusions

In this study, we have found a signature of chromospheric downflows in the differences between the acoustic travel times measured contemporaneously in the photosphere and the chromosphere. Note that we have not directly subtracted the photospheric travel times from the chromospheric ones to infer the downflow speed. Since the photospheric travel-time maps exhibit only the supergranular patterns and have no peculiar signal in the plage region, as shown in Figure 4.2, we assume that outward–inward travel-time difference at

the 'surface' is of the supergranulation origin only and negligible, and that we can use only the chromospheric travel-time difference to estimate the downflow speed. The fact that the outward–inward travel-time anomaly is found only in the chromospheric measurements of a plage region supports our interpretation that the anomaly found in the chromospheric travel-time map is due to chromospheric downflows in the plage region. This is the first example in local helioseismology in which the difference in travel-time maps, in chromospheric and photospheric lines, has been detected and then interpreted.

This kind of signature reminds us that chromospheric helioseismology data may include not only information about subsurface structures but also about chromospheric structures and dynamics. This needs to be taken into account in analysis and interpretation of helioseismic observations in the chromosphere. Such effects have not been sufficiently studied.

On the other hand, this result opens new possibilities of multiwavelength time–distance helioseismology studies of chromospheric flows and structures, though it is not clear what kind of advantages such a method has over more direct Doppler measurements in chromospheric lines, perhaps except in high latitude regions where downflow signal is hard to measure because of the projection effect. As recent high-resolution observations have revealed, the chromosphere is full of activities and flows (e.g., Katsukawa et al. 2007a). Multiwavelength helioseismic observations may provide a new method for detecting chromospheric flows, which may be of great importance for revealing dynamics of the chromosphere.

Table 4.1. Travel times (in minutes) for various datasets, regions and spectral lines

	Dataset 1		Dataset 2	
	Ca II H	Fe I	Ca II H	Fe I
Plage				
In	22.043 ± 2.8E-03	21.725 ± 1.8E-03	22.104 ± 3.0E-03	21.788 ± 1.8E-03
Out	21.372 ± 3.0E-03	21.646 ± 2.0E-03	21.685 ± 3.4E-03	21.892 ± 2.0E-03
Out-In	-6.72E-01 ± 4.1E-03	-7.82E-02 ± 2.7E-03	-4.19E-01 ± 4.6E-03	1.03E-01 ± 2.7E-03
QS				
In	21.964 ± 2.1E-03	21.806 ± 1.5E-03	22.232 ± 2.8E-03	22.019 ± 2.2E-03
Out	22.027 ± 3.3E-03	21.939 ± 2.1E-03	22.249 ± 3.2E-03	21.993 ± 2.1E-03
Out-In	6.34E-02 ± 3.9E-03	1.33E-01 ± 2.6E-03	1.66E-02 ± 4.3E-03	-2.55E-02 ± 3.1E-03

Chapter 5

Statistical Property of the Cross-Correlation Functions

In this chapter, we investigate the statistical property of the time–distance cross-correlation function in detail. We derive the distribution function of the cross-correlation function by assuming stochastic excitation of the solar oscillation. We discuss that cross-correlation function is normally distributed, and derive expressions for average and variance of the cross-correlation function; formulation is presented in §5.2. We also consider correlation of cross-correlation functions in §5.3. This work would enable us to do forward statistical modelling of cross-correlation function as well as to estimate errors in the travel times and inversion results; such applications of this work are discussed in §5.4.

5.1 Motivation

In time–distance helioseismology, travel times are measured via cross-correlation functions of surface wavefield and have been used to probe the subsurface structure of the Sun. However, the cross-correlation functions contain information other than the travel times.

For example, amplitude of cross-correlation function differs from place to place. Above all, in active regions the outward components often show smaller amplitude than the inward components, as shown in Figure 5.1. It may be an indication of some kind of absorption or reduced excitation in the active region by strong magnetic field (e.g., Braun et al. 1987; Hindman & Brown 1998). We analyzed the cross-correlation functions in Figure 5.1 in our work described in Chapter 4, where we fitted a Gabor wavelet to the cross-correlation

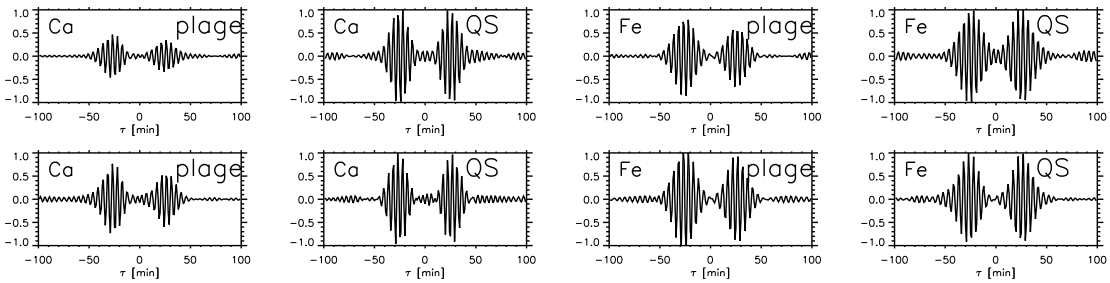

Figure 5.1 Cross-correlation functions averaged in the plage and in the quiet-Sun region (QS). The upper panels are for dataset 1, and the lower panels are for dataset 2. About the datasets, see Chapter 4. The QS cross-correlation functions are normalized by their maximum values, and the same normalization factors are used for their plage counterparts. In the horizontal axis, the positive values correspond to outward travel times and the negative values correspond to the inward travel times.

function and used only the phase travel-time parameter to examine flows. However, we think that further examinations of more details of the cross-correlation functions, such as their shape and amplitude, may be useful in investigating various aspects of wave propagation. If the structure and/or flows varies, the cross-correlation function varies accordingly, and the parameters of the cross-correlation function varies as well. Since using the whole cross-correlation function to infer the subsurface structure/dynamics requires heavy computation, the study using only a single parameter (travel time) is current mainstream. In recent years the direct inversion of cross-correlation function for subsurface flows have been discussed and tried by Woodard (2002, 2006, 2007). Their attempt is to detect flows by using the flow-induced correlations. For instance, Woodard (2002) analyzed f mode oscillations and obtained supergranular-scale flows in a shallow subphotospheric layer, which shows a good correlation with the surface Doppler velocity fields.

Examining statistical property of the cross-correlation function has a wide range of application. First, this enables us to do forward modelling of the cross-correlation function including its stochastic nature. Second, we can estimate errors in the travel times which are measured via cross-correlation function from the variance of the cross-correlation function. Third, if we can calculate the intrinsic dispersion of cross-correlation function, it can be used to measure significance of differences between the cross-correlation functions; we can test if anisotropy exists in the cross-correlation functions, for example.

5.2 Distribution Function of Cross-Correlation Function

5.2.1 Model

Since the oscillations in the Sun are excited by turbulent convection in the convection zone, we need to consider the stochastic excitation process to model the oscillations.

We define $P(k,\omega)$ as the power spectrum determined by the solar structure. Assuming every mode (k,ω) is excited stochastically, we model the Fourier transform of a wavefield, $a(k,\omega)$, as

$$a(k,\omega) = \alpha\sqrt{P(k,\omega)}\big(q_R(k,\omega) + iq_I(k,\omega)\big), \tag{5.1}$$

where q_R and q_I are the independent random variables with the standard normal distribution $\mathrm{N}(0,1)$, and $\alpha = \sqrt{1/2}$ is a normalization factor. That is, $< q >= 0$, $< q^2 >= 1$, and $< qq' >= 0$ if $q \neq q'$, where bracket denotes the ensemble average. Ensemble average of $|a(k,\omega)^2|$ is the power determined by the solar interior structure,

$$< |a(k,\omega)^2| >= P(k,\omega), \tag{5.2}$$

and each samples of $a(k,\omega)$ is distributed around the average with chi-square distribution with two degree of freedom[1]. It is known observationally (Woodard 1984; Appourchaux et al. 1998, 2000) that distribution of the power spectrum obtained by observational data, normalized by the fitted power spectrum, which corresponds to $|a(k,\omega)|^2/P$, is the chi-square distribution with two degree of freedom.

5.2.2 Distribution of cross-correlation function

As described in Appendix B.1, distribution of cross-correlation function is approximated by a normal distribution. Therefore, the distribution is determined completely if we know its average and variance. In the next subsection, we derive the average and variance.

5.2.3 Formulation

Consider a one-dimensional wavefield, $u(x,t)$. We define the cross-correlation function between a pair of points x and $x+d$ as

$$C(x,d,\tau) = \frac{h_t}{T}\sum_t u(x,t)u(x+d,t+\tau), \tag{5.3}$$

[1]Chi-square distribution with two degree of freedom is also called Boltzmann distribution.

where T is total period of the wavefield data and h_t is the spacing of temporal grid. Number of the data points in x and t domains are N_k and N_ω, respectively ($N_\omega h_t = T$). Using the Fourier decomposition of u,

$$u(x,t) = h_k h_\omega \sum_k \sum_\omega a(k,\omega) e^{i(kx-\omega t)}, \tag{5.4}$$

where $a(k,\omega)$ is the Fourier component, the cross-correlation function is found to be

$$C(x,d,\tau) = (h_k h_\omega)^2 \sum_\omega \sum_k \sum_{k'} a^*(k,\omega) a(k',\omega) e^{i(k'-k)x} e^{i(kd-\omega\tau)}. \tag{5.5}$$

By the model described by Equation (5.1), we obtain

$$\begin{aligned} a^*(k,\omega)a(k',\omega) &= \alpha^2 \sqrt{P(k,\omega)}\sqrt{P(k',\omega)}\{(q_R(k,\omega)q_R(k',\omega) + q_I(k,\omega)q_I(k',\omega)) \\ &\quad + i(q_R(k',\omega)q_I(k,\omega) - q_I(k',\omega)q_R(k,\omega))\}. \end{aligned} \tag{5.6}$$

When we express the discretized grid explicitly as $x_r = h_x r$, $d_s = h_x s$, $\tau_l = h_t l$, where $r, s = 0, 1, 2, \ldots, N_k - 1$ and $l = 0, 1, 2, \ldots, N_\omega - 1$, and using the indices instead of the variables themselves, cross correlation function, $C(x_r, d_s, \tau_l)$, is casted into the form

$$\begin{aligned} C_{r,s,l} = (\alpha h_\omega h_k)^2 \sum_{j=0}^{N_\omega-1} \sum_{m=0}^{N_k-1} \sum_{n=0}^{N_k-1} \sqrt{P_{mj}}\sqrt{P_{nj}} e^{i(n-m)h_k h_x r} e^{i(h_k h_x m s - h_\omega h_t j l)} \\ \times \{(q_{Rm,j}q_{Rn,j} + q_{Im,j}q_{In,j}) + i(q_{Rm,j}q_{In,j} - q_{Rm,j}q_{In,j})\}, \end{aligned} \tag{5.7}$$

where I used simpler notation $C_{r,s,l}$ instead of $C(x_r, d_s, \tau_l)$. Note that $h_k h_x = 2\pi/N_k$ and $h_t h_\omega = 2\pi/N_\omega$.

5.2.3.1 Symmetric properties of a, q, and P

Here we check the symmetric properties of the Fourier transform of a wavefield, $a_{i,j}$. Since the wavefield, u, is a real function, u^*, the complex conjugate of u, is equal to u, i.e.,

$$\begin{aligned} u(x,t) = u^*(x,t) &= h_\omega h_k \sum_{j=0}^{N_\omega-1} \sum_{m=0}^{N_k-1} a^*_{m,j} e^{-i(k_m x - \omega_j t)} \\ &= h_\omega h_k \sum_{j=0}^{N_\omega-1} \sum_{m=0}^{N_k-1} a^*_{m,j} e^{i(k_{(N_k-m)} x - \omega_{(N_\omega-j)} t)}. \end{aligned} \tag{5.8}$$

Hence, [2]

$$a_{m,j} = a^*_{N_k-m,N_\omega-j}, \tag{5.9}$$

and by using Equation (5.1),

$$\begin{aligned} a_{N_k-m,N_\omega-j} &= \alpha\sqrt{P_{N_k-m,N_\omega-j}}(q_{RN_k-mN_\omega-j} + iq_{IN_k-m,N_\omega-j}) \\ &= \alpha\sqrt{P_{m,j}}(q_{Rm,j} - iq_{Im,j}) \left(= a^*_{m,j}\right). \end{aligned} \tag{5.10}$$

This means

$$q_{RN_k-m,N_\omega-j} = q_{Rm,j} \tag{5.11}$$

$$q_{IN_k-m,N_\omega-j} = -q_{Im,j}, \tag{5.12}$$

and also means

$$a^*_{m,j}a_{m,j} = a_{N_k-m,N_\omega-j}a^*_{N_k-m,N_\omega-j}. \tag{5.13}$$

Therefore,

$$P_{m,j} = P_{N_k-m,N_\omega-j}. \tag{5.14}$$

By these properties, the cross-correlation function, C, in Equation (5.7) is proven to be a real function. This is because $\xi_{N_\omega-j,N_k-m,N_k-n} = \xi^*_{jmn}$, if we define what is summed in Equation (5.7) as ξ_{jmn}.

5.2.3.2 Average of cross-correlation function

The ensemble average of cross-correlation function, C, is written as

$$\begin{aligned} < C_{r,s,l} > = (\alpha h_\omega h_k)^2 \sum_{j=0}^{N_\omega-1}\sum_{m=0}^{N_k-1}\sum_{n=0}^{N_k-1} \sqrt{P_{mj}}\sqrt{P_{nj}} e^{i2\pi(n-m)r/N_k} e^{i2\pi(ms/N_k - jl/N_\omega)} \\ \times < (q_{Rm,j}q_{Rn,j} + q_{Im,j}q_{In,j}) + i(q_{Rm,j}q_{In,j} - q_{Rm,j}q_{In,j}) > . \end{aligned} \tag{5.15}$$

[2] Actually, we apply Equation (5.9) only if $m \geq 1$、 $j \geq 1$. In the cases with $m = 0$ and $j = 0$, or $m = N_k/2$ and $j = N_\omega/2$, $a_{m,j}$ is real by its definition. Also, from the definition it follows that $a_{0,j} = a^*_{0,N_\omega-j}$, $a_{m,0} = a^*_{N_k-j,0}$, $a_{N_k/2,j} = a^*_{N_k/2,N_\omega-j}$, $a_{m,N_\omega/2} = a^*_{N_k-m,N_\omega/2}$, and so on. Hence, strictly speaking, we need to discriminate the case with $m = 0, N/2$ and/or $j = 0, N/2$, because, for example, $< {q_{I}}_{0,0}{}^2 >= 0$, not 1. However, if N_ω and N_k are large enough, the contribution of these terms is negligible. In the discussions below, therefore, we use Equation (5.9) and neglect the exceptions.

We define ρ as the product of q in the right hand side in the above equation. In the case of $m = n$ we obtain

$$\rho_{mmj} = (q_{Rmj}^2 + q_{Imj}^2) + i(q_{Rmj}q_{Imj} - q_{Imj}q_{Rmj}) = (q_{Rmj}^2 + q_{Imj}^2). \tag{5.16}$$

Hence, the ensemble average of ρ_{mmj} is

$$< \rho_{mmj} >= 2 < q^2 >= 2. \tag{5.17}$$

On the other hand, in the case of $m \neq n$, since $q_{Rmj} \neq q_{Rnj}$ and $q_{Imj} \neq q_{Inj}$, we obtain

$$< \rho_{mnj} >=< q_{Rmj}q_{Rn,j} > + < q_{Im,j}q_{In,j} > +i(< q_{Rmj}q_{Inj} > - < q_{Imj}q_{Rnj} >) = 0. \tag{5.18}$$

As a result, in the summation of $< C >$ in Equation (5.15) there remain only terms of $m = n$. The ensemble average of the cross-correlation function is therefore

$$\begin{aligned} < C_{r,s,l} > &= (\alpha h_\omega h_k)^2 \sum_{j=0}^{N_\omega-1} \sum_{m=0}^{N_k-1} P_{mj} e^{i2\pi(ms/N_k - jl/N_\omega)} \times 2 \\ &= (h_\omega h_k)^2 \sum_{j=0}^{N_\omega-1} \sum_{m=0}^{N_k-1} P_{mj} e^{i2\pi(ms/N_k - jl/N_\omega)}. \end{aligned} \tag{5.19}$$

This is the Fourier transform of the power spectrum P.

5.2.3.3 Variance of cross-correlation function

Next, we consider the ensemble average of squared cross-correlation function to estimate the variance. Since the cross-correlation function, C, is a real function, $C^2 = C^*C$. Therefore, we use C^*C instead of C^2 to make the calculation convenient. The product C^*C is given by

$$\begin{aligned} C_{r,s,l}C^*_{r,s,l} &= (\alpha h_\omega h_k)^4 \sum_{j=0}^{N_\omega-1} \sum_{m=0}^{N_k-1} \sum_{n=0}^{N_k-1} \sum_{j'=0}^{N_\omega-1} \sum_{m'=0}^{N_k-1} \sum_{n'=0}^{N_k-1} \sqrt{P_{mj}}\sqrt{P_{nj}}\sqrt{P_{m'j'}}\sqrt{P_{n'j'}} \\ &\times e^{i2\pi(n-m)r/N_k} e^{-i2\pi(n'-m')r/N_k} e^{i2\pi(ms/N_k - jl/N_\omega)} e^{-i2\pi(m's/N_k - j'l/N_\omega)} \\ &\times \{(q_{Rm,j}q_{Rn,j} + q_{Im,j}q_{In,j}) + i(q_{Rm,j}q_{In,j} - q_{Im,j}q_{Rn,j})\} \\ &\quad \{(q_{Rm',j'}q_{Rn',j'} + q_{Im',j'}q_{In',j'}) - i(q_{Rm',j'}q_{In',j'} - q_{Im',j'}q_{Rn',j'})\} \\ &= (\alpha h_\omega h_k)^4 \sum_{j=0}^{N_\omega-1} \sum_{m=0}^{N_k-1} \sum_{n=0}^{N_k-1} \sum_{j'=0}^{N_\omega-1} \sum_{m'=0}^{N_k-1} \sum_{n'=0}^{N_k-1} \sqrt{P_{mj}}\sqrt{P_{nj}}\sqrt{P_{m'j'}}\sqrt{P_{n'j'}} \end{aligned} \tag{5.20}$$

$$
\begin{aligned}
\times \quad & e^{i2\pi[(n-m)-(n'-m')]r/N_k} e^{i2\pi((m-m')s/N_k-(j-j')l/N_\omega)} \\
\times \quad & [(q_{Rm,j}q_{Rn,j}+q_{Im,j}q_{In,j})(q_{Rm',j'}q_{Rn',j'}+q_{Im',j'}q_{In',j'}) \\
& +(q_{Rm,j}q_{In,j}-q_{Im,j}q_{Rn,j})(q_{Rm',j'}q_{In',j'}-q_{Im',j'}q_{Rn',j'}) \\
& +i\{(q_{Rm,j}q_{In,j}-q_{Im,j}q_{Rn,j})(q_{Rm',j'}q_{Rn',j'}+q_{Im',j'}q_{In',j'}) \\
& -(q_{Rm,j}q_{Rn,j}+q_{Im,j}q_{In,j})(q_{Rm',j'}q_{In',j'}-q_{Im',j'}q_{Rn',j'})\}]. \qquad (5.21)
\end{aligned}
$$

By the calculation presented in Appendix B.2, we obtain $< C^*C >$ as

$$
\begin{aligned}
< C^*C > \quad = \quad & (h_\omega h_k)^4 \times \left\{ \sum_{j=0}^{N_\omega-1} \sum_{m=0}^{N_k-1} \sum_{n=0}^{N_k-1} P_{mj}P_{nj} \right. \\
& + \sum_{j=0}^{N_\omega-1} \sum_{j'=0}^{N_\omega-1} \sum_{m=0}^{N_k-1} \sum_{m'=0}^{N_k-1} P_{mj}P_{m'j'} e^{i2\pi\{(m-m')s/N_k-(j-j')l/N_\omega\}} \\
& + \left. \sum_{j=0}^{N_\omega-1} \sum_{m=0}^{N_k-1} \sum_{n=0}^{N_k-1} P_{mj}P_{nj} e^{i2\pi\{(m+n)s/N_k-2jl/N_\omega\}} \right\}. \qquad (5.22)
\end{aligned}
$$

The second summation in Equation (5.22) corresponds to the squared average of cross-correlation function, $< C >^2$. Therefore, the variance is

$$
\begin{aligned}
< C^*C > - < C >^2 \quad = \quad & (h_\omega h_k)^4 \times \left\{ \sum_{j=0}^{N_\omega-1} \sum_{m=0}^{N_k-1} \sum_{n=0}^{N_k-1} P_{mj}P_{nj} \right. \\
& + \left. \sum_{j=0}^{N_\omega-1} \sum_{m=0}^{N_k-1} \sum_{n=0}^{N_k-1} P_{mj}P_{nj} e^{i2\pi\{(m+n)s/N_k-2jl/N_\omega\}} \right\}. \qquad (5.23)
\end{aligned}
$$

5.2.3.4 In the case of two-dimensional wavefield

So far, we consider the one-dimensional wavefield, $u(x,t)$. In practice, we observe the Sun in two dimension in space and obtain the two-dimensional wavefield, $u(x,y,t)$. In this case, we need slight modification to the formula in one dimension. Basically, we need to modify a product of scalar (the wavenumber and the position) kx to an inner product of two vectors (the wavenumber vector and the position vector) $k_x x + k_y y$. Since in the formula we use discretized form, we need additional summation for y. Therefore, for the two-dimensional wavefield, following formula are obtained instead of Equations (5.19) and (5.23):

$$
< C_{r,r',s,s',l} >= (h_\omega h_k^2)^2 \sum_{j=0}^{N_\omega-1} \sum_{m=0}^{N_k-1} \sum_{m'=0}^{N_k-1} P_{mm'j} e^{i2\pi(ms/N_k+m's'/N_k-jl/N_\omega)}. \qquad (5.24)
$$

and

$$< C^*C > - < C >^2 = (h_\omega {h_k}^2)^4 \times \left\{ \sum_{j=0}^{N_\omega-1} \sum_{m=0}^{N_k-1} \sum_{n=0}^{N_k-1} \sum_{m'=0}^{N_k-1} \sum_{n='0}^{N_k-1} P_{mm'j} P_{nn'j} \right.$$
$$\left. + \sum_{j=0}^{N_\omega-1} \sum_{m=0}^{N_k-1} \sum_{n=0}^{N_k-1} \sum_{m'=0}^{N_k-1} \sum_{n'=0}^{N_k-1} P_{mm'j} P_{nn'j} e^{i2\pi\{(m+n)s/N_k + (m'+n')s'/N_k - 2jl/N_\omega\}} \right\} . \quad (5.25)$$

5.2.4 Numerical test of the distribution function of the cross-correlation function

We test the distribution function of cross-correlation function obtained in the previous subsection by Monte Carlo simulations.

5.2.4.1 Wavefield of a single mode

Let us consider the case of a one-dimensional wavefield which consists of a single oscillation mode. The power distribution is given by

$$P_{m,j} = P(\delta_{m,m_0}\delta_{j,j_0} + \delta_{m,N_k-m_0}\delta_{j,N_\omega-j_0}) \ , \quad (5.26)$$

where δ_{m,m_0} is the Kronecker delta, and the average cross-correlation function is given by Equation (5.19),

$$< C_{r,s,l} >= 4(\alpha h_\omega h_k)^2 P^2 \cos\left(2\pi(j_0 l/N_\omega - m_0 s/N_k)\right) . \quad (5.27)$$

In this case, we calculate 200 samples of wavefields realized by the Monte Carlo simulation. Using random variables with the standard normal distribution, we calculate the average of 200 samples of C^2 and compare with the theoretical value of $< C^*C >$ obtained by Equation (5.22). Figure 5.2 shows the results. In this calculation, we define $(\alpha h_\omega h_k)^2 = 1$.

The variance of C is of the same order of magnitude as the amplitude of C, in this case, 4. In this power distribution, the power is non-zero at a single point in (k, ω) plane. Hence, only one pair of the random variables (q_R, q_I) affects each sample.

The calculation demonstrates that the distribution of the cross-correlation function of the simulated samples are well explained by our model.

5.2.4.2 Wavefield of an f-mode-like power distribution

Let us consider the power spectrum shown in the upper-left panel of Figure 5.3, which is imitating the f-mode ridges in the power spectrum of the Sun. In this case, we force the

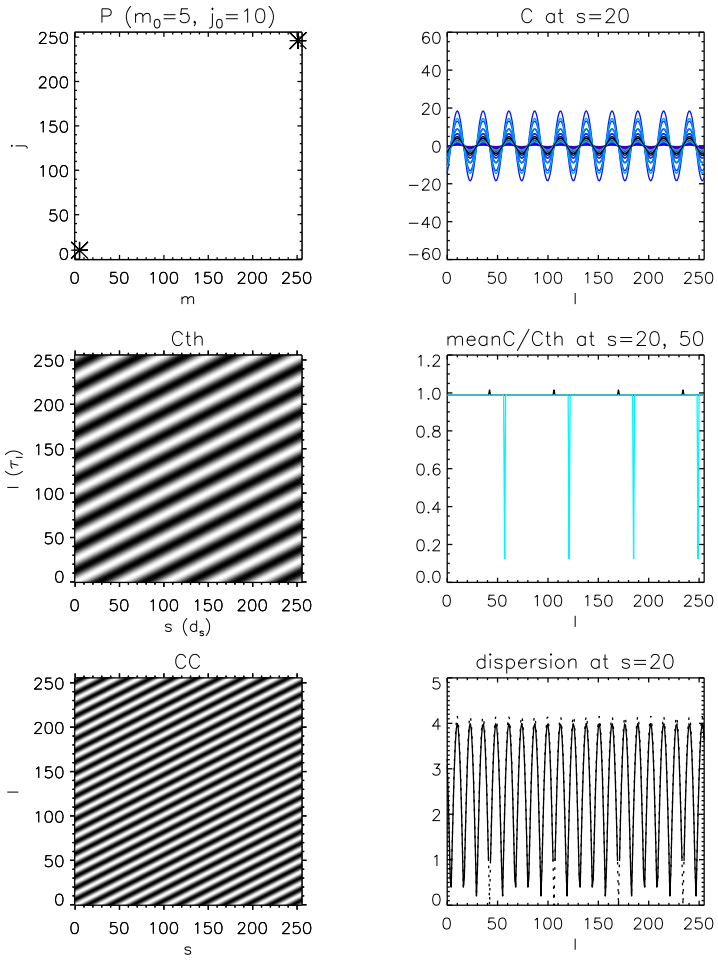

Figure 5.2 Results of Monte Carlo simulation in the case of a wavefield of a single mode. *Left*: Power distribution P(top), cross-correlation function $< C >$ obtained by Equation (5.19) (middle), and $< C^*C >$ obtained by Equation (5.22) (bottom). The power is 1 for the modes indicated by asterisks only; except for the modes, the power is 0. *Right*: Cross section at $s = 20$. Cross-correlation function C (top), the ratio of the sample average of C obtained by Monte Carlo simulation to the $< C >$ obtained by Equation (5.19) (middle), and standard deviation (bottom). In the top-right panel, black indicates the sample average, while the colour line indicates each sample. In the middle row, blue indicates the cross section at $s = 50$. In the bottom panel, the solid line indicates the square root of the variance obtained by Equation (5.23), and the dotted line indicates the sample standard deviation, i.e., square root of the difference between the 200-sample average of C^2 and squared the average of C.

power $P_{m,j}$ to vanish at $m = 0$ or $N_k/2$, or $j = 0$ or $N_\omega/2$. In the way similar to the previous case, we compare the average of 100 samples of C^2 obtained by Monte Carlo calculation and $< C^*C >$ obtained by Equation (5.22). The results are shown in Figure 5.3. The ratio of the sample average of C to $< C >$ is distributed around 1 and the dispersion around the average of 100 samples is consistent with what we expect from Equation (5.23) . In this example also, the distribution obtained by Monte Carlo simulations is well explained by Equations (5.19) and (5.22).

Here we compare the ensemble average of spatial average with spatial average of ensemble average. In Figure 5.4, we show the result. The cross-correlation function is the function of the position, x_r, the displacement, d_s, and the time shift, τ_l, in the case of a one-dimensional wavefield, and it is denoted by $C_{r,s,l}$ (see Equation 5.7). We compare the ensemble average of $C_{r,s,l}$, $< C_{r,s,l} >$, with the ensemble average of spatial average of $C_{r,s,l}$, $\overline{C}$, and with the ensemble average of the cross-correlation function at a certain point $r = r_0$ as well. In the left column, spatial average of cross-correlation function for each sample and the 100-sample average of the spatial average are shown in the top panel, while in the middle panel, differences between the spatial average of each sample and the 100-sample average of the spatial average are shown. The white line in the middle panel is $\sqrt{< \overline{CC^*} > - < \overline{C}^2 >}$, which explains well the dispersion of the samples. About the formulation of $\sqrt{< \overline{CC^*} > - < \overline{C}^2 >}$, see the next subsection. On the other hand, in the right column, cross-correlation function at a certain point, $r = 10$, of each sample is shown with the 100-sample average of them (black) in the top panel. In the middle panel, the difference between the sample cross-correlation functions and the mean of them at the point are shown, and the white line, which corresponds to $\sqrt{< CC^* > - < C >^2}$, is consistent with the sample dispersion. The ratio of 100-sample average of the spatial average to the expectation value $< C >$, which is indicated by black line in the bottom-left panel, and the ratio of 100-sample average at $r = 10$ to $< C >$, indicated by orange line, are distributed around 1, and this implies that both the sample average of the spatial average and the sample average at a certain point can be approximated by the same $< C >$, which will be proved by formulation in the next subsection. As is shown in the bottom-right panel, difference of $\sqrt{< \overline{CC^*} > - < \overline{C}^2 >}$ and $\sqrt{< CC^* > - < C >^2}$ is clear and the dispersion expected from our formulation and that of samples obtained by Monte Carlo simulation are certainly consistent.

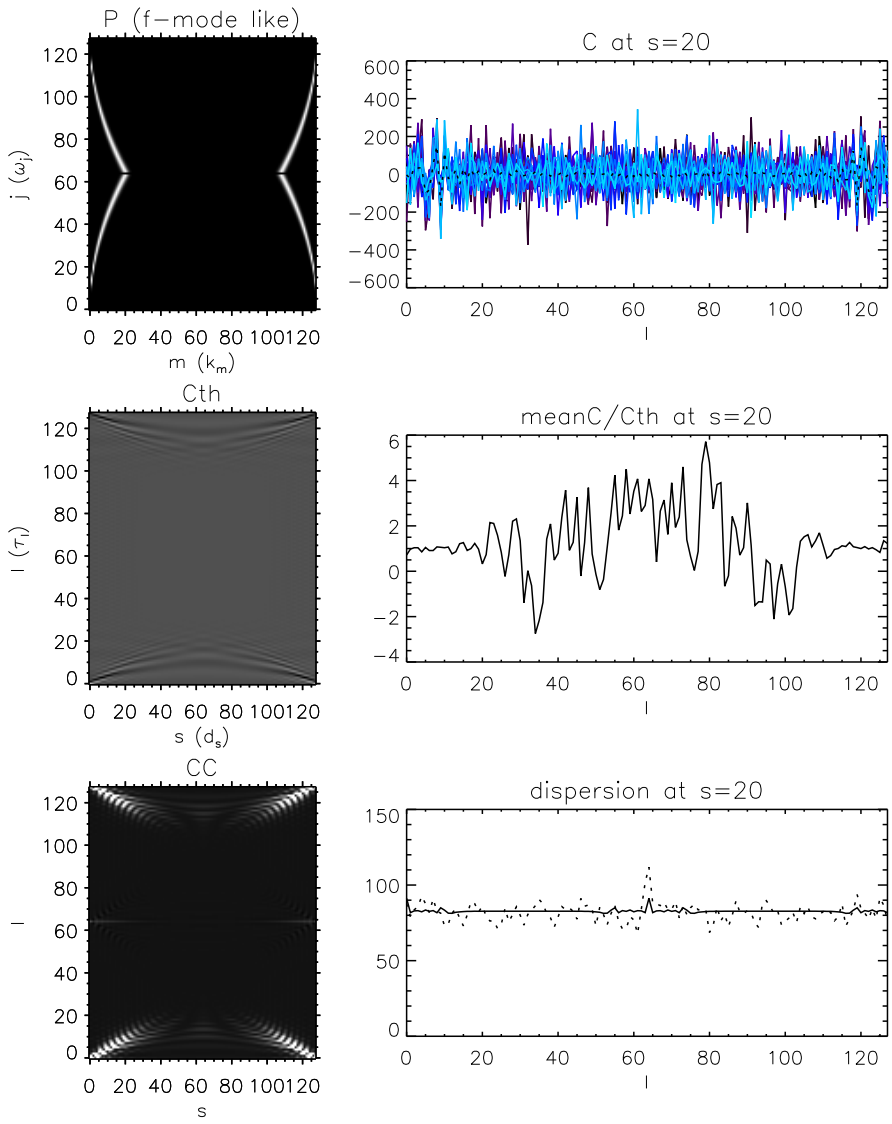

Figure 5.3 Results of Monte Carlo simulation in the case of wavefield of an f-mode-like power distribution. *Left*: power distribution P (top), cross-correlation function $< C >$ obtained by Equation (5.19) (middle), and $< C^*C >$ obtained by Equation (5.22) (bottom). *Right*: Cross section at $s = 20$. Cross-correlation function (top), the ratio of the sample average of C to the cross-correlation function obtained by Equation (5.19) (middle), and standard deviation (bottom). Details are similar to those in Figure 5.2.

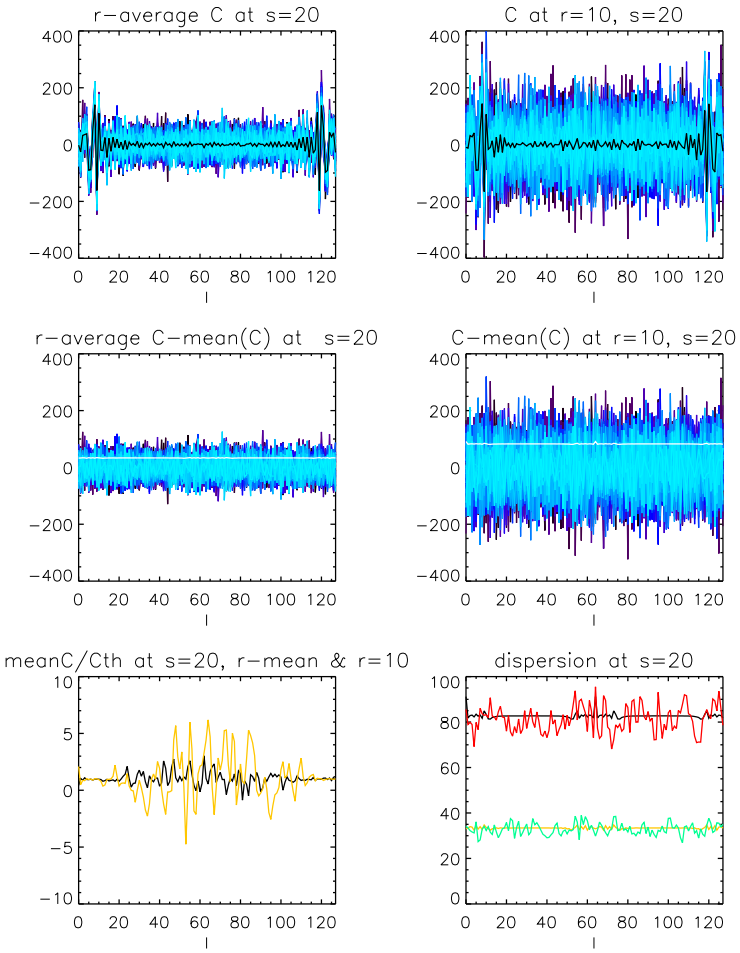

Figure 5.4 Comparison between the spatial average cross-correlation function and the cross-correlation function evaluated at a point. *Upper-left*: 100 samples of $\overline{C}$ at $s = 20$ (colours) and the average of them (black). *Upper-right*: 100 samples of C at $r = 10$ and $s = 20$ (colours) and the average of them (black). *Middle-left*: difference between 100 samples of $\overline{C}$ at $r = 20$ and the average of them (colours) and $\sqrt{< \overline{C}\overline{C}^* > - < \overline{C}^2 >}$ (white). *Middle-right*: difference between 100 samples of C at $r = 10$, $s = 20$ and the average of them (colours), and $\sqrt{< CC^* > - < C >^2}$ (white). *Bottom-left*: ratio of 100-sample average of C to $< C >$. Black line indicates the ratio of the spatial average $\overline{C}$ to $< C >$, while the orange line indicates the ratio of average of 100 samples of C at $r = 10$ to $< C >$. *Bottom-right*: variance at $s = 20$ plotted against time. Black indicates theoretical values of $\sqrt{< C^*C > - < C >^2}$ at $r = 10$, and red indicates the sample variance. The spatial average of $\sqrt{< \overline{C}^*\overline{C} > - < C >^2}$ is indicated by orange while the 100-sample spatial average is given by green.

5.2.4.3 Spatial average and ensemble average

For a one-dimensional case, we define the spatial average of the cross-correlation function as

$$\overline{C}(d,\tau) = \frac{1}{L}\int dx C(x,d,\tau), \tag{5.28}$$

where L is the spatial extent. In a discretized form,

$$\overline{C}(d_s,\tau_l) = \frac{1}{h_x N_k} h_x \sum_{r=0}^{N_k-1} C_{rsl} = \frac{1}{N_k}\sum_{r=0}^{N_k-1} C_{rsl}. \tag{5.29}$$

This can be written in the form

$$\begin{aligned}
\overline{C}_{s,l} &= \frac{(\alpha h_\omega h_k)^2}{N_k}\sum_{r=0}^{N_k-1}\sum_{j=0}^{N_\omega-1}\sum_{m=0}^{N_k-1}\sum_{n=0}^{N_k-1}\sqrt{P_{mj}}\sqrt{P_{nj}}e^{i2\pi(n-m)r/N_k}e^{i2\pi(ms/N_k-jl/N_\omega)} \\
&\quad\times\{(q_{Rmj}q_{R,j}+q_{Imj}q_{Inj})+i(q_{Rmj}q_{Inj}-q_{Rmj}q_{Inj})\} \qquad (5.30)\\
&= (\alpha h_\omega h_k)^2\sum_{j=0}^{N_\omega-1}\sum_{m=0}^{N_k-1} P_{mj}e^{i2\pi(ms/N_k-jl/N_\omega)}(q_{Rmj}^2+q_{Imj}^2) \qquad (5.31)
\end{aligned}$$

by using Equation (5.7). Therefore, the ensemble average of the spatial average is

$$< \overline{C}_{s,l} >= 2(\alpha h_k h_\omega)^2\sum_{j=0}^{N_\omega-1}\sum_{m=0}^{N_k-1} P_{mj}e^{i2\pi(ms/N_k-jl/N_\omega)}. \tag{5.32}$$

and, according to Equation (5.19), from this it follows that $< \overline{C}(d,\tau) >=< C(x,d,\tau) >$.

Next, we consider $< \overline{CC^*} - \overline{C}^2 >$. The spatial average of squared cross-correlation function, $\overline{CC^*}$, is given as

$$\begin{aligned}
\overline{C_{r,s,l}C^*_{r,s,l}} &= (\alpha h_\omega h_k)^4\frac{1}{N_k}\sum_{r=0}^{N_k-1}\sum_{j,j',m,n,m',n'}\sqrt{P_{mj}P_{nj}P_{m'j'}P_{n'j'}}e^{i2\pi(n-m)r/N_k}e^{-i2\pi(n'-m')r/N_k} \\
&\quad\times e^{i2\pi(ms/N_k-jl/N_\omega)}e^{-i2\pi(m's/N_k-j'l/N_\omega)} \\
&\quad\times\{(q_{Rmj}q_{Rnj}+q_{Imj}q_{Inj})+i(q_{Rmj}q_{Inj}-q_{Imj}q_{Rnj})\} \\
&\quad\times\{(q_{Rm'j'}q_{Rn'j'}+q_{Im'j'}q_{In'j'})-i(q_{Rm'j'}q_{In'j'}-q_{Im'j'}q_{Rn'j'})\}. \qquad (5.33)
\end{aligned}$$

By taking the ensemble average of this, you will find that $< \overline{CC^*} >$ is the same as $< CC^* >$ in Equation (5.22). With Equation (5.31), the squared spatial average, $\overline{C}\ \overline{C^*}$, is

$$\overline{C}_{s,l}\overline{C^*_{s,l}} = (\alpha h_\omega h_k)^4\sum_{j=0}^{N_\omega-1}\sum_{m=0}^{N_k-1}\sum_{j'=0}^{N_\omega-1}\sum_{m'=0}^{N_k-1} e^{i2\pi(ms/N_k-jl/N_\omega)}e^{-i2\pi(m's/N_k-j'l/N_\omega)}$$

$$\times P_{mj}P_{m'j'}(q_{R_{mj}}^2 + q_{I_{mj}}^2)(q_{R_{m'j'}}^2 + q_{I_{m'j'}}^2) \tag{5.34}$$

$$< \overline{C}_{s,l}\overline{C^*}_{s,l} > = (\alpha h_\omega h_k)^4 \times 4\Big(\sum_{j=0}^{N_\omega-1} \sum_{m=0}^{N_k-1} P_{mj}^2 (1 + e^{i2\pi(2ms/N_k - 2jl/N_\omega)}) + \sum_{j=0}^{N_\omega-1} \sum_{m=0}^{N_k-1} \sum_{j'=0}^{N_\omega-1} \sum_{m'=0}^{N_k-1} P_{mj}P_{m'j'} e^{i2\pi\{(m-m')s/N_k - (j-j')l/N_\omega\}} \Big) \tag{5.35}$$

and this equation, by taking ensemble average in the same manner as that in Appendix B.2, we obtain

$$< \overline{CC^*} - \overline{C}^2 > = (h_k h_\omega)^4 \Big(\sum_m \sum_{m'} \sum_j P_{mj}P_{m'j}(1 + e^{i2\pi((m+m')/N_k s - 2jl/N_\omega)}) - \sum_m \sum_j {P_{mj}}^2 (1 + e^{i2\pi(2m/N_k s - 2jl/N_\omega)}) \Big). \tag{5.36}$$

Note that as shown in Equation (5.23), $< CC^* > - < C >^2$ has only the first term of Equation (5.36).

This explains the difference between spatial average and ensemble average shown in Figure 5.4.

5.2.5 Discussions

Gizon & Birch (2004) discussed noise estimation of travel times using the wavefield model which is essentially the same as our model (§5.2.1), although they did not focus on the cross-correlation function itself but discussed the travel times computed from the linear combination of cross-correlation functions (Equation (3.17) in §3.4.4).

Woodard (2007) pointed out that the model used in Gizon & Birch (2004) does not include the effect of flow-dependent correlations between oscillation modes. That is the case for our analysis as well; we assume all the modes are independent (see Equation (5.1) in §5.2.1). By exploiting such effect by flow for the correlation, Woodard (2007) inverted directly the correlation function data for subsurface flow. Note that the inversion of the whole cross-correlation function, not a single parameter (a travel time, for example) extracted from the function, requires heavy computational tasks.

5.2.6 Conclusions

By modelling the stochastic excitation of the oscillations of the Sun, we have established that the distribution function of the cross-correlation function is a normal distribution, and

derived the relationship between mean power spectrum and the statistical distribution of the cross-correlation function, by calculating the mean and variance of the distribution. The distribution function has been checked by the Monte Carlo calculations demonstrated in §5.2.4.

Equation (5.23) tells us that the variance is nearly independent of the position or time shift, and therefore, the amplitude of the cross-correlation function. This is because the second summation in Equation (5.23) is much less than the first summation, and the first summation is a constant determined only by the power spectrum P. This property is clearly seen in the lower-right panel of Figure 5.3.

If we take average of cross-correlation functions in some spatial range, we may reduce the signal-to-noise ratio. This means the variance is reduced by factor N, where N is the number of independent cross-correlation functions to be averaged. To estimate the degree of independence of the cross-correlation functions to be averaged, we discuss the correlation of cross-correlation functions in the next section.

5.3 Correlation of Cross-Correlation Functions

In this section, we examine the correlation of the cross-correlation functions. In the previous sections we have established the way to estimate the variance of cross-correlation function. This is not enough, however, when we compare two cross-correlation functions to decide whether they are significantly different or not; we need to know how they are expected to correlate with each other.

For example, if we compare a cross-correlation function between the signals at points A and B with a cross-correlation function between the signals at points next to A and next to B, they will look alike. If on the other hand we compare the original cross-correlation function with cross-correlation functions between signals at points far from the original pair, they will be very different. For another example, to check anisotropy of the cross-correlation function, which might be caused by presence of strong magnetic field, one may need to consider a set of cross-correlation functions and carry out a statistical test to see if this set is uniform or not. To run this test one need to know beforehand how the each function in the set is correlated with each other.

We define the correlation of cross-correlation function of two points, c, as

$$c \equiv \frac{\int f(t)g(t)dt}{\sqrt{\int f(t)^2 dt}\sqrt{\int g(t)^2 dt}}, \tag{5.37}$$

where $f(t)$ and $g(t)$ are the cross-correlation function of two points.

5.3.1 Calculation of the correlation using an observational dataset

We check this correlation using observational datasets. For this purpose, we use the Ca II H intensity data of the Quiet Sun near the disc centre taken by *Hinode*/SOT on 1 January 2007 with 1-minute cadence. We use the first 128-min dataset and take running difference. We only use the left half of the field of view; the field of view is 109-arcsec square (1024-pixel square). In this check, we set the distance between the two points as $\Delta_0 = 14.86$ Mm and calculate the cross-correlation function between a central point in the field of view and points on annulus with the radius of Δ_0 around the central point. This Δ_0 corresponds to 191 pixels and on the annulus there are 1146 pixels.

5.3.1.1 Correlation of raw cross-correlation function

First, we calculate the correlation without any filters. The k–ω and the corresponding time–distance diagrams are shown in Figure 5.5.

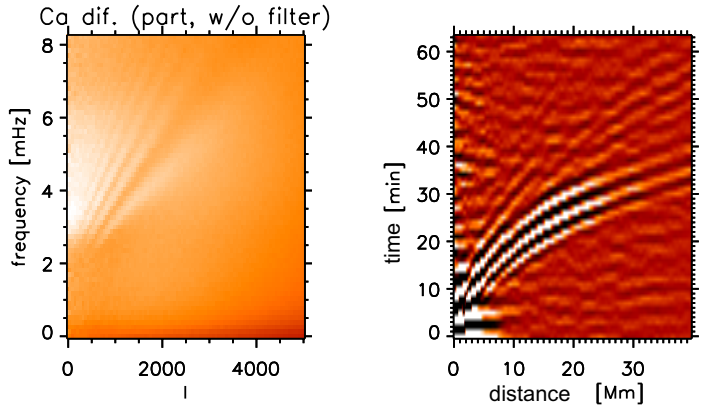

Figure 5.5 k–ω diagram (left) and time-distance diagram (right) by running difference intensity dataset in Ca II H.

In Figure 5.6 the correlation c is plotted against the azimuthal angle, and in Figure 5.7 the correlation c is plotted against the distance. The correlation falls to 0.5 around

the azimuthal angle of 0.05 radian. This means that two cross-correlation functions for two points separated by $\Delta_0 \times 0.05$ rad $= 0.7$ Mm resemble each other fairly well. This is consistent with the fact that the correlation falls to 0.5 around the distance of 0.5 Mm found in Figure 5.7. This length scale corresponds to $l \sim 8000$. The significance of the correlation length is discussed in §5.3.1.3.

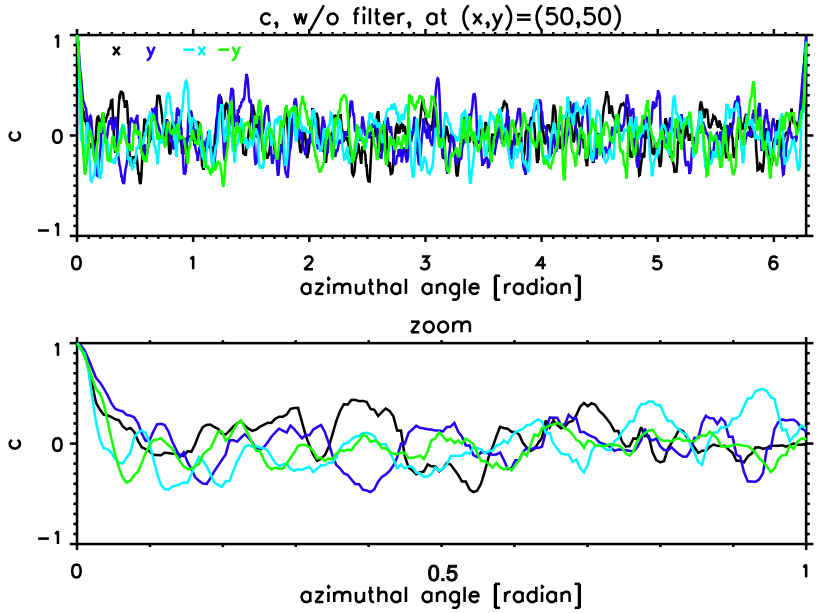

Figure 5.6 Correlation of the cross-correlation function at a point with that of different directions at the same point. The bottom panel shows the close-up of the top panel in a smaller angle range. Azimuthal angle indicates the difference of the direction of the two correlation functions. The colour indicates the direction of the reference ('fixed') cross-correlation function; black is for $+\boldsymbol{x}$, blue for $+\boldsymbol{y}$, skyblue for $-\boldsymbol{x}$, and green for $-\boldsymbol{y}$.

5.3.1.2 Correlation of filtered cross-correlation function

Removing the f-mode ridge and using the phase-speed filter for $\Delta_0 = 14.86$ Mm in k–ω space (see §3.4.1), we calculate the cross-correlation function of the filtered wavefield. The filtered $k-\omega$ and time-distance diagrams are shown in Figure 5.8. The main components in k–ω diagram are around $l \sim 1000$ and the corresponding spatial scale of the components is $\lambda \sim 4$ Mm.

Figure 5.9 shows the correlation as a function of the difference in azimuthal angle.

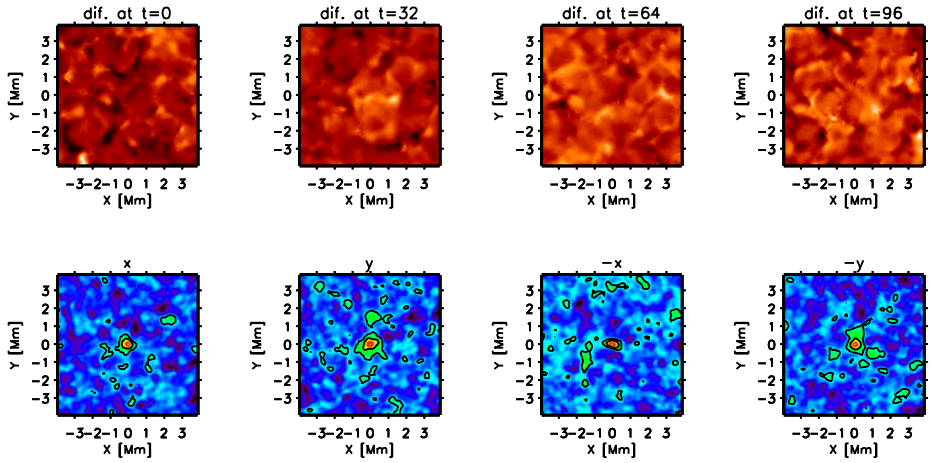

Figure 5.7 *Top*: Sample running difference images in Ca II H. *Bottom*: Distribution of correlation, c, in the direction of $\boldsymbol{x}, \boldsymbol{y}, -\boldsymbol{x}$, and$-\boldsymbol{y}$. Red indicates higher correlation, while blue indicates lower correlation. The contour levels are 0.2 and 0.5.

Figure 5.10 shows the correlation distribution. The points (50,50) and (50, 80) correspond to (500,500) and (500, 530), respectively, in the whole field of view (1024 × 1024 pixels). In Figure 5.11, the distribution of the correlation around the point (500,500) is shown in a wider field of view (100 × 100 pixels).

This result shows that the correlation falls to 0.5 around the angle of 0.15 radian. This corresponds to comparing two cross-correlation functions for two points separated by $\Delta_0 \times 0.15$ rad = 2.2 Mm. Actually, Figure 5.10 shows that the correlation drops to 0.5 around the distance of 2 Mm. Therefore, the correlation length for the filtered wave field is about 2 Mm, which corresponds to $l \sim 2000$. By referring to the power spectrum (Figure 5.8), the main components are up to this scale ($l \sim 2000$).

In the case we have just considered, we examined how the two-point cross-correlation function, between the centre of a circle and a point on the circle, loses coherence when we move the latter on the circle. We have also considered the case where cross-correlations are taken between two points on a circle, positioned opposite to each other so that they sit on the ends of a diameter, with varying angle. We have found that the bahaviour of the correlation is very similar.

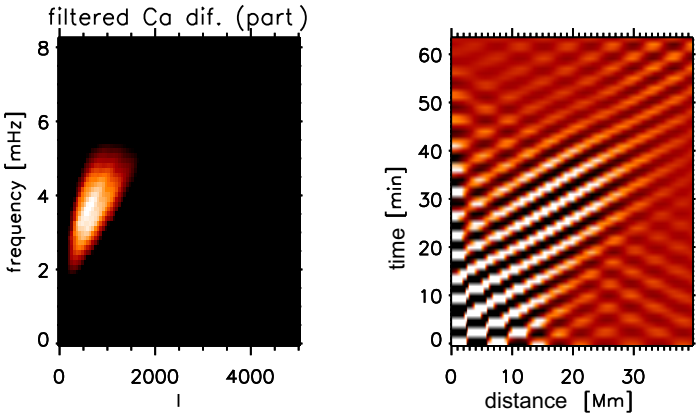

Figure 5.8 Filtered k–ω diagram (left) and time-distance diagram (right).

5.3.1.3 Conclusions

For the cross-correlation function for $\Delta_0 = 14.86$ Mm, the correlation length of a non-filtered wavefield is about 0.5 Mm, while that of a filtered wavefield is 2 Mm. What makes the difference of the correlation length? We concluded that the largest-k component determines the correlation length.

In the case of §5.3.1.2, apparently, spatial scale of dominant components corresponds to the correlation length. However, in the case of §5.3.1.1, although the main components in the power spectrum (k–ω diagram) is not so different from those of the filtered wavefield and is on the p- and f-modes ridges, the correlation length is much smaller. The power of small-scale components is one order of magnitude smaller than that on the ridges, but not zero, in the case without filter. Since the correlation length in the case without filter corresponds to the spatial scale of $l \sim 8000$, the components around $l \sim 8000$ determine the correlation length. This was confirmed by checking some other filtered wavefields. For example, when we checked the correlation length for the wavefield in which the components $l > 4000$ were filtered out, the correlation length is about 1 Mm, corresponding to $l \sim 4000$.

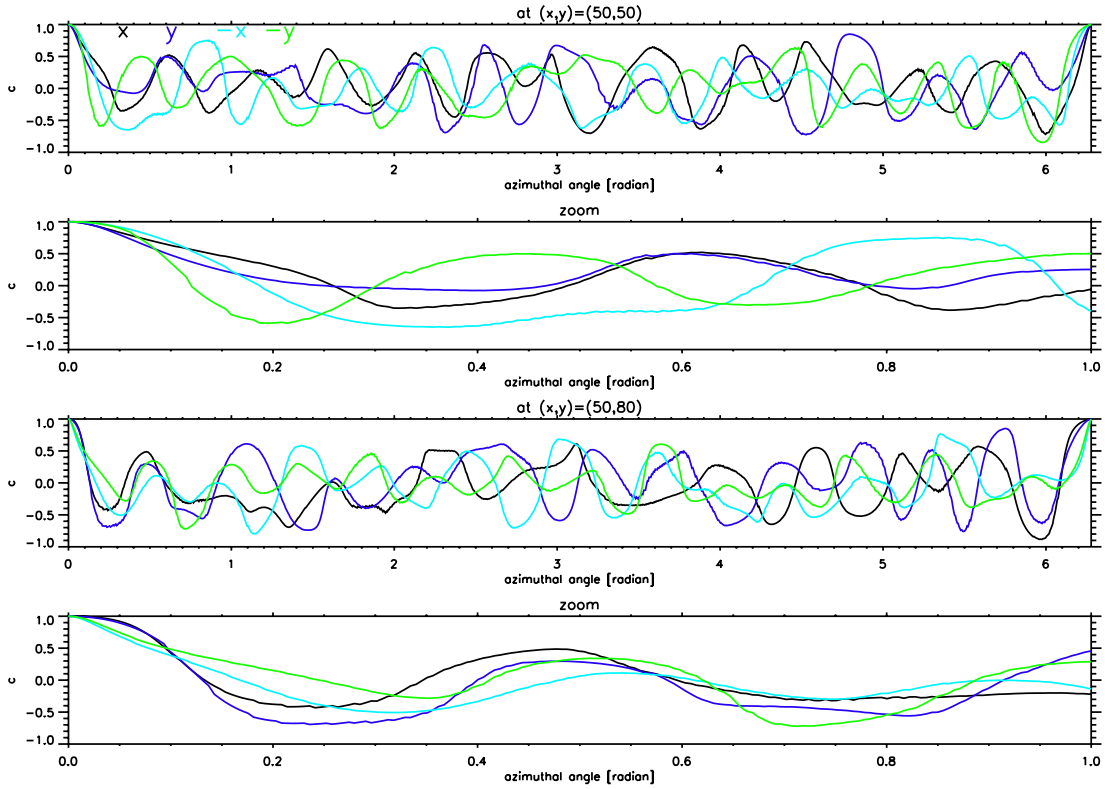

Figure 5.9 Correlation of the cross-correlation function at two certain points in a filtered wavefield with that of different directions at the same points. Azimuthal angle indicates the difference of the direction of the two cross-correlation functions. The colour indicates the direction of the reference ('fixed') cross-correlation function; black is for $+\boldsymbol{x}$, blue for $+\boldsymbol{y}$, skyblue for $-\boldsymbol{x}$, and green for $-\boldsymbol{y}$. The first two rows and bottom two rows show different positions in the field of view, and the lower panel in each pair is a close-up of the upper panel.

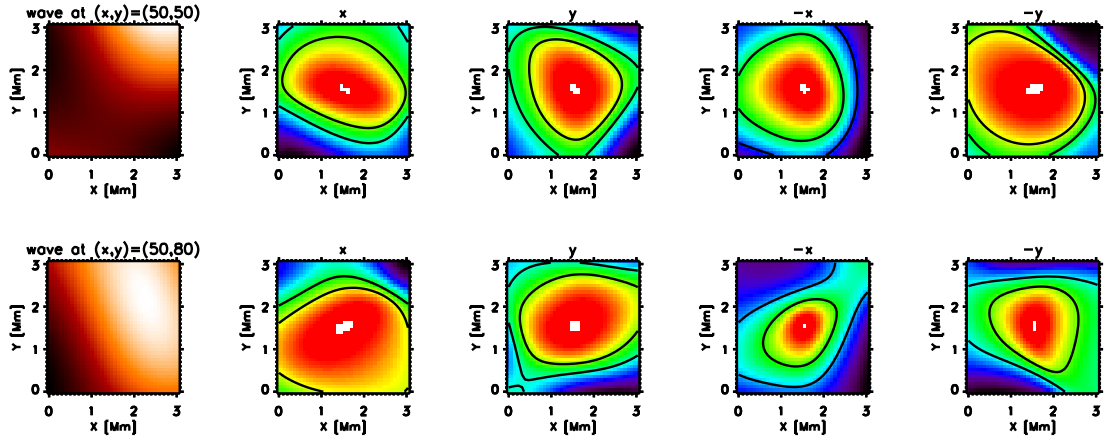

Figure 5.10 *Left*: Sample snapshots of the filtered wavefield around two certain points in the field of view. These are the running difference intensity images in Ca II H. *Others*: Distribution of correlation, c, in the direction of $\boldsymbol{x}$, $\boldsymbol{y}$, $-\boldsymbol{x}$, and $-\boldsymbol{y}$. The contour levels are 0.2 and 0.5. Red indicates higher correlation, while blue indicates lower correlation. Top and bottom rows show different positions in the field of view.

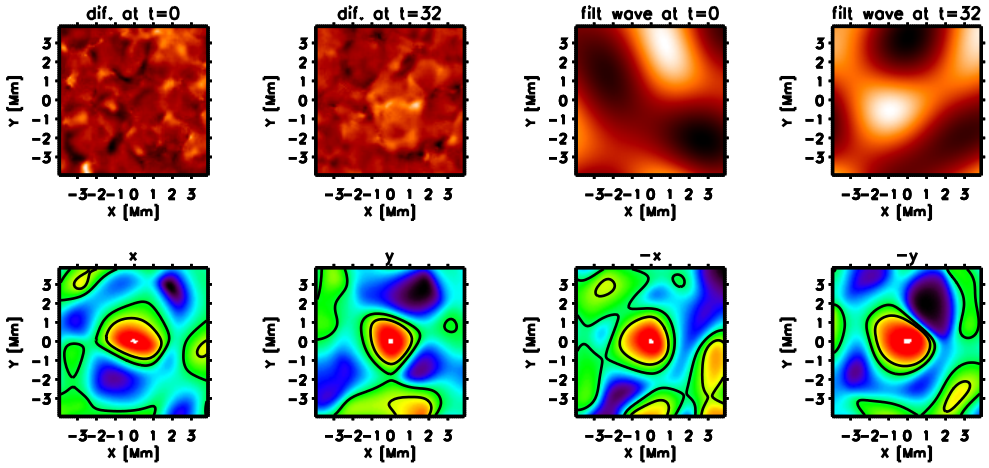

Figure 5.11 *Top*: Sample running difference intensity images in Ca II H without filters (first and second columns) and sample snapshots of the filtered wavefield (third and fourth columns). *Bottom*: Distribution of correlation, c, in the direction of $\boldsymbol{x}$, $\boldsymbol{y}$, $-\boldsymbol{x}$, and $-\boldsymbol{y}$. Red indicates higher correlation, while blue indicates lower correlation. The contour levels are 0.2 and 0.5.

5.4 Applications

In this section, we discuss applications of the statistical study we described in the previous sections.

5.4.1 Forward modelling of cross-correlation functions

Equations (5.24) and (5.25), expressions for ensemble averages for the cross-correlation function and its variance, enable us to model cross-correlation functions for a given power spectrum, P. Here we show two examples of the forward modelling.

One example of the forward modelling of cross-correlation function is shown in Figure 5.12. We mimic a f-mode power spectrum and construct an artificial two-dimensional power spectrum, $P(k, \omega)$, as shown in panel (a1). The power spectrum is exactly symmetric, i.e., it is for an isotropic wavefield. Using Equations (5.19) and (5.23), we obtain the cross-correlation function expected, $< C(\Delta, \tau) >$, and the square root of variance, $\sqrt{< CC > - < C >^2}$: Panels (a2) and (a3) are cuts of $< C(\Delta, \tau) >$ and $\sqrt{< CC > - < C >^2}$ at a specific value of Δ ($\Delta = 100$). To model the amplitude suppression of outward components around active regions, we modified the power spectrum to what is shown in panel (b1). In this power spectrum, the components which propagate in the $-x$ direction is a half of the components which propagate in the $+x$ direction. A cut of the cross-correlation function and a cut of the square root of the variance is shown in panels (b2) and (b3), respectively. The amplitude in the positive τ domain is larger than the amplitude in the negative τ domain. It is also noted that the variance remains essentially constant over the range of τ, and is smaller than in the isotropic case.

For another test for the forward modelling, we compare the cross-correlation functions derived from three-dimensional filtered/non-filtered wavefield and show how the filter works.

Figure 5.13 shows the power spectra and cross-correlation functions used for this test. They are (Figure 5.13, top row) the oscillation powers averaged over all the azimuthal direction in Fourier domain. We based them on the power spectrum in Ca II H obtained by SOT on December 04, 2007, which are used in the analyses in Chapter 4. To make the wavefield isotropic, we averaged the power in azimuthal direction, and made three-dimensional power distribution using the averaged power, by replacing each azimuthal component with the azimuthal average. Applying phase-speed filters for the rays whose skip angle is about 15 Mm to the power, we made a filtered power spectrum shown in panel (b), in the second column,

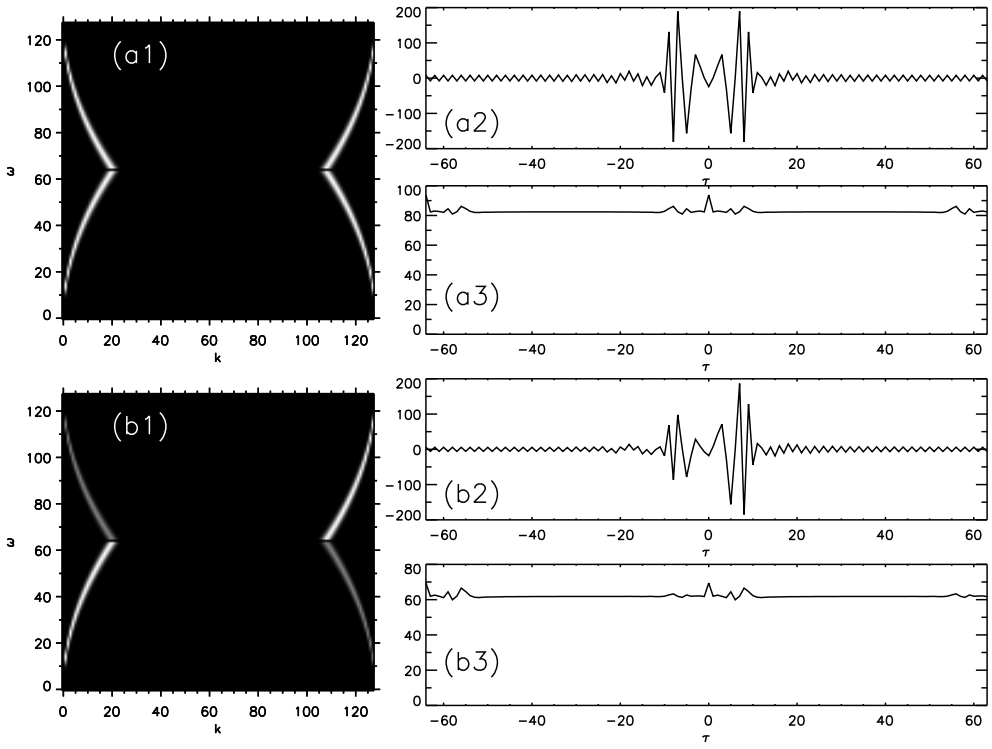

Figure 5.12 An example of forward modelling of cross-correlation function. In the left column, artificial power spectra are shown: (a1) is for an isotropic wavefield and (b1) is for a non-isotropic wavefield. White indicates higher power, and the darker colour indicates the lower power. In the right column, cross-correlation functions are in panels (a2) and (b2) and their standard deviations are shown in panels (a3) and (b3).

in the figure. In the analyses in Chapter 4, we used a filter to remove f modes and an ω filter as well. The power spectrum for the wavefield with those filters are shown in panel (c), in the third column. The expectation value of cross-correlation functions obtained by Equation (5.24) for these wavefields are shown in the second row. Since the wavefields are isotropic, only a cross-section for a direction ($+x$ direction) is shown. The cross-sections of the cross-correlation functions at the distance Δ of 15 Mm are in the third row. The wavepackets in the cross-correlation functions of the filtered wavefields are broader, because the filtered power concentrated in a narrower range in Fourier (ω) domain.

The square roots of the variance of the cross-correlation functions are shown in the bottom row in Figure 5.13. These are derived from Equation (5.25). Note that the filtered wavefield has less power in total, and the amplitude of the wavepacket itself is smaller

in the filtered wavefield. The 'noise' is more than ten times as large as the amplitude in the non-filtered wavefield, while in the filtered wavefields, it is 2-3 times as large as the amplitude only. In this example, the noise level is the lowest in the wavefield with f-mode and ω filters as well as a phase-speed filter. Hence, we have confirmed how the filters work to reduce the noise level by applying filters to power spectrum. Since filters normally make the wavepackets broader, however, we have to take into account the trade-off between the noise level and the broadness of the wavepacket in time-distance analyses.

In this way, the formulation described in this chapter enables us to carry out forward modelling of the cross-correlation functions and their variances.

5.4.2 Estimation of errors in the travel times

In the time–distance method, we use travel times to investigate the subsurface structure, and the travel times are calculated from the cross-correlation functions. Therefore, by considering error propagations, we can estimate the error of the travel times, using the error of cross-correlation functions.

Gizon & Birch (2004) discussed noise estimation of travel times. Since in their definition, the travel times are computed from the linear combination of cross-correlation functions, estimating the error propagation is rather straightforward.

To estimate the error in the travel times calculated by fitting a Gabor-wavelet function to the cross-correlation function (Kosovichev & Duvall 1997), we use the error of cross-correlation function in the fitting process. As we mentioned in §4.3, we determine the parameters by applying a nonlinear least-squares fitting method.

Let us consider fitting the observed cross-correlation function, $C(\tau)$, for a specific Δ by a Gabor-wavelet:

$$G(\tau; \boldsymbol{a}) = a_1 \cos(a_2(\tau - a_3)) \exp\left[-\left(\frac{a_4}{2}(\tau - a_5)\right)^2\right], \tag{5.38}$$

where $\boldsymbol{a} = (a_1, a_2, \ldots, a_5)$ is the fitting parameters. The best fitting parameters should minimize the merit function

$$\chi^2(\boldsymbol{a}) = (C(\tau_i) - G(\tau_i; \boldsymbol{a}))\, \mathcal{Q}_{ij}\, (C(\tau_j) - G(\tau_j; \boldsymbol{a}))\,, \tag{5.39}$$

where $\mathcal{Q} = E^{-1}$, and E is the covariance matrix:

$$E_{ij} = < C(\tau_i)C(\tau_j) > - < C(\tau_i) >< C(\tau_j) > . \tag{5.40}$$

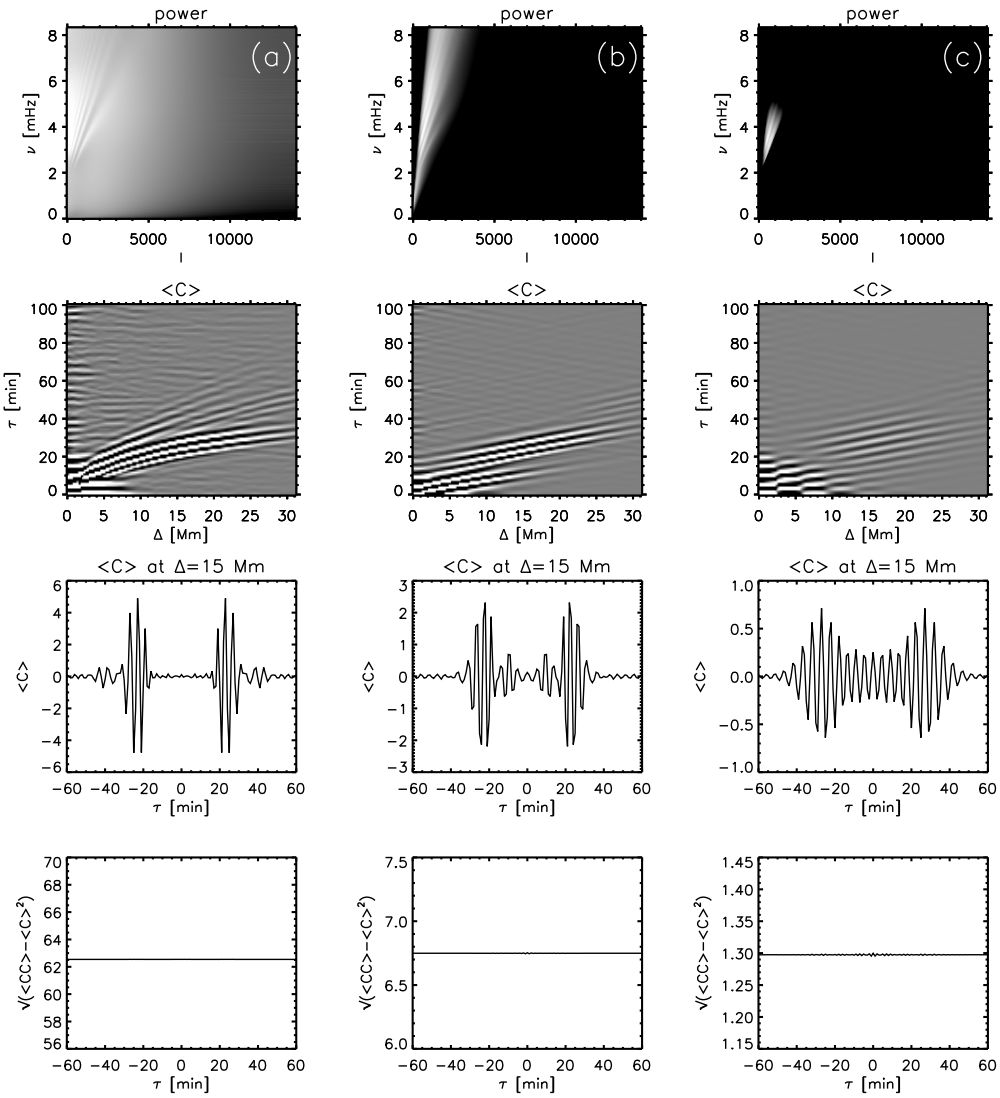

Figure 5.13 Comparison of the cross-correlation functions for wavefields with different filtering. The left, middle, and right columns are for a raw wavefield (a), a wavefield with a phase-speed filter (b), and a wavefield with phase-speed, f-mode, and ω filters (c), respectively. In each rows, the power spectra in logarithmic grayscaling (top), the cross-correlation functions, or the time-distance diagrams (second), the cross-correlation functions at $\Delta = 15$ Mm (third), and the standard deviations at $\Delta = 15$ Mm (bottom) are shown. Note that the cross-correlation functions and the standard deviations are expectation values and derived from Equations (5.24) and (5.25).

If $C(\tau)$ at different data points are uncorrelated, i.e., the covariance E is a diagonal matrix, Equation (5.39) is reduced to

$$\chi^2(\boldsymbol{a}) = \sum_{i=1}^{N} \left(\frac{C(\tau_i) - G(\tau_i; \boldsymbol{a})}{\sigma_i} \right)^2, \tag{5.41}$$

where ${\sigma_i}^2 =< C(\tau_i)^2 > - < C(\tau_i) >^2$ is the variance of each $C(\tau_i)$. In §4.3, we used $\sigma_i = \sigma$ for all the data points, i. Now that we can obtain σ_i due to the stochastic excitation modelling of the solar oscillations, we can use the estimates to improve the fitting method. Actually, as we discussed in §5.2.6, σ_i is almost independent on i, however, under the assumption in the model (§5.2.1). Hence, it turns out that our fitting method with constant σ was not so bad.

Finally, the covariance of the fitted parameters, $\mathcal{V}$, can be calculated using the formula

$$\mathcal{V} = \left[\frac{\partial^2 \chi^2}{\partial a_k \partial a_l} \right]^{-1}. \tag{5.42}$$

Note that this expression is from the Cramer-Rao bound.

5.4.3 Test of anisotropy of the cross-correlation function

From Equations (5.24) and (5.25), we obtain intrinsic dispersion of cross-correlation functions which results from the stochastic excitation process of the solar oscillation. Therefore, we can measure significance of differences between the cross-correlation functions. For example, we may test if anisotropy exists in the cross-correlation function by comparing the cross-correlation functions for different directions. Although we expect that magnetic fields may cause anisotropy of wave propagation, such an anisotropy has never been observationally reported.

Chapter 6

Supergranulation in the Polar Region of the Sun

In this chapter, we study supergranulation in the polar region of the Sun by local helioseismology. We observe the polar regions by *Hinode*/SOT and carry out travel–time analyses. The observation details are in §6.2. In §6.3, we briefly introduce our analysis method, including the projection calibrations. Next, we carry out inversion of the subsurface flow; the inversion method is presented in §6.4. As is shown in §6.5, we have found 'alignment' of the supergranular cells characteristic in the polar region, and discuss what it might mean (§6.6). We are attempting to investigate meridional flows and rotation profiles in the polar region as well; in §6.7 we discuss our future work on polar dynamics, showing a preliminary inversion result of such flows.

6.1 Introduction

There are various flows present in the Sun: convection, differential rotation, and meridional circulation. It is important for us to understand the solar interior dynamics, as it is believed to be playing crucial roles in the solar activity through dynamo processes. The interior dynamics has not been fully investigated from the observational point of view, especially in the polar region, because of the difficulty in observing the polar region from the earth due to foreshortening. However, the high-resolution of *Hinode*/SOT enables us to observe the polar region with "moderate" resolution. Hence, we investigate the polar region dynamics using the local helioseismology technique and SOT observation datasets.

6.1.1 Supergranulation

It has been pointed out that the behaviour of the supergranular convection in the polar regions may differ from that in the low-latitude regions, because of the difference in the way the Coriolis force affects the flow (Duvall & Gizon 2000).

The outer 30% of the Sun is a convection zone where the energy is transported mainly by convective motion of plasma. The Sun shows convective patterns in several scales on the surface. The clearest pattern is that of granules with a typical size of 1 Mm. Granular cells are clearly seen all over the Sun when we observe the Sun in photospheric lines. Another distinct pattern is due to supergranules, whose cells are typically $20 - 30$ Mm in diameter. Supergranules were first discovered by Hart (1954). They measured the line-of-sight surface velocity on the Sun and found velocity variation with a typical amplitude of 0.3 km s^{-1} with a spatial scale of 75 Mm. The velocity variation initially was not interpreted as convective patterns, but later Leighton et al. (1962) interpret them in connection with convection, based on their observations. Between the scales of granules and supergranules, mesogranules (November et al. 1981) with spatial scale of $5 - 10$ Mm have been reported, although they have not been confirmed beyond doubt. The largest convection cells expected, which extend to the entire depth of the convection zone, are called giant cells and the spatial scale of them is $\sim 10^2$ Mm. This scale of cells are more strongly affected by solar rotation than the smaller-scale cells. There is no conclusive observational evidence of giant cells, however. Convective cells of giant-cell scale are discussed based on numerical simulations by several authors (e.g., Brun & Toomre 2002; Miesch et al. 2006).

Hathaway et al. (2000) reported on a measured power spectrum for the cellular photospheric flows in the full-disc *SOHO*/MDI data. The spectrum shows a prominent peak at $l \sim 120$ which corresponds to the supergranular scale, although there was no obvious peak around $l \sim 600$ for the mesogranular scale or $l \sim 30$ for the giant-cell scale. The highest degree (wavenumber) they resolved with the MDI dataset was $l \sim 1000$, which was insufficient for resolving the granular scale. Figure 6.1 shows an example of a power spectrum obtained by *Hinode*/SOT. We use a 12-hr observation dataset with (chromospheric) Ca II H line taken on 23 November 2007, which is used in Chapter 4. Although we cannot identify the lower-wavenumber peaks due to the limit of the field of view of SOT, we detect the peak around $l \sim 2500$ which is for the granular scale.

What determines these discrete convective scales in the Sun is not clear. Simon &

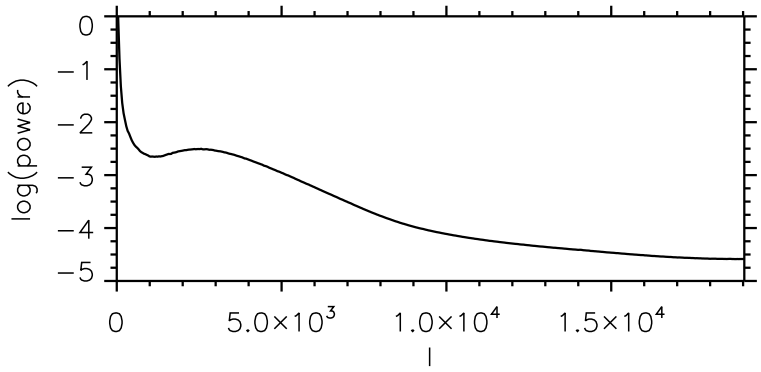

Figure 6.1 Power spectrum of the Ca II H intensity dataset obtained by *Hinode*/SOT. The total power for each l is shown in arbitrary unit.

Leighton (1964) suggested He ionization zone produces the supergranular cells. The He II ionization zone lies at a depth of 20 Mm, which is of the same order as the typical horizontal extent of supergranular cells, while the He I ionization zone lies at a depth of $2 - 7$ Mm. Stein et al. (2007) reported from their numerical simulation that power enhancement was not found for the convective components of the supergranular scale if there is no magnetic field. They carried out numerical simulations of a surface convection including the effect of ionization and radiative heating/cooling and suggested that the balance between the magnetic emergence rate and the sweeping rate of the magnetic elements by supergranular motion causes the pile-up of the magnetic flux density in the magnetic network, and results in the power excess in the scale of supergranules.

Convection cells of supergranulation scale have not been reconstructed very well in the more global simulation of convection zone either, except in a shallow spherical shell study (De Rosa et al. 2002). The cells resolved in global numerical simulations of turbulent convection are in a giant-cell scale. According to recent numerical simulations of turbulent convection (e.g., Brun & Toomre 2002; Miesch et al. 2006), the convective cells in the lower latitude region align parallel to the rotation axis. They refer to these cells as banana cells. In the higher-latitude region, the structure of the cells looks more complicated.

Lisle et al. (2004) found the alignment of supergranular cells within 60 degrees in latitude observationally and suggested that the alignment is of a giant cell origin; the convergent flows at giant cell boundaries, i.e., banana-cell boundaries, render the supergranular cells aligned.

There are lots of mysteries around supergranules: the rotation rate of supergranular pattern appears to be faster than the magnetic features (Hathaway 1982; Snodgrass & Ulrich 1990; Duvall & Gizon 2000). Also, supergranulation is suggested to be interpreted as the superposition of travelling waves (Gizon et al. 2003). For a recent discussion about supergranulation, see Rast (2003).

In this work, we would like to investigate the supergranular structures in the polar region, the knowledge of which is most insufficient in the study of the supergranulation.

6.2 Observation

SOT observed the polar region in the southern hemisphere on 9 March, 2009, and in the northern hemisphere on 25 September, 2009. Since the absolute value of the B_0 angle of the Sun, the heliographic latitude of the disc centre, attains its maximum (about 7 degree) in March and September every year, we can observe the region at the highest latitude best in these periods. For comparison, we also obtained datasets of a region close to the east limb on 27 September, 2009, and a region on the disc centre on 11 December, 2009. All the observing periods are 16 hours. We obtained the Ca II H line intensity maps as well as the Fe I 557.6 nm intensity maps. Since the field of view of Fe line maps obtained by NFI is broader than that of Ca line maps obtained by BFI, we include the solar limb within the NFI field of view and use the limb for tracking the images and determining the coordinate on the Sun. We used the Ca II H line intensity maps for time–distance helioseismology analyses. A set of sample images from the north polar region observation is shown in Figure 6.2.

6.3 Data Analysis Process

For the travel-time analyses, first we tracked the images obtained by SOT. Next, we chose several points on the Sun within the SOT field of view, as projection centres for Postel's projection. Using the projected images, we carried out the travel-time analysis for detecting subsurface flow structure in the observed region.

6.3.1 Tracking

The SOT observations of the region close to the limb were carried out with fixed pointings. Although the image stabilization system (CT) was on during the observations,

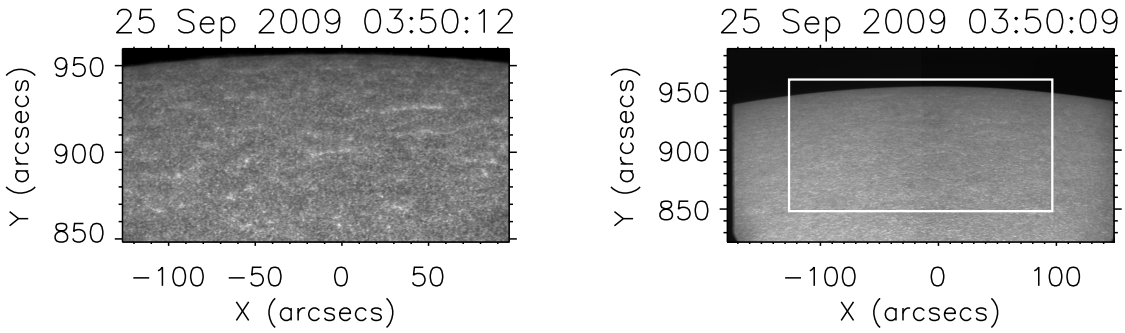

Figure 6.2 Sample snapshots from the north polar region observation on 25 September 2009. *Left*: Ca II H intensity map. *Right*: Fe I 557.6 nm intensity map. The white box in the right panel indicates the field of view of the left panel.

the field of view was gradually drifting toward the disc centre mainly due to the limb darkening. Therefore, we need to track the image by ensuring that the limb stays in the same position in the field of view.

The tracking process is as follows:

1. First, we generate two-value maps for NFI Fe I 557.6 nm intensity dataset. We define the limb as the extremum of intensity gradient, and any pixel outside the limb is given the value of 0 and any pixel inside the limb is given the value of 1.

2. Second, we measure the shift of a two-value map from the map taken at the beginning of the observation period by calculating the correlation between two frames.

3. We shift the images so that the limb is fixed in the field of view.

4. Next, we track the Ca II H intensity dataset using the shift measured by the Fe I dataset.

5. We measure the coordinate of the central point of the field of view using the solar limb in the first frame of Fe I image and determine the coordinate of the central point of Ca II H image taking the offset between images with two wavelength into account.

6. Finally, we track the rotation using the Snodgrass rate (Snodgrass 1984):

$$\frac{\Omega}{2\pi}\ [\mathrm{nHz}] = 451 - 55\sin^2\lambda - 80\sin^4\lambda, \tag{6.1}$$

where Ω is angular speed of the differential rotation of the Sun and λ is the latitude on the Sun. We track the projection centre with this rate.

Note that for the disc centre dataset, we did not apply these tracking; SOT observed the disc centre region tracking with the rotation rate of the Sun, and we used the tracked data for analyses.

6.3.2 Postel's projection

Since the Sun is spherical in shape, the images taken by any telescopes are maps of the Sun projected to planes. When we observe the Sun near the limb, foreshortening is significant, and appropriate remapping is required for time–distance analysis.

We used Postel's azimuthal equidistant projection (e.g., Bogart et al. 1995; Zaatri et al. 2008). The centre of projection is defined in the heliocentric latitude, θ_0, and longitude, ϕ_0. In the projected map, the Cartesian coordinates of the map are denoted by (X, Y), where X and Y are normalized by the solar radius. Note that the origin of the coordinate, $(X, Y) = (0, 0)$, is at the centre of the projection. The heliocentric coordinates (θ, ϕ) corresponding to the points (X, Y) on the projected map are then

$$\theta = \arcsin\left(\cos\Theta\sin\theta_0 + Y\frac{\sin\Theta\cos\theta_0}{\Theta}\right) \tag{6.2}$$

$$\phi = \phi_0 + \arctan\left(\frac{X\sin\Theta}{\Theta\cos\theta_0\cos\Theta - Y\sin\theta_0\sin\Theta}\right), \tag{6.3}$$

where Θ is the angular distance from the centre of the field of view (θ_0, ϕ_0) to the point (X, Y):

$$\cos\Theta = \sqrt{X^2 + Y^2} = \sin\theta_0\sin\theta + \cos\theta_0\cos\theta\cos(\phi - \phi_0). \tag{6.4}$$

The field of view of the observation in Ca II H line of the north pole is indicated by a box in Figure 6.3. In the North polar observation case, we chose three points indicated by asterisks in Figure 6.3, and made three projected maps whose fields of view correspond to the skyblue, green, and orange areas in the figure. As for the south polar observation, we chose three points in the same manner, while in the case of East limb observation, we chose two points as the projection centres.

In fact, this projection is required regardless of location on the Sun; the distance on the image obtained by SOT is distorted to some extent anywhere. For the dataset from disc

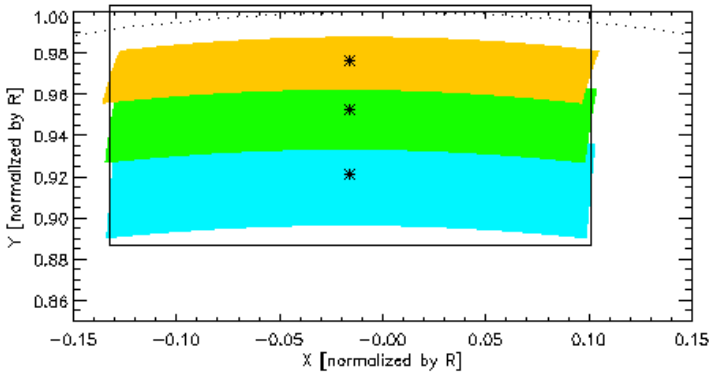

Figure 6.3 Polar region map for observation on 25 September 2009. The dotted curve indicates the solar limb, and the box indicates the field of view for the observation in Ca II H line.

centre observation, however, we did not project the images, because the effect is so small as will see below.

If the centre of the field of view is exactly on the disc centre, the west-most point in the SOT/BFI field of view is located 109 arcsec from the centre on the image. The angular distance between the centre and the west-most point is $\Theta \sim \arcsin(109"/960") \sim 0.114$ radian, where the solar radius in angle has been set to be 960". Therefore, the difference between the real distance on the Sun, $R_\odot\Theta$, and the distance on the image, $R_\odot \sin\Theta$, relative to the distance itself is estimated at $R_\odot(\Theta - \sin\Theta)/(R_\odot\Theta) \sim 2 \times 10^{-3}$, and we conclude that the effect is small enough to be ignored around the disc centre.

6.3.3 Travel–time analysis

Using the tracked and projected datasets, we calculate acoustic travel times based on the process described in §3.4. We measure the travel times by fitting the Gabor-type wavelet (see §3.4.3) and use the phase travel times.

The central radii of the annuli used are 5.4, 8.4, 11.3, 14.4, 17.6, 21.1, and 26.3 Mm, and they are referred to as from p1 (smallest) to p7 (largest).

6.4 Inversion

Using the ray-approximation kernels we attempt the inversion of the flows in the polar region. The inversion technique is based on Zhao (2004) and the inversion code was provided by Dr. Junwei Zhao.

6.4.1 Ray-approximation kernels and Multi-channel decomposition technique

In this study, we investigate the subsurface flow. As was mentioned in §3.4.5, under the ray approximation, the travel-time perturbation, $\delta\tau$, due to the perturbation flows are given by the form:

$$\delta\tau_{\mathrm{diff},i}(\boldsymbol{x'}) = \int d\boldsymbol{x}dz \sum_{\alpha} K^{v_\alpha,i}(\boldsymbol{x},z;\boldsymbol{x'})q_\alpha(\boldsymbol{x},z), \tag{6.5}$$

where α indicates the direction (x, y, or z) of each component of flows, q is the ratio of the flow to local sound speed, i.e., $q(\boldsymbol{x},z) = v_\alpha(\boldsymbol{x},z)/c(\boldsymbol{x},z)$, and $\boldsymbol{x}$ and z are the position in the Sun. The index i indicates the annulus size and/or the difference type, such as outward-inward, eastward-westward, and northward-southward.

Since the ray-approximation kernels, K, are transversally invariant, i.e.,

$$K^{v_\alpha,i}(\boldsymbol{x},z;\boldsymbol{x'}) = K^{v_\alpha,i}(\boldsymbol{x}-\boldsymbol{x'},z), \tag{6.6}$$

the Fourier transform of the travel-time perturbation, $\delta\tilde{\tau}$, is

$$\delta\tilde{\tau}_{\mathrm{diff},i}(\boldsymbol{k}) = (2\pi)^2 \int dz \sum_{\alpha} \tilde{K}^{*\ v_\alpha,i}(\boldsymbol{k},z)\tilde{q}_\alpha(\boldsymbol{k},z), \tag{6.7}$$

where

$$\tilde{q}_\alpha(\boldsymbol{k},z) = \frac{1}{(2\pi)^2}\int d\boldsymbol{x}q_\alpha(\boldsymbol{x},z)e^{-i\boldsymbol{k}\cdot\boldsymbol{x}} \tag{6.8}$$

$$\tilde{K}^{v_\alpha,i}(\boldsymbol{k},z) = \frac{1}{(2\pi)^2}\int d(\boldsymbol{x'}-\boldsymbol{x})K^{v_\alpha,i}((\boldsymbol{x'}-\boldsymbol{x}),z)e^{-i\boldsymbol{k}\cdot(\boldsymbol{x'}-\boldsymbol{x})}. \tag{6.9}$$

With Equation (6.7), we obtain the Fourier transform of the flow distribution, q, for each $\boldsymbol{k}$. Therefore, solving one-dimensional inversion is required to obtain Fourier component of the flow distribution.

This technique is called multi-channel deconvolution (MCD), and by this technique the three-dimensional inversion can be decomposed into a series of one-dimensional inversions.

6.4.2 Solving the 1-D inverse problems

Equation (6.7) is in the form of

$$\boldsymbol{t} = \mathcal{K}\boldsymbol{q} \tag{6.10}$$

for each $\boldsymbol{k}$, where

$$\boldsymbol{t} = \{\delta\tilde{\tau}_{\mathrm{diff,i}}(\boldsymbol{k})\} \tag{6.11}$$

$$\mathcal{K} = \{\tilde{K}^{v_x,i}(\boldsymbol{k}, z_j), \tilde{K}^{v_y,i}(\boldsymbol{k}, z_j), \tilde{K}^{v_z,i}(\boldsymbol{k}, z_j)\} \tag{6.12}$$

$$\boldsymbol{q} = \{\tilde{q}_x(\boldsymbol{k}, z_j), \tilde{q}_y(\boldsymbol{k}, z_j), \tilde{q}_z(\boldsymbol{k}, z_j)\}^{\mathrm{T}}, \tag{6.13}$$

and the matrix with a superscript T is the transpose of the original matrix. In this case, i indicates the annulus size (7) and the type of the travel-time difference (3). Therefore, the column vector $\boldsymbol{t}$ has $7 \times 3 = 21$ components for each $\boldsymbol{k}$. The column vector $\boldsymbol{q}$ has $3 \times 7 = 21$ components: three-dimensional components of velocity for each depth z_j, where $1 \leq j \leq 7$. The square matrix $\mathcal{K}$ has $(3 \times 7)^2 = 441$ components for each $\boldsymbol{k}$. To obtain the flow field $q_\alpha(\boldsymbol{x}, z) = v_\alpha(\boldsymbol{x}, z)/c(\boldsymbol{x}, z)$, we calculate a Fourier transform of $\tilde{q}_\alpha(\boldsymbol{k}, z_j)$ for $n_x \times n_y$ $\boldsymbol{k}$. In our case, $n_x = 256$ and $n_y = 128$.

If we use LSQR algorithm which is one of the standard algorithms to solve such equations, we have to handle a matrix of a huge size because we have to solve a three-dimensional inversion all at once. Therefore, to solve Equation (6.5) which is in a matrix form

$$\delta\tau^{\lambda\mu\nu} = \sum_{ijk} K^{\lambda\mu\nu}_{ijk,\alpha} q_{ijk,\alpha}, \tag{6.14}$$

we need to handle two-dimensional matrix, $\mathcal{K}$, whose size is $3n_xn_yn_z \times 21 = 3(128)^2 \cdot 7 \times 21$. Compared to the calculation involving the huge matrix, MCD has an advantage in having to handle (at once) matrices of a smaller size.

To solve Equation (6.10) obtained by MCD, we adopt the regularized least-squares fitting. The 'solution' $\boldsymbol{q}$ which is obtained by the straight least-squares fitting would minimize the badness of the fitting E:

$$E = (\boldsymbol{t} - \mathcal{K}\boldsymbol{q})^+(\boldsymbol{t} - \mathcal{K}\boldsymbol{q}) = \sum_i \left({t_i}^* \sum_j {\mathcal{K}_{ij}}^* {q_j}^* \right) \left(t_i \sum_{j'} \mathcal{K}_{ij'} q_{j'} \right) \tag{6.15}$$

where the superscript + indicates the Hermitian conjugate, and t_i is the ith component of $\boldsymbol{t}$. Instead, here we minimize Φ:

$$\Phi(\boldsymbol{q}) = (\boldsymbol{t} - \mathcal{K}\boldsymbol{q})^+(\boldsymbol{t} - \mathcal{K}\boldsymbol{q}) + \alpha(L\boldsymbol{q})^+(L\boldsymbol{q})$$

$$= \sum_i {t_i}^* \sum_j {\mathcal{K}_{ij}}^* {q_j}^* t_i \sum_{j'} \mathcal{K}_{ij'} q_{j'} + \alpha \sum_i \sum_j {L_{ij}}^* {q_j}^* \sum_{j'} L_{ij'} q_{j'}, \qquad (6.16)$$

where α is a scalar parameter and L is a matrix chosen according to our prejudice that $|L\boldsymbol{q}|^2$ is small. The derivative $\partial\Phi/\partial q_m$ is equal to zero when Φ attains its minimum. Hence, we have

$$\left.\frac{\partial\Phi}{\partial q_m}\right|_{\boldsymbol{q}^{\rm est}} = \sum_i ({t_i}^* - \sum_j {\mathcal{K}_{ij}}^* {q_j^{\rm est}}^*)(-\mathcal{K}_{im}) + \alpha \sum_i \sum_j {L_{ij}}^* {q_j^{\rm est}}^* L_{im} = 0, \qquad (6.17)$$

and in the matrix form,

$$(\mathcal{K}^{\rm T}\mathcal{K}^* + \alpha L^{\rm T} L^*)\boldsymbol{q}^{\rm est *} = \mathcal{K}^{\rm T}\boldsymbol{t}^*. \qquad (6.18)$$

If the inverse matrix of $(\mathcal{K}^{\rm T}\mathcal{K}^* + \alpha L^{\rm T} L^*)$ is available, we have

$$\boldsymbol{q}^{\rm est} = (\mathcal{K}^+\mathcal{K} + \alpha L^+ L)^{-1}\mathcal{K}^+\boldsymbol{t}. \qquad (6.19)$$

Note that we take the complex conjugate of the equation. This is the solution obtained by the regularized least-square fitting.

In this calculation, we set

$$\alpha = \varepsilon^2 \qquad (6.20)$$

$$L^+L = V = \begin{pmatrix} 1 & 0 & 0 & \dots & 0 \\ 0 & c_2/c_1 & 0 & \dots & 0 \\ \vdots & & \ddots & & \vdots \\ 0 & \dots & 0 & c_{n-1}/c_1 & 0 \\ 0 & \dots & 0 & 0 & c_{n_z}/c_1 \end{pmatrix}, \qquad (6.21)$$

where ε is a damping parameter and c_i $(i = 1, 2, \dots n_z = 7)$ is the sound speed in ith layer in depth. Hence, the solution is given by

$$\boldsymbol{q}^{\rm est} = (\mathcal{K}^+\mathcal{K} + \varepsilon^2 V)^{-1}\mathcal{K}^+\boldsymbol{t}. \qquad (6.22)$$

This is a damped least-squares solution. If ε is 0, this equation is for the least-squares fitting. However, in practice, since the problems are ill-posed, there are infinite numbers of solutions for the least-squares fitting (Equation 6.15). For a smaller ε, error is large while resolution is fine. For larger ε, resolution is large, while error is poor, We need to choose a reasonable value for the parameter, ε, through a trial and error process.

Figure 6.4 shows averaging kernels for the horizontal flow-speed inversion. Averaging kernel indicates the sensitivity variation in depth for the flow. When the parameters estimated by the inversion are written in the form of

$$\boldsymbol{q}^{\rm est} = \mathcal{R}\boldsymbol{t} \tag{6.23}$$

as in Equation (6.22), where $\mathcal{R} = (\mathcal{K}^{+}\mathcal{K} + \varepsilon^2 V)^{-1}\mathcal{K}^{+}$, we have

$$\boldsymbol{q}^{\rm est} = \mathcal{R}\mathcal{K}\boldsymbol{q} \tag{6.24}$$

using Equation (6.10). In integral form, using

$$t_i(\boldsymbol{k}) = \int dz \mathcal{K}_i(\boldsymbol{k}, z) q(\boldsymbol{k}, z) + e \tag{6.25}$$

$$q^{\rm est}(\boldsymbol{k}, z_0) = \sum_j \mathcal{R}_j(\boldsymbol{k}, z_0) t_j(\boldsymbol{k}) \tag{6.26}$$

we have

$$q^{\rm est}(\boldsymbol{k}, z_0) = \sum_j \int dz \mathcal{R}_j(\boldsymbol{k}, z_0) \mathcal{K}_j(\boldsymbol{x}, z) q(\boldsymbol{k}, z) + e' \tag{6.27}$$

$$= \int dz D(\boldsymbol{k}, z_0; z) q(\boldsymbol{k}, z) + e'. \tag{6.28}$$

The D in this equation is the averaging kernel, which relates the estimate $q^{\rm est}$ to the 'true' function q.

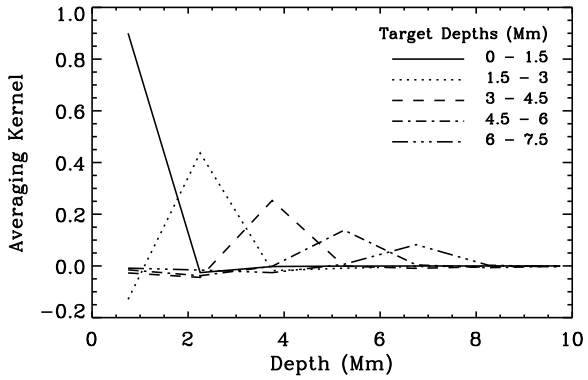

Figure 6.4 Averaging kernels as a function of depth obtained from horizontal flow-speed inversion. Courtesy of Dr. Junwei Zhao.

6.5 Results

6.5.1 Travel-time maps

Outward–inward travel-time difference maps of the north polar region datasets are shown in Figure 6.5. The names, top, middle, and bottom, in the title of the panels indicate the yellow, green, and blue regions in Figure 6.3, respectively. The black region where the outward travel times are shorter than the inward travel times indicates the region with diverging flow, while the white region indicates the region with converging flow. There are $\sim$ 30-Mm size dark cells with white boundaries; they are supergranular cells. In the maps for larger annuli, especially for p6 and p7, the supergranular patterns are rather faint. Judging from the depths of these rays (see Figure A.3), this would lead to indication that the supergranules are not deeper than, say, 5 Mm, which is consistent with our inference based on inversions (see §6.5.2).

Figure 6.6 shows the outward–inward travel-time difference maps for the annulus of 14.4 Mm radius (p4), which clearly show the supergranular patterns, for the north and south polar-region datasets. The projected travel-time maps of the three regions in Figure 6.3, namely, the three panels in the 4th row in Figure 6.5, are combined into a single map, which is shown in the left panel in Figure 6.6. Figure 6.7 shows those for the east limb dataset. Note that the travel times in the region close to the edge of the field of view are noisy, because some part of the annulus around the point in the region is outside the field of view and we cannot calculate the cross-correlation function averaged over the annulus properly.

The supergranular patterns in both the polar regions and the east limb region are clearly seen in the way similar to Figure 4.2 in Chapter 4. In the higher-latitude region, however, the cells seem to align in the northeast-southwest direction. The 'alignment' pattern seems to exist both in north and south polar regions. There also seem to be areas with weak diverging flows between the aligned cells. However, in the below, we refer to this structure simply as 'alignment'. The alignment seems to be coherent for a few-cell distance.

6.5.1.1 Correlation of the travel-time difference maps

To check if the 'alignment' is really there, we calculated two-dimensional correlation of the travel-time difference maps. Figure 6.8 shows the correlation functions. In the top and

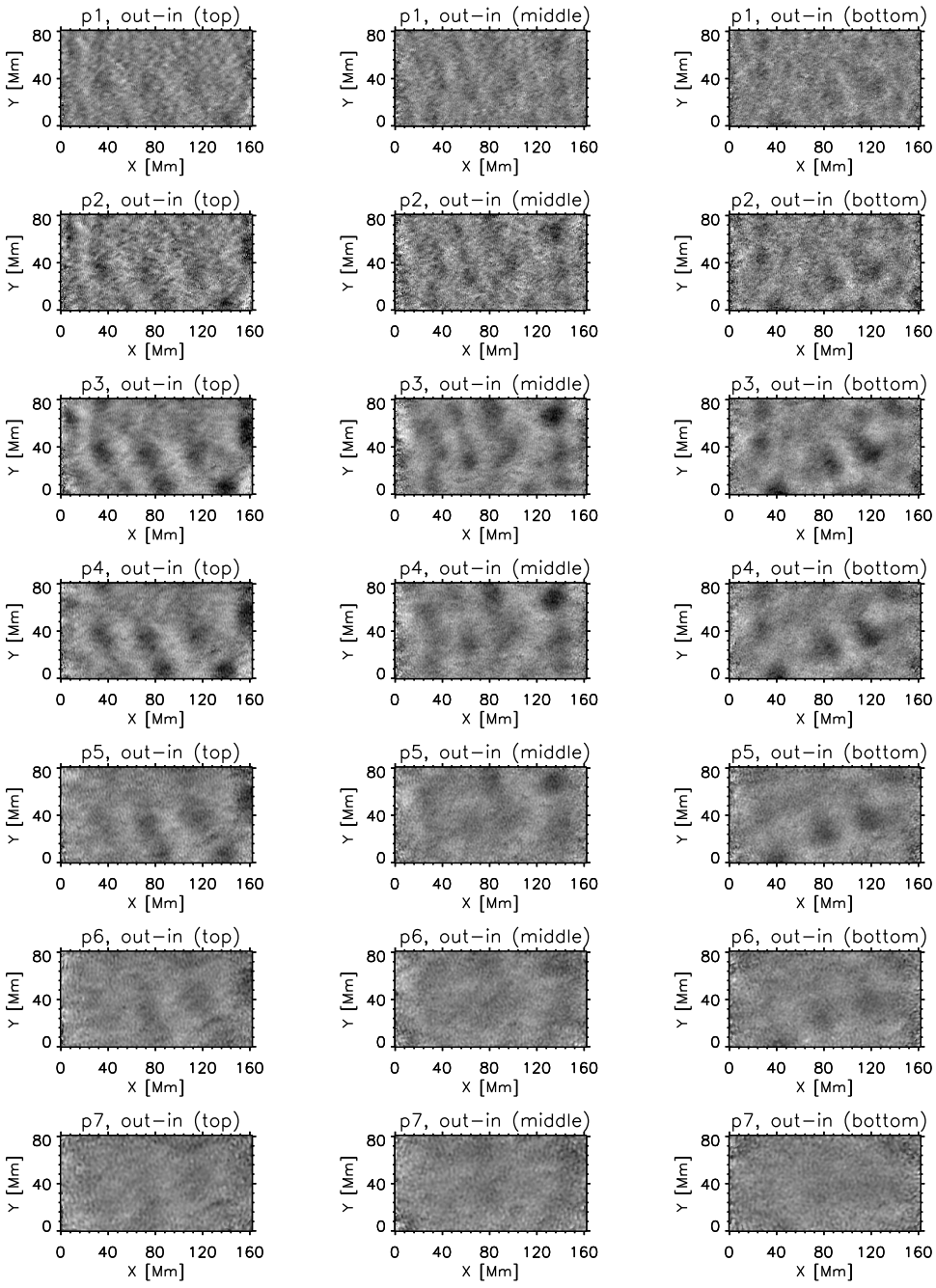

Figure 6.5 Outward–inward travel-time difference maps in the north polar region. The gray scale corresponds to the range from -1 minute to +1 minute. See text for the details.

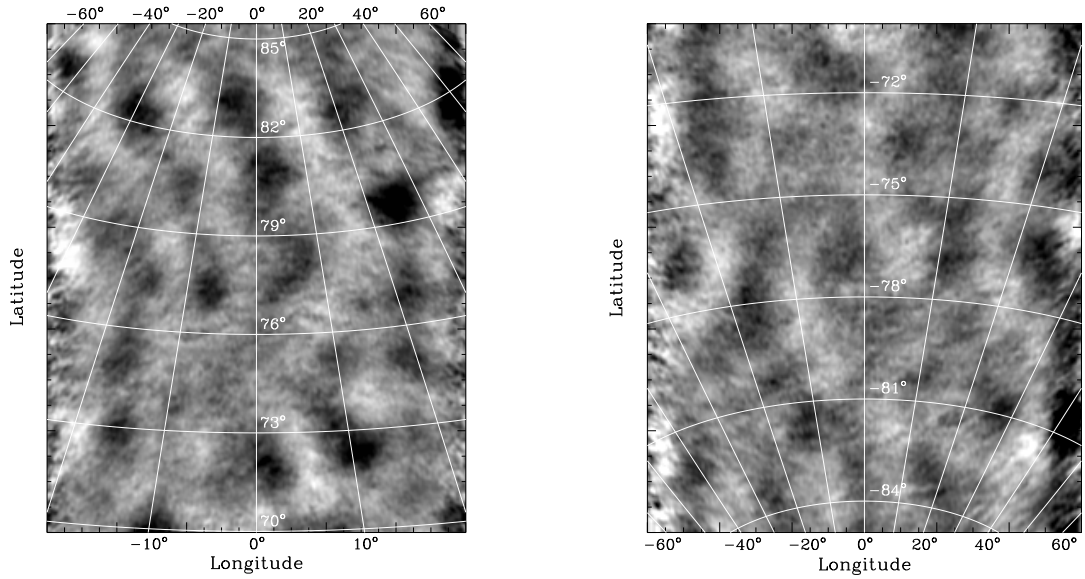

Figure 6.6 Outward–inward travel-time difference maps of the north pole dataset (left) and the south pole dataset (right). The grayscale indicates the range from -0.6 min to 0.6 min.

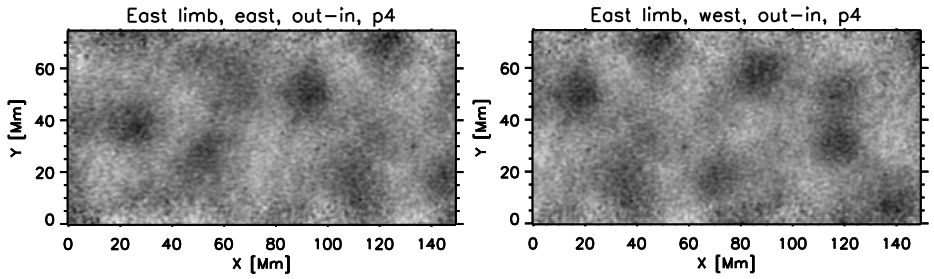

Figure 6.7 Outward–inward travel-time difference maps of the east limb dataset. The left panel shows the east-most part of the field of view where the central longitude is about 70°, and the right panel shows the west-most part of the field of view where the central longitude is about 60°. The right half of the left image and the left half of the right image are overlapped.

middle parts of the north polar region dataset, the correlations do show striking alignment, i.e., the correlation is large in a certain direction. On the other hand, around the disc centre the correlation shows no particular preference in direction, namely, nearly random distribution.

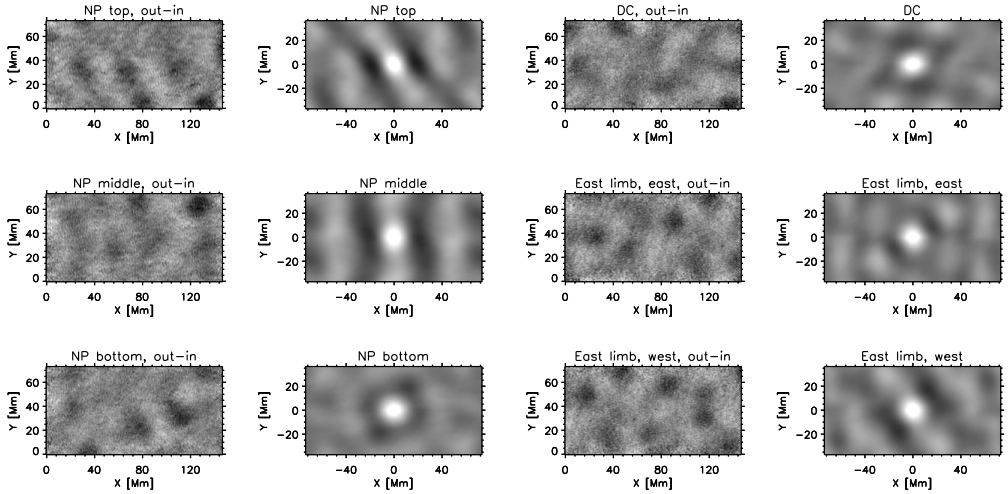

Figure 6.8 Travel-time difference maps (left) and two-dimensional correlation maps of the travel-time difference (right).

We may have to be cautious in interpreting the correlation distribution, however. In the west-most part of the east limb region, the correlation map apparently shows some alignment (see the lower-right panel in the figure), although on the close inspection on the travel-time maps the pattern is dissimilar to that in the north polar region. This warns us, however, that we should be careful in using the correlation in such a narrow field of view to infer alignment.

Let us suppose it is the north-south alignment. In this point of view, the inclination angle to the meridional line is 40° at most in the north polar region, and the alignment is rather in a northeast-southwest direction. The differential rotation may cause such alignment. By Snodgrass rate rotation (Snodgrass 1984, see Equation (6.1) in §6.3.1 in this thesis) the rotation speeds at the latitude of 85° and 80° are 1.39 and 1.41 km s^{-1}, respectively. A bar which drifts from the meridional line between these latitudes by the differential rotation will have an inclination angle of 2° after one lifetime of a supergranule, about a day, and after a month, which is the lifetime of the giant cells, the inclination angle will be

Table 6.1. Cell size in various regions

	North polar region			Disc centre	East limb region	
latitude / longitude	85° /0°	76° /0°	72° /0°	0°/0°	0°/70°	0°/60°
radius [Mm]	10.52	12.20	14.13	14.87	13.65	13.33

27°. Therefore, the inclination angle can be explained by the differential rotation, roughly speaking. However, in contrast to the north polar region, the alignment line in the south polar region is more vague, and the inclination angle is not so rigid. Therefore we speculate that the differential rotation is not the origin of the alignment angle.

The alignment may be of a giant cell origin. As was mentioned in §6.1.1, Lisle et al. (2004) reported that supergranular cells are aligned in north-south direction within 60 degrees in latitude where they investigated. They suggested it is of a giant cell origin, and the convergent flows at giant cell boundaries may be the cause of the alignment. According to recent numerical simulations of turbulent convection, the convective cell in the scale of giant cell ($\sim 10^2$ Mm) aligns parallel to the rotation axis in the lower-latitude region, but not in the higher-latitude region. We will return to this issue later (§6.6.2). If it is the case that the supergranular cells are located along the giant cell boundaries, the alignment should be roughly in the north-south direction, but the deviation from the direction may not be so important in high latitude. As far as we know, giant cells have never been observationally confirmed. Therefore, it is significantly important if this alignment is indeed of a giant-cell origin; further studies for confirmation of these features are urgent tasks for us.

The correlation in Figure 6.8 also shows us the cell size variation with the latitude. We define the cell size as the correlation length; the distance in x direction from the origin to the point where the correlation is down to zero in the correlation map. Table 6.1 shows the size of cells in the north polar region, the east limb region, and the disc centre. Cell size tends to be smaller in the higher-latitude region. Note that the 'size' mentioned here is measured along x direction only; the correlation maps (in Figure 6.8) show that the size along y direction, the direction of alignment, is slightly larger in the higher-latitude region. This may be related to the cell aligned largely in the y direction.

6.5.2 Subsurface supergranular flows

Figure 6.9 shows subsurface horizontal flows in the north polar region obtained by the inversion. These maps indicate the flow field with the average horizontal speed, namely, rotation and meridional flow, removed. The inversion was carried out in the three projected regions (see Figure 6.3) separately, and the results were combined into a single map.

The correlation coefficient of the horizontal flow field between each pair of two layers,

$$c_{h,ab} = \frac{\int \boldsymbol{v}_{\boldsymbol{a}h}(x,y) \cdot \boldsymbol{v}_{\boldsymbol{b}h}(x,y) dxdy}{\sqrt{\int |\boldsymbol{v}_{\boldsymbol{a}h}(x,y)|^2 dxdy} \sqrt{\int |\boldsymbol{v}_{\boldsymbol{b}h}(x,y)|^2 dxdy}}, \tag{6.29}$$

where $\boldsymbol{v}_{\boldsymbol{a}h}$ is the horizontal (x and y) flow field in the ath layer, are shown in Table 6.2. The correlation coefficient between the adjacent two layers are about 0.7 and that between the layers with depth interval of 3 Mm is down to 0.5, except for the deepest layer. Because of the small number of rays passing in the deepest layers and low sensitivity shown in the averaging kernels (Figure 6.4), we exclude the deepest layer with the depth of 6.75 Mm from this discussion. For comparison, the correlation coefficients for the disc centre dataset obtained on 1 Jan 2007 (Sekii et al. 2007) are shown in Table 6.3. The correlation coefficients around the disc centre apparently decrease more rapidly with depth than those in the north polar region, and this implies that the supergranular cells are shallower in the disc centre region.

The horizontal divergence, $\partial v_x/\partial x + \partial v_y/\partial y$, is calculated for each subsurface layer; Figure 6.10 shows the divergence maps. By comparing these maps with the travel-time map (Figure 6.6), one can identify the characteristic cell alignment in the higher-latitude region in these layers, too. Note that black indicates converging in this figure, while white indicates converging in Figure 6.6. This is another hint that the coherence of supergranular patterns last at least a few Mm deep.

We obtain the vertical component of the flow as well, although time-distance inversion is less sensitive to the vertical component of the flow field compared to the horizontal component. This is because the sensitivity is highest around the total reflection point of the ray path and around the point the ray is almost horizontal. Figure 6.11 shows the vertical component of the flow in the two shallower layers. Here we omit the maps for deeper layers because the signal is too weak. In the shallowest layer, the upflow region (white area in the map) corresponds to the region with diverging horizontal components. This is consistent with the flow field expected in convection cells.

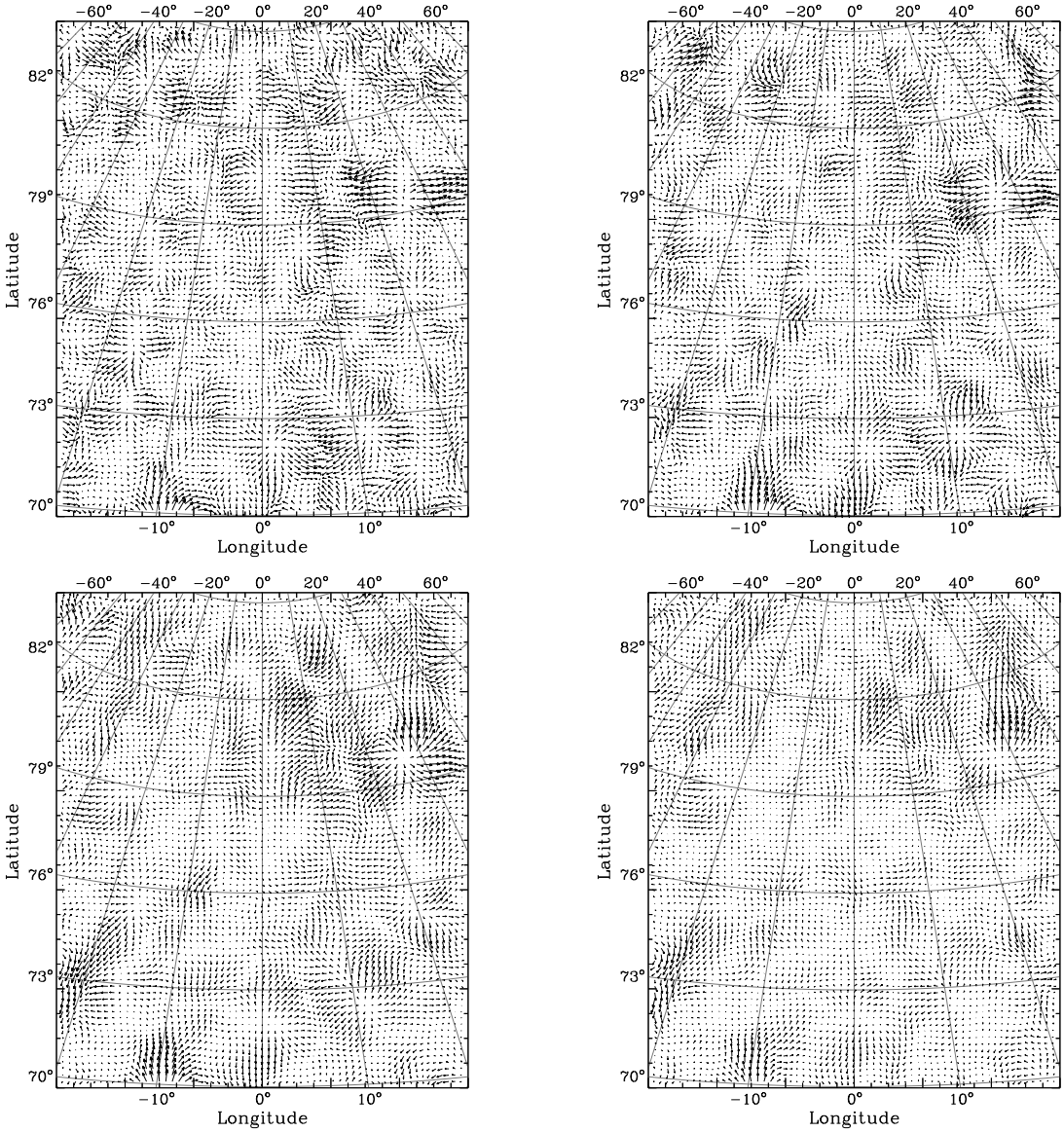

Figure 6.9 Subsurface horizontal flows in several layers in depth for the north polar region. Depths for each panel are 0.75 Mm (upper left), 2.25 Mm (upper right), 3.75 Mm (lower left), and 5.25 Mm (lower right). The longest arrow in each panel corresponds to 4.1×10^{-2}, 3.8×10^{-2}, 3.1×10^{-2}, and 1.9×10^{-2} times the local sound speed at the depth (7.94, 11.84, 14.46, and 17.02 km s^{-1}, respectively).

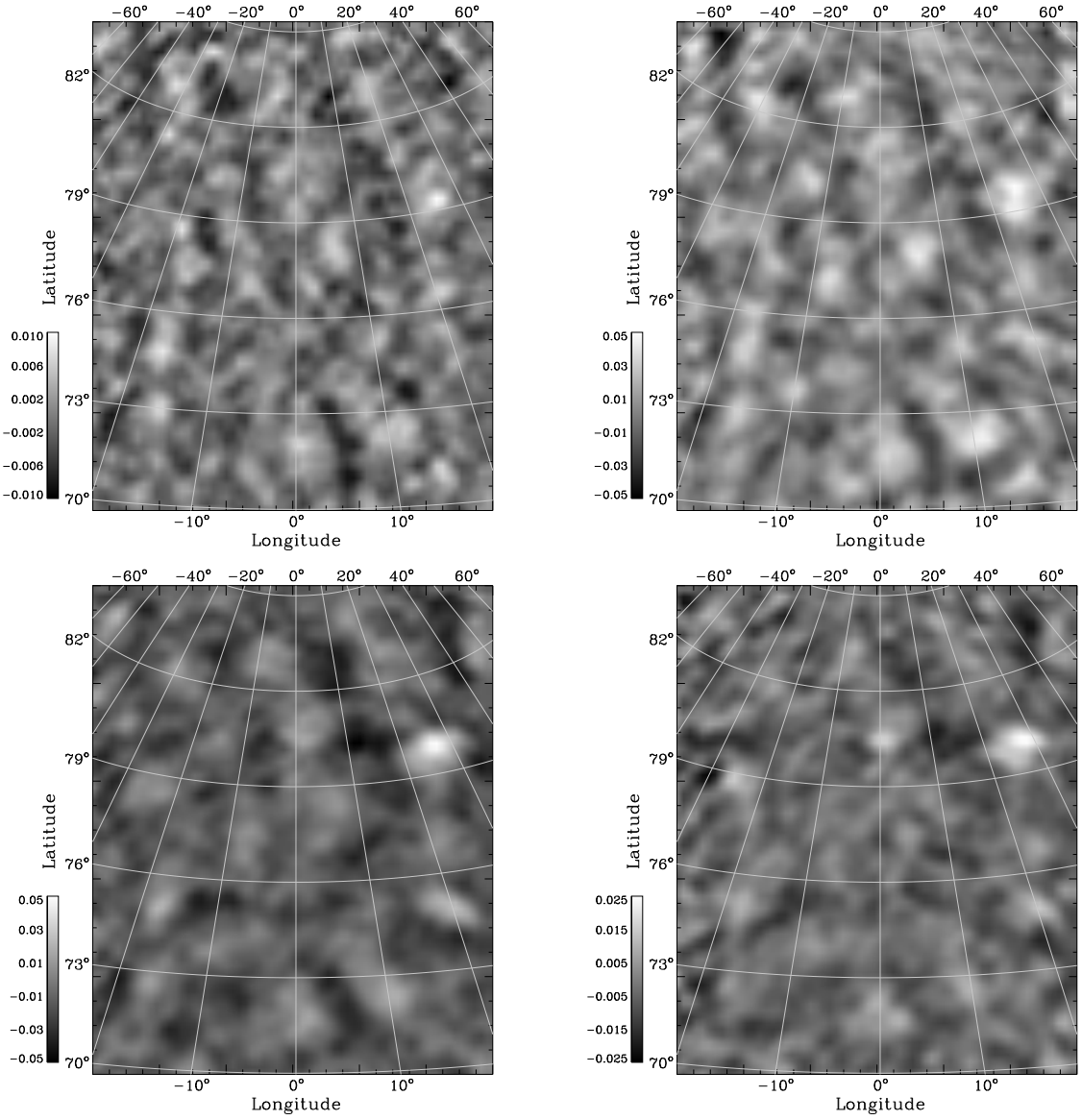

Figure 6.10 Subsurface horizontal flow divergence maps for the north polar region. Depths for each panel are 0.75 Mm (upper left), 2.25 Mm (upper right), 3.75 Mm (lower left), and 5.25 Mm (lower right), which is the same as those in Figure 6.9. White indicates diverging regions while black indicates converging regions. The value of divergence is proportional to the local sound speed in each layer.

Table 6.2 Correlation coefficient of horizontal flow fields between different depth layers in the north polar region

$a \setminus b$	0.75 Mm	2.25 Mm	3.75 Mm	5.25 Mm	6.75 Mm
0.75 Mm	1.0000	0.6877	0.5441	0.3559	0.0589
2.25 Mm	0.6877	1.0000	0.7730	0.5142	0.1240
3.75 Mm	0.5441	0.7730	1.0000	0.8354	0.3661
5.25 Mm	0.3559	0.5142	0.8354	1.0000	0.7277
6.75 Mm	0.0589	0.1240	0.3661	0.7277	1.0000

Table 6.3 Correlation coefficient of horizontal flow fields between different depth layers around the disc centre

$a \setminus b$	0.75 Mm	2.25 Mm	3.75 Mm	5.25 Mm	6.75 Mm
0.75 Mm	1.0000	0.4198	0.3000	0.1617	0.0400
2.25 Mm	0.4198	1.0000	0.6458	0.3186	0.1040
3.75 Mm	0.3000	0.6458	1.0000	0.7247	0.3419
5.25 Mm	0.1617	0.3186	0.7247	1.0000	0.7077
6.75 Mm	0.0400	0.1040	0.3419	0.7077	1.0000

6.6 Discussions

6.6.1 Forward modelling of the travel-time shift due to flow fields

The acoustic travel times for various skip distances allow us to infer the subsurface flows in various layers. Here we want to consider how travel times are shifted by the flow field under the ray approximation. In this subsection, we show examples of such a forward modelling of travel-time shift by a given flow field.

In our attempt to mimic supergranular-scale convective cells, we assume the flow field to be the one given by Drobyshevski & Yuferev (1974):

$$\begin{aligned} v_x &= v\sin(kx)\left(1+\frac{1}{2}\cos(ky)\right)\cos(k(z-1)) \\ v_y &= v\left(1+\frac{1}{2}\cos(kx)\right)\sin(ky)\cos(k(z-1)) \\ v_z &= v\left[(1+\cos(kx))(1+\cos(ky))-1\right]\sin(kz), \end{aligned} \tag{6.30}$$

where $k = \pi/s$, and $1 - s \leq z \leq 1$. The Cartesian coordinates x, y, and z are normalized by the solar radius. We assume the supergranular cell radius is 15 Mm and s denotes the

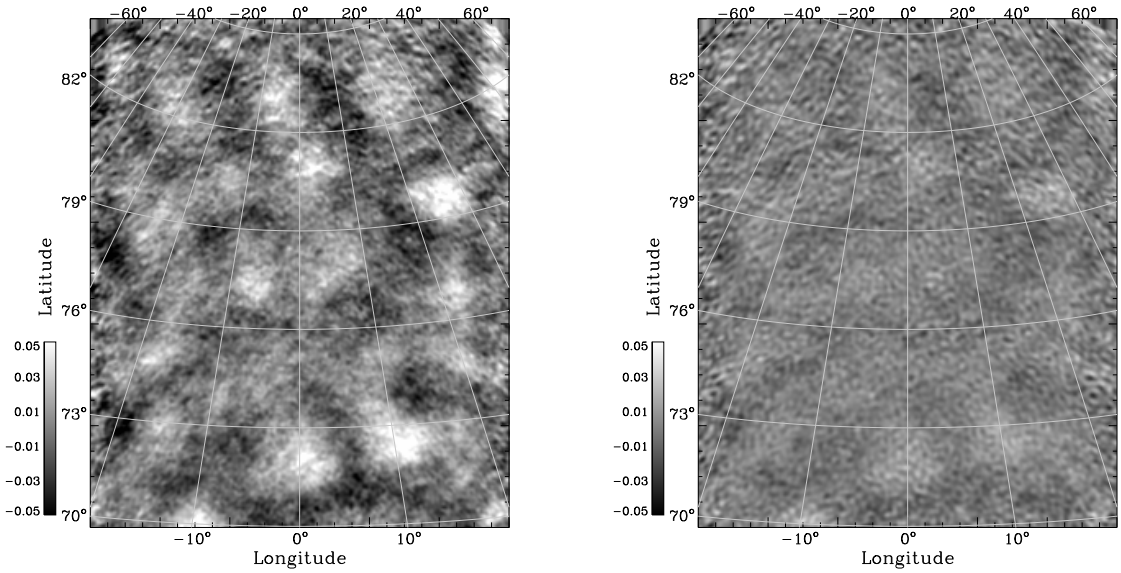

Figure 6.11 Subsurface vertical flow maps for the north polar region. Depths for each panel are 0.75 Mm (left) and 2.25 Mm (right), and these layers are the same as the shallower two layers in Figure 6.9. The vertical component of flow normalized by the local sound speed is shown in grayscale. Positive flow speed indicates upflow.

size normalized by the solar radius ($s \sim 0.022$). Since the depth of the cell is s, the aspect ratio of the cell is 2:1. The amplitude, v, is set to be 1 km s^{-1}. The slices of this flow field are shown in Figure 6.12. This flow field satisfies $\nabla \cdot \boldsymbol{v} = 0$.

According to Equation (3.14), the difference of the reciprocal travel time is

$$\delta\tau_{\text{diff}} = -2 \int_{\Gamma} \frac{\boldsymbol{n} \cdot \boldsymbol{v}}{c^2} ds.$$

We calculate the ray path, Γ, using the model S (Christensen-Dalsgaard et al. 1996) in the way described in Appendix A. At each point along the ray path, we calculate the flow field at the point and inner product of the flow velocity and the small element of the ray, $\boldsymbol{n} \cdot \boldsymbol{v} ds$, and then integrate.

We use ten rays shown in Figure 6.13; the properties of the rays are summarized in Table 6.4. We calculate $\delta\tau_{\text{diff}}$ for each rays at several points in the flow field. The bottom panel in Figure 6.13 shows the travel-time difference shift for each ray at the location indicated in the top panel. These values indicate the travel-time difference between $+x$ and $-x$ directions for the rays starting from or ending at $(x, y) = (0, 0)$.

Next, we calculate the travel-time shift for each direction equally spaced every $\pi/16$

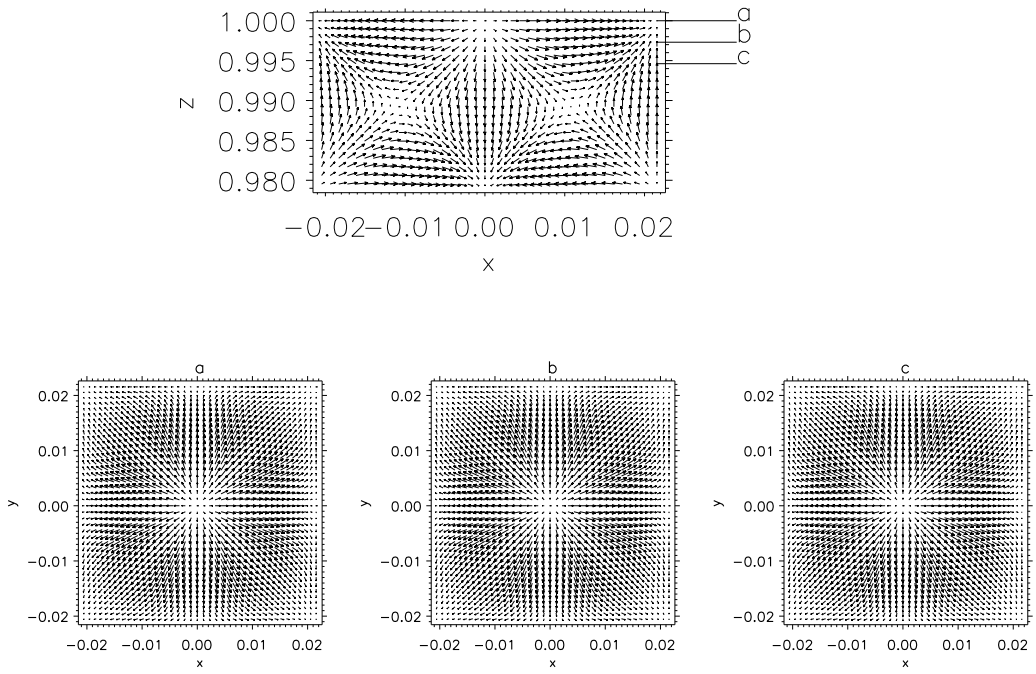

Figure 6.12 Flow field given by Equation (6.30). The top panel shows the vertical cut at $y = 0$, while the bottom panels show the horizontal cut at $z = 0$ (left), $z = -s/8$ (middle), and $z = -s/8$ (right). All coordinates are normalized by the solar radius. The longest arrow in the panels correspond to $1.5v$ (top), $1.56v$ (left), $1.44v$ (middle), and $1.1v$ (right), respectively.

radian, and obtain the outward–inward travel-time difference by averaging the shift over all the directions to mimic the annulus geometry of our travel-time analyses. Figure 6.14 shows the outward–inward travel-time difference map for each ray. For the rays with smaller skip distances, the travel-time difference around the central point of the horizontal divergence at the surface ($(x, y) = (0, 0)$, for example) is negative, which is consistent with the surface divergence. On the other hand, for the rays with larger skip distance, the travel-time difference at the same point is positive. This apparent inconsistency results from the structure of the subsurface flow along the ray path.

The travel-time maps of the real observational datasets shown in Figures 6.6 and 6.7 are for the skip distance of 14.4 Mm, and they correspond to Ray D or E in this model. Even the travel-time maps for the largest annulus (p7) that we have used in the polar region

Table 6.4. Skip distance and depth of the rays

	A	B	C	D	E	F	G	H	I	J
l	2000	1400	1000	800	600	410	360	300	250	200
ν [mHz]	5.0	4.0	3.3	3.3	3.3	3.3	3.3	3.3	3.3	3.3
distance [Mm]	3.96	6.07	8.39	11.68	15.97	23.86	30.84	42.75	55.16	78.58
depth [Mm]	0.69	1.24	1.99	3.38	5.54	9.29	11.41	15.61	20.75	28.44

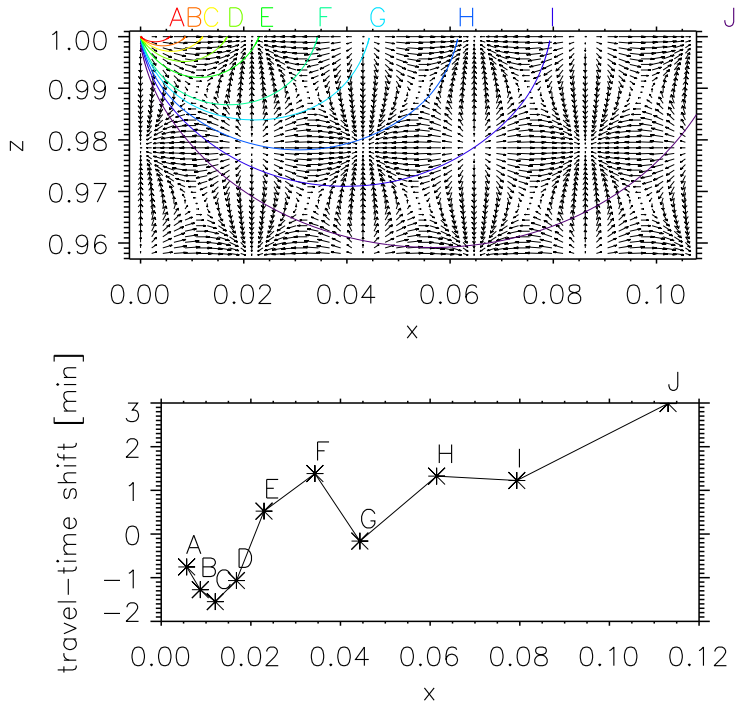

Figure 6.13 Ray paths with the flow field at $y = 0$ (top) and the travel-time shift, $\delta\tau_{\rm diff}$ (bottom).

analyses show no sign changes of the divergence/convergence to the travel-time maps for smaller annuli, like panel F in Figure 6.14, because the size of annulus is limited by the field of view of SOT and even the largest one (p7; 26.3 Mm) is in the same order of the supergranular cell size.

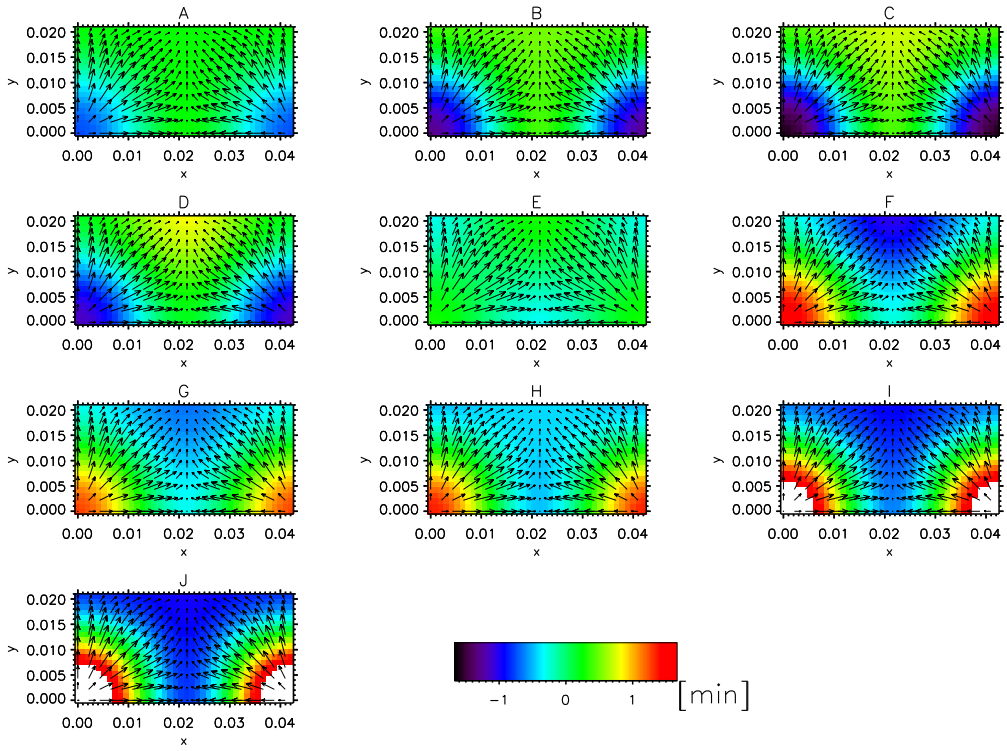

Figure 6.14 Outward–inward travel-time difference with the flow field on the surface ($z = 0$; arrows). Labels "A" to "J" indicates the ray listed in Table 6.4. The positive travel-time difference implies that the outward travel time at the point is longer than the inward travel time.

Another important feature found in the results of this forward modelling is the 'blank regions' in travel–time difference maps. Those maps, such as Figure 6.6, have seemingly 'blank regions' between the 'diverging areas' and 'converging areas'. Such a region is reconstructed in Figure 6.14; the 'blank region' does not mean the region without flow. Moreover, for some annulus size which is close to the cell radius (Ray E), travel-time signal becomes weak not only the mid-point of the cell boundary and the centre but also the diverging/converging centres.

Part of our intension in doing the forward modelling was to understand how the nearly-connected cells in the polar regions might appear in the travel-time maps. But it does not seem that this 'standard' flow field of the convection cell, a diverging flow from the central point of the cell, would produce such structures. If the cell is elongated in one direction and it has a diverging flow from the central point, the travel-time maps would show the

diverging region (with negative $\tau_{\rm out} - \tau_{\rm in}$) of just an elongated shape too.

On the other hand, if the cell is elongated in one direction and the diverging centre is shaped as a line in the centre of the cell, the outward–inward travel-time maps for the flow field would have an hourglass-shaped diverging region on the cell. This is one possibility how to make the aligned cell structures in the polar region; the subsurface flow field obtained the inversion (Figure 6.10) shows the elongated diverging/converging region along the alignment directions.

We can obtain the subsurface flow field by inversion of the travel times, but we can also exploit the forward modelling to interpret the results obtained by travel-time analysis. Here, we have confirmed by the forward modelling that the features of the observed outward–inward travel-time difference is consistent with the model flow field of the supergranular cells.

6.6.2 Supergranular structure in the polar region

As was mentioned in the previous sections, we have found evidence indicating the followings:

- The horizontal (east-west) size of the cells decreases towards higher latitudes, while the depth of the cells is larger in the higher latitudes.

- Supergranular cells seem to align in roughly north-south direction in the polar regions. There also seem to be areas with weak diverging flows between the aligned cells. The alignment seems to be coherent for a few-cell distance.

Rimmele & Schröter (1989) reported the variation of supergranular cell size and velocities with latitude. They found that the mean cell diameter of the supergranulation attains its minimum in mid-latitude (around 45 degree); their interpretation of this result was that the supergranular cell size and flow are affected by the latitude-depending convective heat flux. They suggested the result implies that the convective flux attains maximum at the equator region. The cell size in latitudinal direction, however, did not show clear latitude dependence, and they mentioned that the cells tend to flatten in the higher-latitude regions; this is contradictory to our results.

On the other hand, the latitude variation of the cell size we have found is consistent with that obtained by f-mode local helioseismology technique by Hirzberger et al. (2008), as

well as that obtained by the observations in Ca II K line of the chromospheric network cell (Brune & Wöhl 1982; Münzer et al. 1989). Note that these observational results are within mid- or lower-latitude regions only, up to the region with the latitude of $\sim 70^\circ$ at most, but if the tendency can be extrapolated to the latitude of 80° or so, it would be consistent with our results.

What makes the dependence of the cell size on the latitude is not clear, however. One possibility is the difference in Coriolis force. If $\boldsymbol{\Omega} = \Omega \boldsymbol{e_z}$ denotes the solar rotation vector and $\boldsymbol{v}$ denotes the flow measured on the Sun, where Ω is the angular rotation rate of the Sun and $\boldsymbol{e_z}$ is the unit vector in z direction, the Coriolis force per unit mass is given by

$$\boldsymbol{a} = -2\boldsymbol{\Omega} \times \boldsymbol{v}.$$

Let us consider a point at the latitude λ in the northern hemisphere; at that point, the north-ward flow will be bent toward west, while the west-ward flow will be bent toward south. The amount of bend the north/south-ward flow feels, depends on the latitude as $\sin\lambda$. Therefore, around the equator, the east/west-ward flows are affected by the Coriolis force, but the south/north-ward flows are not, while in the polar region, the east/west-ward flows are affected in the manner similar to the equatorial region, but the effect to the south/north-ward flows is weaker. Thus, supergranular horizontal flow in the polar region would be disturbed by the Coriolis force in all the directions, which makes the cell size smaller. On the other hand, since the supergranular horizontal flow in the equatorial region tends to be disturbed only in the east/west direction, one might think that this would make the cells in the equatorial region anisotropic, i.e., elongated in the latitudinal direction. This, however, is not consistent with the structure of the travel-time maps in the equatorial region.

As for the radial component of the flow in the convective cell, the Coriolis force works for an ascending flow as the eastward force and is proportional to $\cos\lambda$ in the northern hemisphere. Therefore, the force is more significant in the lower-latitude region. This may explain the latitude-dependence of cell depth; the radial components of the convective flows are disturbed more significantly in the lower-latitude region, and the depth of the cell is larger in the higher-latitude region.

One thing we should consider is significance of the Coriolis force effect. How large the Coriolis force affects to the supergranular flows is evaluated by the Rossby number, or more

simply the ratio of the supergranulation time scale to the rotation time scale:

$$\frac{\tau_{\text{supergranule}}}{\tau_{\text{rotation}}} \sim \frac{1 \text{ day}}{30 \text{ day}} \sim 3 \times 10^{-2}.$$

This is much less than the observed difference between the polar and equatorial regions. Therefore, if the Coriolis force does cause the difference, some non-linear processes with positive feedback are likely involved.

The supergranular structure, not only about the size but also the alignment, may be also affected by larger-scale flow structures such as giant cells or rotation. Meridional flow, on the other hand, is probably too slow to affect supergranulation.

The alignment reported by Lisle et al. (2004) was found in an 8-day observation, while our observation was only 16-hour long. Since the lifetime of a supergranular cell is considered to be about a day, the alignment found by them is somewhat statistical, i.e., it does not mean that supergranules are aligning at a given time, as was found by us. And yet, they might both be a result of giant-cell flow driving smaller-scale flow field.

Global magnetic structure of the Sun may also be affecting supergranules. There are some evidence that supergranules are not as deep as they are wide, and that Simon & Leighton's (1964) argument that the second ionization of Helium is driving supergranulation may not be valid. In fact, some researchers argue that there is nothing special about supergranulation scale except that is the scale favoured by magnetic field that is interacting with convective flows (Stein et al. 2007).

Solar physicists have been aware of the existence of active longitudes, along which active regions appear repeatedly and which are, in theoretical context, conjectured to be manifestation of non-axisymmetric dynamo process. If there is a coherent subsurface magnetic structure that is lying more or less along an active longitude, would such structure give rise to aligned supergranules?

Obviously, to understand the nature of the alignment we found in the polar region of the Sun, we first need to know if the alignment is transient or permanent in supergranular and in giant-cell time scale. We would also need to investigate the supergranular structure at various latitudes.

6.7 Future Work: Polar Region Dynamics

We have carried out several sets of north and south polar observations by SOT. The results described in this chapter are just a part of the datasets, and we need to analyze other datasets as well to confirm the characteristic cell structures in the polar region.

In addition to the supergranular structure, we are interested in the subsurface flows in the polar region, such as meridional circulation and rotation profiles, which would be detected from the same datasets and by the same inversion method. In this thesis, we just show our preliminary calculation of the profiles in the north polar region in Figure 6.15. We still have offsets of unknown origin in the rotation profiles, but the trend is consistent with the speed in the lower-latitude regions obtained in previous works. As for the meridional flows, the flow in the layer most close to the surface is poleward, while the flows in the deeper layers are equatorward, though they show fluctuation with a large amplitude. We have examined the datasets of the south polar region as well, and the same tendency has been found. Since the spatial scale of the fluctuation is about the size of the supergranule, the supergranular flow component may still be existent and superimposed on this profile. We need further work to understand the entire properties of the profiles. As is discussed in §7.2.2, these flows are of great importance in our attempt to understand the dynamo mechanism.

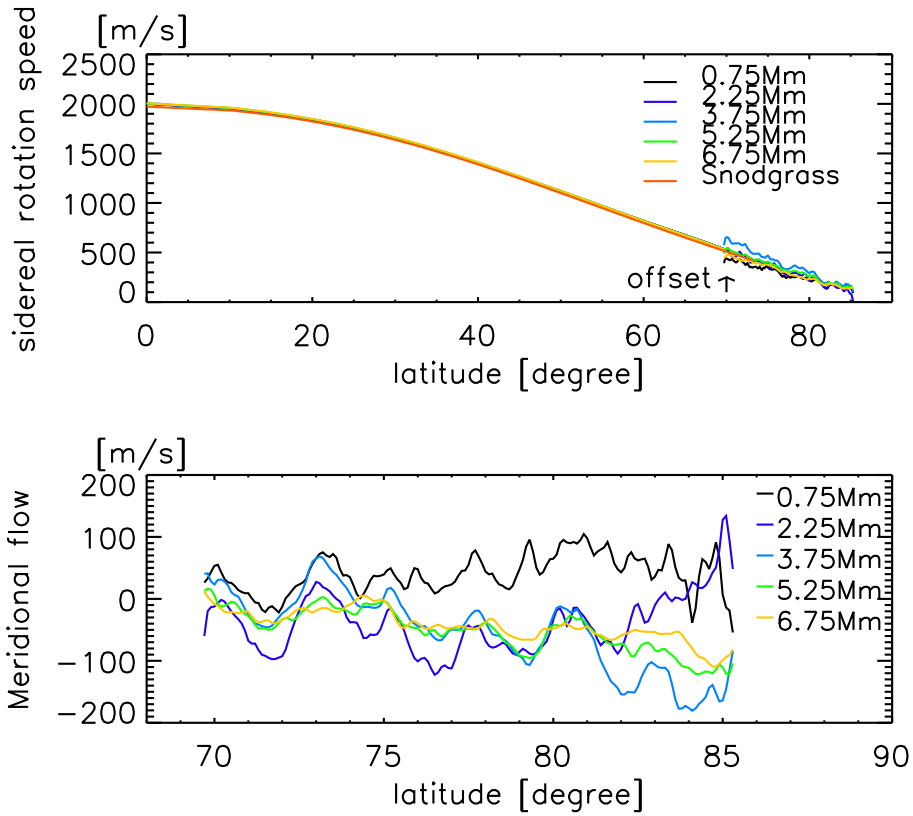

Figure 6.15 One example of rotation and meridional-flow profiles in the north polar region. *Top*: Rotation profiles in several depth layers. Lines with different colors are for different depths. The length of the arrow indicates the unknown offset (150 m s^{-1}). The profiles in the lower-latitude region are obtained by global helioseismology with MDI (courtesy of Dr. Takashi Sekii), except the red line which indicates Snodgrass rate (Equation 6.1). *Bottom*: Meridional flow profiles in the north polar region in several depth layers. Positive flow indicates the northward flow, i.e., poleward flow in the northern hemisphere.

Chapter 7

Summary and Future Prospects

7.1 Summary

We carried out local helioseismology mainly exploiting *Hinode*/SOT datasets but partly theoretically, ultimately motivated by a desire to understand the activity phenomena on the Sun. A brief summary follows.

Sunspot oscillations First, we studied Sunspot oscillations (Chapter 2). We succeeded in detecting oscillation signals in and around sunspots by SOT. In all the sunspots we observed, so-called umbral flash was detected in chromospheric lines. We did not only confirm several known features of the sunspot oscillations, such as the peak frequency in a sunspot decreasing outwards throughout umbra and penumbra, but also found fine structures in power distribution. These results give important constraints on the sunspot models. To discuss further, we require more datasets, especially in Dopplergrams of a highly axisymmetric circular sunspot. After the observations mentioned in this thesis, however, the solar activity became, and then unexpectedly remained, low and we could not obtain datasets for further analyses. We hope that in near future the Sun will be active again and we can resume the sunspot oscillation study using SOT datasets.

Chromospheric time–distance helioseismology Second, we reconsidered acoustic wave behaviour above the photosphere, which has never been sufficiently studied as we discussed in §3.5 in Chapter 3. Though for more precise analyses we still need to model the wave propagation process dynamically, preferably with radiative magnetohydrodynamics, this helped

us to interpret the travel-time anomaly found in the lower chromosphere; we succeeded in detecting the chromospheric downflows in active regions (Chapter 4). This reminds us that the oscillation signal in the chromosphere includes not only information about the subsurface structures but also about the chromospheric structure, and since the chromosphere is highly dynamic, we have to be cautious in interpreting the chromospheric inversion results by taking these facts into account. Meanwhile, our result opens up new possibilities of studying chromospheric dynamics by helioseismology, which may be useful in the polar regions.

Statistical property of cross-correlation functions Third, we investigated the statistical property of cross-correlation functions by considering the stochastic excitation of the solar oscillation (Chapter 5) . We concluded that the distribution function of the cross-correlation function is a normal distribution, and derived the relationship between mean power spectrum and the mean and variance of the cross-correlation functions. This enabled us to do forward statistical modelling of the cross-correlation function as well as, eventually, to estimate errors in the subsurface structures obtained by inversions in time–distance helioseismology.

Supergranulation in the polar region of the Sun Finally, we have studied the supergranulation in the polar region of the Sun, the knowledge of which is most insufficient in the study of the supergranulation, by time–distance helioseismology (Chapter 6). Regarding the supergranular cell size, we found the tendency that the east-west width is smaller and the depth is larger, in the higher-latitude regions, compared to the equatorial region. Moreover, we found some kind of cell alignment in higher-latitude regions. We need further data and work for confirmation, but it may be indication of a giant cell, the largest convection cell of the Sun. To understand polar region dynamics is of great importance in comprehending solar dynamo mechanism.

7.2 Future Prospects

7.2.1 Methodology: Time–distance helioseismology

Local helioseismology has an advantage in probing local and transient structure and is a unique method in studying such structure and dynamics of the Sun. It is, however, still

in an immature state compared to the global helioseismology. In this thesis (in Chapter 5), we have examined the statistical property of the cross-correlation function which is used in time–distance helioseismology. By what we obtained in this thesis, we can estimate errors in the inversion results obtained by the time–distance helioseismology. It will be essential in interpreting the inversion results.

Another task we have not done yet is time–distance analyses with f modes using the SOT high-resolution observations. In our time–distance analyses, we filtered out the f modes and used p modes of the Sun only. The f modes, however, are useful in investigating the shallower layers of the Sun; the f-mode sensitivity is within the depth of 2 Mm (Duvall & Gizon 2000). Since all the p modes pass through the shallower layers regardless of their frequency and wavenumber, the resolution of the p modes in the shallower layers are worse than that in the deeper layers. Moreover, by using f modes we can detect horizontal flow field near the surface which is difficult to detect by Doppler velocity observation, unlike the vertical flow components. Time–distance analyses of f modes have been fully developed only recently (e.g., Duvall & Gizon 2000; Jackiewicz et al. 2007; Hirzberger et al. 2008). There was also an attempt for direct inversions of the f-mode cross-correlation functions (Woodard 2002). The high-resolution observation by *Hinode*/SOT would enable us to detect fine structure of near-surface flow fields.

As we demonstrated in Chapter 4, observations not only in the photospheric lines but also in chromospheric lines are useful for the helioseismology analyses to investigate the dynamics above the photosphere. Although we still need further careful modelling for the acoustic wave behaviour in the 'evanescent' region, multi-wavelength time–distance helioseismology may be a useful tool to infer flows in the chromosphere which is full of activities.

7.2.2 Scientific objectives: Dynamics inside the Sun and solar dynamo

To reveal how the solar activity phenomena are driven is a challenging task. Investigating subsurface structure and dynamics of active regions by local helioseismology is exactly what we are intending to carry out when the solar activity level comes up, and this is the most obvious and important target in the immediate future. In this section, however, we would like to discuss what we need to do in longer term.

Activity phenomena on the Sun are thought to be driven by interaction between the

plasma and the magnetic field in the Sun, dynamo mechanism. To understand the dynamo mechanism observationally, we need to investigate not only local structure/dynamics of active regions but also the global dynamics in the Sun, especially, meridional circulation and differential rotation, by helioseismology technique.

7.2.2.1 Meridional circulation

Meridional circulation which is the flow component in the meridian planes of the Sun is important to understand the dynamics of the convection zone, because it transports angular momentum and magnetic flux.

The poleward flow with the typical speed of 20 m s^{-1} has been reported by surface Doppler observations (e.g., Hathaway 1996) and by tracking the surface features, such as sunspots or small magnetic features. By time–distance technique, Giles et al. (1997) showed that the meridional flow is poleward in both hemispheres and the near-surface flow reaches the speed of about 20 m s^{-1}.

The circulation flow in the deeper layers is expected to be equatorward, although no clear evidence of such an equatorward flow has been found. The difficulty in detecting such flows lies partly in that the expected slow speed of the flow and also in the depth of the flow. To detect the equatorward-flow in the deeper layers by time–distance helioseismology, we need to measure the travel times for larger travel distance. Such measurements may be possible when an instrument is launched into an out-of-ecliptic orbit, like Solar-C plan A (see §7.2.3), or when we can observe the polar region with very high resolution with some new instruments to be developed. As for the flow speed factor, however, Braun & Birch (2008) estimated that the flow may be too slow to detect with a significant signal-to-noise ratio by local helioseismology technique, even if we observe the Sun over a whole solar cycle.

7.2.2.2 Differential rotation

By tracking the surface feature, such as sunspots, coronal holes, or bright points, people have measured the solar rotation rate. The solar rotation rate depends on latitude; the lower-latitude region rotates faster than the higher-latitude region. Periods of the rotation are about 26 days around the equator and about 37 days near the polar region. This differential rotation causes so-called ω-effect in the solar dynamo. If there is a poloidal magnetic field component along the meridional line on the Sun, it is twisted as the Sun

rotates and a toroidal magnetic component will be created. In such a way, differential rotation plays a key role in dynamo mechanism. The rotation rate in the Sun has been investigated by helioseismology technique. In the convection zone in lower-latitude region the rotation rate has been investigated relatively well (e.g., Thompson et al. 1996; Schou et al. 1998), while it has not been in the higher-latitude region. Since we observe the Sun from the ecliptic plane only, we cannot resolve in the high-latitude region.

Polar observation by *Hinode*/SOT as well as the full observation by *SDO*/HMI (mentioned later) will provide us chances to study the polar region dynamics in more details.

7.2.3 New instruments to be launched: Promising datasets for helioseismology

In addition to the instruments now in operation, some instruments for solar observation are planned in near future. We refer to two of them, which are especially promising for the helioseismology study.

7.2.3.1 Helioseismic and Magnetic Imager onboard *Solar Dynamics Observatory* (*SDO*)

Solar Dynamics Observatory (*SDO*) is scheduled to be launched in 2010. It will be put into a geostationary orbit, which makes it possible to transfer huge amount of data to the earth. One of the three instruments to be loaded, the Helioseismic and Magnetic Imager (HMI; Kosovichev & HMI Science Team 2007) instrument, will take full-disc Dopplergrams with 1-arcsec spatial resolution as well as full-disc vector magnetograms with the same spatial resolution. The predecessor of HMI, MDI onboard *SOHO*, could take full-disc Dopplergrams with 2-arcsec resolution, and narrower field-of-view Dopplergrams in high-resolution mode (1-arcsec resolution) as well. The field of view in high-resolution mode of MDI is, however, limited to close to the disc centre. The full-disc datasets to be provided by HMI will enable us to study not only the sunspot anywhere on the Sun but also the polar regions with higher spatial resolution. Combining the full-disc observation by *SDO*/HMI with the high-resolution observation by *Hinode*/SOT, we can investigate the subsurface dynamics and structure in more detail by helioseismology.

7.2.3.2 Solar-C

Solar-C mission is the next space solar telescope planned in Japan and targeted on the solar maximum after next (around 2020). As of 2009, two plans are under consideration: a mission for out-of-ecliptic-plane observation (plan A) and a mission for a high-resolution observation throughout the atmosphere of the Sun (plan B). Since as helioseismologists we are interested in plan A, here we introduce Solar-C plan A briefly.

Solar-C plan A will be launched into an orbit inclined to the ecliptic plane so that it can image the higher-latitude regions of the Sun directly above, which has never been possible. To understand the polar dynamics is essential for solving the solar dynamo problems which is the largest unsolved issue remaining in solar physics. Besides, it may provide information about the deeper interior of the Sun with the helioseismology techniques, by collaborating with satellites or other instruments on the ecliptic plane. Exploiting the Doppler velocity datasets in the higher-latitude region of the Sun without severe projection, we can cross-correlate the signals in the polar region with those around the equator obtained with other normal satellites. The penetrating depth of the ray is larger when the skip angle is larger, and if the skip angle is above 45 degrees, the ray penetrates down to the base of the convection zone, where the velocity shear may be playing a key role in dynamo mechanism.

Appendix A

Calculation of Acoustic Ray Paths in the Sun

In this chapter, we summarise the calculation of acoustic ray paths in the Sun. This is required for the time–distance analysis to choose appropriate phase-speed filters and to interpret the results.

To choose an appropriate phase-speed filter in time–distance analysis, we need to know the relationship between travel times, skip angles, and horizontal phase speeds. If an incident angle of a purely acoustic wave is given, horizontal phase speed is uniquely determined, and the travel time and the skip angle of the wave can also be computed for a given solar structural model. The slope of a time–distance curve in a time–distance diagram indicates the phase speed of the wave (see §A.1). Therefore, in time–distance analysis, once we choose a distance of a pair of points, or a radius of the annulus that is being analyzed, an appropriate phase-speed filter can easily be designed.

A.1 Time–Distance Diagram and Phase Speed

Followings are based on the description in Mizuguchi (2007).

If we consider the case of a purely acoustic wave, the travel time between two surface points A and B is given by

$$\int_{\mathrm{B}}^{\mathrm{A}} \frac{ds}{c(r)} = 2 \int_{\mathrm{C}}^{\mathrm{A}} \frac{ds}{c(r)} \equiv 2 \times T, \tag{A.1}$$

where $c(r)$ is the sound speed and the integral is along the ray. Here, C is the turning point

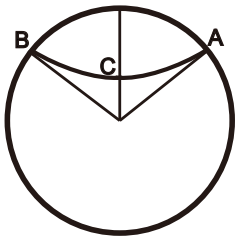

Figure A.1 Ray path in the Sun.

(see Figure A.1). Using

$$ds = dr\sqrt{(r\frac{d\phi}{dr})^2 + 1}, \tag{A.2}$$

we obtain

$$T = \int_{r_\mathrm{t}}^{R_\odot} \sqrt{\left(r\frac{d\phi}{dr}\right)^2 + 1}\ \frac{dr}{c(r)}, \tag{A.3}$$

where r_t indicates the radius of the inner turning point and $R_\odot$ is the solar radius. By the dispersion relation of purely acoustic wave

$$\omega = c\sqrt{k_\mathrm{r}^2 + {k_\phi}^2},$$

where k_r and k_ϕ are radial and azimuthal components of wavenumber vector, respectively, the radial and azimuthal components of the group velocity are given by

$$v_r = \frac{\partial\omega}{\partial k_\mathrm{r}} = \frac{c^2 k_\mathrm{r}}{\omega} \quad \text{and} \quad v_\phi = \frac{\partial\omega}{\partial k_\phi} = \frac{c^2 k_\phi}{\omega}. \tag{A.4}$$

The azimuthal component of the wavenumber is

$$k_\phi = \frac{L}{r} = \frac{L}{\omega}\frac{c\omega}{rc} = \frac{a}{w}\frac{\omega}{c} = \frac{ak}{w}, \tag{A.5}$$

where $L = \sqrt{l(l+1)}$, and l is an integer that is identified to be the degree of the corresponding spherical harmonic function. Other quantities introduced here are $w \equiv \omega/L$, and $a = c/r$. The radial wavenumber is

$$k_\mathrm{r}^2 = k^2 - {k_\phi}^2 = k^2 - \left(\frac{ak}{w}\right)^2. \tag{A.6}$$

Hence, the first term in the square root in the integrand in Equation (A.3) is

$$r\frac{d\phi}{dr} = \frac{v_\phi}{v_r} = \frac{\partial\omega/\partial k_\phi}{\partial\omega/\partial k_\mathrm{r}} = \frac{c^2 k_\phi/\omega}{c^2 k_\mathrm{r}/\omega} = \frac{k_\phi}{k_\mathrm{r}} = \frac{ak/w}{\sqrt{1-(a/w)^2}} = \frac{1}{\sqrt{(w/a)^2 - 1}}. \tag{A.7}$$

The half travel time between A and B is, therefore, function of w only:

$$T(w) = \int_{r_t}^{R_\odot} \frac{dr}{c(r)} \sqrt{\frac{1}{(w/a)^2 - 1} + 1} = \int_{r_t}^{R_\odot} \frac{dr}{c(r)\sqrt{1 - (a/w)^2}}. \tag{A.8}$$

On the other hand, the skip angle between A and B is given by

$$2\Phi(w) \quad = \quad 2\int_C^A \frac{d\phi}{dr} dr, \tag{A.9}$$

or, the angle between A and C is

$$\Phi(w) \quad = \quad \int_{r_t}^{R_\odot} \frac{a}{c} \frac{dr}{\sqrt{(w/a)^2 - 1}}. \tag{A.10}$$

Hence,

$$\Phi(w) = \int_{r_t}^{R_\odot} \left(\frac{a}{w}\right)^2 \frac{1}{\sqrt{1 - (w/a)^2}} \frac{dr}{c}. \tag{A.11}$$

By the way, Duvall's function, $F(w)$, is defined as

$$F(w) = \frac{1}{\omega} \int_{r_t}^{R_\odot} k_r dr = \int_{r_t}^{R_\odot} \frac{1 - (a/w)^2}{\sqrt{1 - (a/w)^2}} \frac{dr}{c}. \tag{A.12}$$

Using this, we have

$$T(w) - F(w) = \int_{r_t}^{R_\odot} \frac{(a/w)^2}{\sqrt{1 - (a/w)^2}} \frac{dr}{c} = \frac{\Phi(w)}{w}, \tag{A.13}$$

i.e.,

$$F(w) = T(w) - \frac{1}{w}\Phi(w). \tag{A.14}$$

Differentiating Equation (A.14) with respect to w yields

$$\frac{dF}{dw} = \frac{dT}{dw} - \frac{1}{w}\frac{d\Phi}{dw} + \frac{\Phi}{w^2}, \tag{A.15}$$

and by differentiating $F(w)$, using Equation (A.12), we obtain

$$\begin{aligned} \frac{dF}{dw} &= \int_{r_t}^{R_\odot} \frac{1}{c(r)} \frac{1}{2} \frac{2a^2 w^{-3}}{\sqrt{1 - (a/w)^2}} dr \\ &= \left(\frac{a}{w}\right)^2 \frac{1}{w\sqrt{1 - (a/w)^2}} \frac{dr}{c} \\ &= \frac{\Phi}{w^2}. \end{aligned} \tag{A.16}$$

By combining Equations (A.15) and (A.16) we have

$$\frac{dT}{dw} = \frac{1}{w}\frac{d\Phi}{dw}. \tag{A.17}$$

Therefore,

$$\frac{dT}{d\Phi} = \frac{1}{w}. \tag{A.18}$$

Since $w = \omega/L$ is proportional to the phase speed, $\omega/k_{\rm h}$, this implies that the slope of the time-distance curve indicates the phase speed and the y-intercept of the tangent of time-distance curve at a certain point is $F(w)$, respectively. This relationship holds regardless of the internal structure model.

A.2 Calculation of the Ray Path

In this section, we describe how to calculate a ray path in the Sun, and show the relationship between the skip angle and the phase speed. For the calculation, we use model S (Christensen-Dalsgaard et al. 1996) as the internal structure model of the Sun. Figure A.2 shows distribution of the main physical quantities in model S.

For the case of a purely acoustic wave (i.e., the acoustic cutoff frequency and the Brunt-Väisälä frequency is omitted), the dispersion relation is

$$k_r{}^2 + k_h{}^2 = \frac{\omega^2}{c^2}. \tag{A.19}$$

Since $k_h{}^2 = l(l+1)/r^2$,

$$k_r{}^2 = \frac{\omega^2}{c^2} - \frac{l(l+1)}{r^2}. \tag{A.20}$$

The group velocity, $\boldsymbol{v}_{\mathbf{gr}}$, is given by

$$\boldsymbol{v}_{\mathbf{gr}} \equiv \frac{\partial\omega}{\partial\boldsymbol{k}} = \frac{c^2}{\omega}\boldsymbol{k} = \frac{\omega}{k}\frac{\boldsymbol{k}}{k}. \tag{A.21}$$

and its radial component is $v_{\rm gr,r} = c^2 k_r/\omega$. Using this, the amount of time, dt, for an acoustic wave to pass through the small radial element, dr, is

$$dt = \frac{dr}{v_{\rm gr,r}} = \frac{\omega dr}{c^2 k_r} = \frac{r/cdr}{\sqrt{r^2 - c^2 l(l+1)/\omega^2}}\ . \tag{A.22}$$

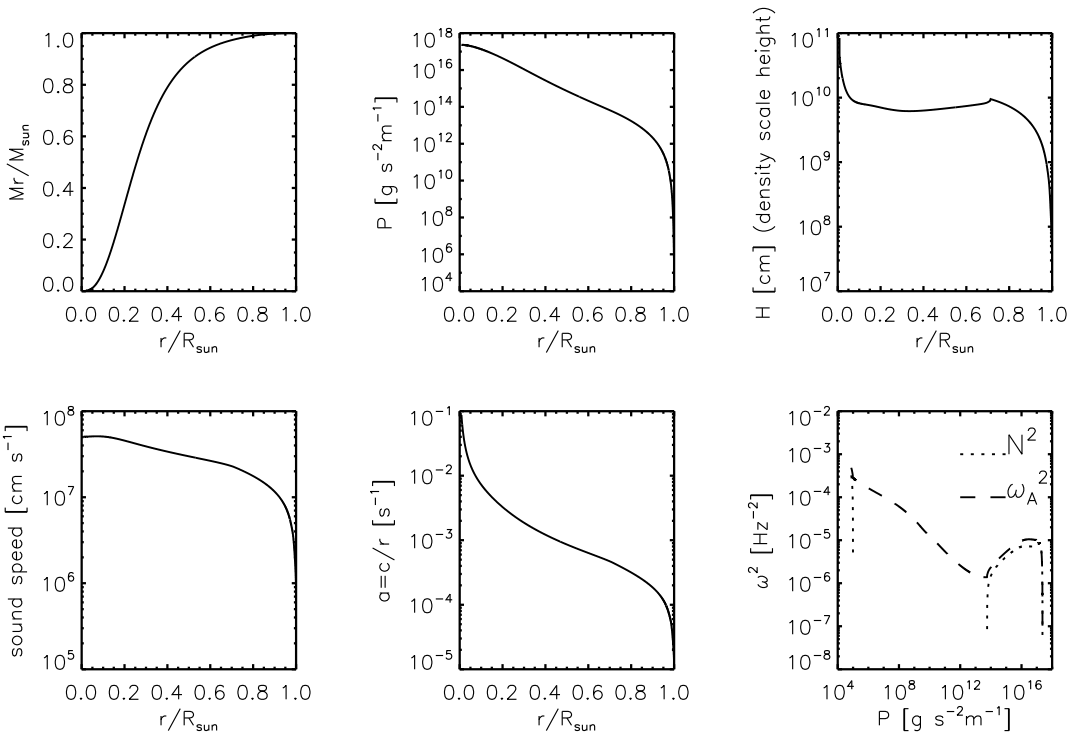

Figure A.2 Parameters of inner structure of the Sun given by the standard model (model S; Christensen-Dalsgaard et al. 1996)

If ω and l are fixed, we need only r and $c(r)$ to calculate the travel time. The travel time from A to B (see Figure A.1) is

$$\tau \;=\; 2\int_{\rm C}^{\rm A} dt = 2\int_{r_t}^{r_\odot} \frac{r/c^2 dr}{\sqrt{r^2/c^2 - l(l+1)/\omega^2}}\ . \tag{A.23}$$

By defining $X \equiv r^2/c^2$, and using $dX = 2rdr(1-(r/c)(dc/dr))/c^2$, we have

$$\tau = \int_{X_t}^{X_\odot} \frac{1}{\sqrt{X - l(l+1)/\omega^2}} \frac{dX}{1-(r/c)(dc/dr)}, \tag{A.24}$$

where $X_\odot = {R_\odot}^2/c({R_\odot})^2$ and $X_t = l(l{+}1)/\omega^2$. By introducing $f(X) = 1/\{1{-}(r/c)(dc/dr)\}$, we obtain

$$\tau = \int_{X_t}^{X_\odot} \frac{f(X)dX}{\sqrt{X - l(l+1)/\omega^2}}. \tag{A.25}$$

In practice, we need to discretize the formula. If we set the number of data point as

N, then

$$\tau = \sum_{i=0}^{N-1} \int_{X_i}^{X_{i+1}} \frac{f(X)dX}{\sqrt{X - l(l+1)/\omega^2}} \equiv \sum_{i=0}^{N-1} \tau_i \ . \tag{A.26}$$

To calculate this, in each integral domain $X_i \leq X \leq X_{i+1}$, $f(X)$ is approximated by a linear function, $p_i X + q_i$, and in each domain the integral is carried out analytically. The coefficients are determined via these formulae:

$$p_i = \frac{f(X_{i+1}) - f(X_i)}{X_{i+1} - X_i} \tag{A.27}$$

$$q_i = \frac{f(X_i)X_{i+1} - f(X_{i+1})X_i}{X_{i+1} - X_i}. \tag{A.28}$$

Using these and $w = \omega/\sqrt{l(l+1)}$, we have

$$\begin{aligned}
\tau_i &= \int_{X_i}^{X_{i+1}} \frac{1}{2} \frac{f(X)dX}{\sqrt{X - w^{-2}}} \\
&\simeq \int_{X_i}^{X_{i+1}} \frac{1}{2} \frac{p_i X + q_i}{\sqrt{X - w^{-2}}} dX \\
&= \int_{X_i - w^{-2}}^{X_{i+1} - w^{-2}} \frac{p_i(X' + w^{-2}) + q_i}{2X'^{1/2}} dX' \\
&= (X_{i+1} - w^{-2})^{1/2} \left[\frac{p_i}{3}(X_{i+1} - w^{-2}) + p_i w^{-2} + q_i \right] \\
&\quad -(X_i - w^{-2})^{1/2} \left[\frac{p_i}{3}(X_i - w^{-2}) + p_i w^{-2} + q_i \right].
\end{aligned} \tag{A.29}$$

We use Equation (A.29) in calculations of the ray path.

At the upper limit of the integral, $X - w^{-2} = 0$. At the point p_i and q_i are determined using the boundary point and the next. In the meantime $X - w^{-2}$ is interpolated by a linear function of X at those points, and the point where $X - w^{-2}$ is exactly equal to 0 is searched. And that point is set to the upper limit of integral.

Figure A.3 shows dependence of the travel times, 2τ (top), the depth of the inner turning points ($R_\odot - r_t$) (middle), and the phase speed, $v_{\rm ph} = wR_\odot$ (bottom), on the skip angle, 2Φ. Using the bottom panel of this figure, we chose appropriate phase-speed filters for a certain skip (angle) distance in our time–distance analyses.

Figure A.4 shows travel time plotted against $w \equiv \omega/\sqrt{l(l+1)}$. Inner turning point, $r_{\rm t}$, for each mode is given by

$$r_{\rm t} = \frac{c}{w}.$$

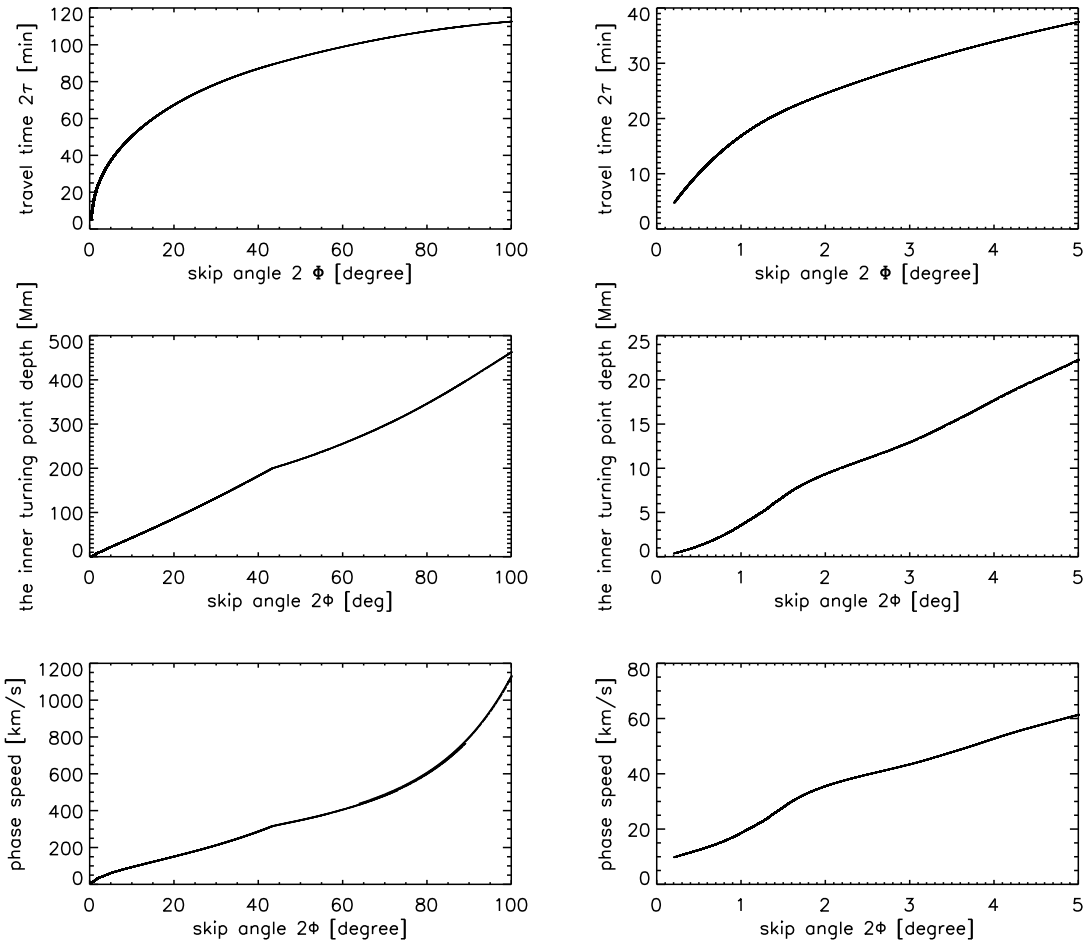

Figure A.3 *Top*: Travel time (2τ) plotted against skip angle (2Φ). *Middle*: Depth of the inner turning point, ($R_\odot - r_t$), plotted against skip angle. *Bottom*: Phase speed plotted against skip angle. Right panels are close-ups in the range of small skip angles.

In the right panel of Figure A.4, the slope of the curve changes at $w \sim 4.5 \times 10^{-4}$. This corresponds to the base of the convection zone. Since below the base of the convection zone, the sound speed gradient is smaller than that in the convection zone, the travel time increases more than expected from the extrapolation of the curve from the upper layer. This point appears also in the second and third panels in the left column in Figure A.3 as a small bump. The middle-left panel in Figure A.3 shows that the skip angle of the wave which propagates down to the base of the convection zone (about 200 Mm deep) is about 45 degrees.

On the other hand, a small dip around $w \sim 5 \times 10^{-5}$ corresponds to the He second ionization layer ($r/R_\odot \sim 0.987$, $P = 4.4 \times 10^9$[dyn cm^{-2}], see Figure 2.4 in Stix 2002). In the ionization zone, specific heat is larger than that in surrounding region. This makes Γ smaller, and since $c^2 \propto \Gamma$, in this region the sound speed decreases and the travel time increases.

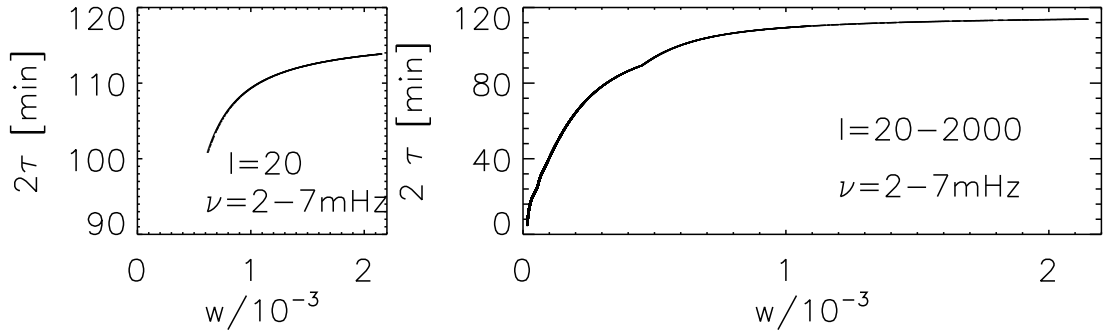

Figure A.4 Travel time plotted against w. *Left*: Travel times for acoustic wave with $l = 20$ and $\nu = 2 - 7$ mHz. *Right*: Travel times for acoustic wave with $l = 20 - 2000$ and $\nu = 2 - 7$ mHz.

Appendix B

Statistical Properties of the Cross-Correlation Functions

In this chapter, we describe in details the calculations results of which are used in Chapter 5. First, we show that the distribution of cross-correlation function is a normal distribution in §B.1. Next, we demonstrate the calculation of average of squared cross-correlation function for evaluating the variance of cross-correlation function (§B.2). Third, covariance of the cross-correlation function is calculated in §B.3.

B.1 Distribution Function of Cross-Correlation Functions

We derive the distribution of the cross-correlation function in this section. Based on the model described in §5.2.1, first we confirm that the distribution function of $a^*(k,\omega)a(k,\omega)$ is the Laplace distribution. Since cross-correlation function is the Fourier transform of $a^*(k,\omega)a(k,\omega)$ (see Equation (5.7)), we check the distribution function of the Fourier transform of a sequence of Laplace random variables.

B.1.1 Laplace distribution

Let q_i $(i = 1, \ldots, 4)$ be independent random variables whose distribution function is the standard normal distribution $\mathrm{N}(0, 1^2)$. We define ζ as $\zeta = q_1 q_2 + q_3 q_4$. The characteristic function of ζ, $M_\zeta(\lambda)$, is given as

$$M_\zeta(\lambda) =< e^{i\lambda\zeta} >=< e^{i\lambda(\xi_1+\xi_2)} >=< e^{i\lambda\xi_1} >< e^{i\lambda\xi_2} >= M_\xi^2(\lambda) = \frac{1}{\lambda^2+1}. \qquad \text{(B.1)}$$

Here ξ is the product of two independent random variables with standard normal distribution, $\xi = q_1 q_2$. Since the probability distribution function of q is

$$\phi(q) = \frac{1}{\sqrt{2\pi}} e^{-q^2/2},$$

the characteristic function of ξ is given by

$$M_\xi(\lambda) = < e^{i\lambda\xi} > = \int\int dq_1 dq_2 \phi(q_1)\phi(q_2) e^{i(\lambda q_1 q_2)} = \frac{1}{\sqrt{\lambda^2+1}}. \tag{B.2}$$

This is what we used to derive Equation (B.1). The probability distribution function of ζ, $\phi(\zeta)$, is

$$\phi(\zeta) = \frac{1}{2\pi}\int M_\zeta(\lambda) e^{-i\lambda\zeta} d\lambda = \frac{1}{2\pi}\int_{-\infty}^{\infty} \frac{e^{-i\lambda\zeta}}{\lambda^2+1} d\lambda. \tag{B.3}$$

To calculate the integral, we divide the integrand into two terms:

$$\frac{e^{-i\lambda\zeta}}{\lambda^2+1} = e^{-i\lambda\zeta}\frac{i}{2}\left(\frac{1}{\lambda+i} - \frac{1}{\lambda-i}\right).$$

We set the integral path as a semicircle Γ whose chord on the real axis in a complex plane. By taking the limit of the radius to infinity, the contribution of the integral along the arc vanishes. The pole in the integral path is at $\lambda = i$ or $-i$, and using the pole, we evaluate the integral. For the first term of the integrand, the integral I_1 is

$$I_1 \equiv \int_\Gamma \frac{i}{2}\frac{e^{-i\lambda\zeta}}{\lambda+i} d\lambda + \int_{-\infty}^{\infty} \frac{i}{2}\frac{e^{-i\lambda\zeta}}{\lambda+i} d\lambda. \tag{B.4}$$

If $\zeta > 0$, we set Γ as a semicircle in the lower half of the complex plane. Using the pole at $\lambda = -i$ we obtain

$$I_1 = \int_{-\infty}^{\infty} \frac{i}{2}\frac{e^{-i\lambda\zeta}}{\lambda+i} d\lambda = -2\pi i \frac{i}{2} e^{-i(-i)\zeta} = \pi e^{-\zeta}. \tag{B.5}$$

If $\zeta < 0$, when we take the integral path as an upper semicircle, there is no pole in the integral path and obtain $I_1 = 0$. As for the second term, we calculate I_2 in the similar way. In the case of $\zeta > 0$, we set the integral path as the lower semicircle and obtain $I_2 = 0$ because there is no pole in the path, while in the case of $\zeta < 0$, we set the integral path as the upper semicircle and obtain $I_2 = -\pi e^{\zeta}$. Therefore, we obtain the distribution function of ζ as

$$\phi(\zeta) = \frac{I_1 - I_2}{2\pi} = \begin{cases} e^{-\zeta}/2 & (\zeta > 0) \\ e^{\zeta}/2 & (\zeta < 0) \end{cases} = e^{-|\zeta|}/2\ . \tag{B.6}$$

This is the Laplace distribution. We may check the normalization as follows:

$$\int_{-\infty}^{\infty} \phi(\zeta) d\zeta = 2 \int_{0}^{\infty} e^{-\zeta}/2 d\zeta = 1. \tag{B.7}$$

When ζ is Laplace distributed, $\phi(\zeta) = e^{-|\zeta|}/2$, average of ζ, $E(\zeta)$, and variance or ζ, $V(\zeta)$, computed as follows:

$$\begin{aligned} E(\zeta) &= \int_{-\infty}^{\infty} \zeta \phi(\zeta) d\zeta = \int_{0}^{\infty} \zeta \frac{e^{-\zeta}}{2} d\zeta + \int_{-\infty}^{0} \zeta \frac{e^{\zeta}}{2} d\zeta \\ &= \int_{0}^{\infty} \zeta \frac{e^{-\zeta}}{2} d\zeta + \int_{\infty}^{0} \zeta \frac{e^{-\zeta}}{2} d\zeta = 0 \ , \end{aligned} \tag{B.8}$$

$$\begin{aligned} V(\zeta) &= \int_{-\infty}^{\infty} \zeta^2 \phi(\zeta) d\zeta - E(\zeta)^2 = 2 \int_{0}^{\infty} \zeta^2 \frac{e^{-\zeta}}{2} d\zeta \\ &= [\zeta^2 (-e^{-\zeta})]_0^{\infty} - \int_{0}^{\infty} 2\zeta (-e^{-\zeta}) d\zeta \\ &= 0 + 2 \left([\zeta (-e^{-\zeta})]_0^{\infty} - \int_{0}^{\infty} (-e^{-\zeta}) d\zeta \right) \\ &= 2. \end{aligned} \tag{B.9}$$

B.1.2 Discrete Fourier transform of the Laplace-distribution variables

As was shown in Equation (5.5), the cross-correlation function is in the form of Fourier transform of $a^*(k,\omega)a(k,\omega)$. Hence, we consider the Fourier transform of a sequence of Laplace-distribution variables.

We define p_i as a Laplace distributed random variable. The characteristic function of p_i, $M_{p_i}(\lambda)$, is

$$M_{p_i}(\lambda) = < e^{i\lambda p_i} > = \frac{1}{1+\lambda^2}. \tag{B.10}$$

Hence, the characteristic function of the sum of the variables, $x_N = \sum_{i=1}^{N} \alpha_i p_i$, is obtained as:

$$M_{x_N}(\lambda) = < e^{i\lambda x_N} > = < e^{i\lambda \sum_{i=1}^{N} \alpha_i p_i} > = \prod_{i=1}^{N} < e^{i\lambda \alpha_i p_i} > = \prod_{i=1}^{N} \frac{1}{1+(\alpha_i \lambda)^2}. \tag{B.11}$$

Next, we define $p_i = q_1 q_2 + q_3 q_4$, where each of q_i is an independent variable characterized by standard normal distribution. In this case, p_i is characterized by Laplace distribution with average of 0 and variance of 2, as was shown in §B.1.1.

Consider the Fourier transform of the sequence of $p_i (i = 1, 2, \ldots N)$, $C(x) = \int dk p(k) e^{ikx}$. Let us define $C_m = C(x_m)$ and consider the discrete Fourier transform, the real part of which is

$$Re(C_m) = h_k \sum_{j=1}^{N} p_j \cos(k_j x_m) = h_k \sum_{j=1}^{N} p_j \cos(2\pi mj/N), \tag{B.12}$$

where $h_k = 2\pi/L$, $x_m = Lm/N$, $k_j = h_k j$, and $m = 1, 2, \ldots N$. The characteristic function of $Re(C_m)$, $M_{Re(C_m)}(\lambda)$, is

$$\begin{aligned} M_{Re(C_m)}(\lambda) &= < e^{i\lambda Re(C_m)} > = \prod_{j=1}^{N} < e^{i\lambda h_k p_j \cos(2\pi mj/N)} > \\ &= \prod_{j=1}^{N} \frac{1}{1 + (\lambda h_k \cos(2\pi mj/N))^2}. \end{aligned} \tag{B.13}$$

Taking the natural logarithm of $M_{Re(C_m)}(\lambda)$, we obtain

$$\begin{aligned} \ln M_{Re(C_m)}(\lambda) &= -\sum_{j=1}^{N} \{1 + (\lambda^2 {h_k}^2 \cos^2(2\pi mj/N))\} \\ &= -\sum_{j=1}^{N} \left\{ 1 + \frac{\lambda^2 {h_k}^2}{2} + \frac{\lambda^2 {h_k}^2}{2} \cos(4\pi mj/N) \right\}. \end{aligned} \tag{B.14}$$

Let us define $x_j = 4\pi mj/N$, (i.e., $x_j = 4\pi m/N, 4\pi m/N \times 2, \ldots, 4\pi m$) and $dx = 4\pi m/N$. Multiplying both sides by dx and taking the limit of $N \to \infty$, we obtain

$$\lim_{N\to\infty} \frac{4\pi m}{N} \ln M_{Re(C_m)}(\lambda) = -\int_0^{4\pi m} dx \left\{ 1 + \frac{\lambda^2 {h_k}^2}{2} + \frac{\lambda^2 {h_k}^2}{2} \cos(x) \right\}. \tag{B.15}$$

We can evaluate the integral by exploiting a known formula (Gradshteyn et al. 2000),

$$\int_0^{\pi} \ln(a + b\cos x) dx = \pi \ln \frac{1}{2}(a + \sqrt{a^2 - b^2}), \quad \text{if} \quad a \geq |b| \tag{B.16}$$

and by defining $a = 1 + \lambda^2 {h_k}^2/2$ and $b = \lambda^2 {h_k}^2/2$ (this satisfies the condition $a \geq |b|$). Since $\cos(n\pi + t) = (-1)^n \cos(t)$ and the integral is independent of the sign of b, $(-1)^n$ is also included in the b part. If we divide the integral range $0 - 4\pi m$ into $4m$ segments with the length of π, all the integral values are identical. Therefore, the total integral is $4m$ times the integral value with the range of $0 - \pi$;

$$-\int_0^{4\pi m} \left\{ 1 + \frac{\lambda^2 {h_k}^2}{2} + \frac{\lambda^2 {h_k}^2}{2} \cos x \right\} dx = -4m\pi \ln \frac{1}{2} \left\{ 1 + \frac{\lambda^2 {h_k}^2}{2} + \sqrt{1 + \lambda^2 {h_k}^2} \right\}. \tag{B.17}$$

Hence,

$$M_{Re(C_m)}(\lambda) = \left[\frac{1}{2}\left(1 + \frac{\lambda^2 {h_k}^2}{2} + \sqrt{1+\lambda^2 {h_k}^2}\right)\right]^{-N}. \tag{B.18}$$

When λ is small enough, we can expand $M(\lambda)$ by λ. Since

$$M'(\lambda) = -N\left[\frac{1+\lambda^2 {h_k}^2/2 + \sqrt{1+\lambda^2 {h_k}^2}}{2}\right]^{-N-1}\left(\frac{1}{2}(\lambda {h_k}^2 + \frac{\lambda {h_k}^2}{\sqrt{1+\lambda^2 {h_k}^2}})\right) \tag{B.19}$$

and

$$\begin{aligned} M''(\lambda) &= -N \times \left\{(-N-1)\left[\frac{1+\lambda^2 {h_k}^2/2 + \sqrt{1+\lambda^2 {h_k}^2}}{2}\right]^{-N-2} \times \right. \\ &\left(\frac{1}{2}(\lambda {h_k}^2 + \frac{\lambda {h_k}^2}{\sqrt{1+\lambda^2 {h_k}^2}})\right)^2 + \left[\frac{1+\lambda^2 {h_k}^2/2 + \sqrt{1+\lambda^2 {h_k}^2}}{2}\right]^{-N-1} \times \\ &\left.\left(\frac{{h_k}^2}{2}\left(1 + \frac{\sqrt{1+\lambda^2 {h_k}^2} - 2\lambda\lambda {h_k}^2/\sqrt{1+\lambda^2 {h_k}^2}}{1+\lambda^2 {h_k}^2}\right)\right)\right\}, \end{aligned} \tag{B.20}$$

we have

$$M(0) = 1, \quad M'(0) = 0, \quad M''(0) = -N {h_k}^2, \tag{B.21}$$

and the second-order expansion is

$$M_{Re(C_m)}(\lambda) = 1 - \frac{N {h_k}^2 \lambda^2}{2}. \tag{B.22}$$

The imaginary part can be evaluated in the same manner. Since the characteristic function of the imaginary part is written as

$$M_{Im(C_m)}(\lambda) = \prod_{j=1}^{N} \frac{1}{1 + (\lambda h_k \sin(2\pi m j/N))^2} \tag{B.23}$$

$$\ln M_{Im(C_m)}(\lambda) = -\sum_{j=1}^{N}\left\{1 + \frac{\lambda^2 {h_k}^2}{2} - \frac{\lambda^2 {h_k}^2}{2}\cos(4\pi m j/N)\right\}, \tag{B.24}$$

which is almost the same as that of the real part, we obtain the same expansion:

$$M_{Im(C_m)}(\lambda) = \left[\frac{1}{2}\left(1 + \frac{\lambda^2 {h_k}^2}{2} + \sqrt{1+\lambda^2 {h_k}^2}\right)\right]^{-N} \to 1 - \frac{N {h_k}^2 \lambda^2}{2} \text{ (if } \lambda \ll 1). \tag{B.25}$$

On the other hand, the characteristic function of normal distribution function $\mathrm{N}(0, \sigma^2)$, $\phi(x) = \exp[-x^2/(2\sigma^2)]/(\sqrt{2\pi}\sigma)$, is

$$M(\lambda) = e^{-\sigma^2\lambda^2/2} \to 1 - \frac{\sigma^2\lambda^2}{2} \text{ (if } \lambda \ll 1). \tag{B.26}$$

Hence, the distribution functions of the real and imaginary parts of C_m are approximately the normal distribution with average of 0 and variance of ${Nh_k}^2$.

Note that Fourier transform of p, C_m, is the sum of N independent random variables characterized by Laplace distribution weighted by cosine function. For the simple sum of N variables (not weighted), the central limit theorem implies that the sum is characterized by $\mathrm{N}(0, 2{Nh_k}^2)$, because the average of p is 0 and the variance of p is 2.

Strictly speaking, the cross-correlation function in the form of Equation (5.7) is not a simple Fourier transform of the Laplace distribution variables; some multiplication factors, products of two $\sqrt{P}$, appear in the formula. But if the factor is not a peculiar function and is distributed in a broad range of its argument, the distribution function of the cross-correlation function discussed in this section may be considered to be a good approximation.

B.2 Details on Calculation of Average of Squared Cross-Correlation Function

As in Equation (5.21), cross-correlation function squared is written in the form of

$$\begin{aligned} C_{r,s,l}C^*_{r,s,l} &= (\alpha h_\omega h_k)^4 \sum_{j=0}^{N_\omega-1}\sum_{m=0}^{N_k-1}\sum_{n=0}^{N_k-1}\sum_{j'=0}^{N_\omega-1}\sum_{m'=0}^{N_k-1}\sum_{n'=0}^{N_k-1} \sqrt{P_{mj}}\sqrt{P_{nj}}\sqrt{P_{m'j'}}\sqrt{P_{n'j'}} \\ &\times e^{i2\pi[(n-m)-(n'-m')]r/N_k} e^{i2\pi((m-m')s/N_k-(j-j')l/N_\omega)} \\ &\times [(\rho_1+\rho_2)+i(\rho_3-\rho_4)], \end{aligned} \tag{B.27}$$

where

$$\rho_1 = (q_{Rm,j}q_{Rn,j}+q_{Im,j}q_{In,j})(q_{Rm',j'}q_{Rn',j'}+q_{Im',j'}q_{In',j'}) \tag{B.28}$$

$$\rho_2 = (q_{Rm,j}q_{In,j}-q_{Im,j}q_{Rn,j})(q_{Rm',j'}q_{In',j'}-q_{Im',j'}q_{Rn',j'}) \tag{B.29}$$

$$\rho_3 = (q_{Rm,j}q_{In,j}-q_{Im,j}q_{Rn,j})(q_{Rm',j'}q_{Rn',j'}+q_{Im',j'}q_{In',j'}) \tag{B.30}$$

$$\rho_4 = (q_{Rm,j}q_{Rn,j}+q_{Im,j}q_{In,j})(q_{Rm',j'}q_{In',j'}-q_{Im',j'}q_{Rn',j'}). \tag{B.31}$$

According to the combination of the indices of q, we classify the products of q into 9 categories, discussed below, to calculate the ensemble average of $(\rho_1+\rho_2)+i(\rho_3-\rho_4)$, using the following relationships:

$$< q >= 0,\ < q^2 >= 1,\ < q^4 >= 3,\ < qq' >= 0\ (q \neq q'). \tag{B.32}$$

The contribution to the ensemble average, $< (\rho_1 + \rho_2) + i(\rho_3 - \rho_4) >$, from all the other combinations of the indices are zero.

B.2.1 Classification

When we take the ensemble average of $(\rho_1 + \rho_2) + i(\rho_3 - \rho_4)$, only those terms I list below can contribute:

1. $j = j'$、$m = n = m' = n'$
2. $j = j'$、$m = n, m' = n', m \neq m'$
3. $j = j'$、$m = m', n = n', m \neq n$
4. $j = j'$、$m = n', n = m', m \neq n$
5. $j \neq j'$、$m = n = m' = n'$
6. $j \neq j'$、$m = n$、$m' = n'$、$m \neq m'$
7. $j = N_\omega - j'$、$m = n = N_k - m' = N_k - n'$
8. $j = N_\omega - j'$、$m = N_k - m'$、$n = N_k - n'$、$m \neq n$
9. $j = N_\omega - j'$、$m = N_k - n'$、$n = N_k - m'$、$m \neq n$

1. In the case of $j = j'$ and $m = n = m' = n'$, all the q_R are identical and the same is true for all the q_I. Using these, we obtain

$$\begin{aligned} < \rho_1 > &= < (q_R^2 + q_I^2)(q_R^2 + q_I^2) >=< q_R^4 + q_I^4 + 2q_R^2 q_I^2 >= 8 \\ < \rho_2 > &= < (q_R q_I - q_I q_R)(q_R q_I - q_I q_R) >= 0 \\ < \rho_3 > &= < (q_R q_I - q_R q_I)(q_R^2 + q_I^2) >= 0 \\ < \rho_4 > &= < (q_R^2 + q_I^2)(q_R q_I - q_I q_R) >= 0. \end{aligned}$$

Therefore,

$$< \rho_1 + \rho_2 + i(\rho_3 + \rho_4) >= 8. \tag{B.33}$$

2. In the case of $j = j'$, $m = n$, $m' = n'$, and $m \neq m'$, $q_{Rmj} = q_{Rnj} = q_R$ and $q_{Rm'j} = q_{Rn'j} = q'_R$, and for the imaginary part we may define q_I and q'_I in the same manner. Hence, we obtain

$$\begin{aligned} < \rho_1 > &= < (q_R^2 + q_I^2)({q'_R}^2 + {q'_I}^2) >= 4 < q^2 q'^2 >= 4 \\ < \rho_2 > &= < (q_R q_I - q_I q_R)(q'_R q'_I - q'_I q'_R) >= 0 \\ < \rho_3 > &= < (q_R q_I - q_R q_I)({q'_R}^2 + {q'_I}^2) >= 0 \\ < \rho_4 > &= < (q_R^2 + q_I^2)(q'_R q'_I - q'_I q'_R) >= 0. \end{aligned}$$

Therefore,

$$< \rho_1 + \rho_2 + i(\rho_3 + \rho_4) >= 4. \tag{B.34}$$

3. In the case of $j = j'$, $m = m'$, $n = n'$, and $m \neq n$, $q_{Rmj} = q_{Rm'j} = q_R$ and $q_{Rnj} = q_{Rn'j} = q'_R$, and for the imaginary part we may define q_I, q'_I in the same manner. Using these, we obtain

$$\begin{aligned} < \rho_1 > &= < (q_R q'_R + q_I q'_I)^2 > \\ &= < {q_R}^2 {q'_R}^2 + {q_I}^2 {q'_I}^2 + 2 q_R q'_R q_I q'_I >= 2 < q^2 >= 2 \\ < \rho_2 > &= < (q_R q'_I - q_I q'_R)^2 > \\ &= < {q_R}^2 {q'_R}^2 + {q_I}^2 {q'_I}^2 - 2 q_R q'_R q_I q'_I >= 2 < q^2 >= 2 \\ < \rho_3 > &= < (q_R q'_I - q_I q'_R)(q_R q'_R + q_I q'_I) >= 0 \\ < \rho_4 > &= < (q_R q'_R + q_I q'_I)(q_R q'_I - q_I q'_R) >= 0. \end{aligned}$$

Therefore,

$$< \rho_1 + \rho_2 + i(\rho_3 + \rho_4) >= 4. \tag{B.35}$$

4. In the case of $j = j'$、 $m = n'$, $n = m'$, and $m \neq n$, $q_{Rmj} = q_{Rn'j} = q_R$, and $q_{Rmj} = q_{Rn'j} = q'_R$. We may define q_I and q'_I for the imaginary part in the same manner. Using these, we obtain

$$\begin{aligned} < \rho_1 > &= < (q_R q'_R + q_I q'_I)(q'_R q_R + q'_I q_I) > \\ &= < {q_R}^2 {q'_R}^2 + {q_I}^2 {q'_I}^2 + 2 q_R q'_R q_I q'_I >= 2 < q^2 >= 2 \\ < \rho_2 > &= < (q_R q'_I - q_I q'_R)(q'_R q_I - q'_I q_R) > \end{aligned}$$

$$
\begin{aligned}
&= < q_R q'_R q_I q'_I - {q'_R}^2 {q_I}^2 - {q_R}^2 {q'_I}^2 + q_I q'_I q'_R q_R >= -2 \\
< \rho_3 > &= 0 \\
< \rho_4 > &= 0.
\end{aligned}
$$

Therefore,

$$< \rho_1 + \rho_2 + i(\rho_3 + \rho_4) >= 0. \tag{B.36}$$

5. In the case of $j \neq j'$ and $m = n = m' = n'$, we define $q_{Rmj} = q_{Rnj} = q_R$, $q_{Rmj'} = q_{Rnj'} = q'_R$ and for the imaginary part q_I and q'_I in the same manner. We obtain

$$
\begin{aligned}
< \rho_1 > &= < (q_R^2 + q_I^2)({q'_R}^2 + {q'_I}^2) >= 4 < q^2 q'^2 >= 4 \\
< \rho_2 > &= < (q_R q_I - q_I q_R)(q'_R q'_I - q'_I q'_R) >= 0 \\
< \rho_3 > &= < (q_R q_I - q_R q_I)({q'_R}^2 + {q'_I}^2) >= 0 \\
< \rho_4 > &= < (q_R^2 + q_I^2)(q'_R q'_I - q'_I q'_R) >= 0.
\end{aligned}
$$

Therefore,

$$< \rho_1 + \rho_2 + i(\rho_3 + \rho_4) >= 4. \tag{B.37}$$

6. In the case of $j \neq j'$, $m = n$、 $m' = n'$, and $m \neq m'$, we define $q_{Rmj} = q_{Rnj} = q_R$, $q_{Rm'j'} = q_{Rn'j'} = q'_R$. In the same manner, we may define q_I and q'_I for the imaginary part as well. We obtain

$$
\begin{aligned}
< \rho_1 > &= < (q_R^2 + q_I^2)({q'_R}^2 + {q'_I}^2) >= 4 < q^2 q'^2 >= 4 \\
< \rho_2 > &= < (q_R q_I - q_I q_R)(q'_R q'_I - q'_I q'_R) >= 0 \\
< \rho_3 > &= < (q_R q_I - q_R q_I)({q'_R}^2 + {q'_I}^2) >= 0 \\
< \rho_4 > &= < (q_R^2 + q_I^2)(q'_R q'_I - q'_I q'_R) >= 0.
\end{aligned}
$$

Therefore,

$$< \rho_1 + \rho_2 + i(\rho_3 + \rho_4) >= 4. \tag{B.38}$$

7. In the case of $j = N_\omega - j'$ and $m = n = N_k - m' = N_k - n'$, we define $q_{Rmj} = q_{Rnj} = q_{Rm'j'} = q_{Rn'j'} = q_R$ and $q_{Imj} = q_{Inj} = -q_{Im'j'} = -q_{In'j'} = q_I$. Therefore,

$$< \rho_1 > = < (q_R q_R + q_I q_I)(q_R q_R + (-q_I)(-q_I)) >= 2 < q^4 > + 2 < q^2 >^2 = 8$$

$$
\begin{aligned}
< \rho_2 > &= < (q_R q_I - q_I q_R)(q_R(-q_I) - (-q_I)q_R) >= 0 \\
< \rho_3 > &= 0 \\
< \rho_4 > &= 0.
\end{aligned}
$$

Therefore,

$$
\Rightarrow \quad < \rho_1 + \rho_2 + i(\rho_3 + \rho_4) >= 8. \tag{B.39}
$$

8. In the case of $j = N_\omega - j'$, $m = N_k - m'$, $n = N_k - n'$, and $m \neq n$, we define $q_{Rmj} = q_{Rm'j'} = q_R$, $q_{Rnj} = q_{Rn'j'} = q'_R$ and $q_{Imj} = -q_{Im'j'} = q_I$, $q_{Inj} = -q_{In'j'} = q'_I$. Using these, we obtain

$$
\begin{aligned}
< \rho_1 > &= < (q_R q'_R + q_I q'_I)(q_R q'_R + (-q_I)(-q'_I)) >= 2 < q^2 >^2 = 2 \\
< \rho_2 > &= < (q_R q'_I - q_I q'_R)(q_R(-q'_I) + (-q_I)q'_R) >= -2 < q^2 >^2 = -2 \\
< \rho_3 > &= 0 \\
< \rho_4 > &= 0.
\end{aligned}
$$

Therefore,

$$
< \rho_1 + \rho_2 + i(\rho_3 + \rho_4) >= 0. \tag{B.40}
$$

9. In the case of $j = N_\omega - j'$, $m = N_k - n'$, $n = N_k - m'$, and $m \neq n$, we define $q_{Rmj} = q_{Rn'j'} = q_R$, $q_{Rnj} = q_{Rm'j'} = q'_R$ and $q_{Imj} = -q_{In'j'} = q_I$, $q_{Inj} = -q_{Im'j'} = q'_I$. Using these, we obtain

$$
\begin{aligned}
< \rho_1 > &= < (q_R q'_R + q_I q'_I)(q'_R q_R + (-q'_I)(-q_I)) >= 2 < q^2 >^2 = 2 \\
< \rho_2 > &= < (q_R q'_I - q_I q'_R)(q'_R(-q_I) - (-q'_I)q_R) >= 2 < q^2 >^2 = 2 \\
< \rho_3 > &= 0 \\
< \rho_4 > &= 0.
\end{aligned}
$$

Therefore,

$$
< \rho_1 + \rho_2 + i(\rho_3 + \rho_4) >= 4. \tag{B.41}
$$

B.2.2 Contribution of summations in each case to $< C^*C >$

We divide the summation in expression (5.21), for $< C^*C >$, into 9 parts, considering the classifications discussed above. Here we omit the factor $(\alpha h_\omega h_k)^4$ and define each summation for each case as $I_i (i = 1 \ldots, 9)$: $< C^*C >= (\alpha h_\omega h_k)^4 \sum_{i=1}^{9} I_i$. Each part of the summation is as follows:

$$I_1 = \sum_{j=0}^{N_\omega-1} \sum_{m=0}^{N_k-1} {P_{mj}}^2 \times 8 \tag{B.42}$$

$$I_2 = \sum_{j=0}^{N_\omega-1} \sum_{m=0}^{N_k-1} \sum_{m'=0}^{N_k-1} P_{mj} P_{m'j} e^{i2\pi(m-m')s/N_k} \times 4 - \sum_{j=0}^{N_\omega-1} \sum_{m=0}^{N_k-1} {P_{mj}}^2 \times 4 \tag{B.43}$$

$$I_3 = \sum_{j=0}^{N_\omega-1} \sum_{m=0}^{N_k-1} \sum_{n=0}^{N_k-1} P_{mj} P_{nj} \times 4 - \sum_{j=0}^{N_\omega-1} \sum_{m=0}^{N_k-1} {P_{mj}}^2 \times 4 \tag{B.44}$$

$$I_4 = 0 \tag{B.45}$$

$$I_5 = \sum_{j=0}^{N_\omega-1} \sum_{j'=0}^{N_\omega-1} \sum_{m=0}^{N_k-1} P_{mj} P_{mj'} e^{-2\pi(j-j')l/N_\omega} \times 4 - \sum_{j=0}^{N_\omega-1} \sum_{m=0}^{N_k-1} {P_{mj}}^2 \times 4 \tag{B.46}$$

$$\begin{aligned} I_6 = & \sum_{j=0}^{N_\omega-1} \sum_{j'=0}^{N_\omega-1} \sum_{m=0}^{N_k-1} \sum_{m'=0}^{N_k-1} P_{mj} P_{m'j'} e^{i2\pi\{(m-m')s/N_k-(j-j')l/N_\omega\}} \times 4 + \sum_{j=0}^{N_\omega-1} \sum_{m=0}^{N_k-1} {P_{mj}}^2 \times 4 \\ & - \sum_{j=0}^{N_\omega-1} \sum_{j'=0}^{N_\omega-1} \sum_{m=0}^{N_k-1} P_{mj} P_{mj'} e^{-i2\pi(j-j')l/N_\omega} \times 4 - \sum_{j=0}^{N_\omega-1} \sum_{m=0}^{N_k-1} \sum_{m'=0}^{N_k-1} P_{mj} P_{m'j} e^{i2\pi(m-m')s/N_k} \times 4 \\ & - \sum_{j=0}^{N_\omega-1} \sum_{m=0}^{N_k-1} {P_{mj}}^2 e^{i2\pi(2ms/N_k-2jl/N_\omega)} \times 4 \end{aligned} \tag{B.47}$$

$$I_7 = \sum_{j=0}^{N_\omega-1} \sum_{m=0}^{N_k-1} {P_{mj}}^2 e^{i2\pi(2ms/N_k-2jl/N_\omega)} \times 8 \tag{B.48}$$

$$I_8 = 0 \tag{B.49}$$

$$\begin{aligned} I_9 = & \sum_{j=0}^{N_\omega-1} \sum_{m=0}^{N_k-1} \sum_{n=0}^{N_k-1} P_{mj} P_{nj} e^{i2\pi\{(m+n)s/N_k-2jl/N_\omega\}} \times 4 \\ & - \sum_{j=0}^{N_\omega-1} \sum_{m=0}^{N_k-1} {P_{mj}}^2 e^{i2\pi\{2ms/N_k-2jl/N_\omega\}} \times 4 \end{aligned} \tag{B.50}$$

Note that the terms listed below cancel each other:

- I_1, second term in I_2, and second term in I_3
- first term in I_2, and fourth term in I_6

- second term in I_5, and second term in I_6
- first term in I_5, and third term in I_6
- I_7, fifth term in I_6, and second term in I_9

Therefore, the terms remain are the first terms in I_3, I_6, and I_9. In this way, we obtain the ensemble average of squared cross-correlation function as Equation (5.22).

B.3 Temporal Covariance of the Cross-Correlation Function

We calculate the covariance of two cross-correlation functions at the same spatial point but at the different times, $< C_i C_j > - < C_i >< C_j >$, where i, j are indices of time. The calculation process is basically the same as that for variance. The covariance is

$$\begin{aligned} & C_{r,s,l} C^*_{r,s,l'} \\ = \; & (\alpha h_\omega h_k)^4 \sum_{j=0}^{N_\omega-1} \sum_{m=0}^{N_k-1} \sum_{n=0}^{N_k-1} \sum_{j'=0}^{N_\omega-1} \sum_{m'=0}^{N_k-1} \sum_{n'=0}^{N_k-1} \sqrt{P_{mj}} \sqrt{P_{nj}} \sqrt{P_{m'j'}} \sqrt{P_{n'j'}} \\ \times \; & e^{i2\pi(n-m)r/N_k} e^{-i2\pi(n'-m')r/N_k} e^{i2\pi(ms/N_k - jl/N_\omega)} e^{-i2\pi(m's/N_k - j'l'/N_\omega)}. \end{aligned} \tag{B.51}$$

Taking the ensemble average of the covariance, we obtain

$$\begin{aligned} & < C_{r,s,l} C^*_{r,s,l'} > \\ = \; & (\alpha h_\omega h_k)^4 \Bigg[\sum_j \sum_m {P_{mj}}^2 e^{i2\pi(l'-l)j/N_\omega} \times 8 \\ & + \Big(\sum_j \sum_m \sum_{m'} P_{mj} P_{m'j} e^{i2\pi j(l'-l)/N_\omega} \times 4 - \sum_j \sum_m {P_{mj}}^2 e^{i2\pi j(l'-l)/N_\omega} \times 4 \Big) \\ & + \Big(\sum_j \sum_m \sum_n P_{mj} P_{nj} e^{i2\pi(jl-j'l')/N_\omega} \times 4 - \sum_j \sum_m {P_{mj}}^2 e^{-2\pi j(l-l')/N_\omega} \times 4 \Big) \\ & + \Big(\sum_j \sum_{j'} \sum_m P_{mj} P_{mj'} e^{-i[2\pi/N_k(2ms) - 2\pi(jl-j'l')/N_\omega]} \times 4 - \sum_j \sum_m {P_{mj}}^2 e^{-2\pi j(l-l')/N_\omega} \times 4 \Big) \\ & + \Big(\sum_j \sum_{j'} \sum_m \sum_{m'} P_{mj} P_{m'j'} e^{i[2\pi(m-m')s/N_k - 2\pi(jl-j'l')/N_\omega]} \times 4 \\ & - \sum_j \sum_m \sum_{m'} P_{mj} P_{m'j} e^{i[2\pi(m-m')s/N_k - 2\pi j(l-l')/N_\omega]} \times 4 \\ & - \sum_j \sum_{j'} \sum_m P_{mj} P_{mj'} e^{-i[2\pi/N_k(2ms) - 2\pi(jl-j'l')/N_\omega]} \times 4 \end{aligned}$$

$$
\begin{aligned}
&- \sum_j \sum_m {P_{mj}}^2 e^{i[2\pi(2ms)/N_k - 2\pi/N_\omega j(l+l')]} \times 4 + \sum_j \sum_m {P_{mj}}^2 e^{-i2\pi(l-l')j/N_\omega} \times 4\Big) \\
&+ \sum_j \sum_m {P_{mj}}^2 e^{-i[2\pi/N_k(2ms) - 2\pi j(l+l')/N_\omega]} \times 8 \\
&+ \Big(\sum_j \sum_m \sum_n P_{mj} P_{nj} e^{-i[2\pi/N_k(m+n)s - j(l+l')/N_\omega]} \times 4 \\
&- \sum_j \sum_m {P_{mj}}^2 e^{-i[2\pi/N_k(2ms) - j(l+l')/N_\omega]} \times 4\Big)\Bigg] \\
= \;& 4(\alpha h_\omega h_k)^4 \Bigg[\sum_j \sum_m \sum_n P_{mj} P_{nj} e^{i2\pi(l'-l)j/N_\omega} + \sum_j \sum_m \sum_n P_{mj} P_{nj} e^{i2\pi[(m+n)s/N_k - j(l+l')/N_\omega]} \\
&+ \sum_j \sum_{j'} \sum_m \sum_m P_{mj} P_{nj} e^{i2\pi[(m-m')s/N_k - (jl - j'l')/N_\omega]} \Bigg]. \qquad \text{(B.52)}
\end{aligned}
$$

Since the third term corresponds to $< C_{rsl} >< {C_{rsl'}}^* >$, we obtain

$$
\begin{aligned}
& < C_{r,s,l} C^*_{r,s,l'} > - < C_{rsl} >< {C_{rsl'}}^* > \\
= \;& (h_\omega h_k)^4 \Bigg[\sum_j \sum_m \sum_n P_{mj} P_{nj} e^{i2\pi(l'-l)j/N_\omega} \\
&+ \sum_j \sum_m \sum_n P_{mj} P_{nj} e^{i2\pi[(m+n)s/N_k - j(l+l')/N_\omega]} \Bigg]. \qquad \text{(B.53)}
\end{aligned}
$$

This reduces to the expression for variance (Equation 5.23) if $l = l'$. As was discussed in §5.2.6, the second summation of Equation (5.23) is much less than the first summation of the equation, which led to the the nearly constant variance. In the case of the covariance (Equation B.53), the situation is similar; the second summation is of a similar construction to the corresponding term in Equation (5.23) and less than the first term in variance. The first term in the covariance, however, is also the sum of the oscillating term if $l \neq l'$ and is normally smaller than the first term in variance. Therefore, the correlation of $C_{r,s,l}$ between different temporal data points (l) is negligible compared to the variance of C, i.e., the cross-correlation functions at different temporal data points are approximately uncorrelated under the assumption for the model of the stochastically excited solar oscillations (§5.2.1).

Figure B.1 shows one example of the covariance matrix. The power spectrum used in the calculation is obtained by the *Hinode*/SOT observation in Ca II H line on 23 November 2007; the dataset is the same as that is used in Chapter 4. Note that we applied the filters mentioned in §4.3 to the wavefield. The top panel shows the covariance matrix of the cross-correlation function for the distance of 14.86 Mm. The indices i and j refer to the temporal

data points. The middle panel displays a cross section along the line $i = -j$. It shows that the correlations between different temporal data points are not always zero, but even within a short time lag it is oscillating fast around zero, and in that sense, roughly speaking, cross-correlation functions at different data points are approximately uncorrelated. In the bottom panel a cross section along the line $i = j$, i.e., the diagonal elements of the covariance matrix (variance), is shown. The variance is nearly constant and is consistent with the discussion in §5.2.6.

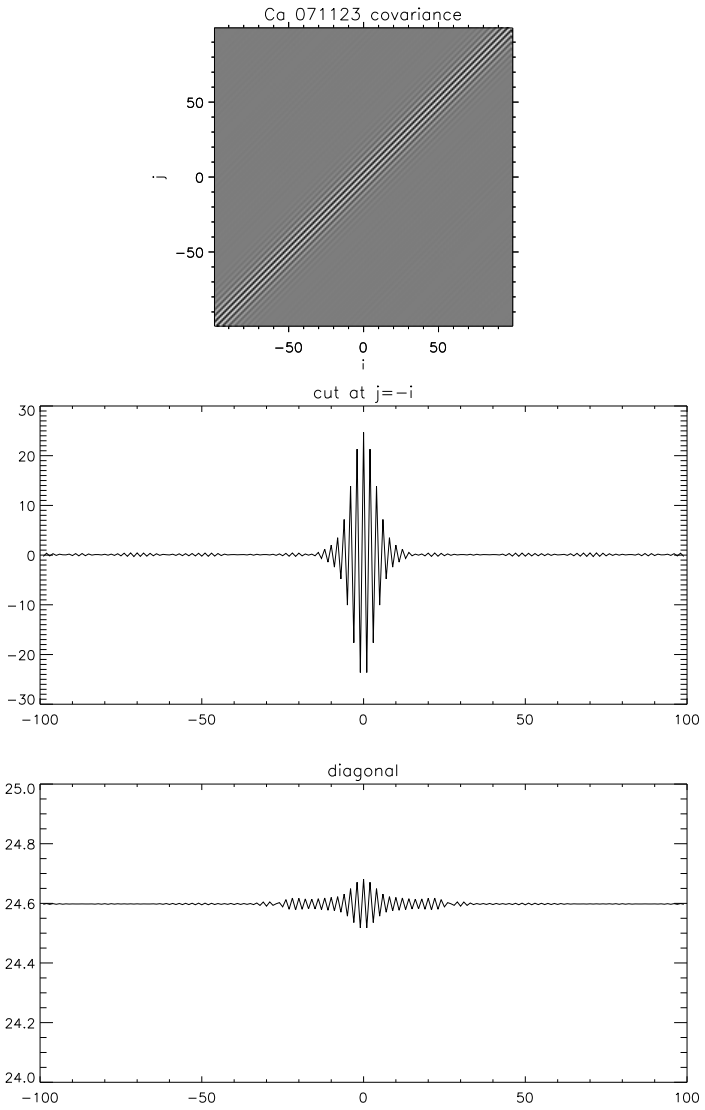

Figure B.1 The covariance matrix of the cross-correlation function, $< C_i C_j > - < C_i >< C_j >$ for filtered Ca II intensity data obtained by SOT on 23 November 2007. The filtering is the same that is mentioned in §4.3; the phase-speed filter used is for the distance of 14.86 Mm.

Appendix C

Derivation of the Green's Function for the Wave Equation in Stratified Atmosphere

Here we consider solving the wave equation (Equation 3.32) in §3.5.2

$$\frac{\partial^2 \xi(z,t)}{\partial t^2} - \frac{1}{\rho_0(z)} \frac{\partial}{\partial z} \left(\rho(z) c^2(z) \frac{\partial \xi(z,t)}{\partial z} \right) = f(z,t),$$

where ξ is the displacement due to the oscillation caused by source function $f(z,t)$ in a plane parallel medium with varying density $\rho(z)$ and sound speed $c(z)$, using a Green's function.

If we introduce a new variable u defined in the following manner:

$$\xi(z,t) = u(z,t) e^{z/2H}, \tag{C.1}$$

where H is the scale height, then by using the acoustic cutoff frequency, $\omega_{\rm ac} \equiv c/(2H)$, the wave equation is

$$\frac{\partial^2 u}{\partial t^2} - c^2 \frac{\partial^2 u}{\partial x^2} + {\omega_{\rm ac}}^2 u = f e^{-z/2H} \ . \tag{C.2}$$

If we consider the case that the source is a pulse, i.e., $f \exp(-z/2H) = A\delta(z)\delta(t)$, where A is an amplitude with appropriate unit, the Green's function in the Fourier domain corresponding to this equation, $A\tilde{G}(k,\omega)$, should satisfy

$$-\omega^2 \tilde{G} + c^2 k^2 \tilde{G} + \omega_{\rm ac}^2 \tilde{G} = \frac{1}{(2\pi)^2}. \tag{C.3}$$

Hence,

$$\tilde{G}(k,\omega) = -\frac{1/(2\pi)^2}{\omega^2 - {\omega_{\rm ac}}^2 - c^2 k^2}. \tag{C.4}$$

The inverse Fourier transform of $\tilde{G}$ is

$$G(z,t) = \int_{-\infty}^{+\infty} dk \int_{-\infty}^{+\infty} d\omega \tilde{G}(k,\omega) e^{i(kz-\omega t)}. \tag{C.5}$$

Considering the appropriate boundary condition for this Green's function, we obtain

$$G(z,t) = \begin{cases} 0 & (t<0) \\ \frac{1}{4\pi}\int_{-\infty}^{+\infty} dk e^{ikz} \frac{\sin(\sqrt{\omega_{\rm ac}^2+k^2c^2}t)}{\sqrt{\omega_{\rm ac}^2+k^2c^2}} & (t>0). \end{cases} \tag{C.6}$$

With

$$\int_{-\infty}^{+\infty} dk e^{ikz} \frac{\sin(\sqrt{k^2+1}t)}{\sqrt{k^2+1}} = \pi J_0(\sqrt{t^2-z^2}) H(t^2-z^2) \tag{C.7}$$

(p.544 in Lamb 1975), we have

$$G(z,t) = \begin{cases} 0 & (t<0) \\ \frac{1}{4c} J_0\left(\frac{\omega_{\rm ac}}{c}\sqrt{c^2t^2-z^2}\right) H\left(\frac{{\omega_{\rm ac}}^2}{c^2}(c^2t^2-z^2)\right) & (t>0), \end{cases} \tag{C.8}$$

where J_0 is Bessel function of the zeroth order, and H is the Heaviside step function. Since

$$H\left(\frac{{\omega_{\rm ac}}^2}{c^2}(c^2t^2-z^2)\right) = \begin{cases} 0 & (-z/c<t<z/c) \\ 1 & (t<-z/c, z/c<t) \end{cases} \tag{C.9}$$

in the domain $z>0$, we have for $t>0$

$$G(z,t) = \frac{1}{4c} J_0\left(\frac{\omega_{\rm ac}}{c}\sqrt{c^2t^2-z^2}\right) H\left(\frac{\omega_{\rm ac}}{c}(ct-z)\right). \tag{C.10}$$

Using this Green's function, we have

$$\begin{aligned} u(z,t) &= \int_{-\infty}^{+\infty} dt' \int_{-\infty}^{+\infty} dz' G(z-z',t-t') f(z',t') e^{-z'/2H} \\ &= \frac{1}{4c}\int_{-\infty}^{+\infty} dt' \int_{-\infty}^{+\infty} dz' J_0\left(\frac{\omega_{\rm ac}}{c}\sqrt{c^2(t-t')^2-(z-z')^2}\right) \\ &\quad \times H\left(\frac{\omega_{\rm ac}}{c}(c(t-t')-(z-z'))\right) f(z',t') e^{-z'/2H}. \end{aligned} \tag{C.11}$$

For the case of $f(z',t')e^{-z'/2H} = f(t')\delta(z')$, we have for the displacement

$$\xi(z,t) = e^{z/2H}\int_{-\infty}^{+\infty} dt' G(z,t-t') f(t') \tag{C.12}$$

$$= \frac{1}{4c} e^{z/2H}\int_{-\infty}^{+\infty} dt' J_0\left(\frac{\omega_{\rm ac}}{c}\sqrt{c^2(t-t')^2-z^2}\right) H\left(\frac{\omega_{\rm ac}}{c}(c(t-t')-z)\right) f(t')$$

$$= \frac{1}{4c} e^{z/2H}\int_{-\infty}^{t-z/c} dt' J_0\left(\frac{\omega_{\rm ac}}{c}\sqrt{c^2(t-t')^2-z^2}\right) f(t'). \tag{C.13}$$

This is Equation (3.33) in §3.5.2.

Appendix D

Diagnostic Diagram of a Cubic Sun and a Uniform Sun

To understand the ridge features in the diagnostic $(k-\omega)$ diagram of the Sun (Figure 1.2 in Chapter 1), we examine two simpler cases: a cubic Sun and a uniform Sun.

D.1 Diagnostic Diagram of a Cubic Sun

Let us consider the diagnostic diagram of a cubic Sun, assuming the Sun as a uniform cube with the size L. We assign the free boundary condition. The wavelength of the eigenoscillation in x-direction is

$$\lambda_{x,l_x} = \frac{2L}{l_x},$$

where $l_x = 1, 2, \cdots$. Hence, the wavenumber is

$$k_{x,l_x} = \frac{\pi l_x}{L} \tag{D.1}$$

by an analogy of the eigenoscillations of a one-dimensional string. We obtain the wavenumbers in y and z directions in the similar way:

$$k_{y,l_y} = \frac{\pi l_y}{L},\ k_{z,l_z} = \frac{\pi l_z}{L}. \tag{D.2}$$

We only consider the purely acoustic case. Thus, the dispersion relation is given by

$$\omega^2 = c^2 k^2 = c^2(k_x^2 + k_y^2 + k_z^2) = c^2 \left(\frac{\pi}{L}\right)^2 (l_x^2 + l_y^2 + l_z^2). \tag{D.3}$$

If we observe only $x-y$ plane on the z axis, we can observe only the component:

$$\boldsymbol{k_h} \equiv (k_x, k_y), \tag{D.4}$$

for which

$$k_h{}^2 = k_x{}^2 + k_y{}^2 = \left(\frac{\pi}{L}\right)^2 (l_x^2 + l_y^2). \tag{D.5}$$

Therefore, if we define $l = \sqrt{l_x^2 + l_y^2}$, the dispersion relation is given by

$$\omega^2 = c^2 \left(\frac{\pi}{L}\right)^2 (l^2 + l_z^2). \tag{D.6}$$

An example of a $l - \nu$ diagram is shown in Figure D.1. We used the solar radius as L, $L = 7 \times 10^5$ km, and the sound speed on the solar surface as c, $c = 10$ km s^{-1}.

In this case, a ridge curve is assigned for each l_z in $l - \nu$ diagram.

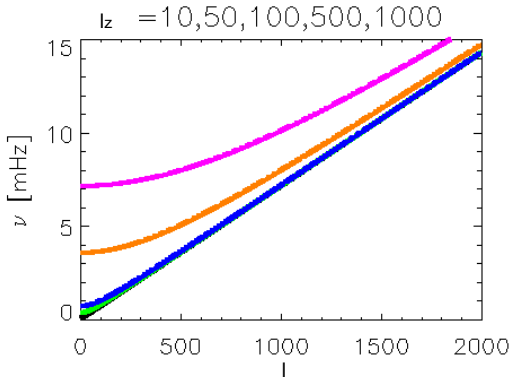

Figure D.1 An example of $l - \nu$ diagram for the cubic Sun. Only the ridges for $l_z = 10$ (black), 50 (green), 100 (blue), 500 (orange), and 1000 (pink) are drawn.

D.2 Diagnostic Diagram of a Uniform Spherical Sun

Let us consider a wave equation in a uniform spherical Sun:

$$\frac{\partial^2 \xi}{\partial t^2} = -c^2 \nabla^2 \xi, \tag{D.7}$$

where ξ is the radial displacement as a function of location and c is the constant sound speed in the Sun. We assume

$$\xi \propto e^{i\omega t},$$

and rewrite the equation using the spherical polar coordinate:

$$\omega^2\xi = c^2\left[\frac{1}{r^2}\frac{\partial}{\partial r}\left(r^2\frac{\partial\xi}{\partial r}\right) + \frac{1}{r^2\sin\theta}\frac{\partial}{\partial\theta}\left(\sin\theta\frac{\partial\xi}{\partial\theta}\right) + \frac{1}{r^2\sin^2\theta}\frac{\partial^2\xi}{\partial\phi^2}\right]. \tag{D.8}$$

Expanding the displacement by the spherical harmonic functions

$$\xi = \sum_{lm} R_l(r)Y_l^m(\theta,\phi), \tag{D.9}$$

we obtain a Bessel-type differential equation:

$$\frac{d^2R_l(r)}{dr^2} + \frac{2}{r}\frac{dR_l(r)}{dr} + \left[\frac{\omega^2}{c^2} - \frac{l(l+1)}{r^2}\right]R_l(r) = 0. \tag{D.10}$$

The solution of this type of differential equation is a spherical Bessel function:

$$R_l(r) \propto j_l(\frac{\omega}{c}r) = j_l(kr)\ . \tag{D.11}$$

For simplicity, we set the fixed boundary condition at the solar surface, namely, $R_l(R_\odot) = 0$. Therefore, for the eigenmodes,

$$j_l(\frac{\omega}{c}R_\odot) = 0, \tag{D.12}$$

i.e., zeros of the spherical Bessel function are on the solar surface. In the limit of sufficiently large arguments z, the spherical Bessel function, $j_l(z)$, is approximated by the asymptotic form:

$$j_l(z) = \frac{1}{z}\cos\left(z - \frac{l+1}{2}\pi\right) \quad (\text{if } z \to \infty). \tag{D.13}$$

In this case, the zeros are

$$z_{n,l} = (n + \frac{l}{2} - 1)\pi, \tag{D.14}$$

where n is an integer. Hence, we obtain

$$\frac{\omega_{n,l}}{c}R_\odot = (n + \frac{l}{2} - 1)\pi, \tag{D.15}$$

and the eigen angular frequency for the uniform spherical Sun is approximately

$$\omega_{n,l} = \frac{c\pi}{R_\odot}\frac{l}{2} + \frac{c\pi}{R_\odot}(n-1). \tag{D.16}$$

In this case, since the eigenfrequency depends linearly on l, the ridge in the diagnostic $l-\nu$ diagram is a straight line. The quantum index, n, indicates each ridge, and the slope of the ridge is proportional to the constant sound speed, c.

The diagnostic diagram of the real Sun (See Figure 1.2 in Chapter 1) shows ridges with steeper slopes in the range of smaller l. This corresponds to the fact that modes with smaller l penetrate deeper in the Sun; the mean sound speed along the path of the mode with smaller l is larger. In this way, the diagnostic diagram reflects the sound speed distribution in the Sun.

Appendix E

Discretized Fourier Transform of Running-Difference Function

To remove any spatial trend from the intensity datasets, we use running-difference intensity to calculate the power via Fourier transform in study of sunspot oscillations (Chapter 2) as well as to calculate cross-correlation functions in the time–distance analyses (Chapters 4 and 6). In this chapter, we summarize the calculations of the discretized Fourier transform using running difference of original series.

Here Δt denotes the interval of the data, N denotes the number of the data, and $f(t)$ denotes the intensity function. The k-th epoch is $t_k = k\Delta t$ $(0 \leq k \leq N-1)$, and f_k denotes $f(t_k)$ for simplicity. The discrete Fourier transform of the function is

$$\mathcal{F}(\omega) = \sum_{k=0}^{N-1} f_k e^{-i\omega t_k} \ . \tag{E.1}$$

This is the 'genuine' discrete Fourier transform of $f(t)$.

Now we would like to know the relationships between the genuine Fourier transform of $f(t)$ and the Fourier transform of the running-difference function $g_k \equiv f_k - f_{k-1}$ $(1 \leq k \leq N-1)$. For that, we define two functions:

$$F_1(\omega) = \sum_{k=1}^{N-1} f_k e^{-i\omega t_k} \tag{E.2}$$

and

$$F_2(\omega) = \sum_{k=0}^{N-2} f_k e^{-i\omega t_k} \, . \tag{E.3}$$

The Fourier transform of g_k is given by

$$G(\omega_j) = \sum_{k=1}^{N-1} g_k e^{-i\omega_j t_k}, \tag{E.4}$$

where

$$\omega_j = \Delta\omega j = \frac{2\pi j}{(N-1)\Delta t}. \tag{E.5}$$

The temporal grid spacing for discretized Fourier transform for the running difference series $\Delta\omega = 2\pi/[(N-1)\Delta t]$. The Fourier transform is calculated as follows:

$$\begin{aligned} G(\omega_j) &= \sum_{k=1}^{N-1} f_k e^{-i\omega_j t_k} - \sum_{k=1}^{N-1} f_{k-1} e^{-i\omega_j t_k} && \text{(E.6)} \\ &= F_1(\omega_j) - \sum_{k'=0}^{N-2} f_{k'} e^{-i\omega_j (t_{k'}+\Delta t)} && \text{(E.7)} \\ &= F_1(\omega_j) - e^{-i\omega_j \Delta t} F_2(\omega_j) && \text{(E.8)} \\ &= \mathcal{F}(\omega_j)(1 - e^{-i\omega_j \Delta t}). && \text{(E.9)} \end{aligned}$$

Note that here we assume $F_1 = F_2 = \mathcal{F}$.

The power for the running-difference series is

$$\begin{aligned} GG^* &= \mathcal{F}\mathcal{F}^*(1 - e^{-i\omega_j \Delta t})(1 - e^{i\omega_j \Delta t}) && \text{(E.10)} \\ &= \mathcal{F}\mathcal{F}^* \times 2\left(1 - \cos(\omega_j \Delta t)\right). && \text{(E.11)} \end{aligned}$$

Therefore, the 'genuine' power is

$$\mathcal{F}\mathcal{F}^* = \frac{GG^*}{1 - \cos(\omega_j \Delta t)}. \tag{E.12}$$

In this way, we can reconstruct the 'genuine' Fourier transform of $f(t)$ by the Fourier transform of the running difference. However, unless the number of samples N is large enough, the assumption $F_1 = F_2 = \mathcal{F}$ is not adequate.

Appendix F

Zero Padding

Computation of cross-correlation function is normally faster when done via Fourier transform, by exploiting (a version of) Wiener-Khintchine's theorem. We use 'zero padding' when we calculate the cross-correlation functions in this thesis. In this chapter, we summarize how the zero padding works. When we calculate a cross-correlation function of $f(t)$ using a discrete finite sequence instead of an infinite sequence, the cross-correlation function obtained is the one which is obtained as if the $f(t)$ is a periodic infinite sequence with the period of $N\Delta t$, where N is the number of data points and Δt is the grid spacing. The zero padding is useful for avoiding this.

For a continuous function $f(t)$, Fourier and inverse Fourier transforms are

$$f(t) = \int_{-\infty}^{\infty} F(\omega) e^{i\omega t} d\omega \tag{F.1}$$

and

$$F(\omega) = \frac{1}{2\pi} \int_{-\infty}^{\infty} f(t) e^{-i\omega t} dt. \tag{F.2}$$

If the functions are discretized, then

$$F(\omega_j) = \frac{\Delta t}{2\pi} \sum_{n=0}^{N-1} f_n e^{-i\omega_j t_n}, \tag{F.3}$$

where f_n is $f_n = f(n\Delta t)$ and N is the number of grid. Discretized angular frequency, ω_j, is given by $\omega_j = j \times \Delta\omega$, where $\Delta\omega = 2\pi/(N\Delta t)$.

Fourier transform of f_n is given by

$$F(\omega_j) = \frac{\Delta t}{2\pi} \sum_{n=0}^{N-1} f_n e^{-i\omega_j t_n} = \frac{\Delta t}{2\pi} \sum_{n=0}^{N-1} f_n e^{-i2\pi nj/N}, \tag{F.4}$$

and the power in Fourier domain, $P(\omega_j)$, is defined as $P(\omega_j) = F(\omega_j)F^*(\omega_j)$.

The cross-correlation function, $\Gamma(\tau)$, is

$$\begin{aligned}
\Gamma(\tau) &= \int_{-\infty}^{\infty} f(t)f^*(t+\tau)dt \\
&= \int_{-\infty}^{\infty}\int_{-\infty}^{\infty}\int_{-\infty}^{\infty} F(\omega)e^{i\omega t}F^*(\omega')e^{-i\omega'(t+\tau)}d\omega d\omega' dt \\
&= \int_{-\infty}^{\infty}\int_{-\infty}^{\infty} d\omega d\omega' F(\omega)F^*(\omega')e^{-i\omega'\tau}\left(\int_{-\infty}^{\infty} e^{i(\omega-\omega')t}dt\right) \\
&= \int_{-\infty}^{\infty}\int_{-\infty}^{\infty} d\omega d\omega' F(\omega)F^*(\omega')e^{-i\omega'\tau}(2\pi\delta(\omega-\omega')) \\
&= 2\pi\int_{-\infty}^{\infty} d\omega P(\omega)e^{-i\omega\tau}. \qquad \text{(F.5)}
\end{aligned}$$

This is also the case when we consider the discretized functions. Therefore, using $\tau_l \equiv (2\pi l)/(N\Delta\omega) = l\Delta t$, where l is a series of positive integers, we obtain

$$\begin{aligned}
\Gamma(\tau_l) &= 2\pi\Delta\omega\sum_{j=0}^{N-1} P(\omega_j)e^{-i\omega_j\tau_l} \\
&= 2\pi\Delta\omega\left(\frac{\Delta t}{2\pi}\right)^2\sum_{j=0}^{N-1}\sum_{n=0}^{N-1}\sum_{n'=0}^{N-1} f_n f^*_{n'}e^{i2\pi j(n'-l-n)/N} \\
&= 2\pi\Delta\omega\left(\frac{\Delta t}{2\pi}\right)^2\sum_{n=0}^{N-1}\sum_{n'=0}^{N-1} f_n f^*_{n'}\left(\sum_{j=0}^{N-1} e^{i2\pi j(n'-l-n)/N}\right). \qquad \text{(F.6)}
\end{aligned}$$

Since

$$\sum_{j=0}^{N-1} e^{i2\pi jm/(N)} = \begin{cases} N & \text{if } m = N\times \text{ integer} \\ \frac{1-e^{i2\pi Nm/(N)}}{1-e^{i2\pi m/(N)}} = 0 & \text{otherwise } (\because m = \text{integer}), \end{cases} \qquad \text{(F.7)}$$

the cross-correlation function is

$$\begin{aligned}
\Gamma(\tau_l) &= 2\pi N\Delta\omega\left(\frac{\Delta t}{2\pi}\right)^2\sum_{n=0}^{N-1}\sum_{n'=0}^{N-1} f_n f^*_{n'}\delta_{n'-n-l,NM} \quad (M\text{: integer}) \\
&= \Delta t\left(\sum_{n=0}^{N-l-1} f_n f^*_{n+l} + \sum_{n=N-l}^{N-1} f_n f^*_{n+l-N}\right). \qquad \text{(F.8)}
\end{aligned}$$

This is the result obtained in the normal way, without the 'zero padding'. For the data points $n \geq N-l$, the product in the (second) summation is the product of f_n with f_{n+l-N}; this would have been all right if f_n were a periodic sequence with the period of N, but

generally we do not expect that to be the case. Essentially, we would like to drop the second summation.

Here we carry out 'zero padding': we add a null sequence of the same length as f_n after f_N:

$$f_n = \begin{cases} f(n\Delta t) & (0 \le n \le N-1) \\ 0 & (N \le n \le 2N-1). \end{cases}$$

Since the length of the sequence has increased to $2N$, we use $\Delta\omega = 2\pi/(\underline{2N}\Delta t)$ in what follows.

In this case, Fourier transform of the new f_n is given by

$$F(\omega_j) = \frac{\Delta t}{2\pi}\sum_{n=0}^{2N-1} f_n e^{-i\omega_j t_n} = \frac{\Delta t}{2\pi}\sum_{n=0}^{2N-1} f_n e^{-i2\pi nj/(2N)}, \tag{F.9}$$

and the power is given by $P = FF^*$. Therefore, the cross-correlation function is

$$\Gamma(\tau_l) = 2\pi\Delta\omega\left(\frac{\Delta t}{2\pi}\right)^2 \sum_{n=0}^{2N-1}\sum_{n'=0}^{2N-1} f_n f^*_{n'} \left(\sum_{j=0}^{2N-1} e^{i2\pi j(n'-l-n)/(2N)}\right). \tag{F.10}$$

In this case,

$$\sum_{j=0}^{2N-1} e^{i2\pi jm/(2N)} = \begin{cases} 2N & \text{if } m = 2N\times \text{ integer} \\ \frac{1-e^{i2\pi 2Nm/(2N)}}{1-e^{i2\pi m/(2N)}} = 0 & \text{otherwise } (\because m = \text{integer}), \end{cases} \tag{F.11}$$

and the cross-correlation function is

$$\begin{aligned} \Gamma(\tau_l) &= 2\pi\Delta\omega\left(\frac{\Delta t}{2\pi}\right)^2 \times 2N \sum_{n=0}^{2N-1}\sum_{n'=0}^{2N-1} f_n f^*_{n'}\delta_{n'-n-l,2NM} \ (M : \text{integer}) \\ &= \Delta t\left(\sum_{n=0}^{2N-l-1} f_n f^*_{n+l} + \sum_{n=2N-l}^{2N-1} f_n f^*_{n+l-2N}\right) \qquad \text{(F.12)} \\ &= \Delta t \sum_{n=0}^{N-l-1} f_n f^*_{n+l} \qquad \text{(F.13)} \end{aligned}$$

because all the f_n for $N \le n \le 2N-1$ are zero.

This is the result we desire.

Bibliography

Ando, H., & Osaki, Y. 1975, PASJ, 27, 581

Appourchaux, T., Chang, H., Gough, D. O., & Sekii, T. 2000, MNRAS, 319, 365

Appourchaux, T., Gizon, L., & Rabello-Soares, M. 1998, A&AS, 132, 107

Beckers, J. M., & Schultz, R. B. 1972, Sol. Phys., 27, 61

Beckers, J. M., & Tallant, P. E. 1969, Sol. Phys., 7, 351

Birch, A. C., Kosovichev, A. G., & Duvall, Jr., T. L. 2004, ApJ, 608, 580

Bogart, R. S., Sá, L. A. D., Haber, D. A., Toomre, J., & Hill, F. 1995, in ESA Special Publication, Vol. 376, Helioseismology, 147–150

Bogdan, T. J. 2000, Sol. Phys., 192, 373

Braun, D. C., & Birch, A. C. 2008, ApJ, 689, L161

Braun, D. C., Duvall, Jr., T. L., & Labonte, B. J. 1987, ApJ, 319, L27

Braun, D. C., Lindsey, C., Fan, Y., & Jefferies, S. M. 1992, ApJ, 392, 739

Brown, T. M., Bogdan, T. J., Lites, B. W., & Thomas, J. H. 1992, ApJ, 394, L65

Brun, A. S., & Toomre, J. 2002, ApJ, 570, 865

Brune, R., & Wöhl, H. 1982, Sol. Phys., 75, 75

Brynildsen, N., Leifsen, T., Kjeldseth-Moe, O., Maltby, P., & Wilhelm, K. 1999, ApJ, 511, L121

Carlsson, M., Hansteen, V. H., de Pontieu, B., McIntosh, S., Tarbell, T. D., Shine, D., Tsuneta, S., Katsukawa, Y., Ichimoto, K., Suematsu, Y., Shimizu, T., & Nagata, S. 2007, PASJ, 59, 663

Centeno, R., Collados, M., & Trujillo Bueno, J. 2006, ApJ, 640, 1153

Chang, H.-K., Chou, D.-Y., Labonte, B., & The TON Team. 1997, Nature, 389, 825

Cheung, M. C. M., Schüssler, M., Tarbell, T. D., & Title, A. M. 2008, ApJ, 687, 1373

Chou, D.-Y., Serebryanskiy, A., Sun, M.-T., & TON Team. 2003, in ESA Special Publication, Vol. 517, GONG+ 2002. Local and Global Helioseismology: the Present and Future, ed. H. Sawaya-Lacoste, 53–60

Christensen-Dalsgaard, J., Dappen, W., Ajukov, S. V., Anderson, E. R., Antia, H. M., Basu, S., Baturin, V. A., Berthomieu, G., Chaboyer, B., Chitre, S. M., Cox, A. N., Demarque, P., Donatowicz, J., Dziembowski, W. A., Gabriel, M., Gough, D. O., Guenther, D. B., Guzik, J. A., Harvey, J. W., Hill, F., Houdek, G., Iglesias, C. A., Kosovichev, A. G., Leibacher, J. W., Morel, P., Proffitt, C. R., Provost, J., Reiter, J., Rhodes, Jr., E. J., Rogers, F. J., Roxburgh, I. W., Thompson, M. J., & Ulrich, R. K. 1996, Science, 272, 1286

Cowling, T. G. 1941, MNRAS, 101, 367

Culhane, J. L., Harra, L. K., James, A. M., Al-Janabi, K., Bradley, L. J., Chaudry, R. A., Rees, K., Tandy, J. A., Thomas, P., Whillock, M. C. R., Winter, B., Doschek, G. A., Korendyke, C. M., Brown, C. M., Myers, S., Mariska, J., Seely, J., Lang, J., Kent, B. J., Shaughnessy, B. M., Young, P. R., Simnett, G. M., Castelli, C. M., Mahmoud, S., Mapson-Menard, H., Probyn, B. J., Thomas, R. J., Davila, J., Dere, K., Windt, D., Shea, J., Hagood, R., Moye, R., Hara, H., Watanabe, T., Matsuzaki, K., Kosugi, T., Hansteen, V., & Wikstol, Ø. 2007, Sol. Phys., 243, 19

de Jager, C., & Duhau, S. 2009, Journal of Atmospheric and Solar-Terrestrial Physics, 71, 239

De Rosa, M. L., Gilman, P. A., & Toomre, J. 2002, ApJ, 581, 1356

Deubner, F.-L. 1975, A&A, 44, 371

Dikpati, M., & Gilman, P. A. 2006, ApJ, 649, 498

Drobyshevski, E. M., & Yuferev, V. S. 1974, Journal of Fluid Mechanics, 65, 33

D'Silva, S. 1996, ApJ, 469, 964

Duvall, Jr., T. L., & Gizon, L. 2000, Sol. Phys., 192, 177

Duvall, Jr., T. L., Jefferies, S. M., Harvey, J. W., & Pomerantz, M. A. 1993, Nature, 362, 430

Evans, J. W., & Michard, R. 1962, ApJ, 136, 493

Giles, P. M., Duvall, T. L., Scherrer, P. H., & Bogart, R. S. 1997, Nature, 390, 52

Giovanelli, R. G. 1972, Sol. Phys., 27, 71

Gizon, L., & Birch, A. C. 2004, Astrophysical Journal, 614, 472

Gizon, L., Duvall, T. L., & Schou, J. 2003, Nature, 421, 43

Gizon, L., Schunker, H., Baldner, C. S., Basu, S., Birch, A. C., Bogart, R. S., Braun, D. C., Cameron, R., Duvall, T. L., Hanasoge, S. M., Jackiewicz, J., Roth, M., Stahn, T., Thompson, M. J., & Zharkov, S. 2009, Space Science Reviews, 144, 249

Golub, L., Deluca, E., Austin, G., Bookbinder, J., Caldwell, D., Cheimets, P., Cirtain, J., Cosmo, M., Reid, P., Sette, A., Weber, M., Sakao, T., Kano, R., Shibasaki, K., Hara, H., Tsuneta, S., Kumagai, K., Tamura, T., Shimojo, M., McCracken, J., Carpenter, J., Haight, H., Siler, R., Wright, E., Tucker, J., Rutledge, H., Barbera, M., Peres, G., & Varisco, S. 2007, Sol. Phys., 243, 63

Goode, P. R., Gough, D., & Kosovichev, A. G. 1992, ApJ, 387, 707

Gough, D. O., & Toomre, J. 1983, Sol. Phys., 82, 401

Gradshteyn, I. S., Ryzhik, I. M., Jeffrey, A., & Zwillinger, D. 2000, Table of Integrals, Series, and Products (Sixth Edition (Hardcover); Academic Press)

Haber, D. A., Hindman, B. W., Toomre, J., Bogart, R. S., Larsen, R. M., & Hill, F. 2002, ApJ, 570, 855

Hart, A. B. 1954, MNRAS, 114, 17

Hathaway, D. H. 1982, Sol. Phys., 77, 341

—. 1996, ApJ, 460, 1027

Hathaway, D. H., Beck, J. G., Bogart, R. S., Bachmann, K. T., Khatri, G., Petitto, J. M., Han, S., & Raymond, J. 2000, Sol. Phys., 193, 299

Havnes, O. 1970, Sol. Phys., 13, 323

Hill, F. 1988, ApJ, 333, 996

Hill, F., Ladenkov, O., Ehgamberdiev, S., & Chou, D.-Y. 2001, in ESA SP-464: SOHO 10/GONG 2000 Workshop: Helio- and Asteroseismology at the Dawn of the Millennium, ed. A. Wilson & P. L. Pallé, Vol. 10, 219–222

Hindman, B. W., & Brown, T. M. 1998, ApJ, 504, 1029

Hirzberger, J., Gizon, L., Solanki, S. K., & Duvall, T. L. 2008, Sol. Phys., 251, 417

Ichimoto, K., Shine, R. A., Lites, B., Kubo, M., Shimizu, T., Suematsu, Y., Tsuneta, S., Katsukawa, Y., Tarbell, T. D., Title, A. M., Nagata, S., Yokoyama, T., & Shimojo, M. 2007, PASJ, 59, 593

Jackiewicz, J., Gizon, L., Birch, A. C., & Duvall, Jr., T. L. 2007, ApJ, 671, 1051

Jain, R., & Haber, D. 2002, A&A, 387, 1092

Jefferies, S. M., McIntosh, S. W., Armstrong, J. D., Bogdan, T. J., Cacciani, A., & Fleck, B. 2006, ApJ, 648, L151

Katsukawa, Y., Berger, T. E., Ichimoto, K., Lites, B. W., Nagata, S., Shimizu, T., Shine, R. A., Suematsu, Y., Tarbell, T. D., Title, A. M., & Tsuneta, S. 2007a, Science, 318, 1594

Katsukawa, Y., Yokoyama, T., Berger, T. E., Ichimoto, K., Kubo, M., Lites, B., Nagata, S., Shimizu, T., Shine, R. A., Suematsu, Y., Tarbell, T. D., Title, A. M., & Tsuneta, S. 2007b, PASJ, 59, 577

Kobanov, N. I., & Makarchik, D. V. 2004, A&A, 424, 671

Kosovichev, A. G., Duvall, T. L. . J., & Scherrer, P. H. 2000, Sol. Phys., 192, 159

Kosovichev, A. G., & Duvall, Jr., T. L. 1997, in Astrophysics and Space Science Library, Vol. 225, SCORe'96 : Solar Convection and Oscillations and their Relationship, ed. F. P. Pijpers, J. Christensen-Dalsgaard, & C. S. Rosenthal (Dordrecht: Kluwer), 241

Kosovichev, A. G., & HMI Science Team. 2007, Astronomische Nachrichten, 328, 339

Kosovichev, A. G., Schou, J., Scherrer, P. H., Bogart, R. S., Bush, R. I., Hoeksema, J. T., Aloise, J., Bacon, L., Burnette, A., de Forest, C., Giles, P. M., Leibrand, K., Nigam, R., Rubin, M., Scott, K., Williams, S. D., Basu, S., Christensen-Dalsgaard, J., Dappen, W., Rhodes, Jr., E. J., Duvall, Jr., T. L., Howe, R., Thompson, M. J., Gough, D. O., Sekii, T., Toomre, J., Tarbell, T. D., Title, A. M., Mathur, D., Morrison, M., Saba, J. L. R., Wolfson, C. J., Zayer, I., & Milford, P. N. 1997, Sol. Phys., 170, 43

Kosugi, T., Matsuzaki, K., Sakao, T., , T., Sone, Y., Tachikawa, S., Hashimoto, T., Minesugi, K., Ohnishi, A., Yamada, T., Tsuneta, S., Hara, H., Ichimoto, K., Suematsu, Y., Shimojo, M., Watanabe, T., Shimada, S., Davis, J. M., Hill, L. D., Owens, J. K., Title, A. M., Culhane, J. L., Harra, L. K., Doschek, G. A., & Golub, L. 2007, Sol. Phys., 243, 3

Kozu, H., Kitai, R., Brooks, D. H., Kurokawa, H., Yoshimura, K., & Berger, T. E. 2006, PASJ, 58, 407

Lamb, H. 1975, Hydrodynamics (6th ed.; Cambridge: Cambridge University Press)

Leibacher, J. W., & Stein, R. F. 1971, Astrophys. Lett., 7, 191

Leighton, R. B., Noyes, R. W., & Simon, G. W. 1962, ApJ, 135, 474

Lindsey, C., & Braun, D. C. 1990, Sol. Phys., 126, 101

—. 1997, ApJ, 485, 895

—. 2000, Science, 287, 1799

Lisle, J. P., Rast, M. P., & Toomre, J. 2004, ApJ, 608, 1167

Lites, B. W. 1992, in NATO ASIC Proc. 375: Sunspots. Theory and Observations, ed. J. H. Thomas & N. O. Weiss, 261–302

López Ariste, A., Socas-Navarro, H., & Molodij, G. 2001, ApJ, 552, 871

Lynden-Bell, D., & Ostriker, J. P. 1967, MNRAS, 136, 293

Magara, T. 2008, ApJ, 685, L91

Maltby, P., Brynildsen, N., Kjeldseth-Moe, O., & Wilhelm, K. 2001, A&A, 373, L1

Masuda, S., Kosugi, T., Hara, H., Sakao, T., Shibata, K., & Tsuneta, S. 1995, PASJ, 47, 677

Miesch, M. S., Brun, A. S., & Toomre, J. 2006, ApJ, 641, 618

Mitra-Kraev, U., Kosovichev, A. G., & Sekii, T. 2008, A&A, 481, L1

Mizuguchi, A. 2007, Master's thesis, Meisei University

Münzer, H., Schröter, E. H., Wöhl, H., & Hanslmeier, A. 1989, A&A, 213, 431

Nagashima, K., Isobe, H., Yokoyama, T., Ishii, T. T., Okamoto, T. J., & Shibata, K. 2007a, ApJ, 668, 533

Nagashima, K., Sekii, T., Kosovichev, A. G., Shibahashi, H., Tsuneta, S., Ichimoto, K., Katsukawa, Y., Lites, B. W., Nagata, S., Shimizu, T., Shine, R. A., Suematsu, Y., Tarbell, T. D., & Title, A. M. 2007b, PASJ, 59, S631

Nagashima, K., Sekii, T., Kosovichev, A. G., Zhao, J., & Tarbell, T. D. 2009, ApJ, 694, L115

Nagashima, K., & Yokoyama, T. 2006, ApJ, 647, 654

Nakajima, H., Nishio, M., Enome, S., Shibasaki, K., Takano, T., Hanaoka, Y., Torii, C., Sekiguchi, H., Bushimata, T., Kawashima, S., Shinohara, N., Irimajiri, Y., Koshiishi, H., Kosugi, T., Shiomi, Y., Sawa, M., & Kai, K. 1994, IEEE Proceedings, 82, 705

Nigam, R., & Kosovichev, A. G. 2010, ApJ, 708, 1475

November, L. J., Toomre, J., Gebbie, K. B., & Simon, G. W. 1981, ApJ, 245, L123

Ogawara, Y., Takano, T., Kato, T., Kosugi, T., Tsuneta, S., Watanabe, T., Kondo, I., & Uchida, Y. 1991, Sol. Phys., 136, 1

Parchevsky, K. V., & Kosovichev, A. G. 2007, ApJ, 666, L53

Parker, E. N. 1957, J. Geophys. Res., 62, 509

Petschek, H. E. 1964, NASA Special Publication, 50, 425

Pevtsov, A., & Lamb, J. B. 2006, in ASP Conf. Ser., Vol. 354, Solar MHD Theory and Observations: A High Spatial Resolution Perspective, ed. J. Leibacher, R. F. Stein, & H. Uitenbroek (San Francisco, CA: ASP), 249

Press, W. H., Teukolsky, S. A., Vetterling, W. T., & Flannery, B. P. 1992, Numerical recipes in FORTRAN. The art of scientific computing (2nd ed.; Cambridge: Cambridge University Press)

Rajaguru, S. P., Birch, A. C., Duvall, Jr., T. L., Thompson, M. J., & Zhao, J. 2006, ApJ, 646, 543

Rast, M. P. 2003, ApJ, 597, 1200

Rhodes, Jr., E. J., Ulrich, R. K., & Simon, G. W. 1977, ApJ, 218, 901

Rimmele, T., & Schröter, E. H. 1989, A&A, 221, 137

Roddier, F. 1975, Academie des Science Paris Comptes Rendus Serie B Sciences Physiques, 281, 93

Rouppe van der Voort, L. H. M., Rutten, R. J., Sütterlin, P., Sloover, P. J., & Krijger, J. M. 2003, A&A, 403, 277

Scherrer, P. H., Bogart, R. S., Bush, R. I., Hoeksema, J. T., Kosovichev, A. G., Schou, J., Rosenberg, W., Springer, L., Tarbell, T. D., Title, A., Wolfson, C. J., Zayer, I., & MDI Engineering Team. 1995, Sol. Phys., 162, 129

Schou, J., Antia, H. M., Basu, S., Bogart, R. S., Bush, R. I., Chitre, S. M., Christensen-Dalsgaard, J., di Mauro, M. P., Dziembowski, W. A., Eff-Darwich, A., Gough, D. O., Haber, D. A., Hoeksema, J. T., Howe, R., Korzennik, S. G., Kosovichev, A. G., Larsen, R. M., Pijpers, F. P., Scherrer, P. H., Sekii, T., Tarbell, T. D., Title, A. M., Thompson, M. J., & Toomre, J. 1998, ApJ, 505, 390

Schou, J., & Bogart, R. S. 1998, ApJ, 504, L131

Sekii, T., Kosovichev, A. G., Zhao, J., Tsuneta, S., Shibahashi, H., Berger, T. E., Ichimoto, K., Katsukawa, Y., Lites, B. W., Nagata, S., Shimizu, T., Shine, R. A., Suematsu, Y., Tarbell, T. D., & Title, A. M. 2007, PASJ, 59, S637

Sekii, T., & Shibahashi, H. 2003, in ESA Special Publication, Vol. 517, GONG+ 2002. Local and Global Helioseismology: the Present and Future, ed. H. Sawaya-Lacoste, 389–392

Shibasaki, K. 2001, ApJ, 550, 1113

Shibasaki, K., Enome, S., Nakajima, H., Nishio, M., Takano, T., Hanaoka, Y., Torii, C., Sekiguchi, H., Kawashima, S., Bushimata, T., Shinohara, N., Koshiishi, H., Shiomi, Y., Irimajiri, Y., Leka, K. D., & Canfield, R. C. 1994, PASJ, 46, L17

Shimizu, T., Nagata, S., Tsuneta, S., Tarbell, T., Edwards, C., Shine, R., Hoffmann, C., Thomas, E., Sour, S., Rehse, R., Ito, O., Kashiwagi, Y., Tabata, M., Kodeki, K., Nagase, M., Matsuzaki, K., Kobayashi, K., Ichimoto, K., & Suematsu, Y. 2008, Sol. Phys., 249, 221

Simon, G. W., & Leighton, R. B. 1964, ApJ, 140, 1120

Snodgrass, H. B. 1984, Sol. Phys., 94, 13

Snodgrass, H. B., & Ulrich, R. K. 1990, ApJ, 351, 309

Staude, J. 1999, in Astronomical Society of the Pacific Conference Series, Vol. 184, Third Advances in Solar Physics Euroconference: Magnetic Fields and Oscillations, ed. B. Schmieder, A. Hofmann, & J. Staude, 113–130

Stein, R. F., Benson, D., Georgobiani, D., Nordlund, Å., & Schaffenberger, W. 2007, in American Institute of Physics Conference Series, Vol. 948, Unsolved Problems in Stellar Physics: A Conference in Honor of Douglas Gough, ed. R. J. Stancliffe, G. Houdek, R. G. Martin, & C. A. Tout, 111–115

Stix, M. 2002, The sun: an introduction (2nd ed. ; Berlin: Springer)

Strous, L. H., Scharmer, G., Tarbell, T. D., Title, A. M., & Zwaan, C. 1996, A&A, 306, 947

Sweet, P. A. 1958, in IAU Symposium, Vol. 6, Electromagnetic Phenomena in Cosmical Physics, ed. B. Lehnert, 123

Tajima, T., & Shibata, K. 2002, Plasma astrophysics (Cambridge, Massachusetts: Perseus Publishing)

Thomas, J. H. 1985, Australian Journal of Physics, 38, 811

Thomas, J. H., Cram, L. E., & Nye, A. H. 1982, Nature, 297, 485

Thompson, M. J., Toomre, J., Anderson, E. R., Antia, H. M., Berthomieu, G., Burtonclay, D., Chitre, S. M., Christensen-Dalsgaard, J., Corbard, T., De Rosa, M., Genovese, C. R., Gough, D. O., Haber, D. A., Harvey, J. W., Hill, F., Howe, R., Korzennik, S. G., Kosovichev, A. G., Leibacher, J. W., Pijpers, F. P., Provost, J., Rhodes, Jr., E. J., Schou, J., Sekii, T., Stark, P. B., & Wilson, P. R. 1996, Science, 272, 1300

Tsuneta, S., Hara, H., Shimizu, T., Acton, L. W., Strong, K. T., Hudson, H. S., & Ogawara, Y. 1992, PASJ, 44, L63

Tsuneta, S., Ichimoto, K., Katsukawa, Y., Nagata, S., Otsubo, M., Shimizu, T., Suematsu, Y., Nakagiri, M., Noguchi, M., Tarbell, T., Title, A., Shine, R., Rosenberg, W., Hoffmann, C., Jurcevich, B., Kushner, G., Levay, M., Lites, B., Elmore, D., Matsushita, T., Kawaguchi, N., Saito, H., Mikami, I., Hill, L. D., & Owens, J. K. 2008, Sol. Phys., 249, 167

Tziotziou, K., Tsiropoula, G., Mein, N., & Mein, P. 2007, A&A, 463, 1153

Uchida, Y., & Sakurai, T. 1975, PASJ, 27, 259

Ulrich, R. K. 1970, ApJ, 162, 993

Vecchio, A., Cauzzi, G., Reardon, K. P., Janssen, K., & Rimmele, T. 2007, A&A, 461, L1

Wolff, C. L. 1972, ApJ, 177, L87

Woodard, M. F. 1984, PhD thesis, AA(University of California, San Diego.)

—. 2002, ApJ, 565, 634

—. 2006, ApJ, 649, 1140

—. 2007, ApJ, 668, 1189

Zaatri, A., Corbard, T., Roth, M., González Hernández, I., & von der Lühe, O. 2008, Journal of Physics Conference Series, 118, 012090

Zhao, J. 2004, PhD thesis, Stanford University

Zhao, J., & Kosovichev, A. G. 2003, ApJ, 591, 446

Zhao, J., Kosovichev, A. G., & Duvall, Jr., T. L. 2001, ApJ, 557, 384

Zhugzhda, I. D., Locans, V., & Staude, J. 1983, Sol. Phys., 82, 369